Study of Dust Aerosol - Climate Interactions using a Regional Climate Model

Athanasios Tsikerdekis

ΑΡΙΣΤΟΤΕΛΕΙΟ ΠΑΝΕΠΙΣΤΗΜΙΟ ΘΕΣΣΑΛΟΝΙΚΗΣ
ΣΧΟΛΗ ΘΕΤΙΚΩΝ ΕΠΙΣΤΗΜΩΝ
ΤΜΗΜΑ ΓΕΩΛΟΓΙΑΣ
ΤΟΜΕΑΣ ΜΕΤΕΩΡΟΛΟΓΙΑΣ ΚΑΙ ΚΛΙΜΑΤΟΛΟΓΙΑΣ

ΑΘΑΝΑΣΙΟΣ ΤΣΙΚΕΡΔΕΚΗΣ

Πτυχιούχος Γεωλόγος
MSc Μετεωρολογίας Κλιματολογίας και Ατμοσφαιρικού Περιβάλλοντος

ΜΕΛΕΤΗ ΤΩΝ ΑΛΛΗΛΕΠΙΔΡΑΣΕΩΝ ΣΩΜΑΤΙΔΙΩΝ ΣΚΟΝΗΣ - ΚΛΙΜΑΤΟΣ ΜΕ ΤΗ ΧΡΗΣΗ ΕΝΟΣ ΚΛΙΜΑΤΙΚΟΥ ΜΟΝΤΕΛΟΥ ΠΕΡΙΟΧΗΣ

ΔΙΔΑΚΤΟΡΙΚΗ ΔΙΑΤΡΙΒΗ

ΘΕΣΣΑΛΟΝΙΚΗ
2017

ΑΘΑΝΑΣΙΟΣ ΤΣΙΚΕΡΔΕΚΗΣ
Πτυχιούχος Γεωλόγος
MSc Μετεωρολογίας Κλιματολογίας και Ατμοσφαιρικού Περιβάλλοντος

ΜΕΛΕΤΗ ΤΩΝ ΑΛΛΗΛΕΠΙΔΡΑΣΕΩΝ ΣΩΜΑΤΙΔΙΩΝ ΣΚΟΝΗΣ - ΚΛΙΜΑΤΟΣ ΜΕ ΤΗ ΧΡΗΣΗ ΕΝΟΣ ΚΛΙΜΑΤΙΚΟΥ ΜΟΝΤΕΛΟΥ ΠΕΡΙΟΧΗΣ

Υποβλήθηκε στο Τμήμα Γεωλογίας
Τομέας Μετεωρολογίας και Κλιματολογίας
Ημερομηνία Προφορικής Εξέτασης:

29 Σεπτεμβρίου 2017

Τριμελής Συμβουλευτική Επιτροπή

Αναπληρωτής Καθηγητής Πρόδρομος Ζάνης, Επιβλέπων
Καθηγητής Θεόδωρος Καρακώστας, Μέλος Τριμελούς Συμβουλευτικής Επιτροπής
Επίκουρη Καθηγήτρια Ελένη Κατράγκου, Μέλος Τριμελούς Συμβουλευτικής Επιτροπής

Εξεταστική Επιτροπή

Αναπληρωτής Καθηγητής Πρόδρομος Ζάνης
Καθηγητής Θεόδωρος Καρακώστας
Επίκουρη Καθηγήτρια Ελένη Κατράγκου
Επίκουρος Καθηγητής Ιωάννης Πυθαρούλης
Καθηγητής Δημήτριος Μελάς
Κύριος Ερευνητής Βασίλης Αμοιρίδης
Αναπληρωτής Καθηγητής Νικόλαος Χατζηαναστασίου

Αριθμός Παραρτήματος Επιστημονικής επετηρίδας Τμήματος Γεωλογίας: 185

ΜΕΛΕΤΗ ΤΩΝ ΑΛΛΗΛΕΠΙΔΡΑΣΕΩΝ ΣΩΜΑΤΙΔΙΩΝ ΣΚΟΝΗΣ - ΚΛΙΜΑΤΟΣ ΜΕ ΤΗ ΧΡΗΣΗ ΕΝΟΣ ΚΛΙΜΑΤΙΚΟΥ ΜΟΝΤΕΛΟΥ ΠΕΡΙΟΧΗΣ

Στους γονείς μου και στον αδερφό μου.

Προλογικό Σημείωμα

Η σκόνη αποτελεί το πιο σύνηθες αιωρούμενο σωματίδιο στην ατμόσφαιρα. Τα σωματίδια σκόνης παίζουν σημαντικό ρόλο στη διαμόρφωση του κλίματος του πλανήτη είτε άμεσα με την επίδραση των σωματιδίων σκόνης στην ακτινοβολία είτε έμμεσα με την τροποποίηση των μικροφυσικών ιδιοτήτων των νεφών. Καίριας σημασίας καθίσταται και η εναπόθεσή της σε ευαίσθητα ηπειρωτικά και θαλάσσια οικοσυστήματα λόγω των συγκεντρώσεων φωσφόρου και σιδήρου που περιέχει.

Η παρούσα διδακτορική διατριβή στοχεύει στην ανάλυση και στη βελτίωση της προσομοίωσης της σκόνης ως αιωρούμενο σωματίδιο σε ένα συζευγμένο (κλίμα+χημεία) μοντέλο περιοχής, στην αξιολόγηση του οπτικού βάθους της σκόνης χρησιμοποιώντας ένα τρισδιάστατο δορυφορικό προϊόν σκόνης και στην ποσοτικοποίηση της επίδρασης της σε μια σειρά φαινομένων όπου συμμετέχει. Το πρώτο κεφάλαιο αφορά στις φυσικές διαδικασίες εκπομπής, μεταφοράς, εναπόθεσης και αλληλεπίδραση της σκόνης με την ακτινοβολία και το πως αυτές προσομοιώνονται στο κλιματικό μοντέλο περιοχής. Στο δεύτερο κεφάλαιο γίνεται η παρουσίαση του κλιματικού μοντέλου περιοχής RegCM4, των δεδομένων από επίγειες και δορυφορικές παρατηρήσεις, των δεδομένων από μοντέλα επ-ανάλυσης και των δεδομένων από παγκόσμια κλιματικά μοντέλα.

Στο τρίτο κεφάλαιο παραθέτονται τα αποτελέσματα που αφορούν την αξιολόγηση του οπτικού βάθους της σκόνης στο οριζόντιο και κατακόρυφο (προφίλ) επίπεδο με το πρωτοποριακό δορυφορικό προϊόν σκόνης LIVAS. Επίσης, παρουσιάζεται η ανάπτυξη και αξιολόγηση μιας νέας μεθόδου αναπαράστασης των ομάδων μεγέθους σκόνης (dust bins) του μοντέλου όπου το εύρος μεγέθους κάθε ομάδες ορίζεται σύμφωνα με μια φυσική διαδικασία. Το τέταρτο κεφάλαιο διαπραγματεύεται τον ρόλο της βροχόπτωσης στη διηπειρωτική μεταφορά σκόνης πάνω από τον Ατλαντικό και την εναπόθεση της σκόνης στο ευαίσθητο οικοσύστημα της λεκάνης του Αμαζονίου. Στο πέμπτο κεφάλαιο ποσοτικοποιείται η άμεση και η ήμι-άμεση επίδραση της σκόνης στην ακτινοβολία και η επιρροή της στις παρούσες και στις μελλοντικές κλιματικές συνθήκες. Το έκτο κεφάλαιο αποτελεί την ανασκόπηση των κύριων συμπερασμάτων του τρίτου, του τέταρτου και του πέμπτου κεφαλαίου.

Η καινοτομία αυτής της διδακτορικής διατριβής συνοψίζεται στα παρακάτω σημεία. Αξιολογούνται τα αποτελέσματα του οπτικού βάθους της σκόνης με ένα τρισδιάστατο δορυφορικό προϊόν σκόνης, το οποίο δίνει την δυνατότητα να αναγνωριστούν και να αποδοθούν τα σφάλματα της σκόνης σε σφάλματα της μετεωρολογίας του μοντέλου. Εισάγεται μια νέα μέθοδος διακριτοποίησης των ομάδων μεγέθους σκόνης στο μοντέλο RegCM4, που βελτιώνεται τις προσομοίωση των φυσικών διεργασιών εναπόθεσης της σκόνης. Για πρώτη φορά χρησιμοποιείται ένα κλιματικό μοντέλο περιοχής για την εκτίμηση της εναπόθεσης σκόνης στο τροπικό δάσος του Αμαζονίου. Τέλος, ποσοτικοποιείται η επίδραση της κλιματικής αλλαγής στις συγκεντρώσεις της σκόνης για το τέλος του 21ου αιώνα και αναλύεται ο ρόλος της σκόνης στις μελλοντικές κλιματικές προσομοιώσεις.

Σε αυτό το σημείο νιώθω την ανάγκη να ευχαριστήσω τον αναπληρωτή καθηγητή του ΑΠΘ και επιβλέποντα της παρούσας διδακτορικής διατριβής Πρόδρομο Ζάνη. Σ' όλη τη διάρκειά των σπουδών μου, μου παρείχε αμέριστη στήριξη και βοήθεια στις δυσκολίες και στα προβλήματα που προέκυπταν. Με την έγκυρη επιστημονική του καθοδήγηση ξεπέρασα πολλά εμπόδια. Αποκόμισα σημαντικές εμπειρίες με επιστημονικές συνεργασίες, καθώς με εμπιστεύτηκε δίνοντάς μου πολλές επαγγελματικές ευκαιρίες. Πάνω από όλα θα ήθελα να τον ευχαριστήσω για την ανθρώπινη στάση του για τις φιλικές και επιστημονικές μας συζητήσεις, χάρη στις οποίες με ενέπνευσε να αγαπήσω την έρευνα και την επιστήμη της μετεωρολογίας, κλιματολογίας και του ατμοσφαιρικού περιβάλλοντος.

Κατά τη διάρκεια της εκπόνησης της διδακτορικής μου διατριβής είχα την ευκαιρία να επισκεφθώ το πανεπιστήμιο του Michigan (UMICH) στις Ηνωμένες Πολιτείες Αμερικής στα πλαίσια προγράμματος Marie Curie “Regional climate-air quality interactions” (REQUA). Για την ευκαιρία αυτή οφείλω να ευχαριστήσω τον υπεύθυνο του προγράμματος καθηγητή του ΑΠΘ Δημήτριο Μελά. Στο πανεπιστήμιο του Michigan συνεργάστηκα με την αναπληρώτρια καθηγήτρια Allison Steiner την οποία θα ήθελα να ευχαριστήσω θερμά, για την εξαιρετική συνεργασία που είχαμε, την ουσιαστική επιστημονική της καθοδήγηση και την πίστη που έδειξε στην δουλειά μου για τους 8 μήνες που παρέμεινα στην Αμερική. Με βοήθησε να ξεπεράσω πολλά πνευματικά και επιστημονικά εμπόδια και να νιώσω φιλόξενος στο πανεπιστήμιο του Michigan και στην ερευνητική της ομάδα.

Ευχαριστώ θερμά τα άλλα δύο μέλη της τριμελούς συμβουλευτικής επιτροπής του διδακτορικού. Την επίκουρη καθηγήτρια του ΑΠΘ Ελένη Κατράγκου για τις εύστοχες παρατηρήσεις της, τις επιμελείς διορθώσεις της και το αμέριστο επιστημονικό ενδιαφέρον που έδειξε στην δουλειά μου. Τον καθηγητή του ΑΠΘ κύριο Θεόδωρο Καρακώστα καθώς αποτέλεσε ένα σημαντικό δάσκαλο για μένα στα θέματα δυναμικής μετεωρολογίας και μικροφυσικής νεφών.

Επίσης, ευχαριστώ θερμά τα υπόλοιπα μέλη της επταμελούς εξεταστικής επιτροπής του διδακτορικού, τον επίκουρο καθηγητή του ΑΠΘ Ιωάννη Πυθαρούλη, τον καθηγητή του ΑΠΘ Δημήτριο Μελά, τον κύριο ερευνητή του ΕΑΑ Βασίλη Αμοιρίδη και τον αναπληρωτή καθηγητή του πανεπιστήμιου Ιωαννίνων Νίκο Χατζηαναστασίου. Οι επιστημονικές επισημάνσεις τους βελτίωσαν το τελικό αποτέλεσμα και με βοήθησαν να αναδείξω καίρια σημεία της έρευνας μου.

Ένα μεγάλο ευχαριστώ στους φίλους και συνεργάτες, Fabien Solmon, Άρη Γεωργούλια, Ελένη Μαρίνου, Δημήτρη Ακριτίδη, Mathiew Wozniak, James Ciarlo, Γεωργία Αλεξανδρή, Γαρυφαλιά Μαρουγιάννη και Ιωάννη Τεγούλια που μέσα από τις ενδιαφέρουσες επιστημονικές μας συζητήσεις αντιμετωπίστηκαν τεχνικά προβλήματα και αναδείχτηκαν νέες ιδέες για έρευνα.

Ένα θερμό ευχαριστώ σε όλους τους φίλους και ανθρώπους που ήταν στην ζωή μου τα τελευταία χρόνια καθώς χωρίς αυτούς δεν θα ήμουν ο άνθρωπος που είμαι σήμερα και δεν θα μπορούσα να φέρω εις πέρας το παρών έργο. Κλείνοντας θα ήθελα να εκφράσω την ευγνωμοσύνη μου στους γονείς μου, που πάντα με στηρίζουν και μου έδωσαν τις αξίες και τα εφόδια να πορευθώ στην ζωή και τον αδερφό μου Μιχάλη που είναι πάντα παρών όποτε τον χρειαστώ.

Table of Contents

1. Introduction

1.1 Sahara geomorphology and climate

Dust is the most abundant aerosol type in the atmosphere and is mainly produced naturally over barren arid and semi-arid environments (Cakmur et al. 2006). The low-latitude barren environments are mainly concentrated in a belt between 25° and 35° latitude in both hemispheres, where the subtropical anticyclonic descending motion of dry air occurs. These descending flow of dry air form high altitudes, is a part of the large scale atmospheric convection cell Hadley, where air masses rise close to the equator and sink somewhere close to ~30° latitude. The sinking dry air prohibits the evaporated water from rising, thus preventing the adiabatic cooling and any convective overturn, making cloud formation very rare and rainfall non-existent. The absence of cloud development increases the down-welling shortwave radiation that reaches the ground, making the near surface mean temperature to be over 30°C in low latitude deserts.

Sahara is the largest low-latitude and most active desert of the planet and lies under the subtropical ridge over the large land mass of Northern Africa (Prospero et al. 2002) (Figure 1.1). The extent of the desert can be generally delimited from 15°N up to the Mediterranean coast and from the North Atlantic ocean to the Red Sea, where the annual precipitation is lower than 200mm. The mean altitude in the desert is low, around 200m from the mean sea level. Though, there are some high altitude mountain masses like Atlas Mountains (Marocco), Hoggar Massif (Southeast Algeria) Air Mountains (Niger), Tibesti and Ennedi Mountains (Chad) (Engelstaedter et al. 2006) that their peaks reach up to 3000m. The topography influences the surface wind pattern which is the main force that controls the dust production and sets the location of dust source regions (Prospero et al. 2002; Washington et al. 2003). One such example of topography and surface wind pattern combination on the Sahara desert is the Bodélé depression, which is located over northern Chad between the Tibesti and Ennedi mountains and constitutes the most active dust source on the world (Koren et al. 2006; Washington et al. 2009).

The main air masses over the desert are under the continental Tropical (cT) category which is characterized as hot and dry. The intense shortwave radiation is heating the near surface air creating a thermal low which is mostly active during the summer months. The thermal low pressure conditions are restrained in the lower levels of the Troposphere since upper-level subsidence limits low-level hot air from rising. During the cold period of the year the Sahara high pressure dominates over the desert

and almost reach the ground, dissipating the low-level thermal low. The unique location of the Atlas mountain ridge, which stretches over the north-western boundary over the Sahara desert, acts as a barrier that prohibits rainy low-pressure atmospheric systems to reach the northern part of Sahara.

Globally more than 2000 Terragrams (Tg: 1 million tonnes) of dust are emitted to the atmosphere every year. The vast majority of dust particles are quickly deposited close to the source region over land (~75%), while a fraction of the total emitted dust is deposited into the oceans (~25%) (Shao et al. 2011b). Using remote sensing measurements of the Total Ozone Mapping Spectrometer (TOMS) sensor on board of the Nimbus 7 satellite, Prospero et al., (2002), identified various dust sources over the Sahara desert. The two major regions are the Bodele Depression, located at the southern border of the Sahara desert in Chad, and the vast area across the western Sahara which includes portions of Mauritania, Mali and Algeria. These two areas receive very low annual rainfall (100-200mm) and dust production is mainly driven by natural causes due to their unique geomorphology and climate (Goudie and Middleton 2001). Less important dust sources in the Sahara are the Tunisian desert, Libya desert and Nubian desert and northeastern Sudan.

Figure 1.1. Topographical and political map of Northern Africa and Mediterranean. Source: Google maps. Obtained using the "RgoogleMaps" library in R.

1.2 Dust in the atmosphere

Dust in the atmosphere has a multipurpose role affecting significantly, the energy budget of the planet, the transport of organic material like iron and phosphorus to oceanic and terrestrial ecosystems, and contributing to the carbon cycle by influencing the productivity of the ocean and the ocean-atmosphere

CO_2 exchange. Figure 1.2 briefly illustrates the intertwined processes of dust in the atmosphere and its impact on various abiotic and biotic ecosystem.

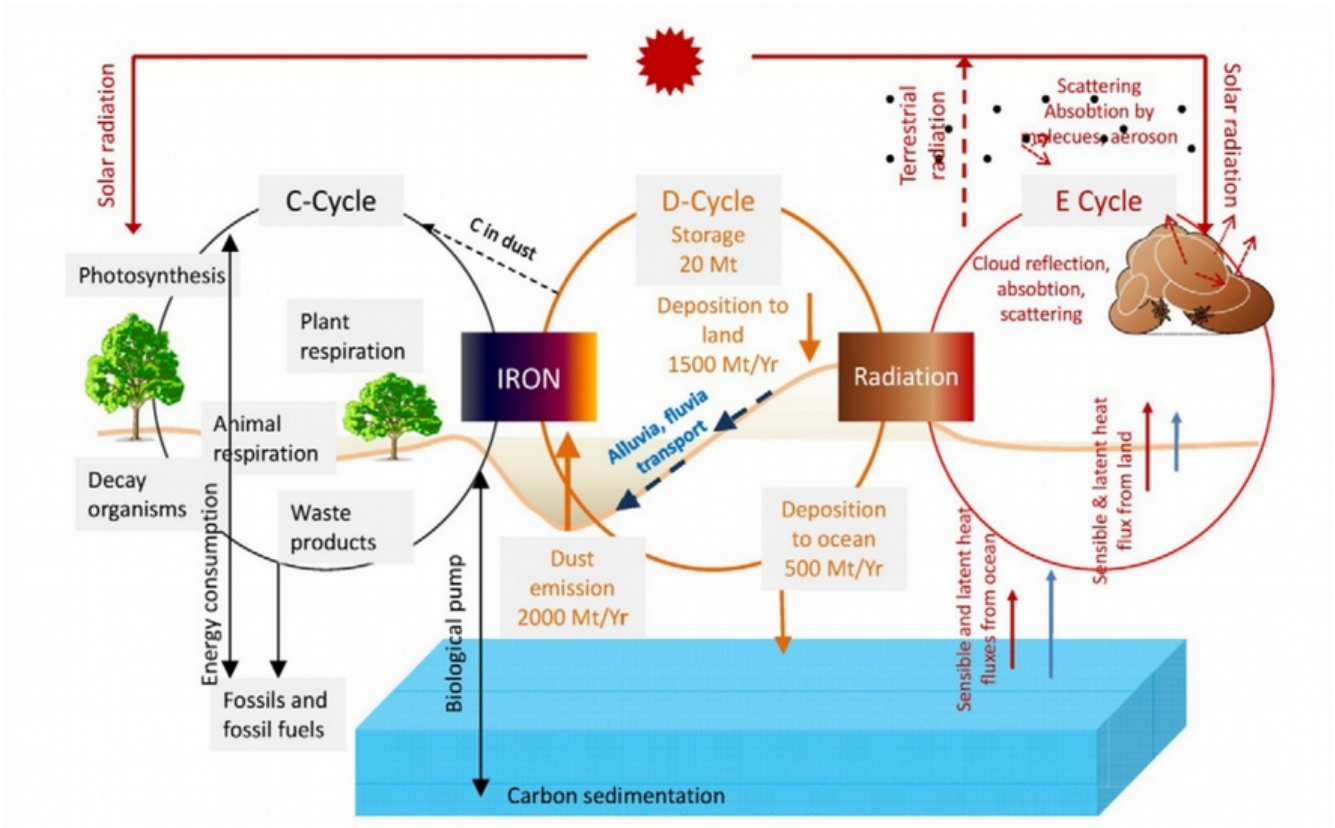

Figure 1.2. Dust cycle (D-Cycle), Energy cycle (E-Cycle), Carbon cycle (C-Cycle) and their interconnected processes in the Earth system. Source: Shao et al. (2011b)

In climate studies dust is an important factor that needs to be taken into account to accurately calculate the radiation budget of the planet (E-Cycle; Figure 1.2). The radiative importance of dust on climate was highlighted by the IPCC 4th Assessment Report (Forster et al. 2007), where it was hinted that the cooling effect of dust can be equal to the warming effect of greenhouse gases in some cases. Dust particles mainly scatter/reflect the incoming shortwave solar radiation and absorb/remit the longwave Earth's radiation depending on their size, color and mineral composition (Liao and Seinfeld 1998; Sokolik and Toon 1999). The primary dust-radiation related processes can be summarized in two categories, the direct and the indirect effect of dust on climate. The direct effect regards explicitly only on the adjustment of radiation due to the presence of dust (scatter, reflect, absorb, remit) in the atmosphere, while the indirect effect concerns the cloud properties changes (cloud fraction, cloud lifetime) due to the presence of dust and how that affects the radiation budget. There is also a hybrid

category which examines how the direct dust effect can change cloud properties (semi-direct) and sometimes locally can be greater even from the direct dust radiative effect. Dust deposition over snow/ice covered areas can also affect the radiative balance of the planet by decreasing surface albedo. Aoki et al. (2005) highlighted that dust deposition over a snow covered area in Japan significantly increased snow impurity in the top 2cm snow layer and decreased surface albedo.

Dust is an important factor on carbon longterm storage deep in the ocean floor (C-Cycle; Figure 1.2). The vast majority of carbon is stored in ocean depth through a process known as “biological pump”. The ocean phytoplankton converts the atmospheric CO_2 to available nutriment which is consumed by the marine zooplankton. Both sea fauna and phytoplankton die and decay, sinking into the ocean bottom accumulating as sediments which can store carbon for millions of years (Shao et al. 2011b). Martin and Fitzwater (1988) proposed the “Iron Hypothesis”, where increased dust deposition provides additional iron supply to the oceans (ocean fertilization) which enhances phytoplankton production and CO_2 intake. This process takes place over extended periods of time. Antarctica ice-core samples showed that during glacial periods, when the atmospheric concentration of CO2 was low, increased dust deposition took place (Martínez-Garcia et al. 2009).

1.2.1 Dust emission mechanisms

The primary mechanisms that can lift dust from the ground can be separated into three distinct processes (Shao et al. 2011a): (a) The direct entrainment of dust particles by the wind (b) disaggregation and (c) saltation, with the later two being the dominant mechanisms that initiate and develop the large intense dust events that we observe in the atmosphere. A descriptive illustration of these processes can be seen in Figure 1.3.

In theory dust particles of all sizes can be aerodynamically lifted from the surface by the force of wind velocity acting upon them (Figure 1.3, a), although in reality this process rarely occurs for particles with diameter smaller than 60μm. The second process that can eject dust particles of all sizes in the atmosphere is known as saltation, which can be interpreted as the bombardment of the soil surface by dust particles usually with diameter between 60μm to 100μm (Figure 1.3, b). These medium size particles, known as saltators, are launched in a ballistic trajectory towards the ground. Upon their impact they splash, ejecting smaller particles (<60μm) as well as equal size particles (60μm-100μm) that can repeat and maintain the same saltating process. A similar mechanism, named disintegration or auto-abrasion, takes place with saltators accumulated from smaller dust grains (Figure 1.3, c). In that

case the aggregated saltator at the time of impact breaks itself into the individual aggregated dust particles ejecting them into the atmosphere. The total dust emission flux ($\mu g \cdot m^{-2} \cdot s^{-1}$) can be derived by the sum of these three processes (Shao et al. 2011a):

$$F_{total} = F_{Entrainment} + F_{Saltation} + F_{Disintegration} \quad \text{(Eq. 1.1)}$$

According to Loosmore and Hunt (2000) the $F_{Entrainment}$ flux in the absence of saltation and disaggregation is an exponential function of wind friction velocity (U^* in $m \cdot s^{-1}$). $F_{Entrainment}$ is responsible for a very small fraction of the F_{Total} since is in the order of 10^0 $\mu g \cdot m^{-2} \cdot s^{-1}$ while $F_{Saltation}$ and $F_{Disintergration}$ are both in the order of 10^2 $\mu g \cdot m^{-2} \cdot s^{-1}$ to 10^3 $\mu g \cdot m^{-2} \cdot s^{-1}$ during typical dust events (Shao et al. 2011a).

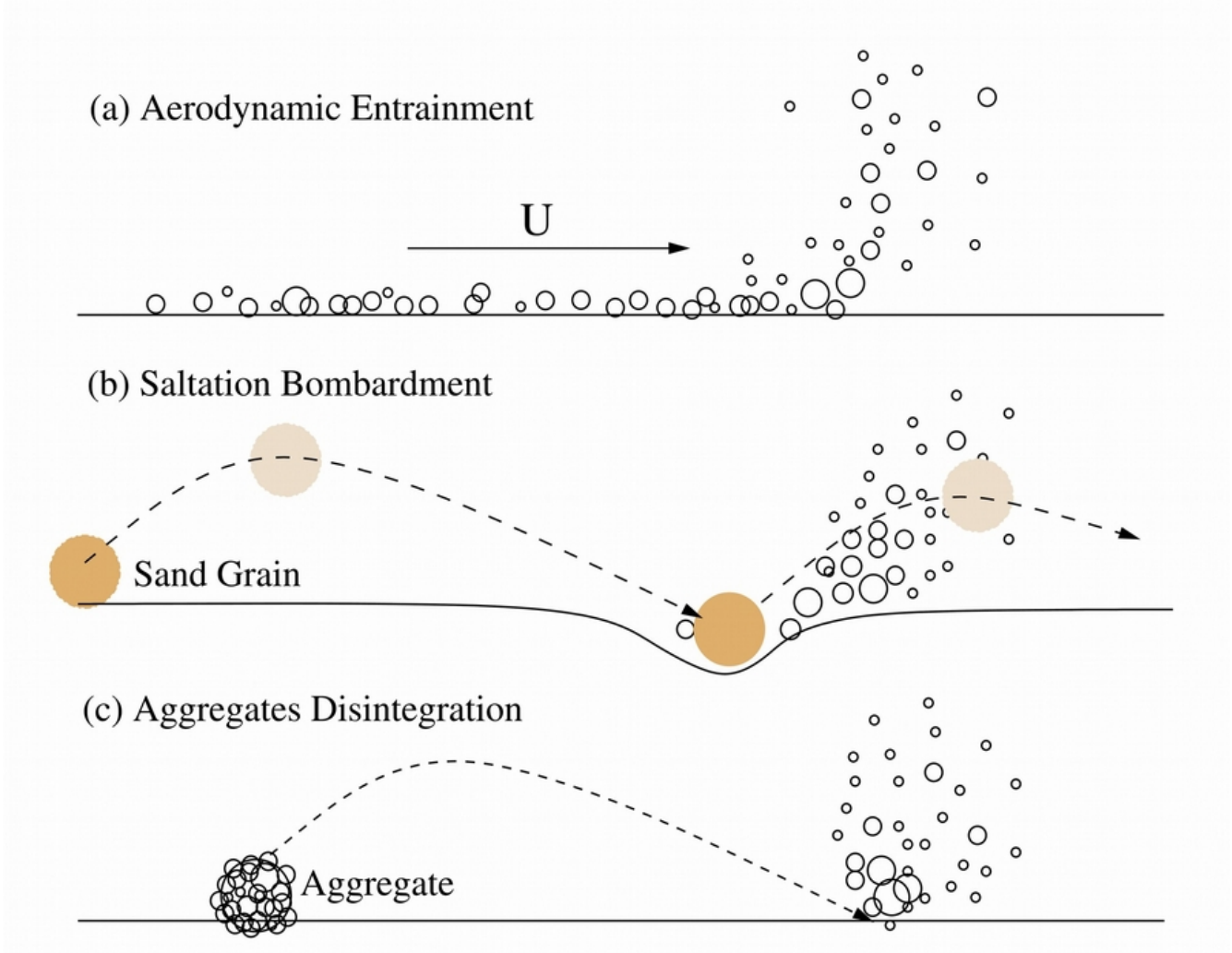

Figure 1.3. Three mechanism of dust emission. Source: Shao et al. (2011).

Saltation is defined as the bouncing motion of sand particles (ranging from 70μm to 1000μm in diameter) across the surface during an erosion event (Shao 2009). The larger particles due to their weight follow a creeping movement on the surface, while the smaller particles are ejected from the ground with an initial steep vertical ascend followed by a more horizontal ballistic trajectory towards the ground (Shao 2009; Kok and Renno 2009). The impact ejects finer particles (<70μm) in the atmosphere which otherwise wouldn't be able to be suspended due to their strong interparticle cohesion forces. Saltation processes can be divided into four stages (Anderson and Haff 1991; Kok and Renno 2009; Kok et al. 2012): (i) The aerodynamic lift of dust particles (saltators), (ii) the trajectories of saltators, (iii) the impact of saltators in the surface (iv) and the modification of wind field in the saltating layer due to the drag of the saltating particles.

Saltation starts when the wind shear stress (τ) can lift the dust particles from the ground. Typically, for loose sand the saltating-creeping motion of dust particles is initiated for τ values close to 0.05 Nm^{-2} (Greeley and Iversen 1985). In aeolian erosion studies wind shear stress is expressed as a function of wind friction velocity (U^*) and air density (ρ_a):

$$\tau = \rho_\alpha \cdot U^{*2} \qquad \text{(Eq. 1.2)}$$

According to Priestley (1959) under neutral conditions where there is no vertical gradient in air potential temperature, the wind friction velocity is a function of wind speed in a certain height (U(z)), the aerodynamic roughness length (Z_0) with values only for smooth surfaces (10^{-3} cm) (Laurent et al. 2008) and the Von Karman constant (k=0.4):

$$U^* = \left(\frac{U(z) \cdot k}{\ln(z/Z_0)} \right) \qquad \text{(Eq. 1.3)}$$

The soil surface variable that determines the initiation of saltation processes is the wind friction velocity threshold (U_t^*) which according to Iversen & White (1982) is the minimal wind velocity that is capable of sustaining particle movement. Basically it describes the ability of the surface to resist wind erosion (Shao 2009). When the wind friction velocity exceeds the value of wind friction velocity threshold ($U^* > U_t^*$) saltation begins. Wind friction velocity threshold, for loose and dry sand on a

smooth surface, is a function of soil particle size and it was initialized by Bagnold (1941) modified by Greeley and Iversen (1985) and updated by Shao and Lu (2000) assuming that the interparticle cohesion forces scale with the diameter of particle:

$$U_t^*(D_p)=\left[f(\mathrm{Re}_{*t})\left(\frac{\rho_p g D_p}{\rho_a}+\frac{\gamma}{\rho_a D_p}\right)\right]^{0.5} \quad \text{(Eq. 1.4)}$$

where ρ_p and ρ_a are the particle and air density respectively and D_p the particle diameter. The function $f(Re_{*t})\approx0.0123$ accounts for the Reynolds number dependency of the aerodynamic drag while $\gamma=(1.65\cdot10^{-4} \sim 5\cdot10^{-4}\ kg\cdot s^{-2})$ relates to the interparticle cohesion forces. Both $f(Re_{*t})$ and γ were adjusted (Shao and Lu 2000) in order $U_t^*(D_p)$ to fit measurements from wind tunnel experiments (Iversen and White 1982).

Assuming that dust particles have a constant density, soil particle size affects particles weight. Thus, larger particles require higher surface friction velocity to initiate dust particle movement. On the other hand the interparticle forces acting upon small dust species (Van der Waals, Capillary, Coulomb forces), that depend on moisture and chemical composition, are higher compared to the larger particles and really hard to estimate since real dust particles are practically not always spherical. Thus, as dust particle shift to smaller sizes the uncertainty in the prediction of U_t^* grows larger (Shao and Lu 2000; Shao 2009). All the above are summarized in Figure 1.4, where the relation between the wind friction velocity threshold ($cm\cdot s^{-1}$) and the dust particles diameter (μm) is illustrated. Due to the opposite dependencies of particles weight and interparticle cohesion forces the minimum wind friction velocity threshold (~20 $cm\cdot s^{-1}$) is found on average size particles with diameter between 60μm to 100μm (Shao and Lu 2000; Shao 2009; Kok et al. 2012; Knippertz 2014). Particles of this size have a higher probability to be emitted first and trigger the initial processes (saltation and disaggregation) of dust cycle in the atmosphere.

Solving the Eq. 1.3 for U(z) and using the theoretical relation between wind friction velocity threshold and particle size in Figure 1.4 we can determine the lowest wind speed at 10m where saltation initiates. For particles with diameter between 60μm to 75μm, wind friction velocity 20 $cm\cdot s^{-1}$ and in a smooth surface ($Z_0\approx10^{-3}$) the U(10m) approaches $7m\cdot s^{-1}$, which is reached pretty frequently in an arid semi-arid environment like the Sahara (Chomette et al. 1999). The corresponding U(10m) value for larger

particles (500μm) is increased slightly to 9m·s^{-1} while for single sub-micron particles sizes (5μm) U(10m) rapidly increases to 25m·s^{-1}. According to this analysis small particles (<10μm) require an unrealistic high wind velocity in order to be directly suspended from the ground, hence the bombardment of larger particles (saltators) towards the ground (saltation) is necessary to initiate their movement (Shao et al. 1993).

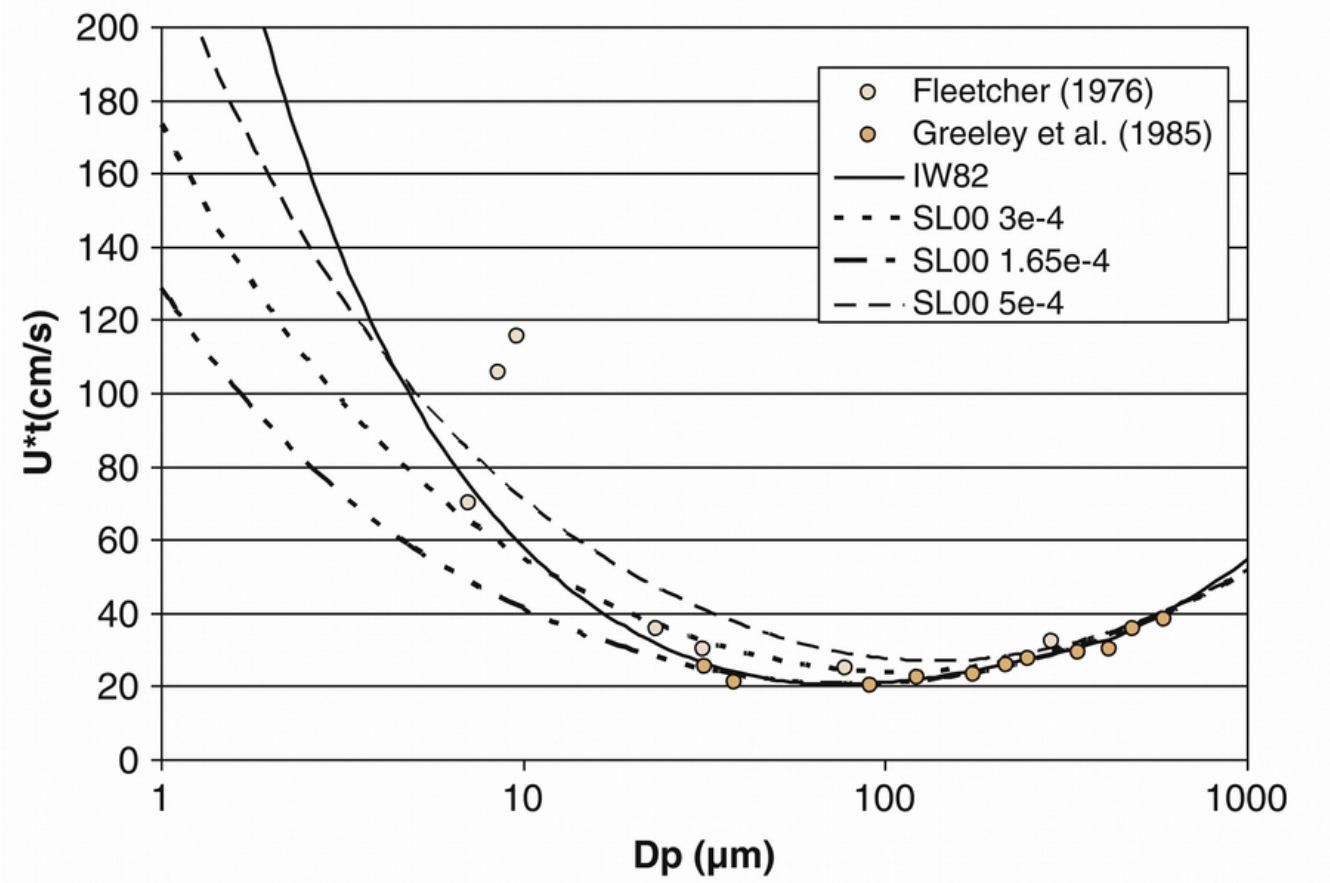

Figure 1.4. Threshold friction velocity relationship with dust particles diameter. Solid line illustrates it by Iversen and White (1982) while dashed lines depict it by Shao and Lu (2000) for various γ values. Beige and brown colored dots represent the experimental measurements by Fletcher (1976a, 1976b) and (Greeley and Iversen 1985) respectively. Source: Knippertz (2014).

After their ejection, saltators trajectory are affected mainly by the force of gravity and the aerodynamic drag of the wind, with a number of other minor forces (Magnus force, Saffman force, Electrostatic force) affecting slightly their movement (Kok and Renno 2009; Kok et al. 2012). Collision between particles is another process that can affect their motion. The midair collision probability between particles is 10%-34% and in a steady state saltation cloud collisions linearly increase with wind friction velocity (Huang et al. 2007). The effect of turbulence in the trajectory of dust particles is important for

saltator particles smaller than 200μm, since larger saltator due to their size are not influenced significantly by the changes in fluid velocity (Kok and Renno 2009).

Upon impact (Figure 1.5), the saltator particle strike the surface in a nearly horizontal angle (θ^{in}). The probability that a saltating particle will rebound after its impact is a function of saltators impact speed (V^{in}) (Anderson and Haff 1991). The speed of the rebounding particle is almost 50-60% of saltators impact speed (Anderson and Haff 1988) which is consistent with Li and Zhou (2007). The rebounding angle (θ^{rb}) of the saltating particles was found to be approximately 40° according to Anderson and Haff (1991), although other studies (Rice et al. 1995; Li and Zhou 2007) note that the rebounding angle of saltators increases with decreasing particle size. The rebounding angles of small saltators (~150μm) are fairly vertical (~90°), while coarser saltator (~500μm) rebounding angle is closer to the horizontal surface (~20°) (Li and Zhou 2007). The number of ejected particles (N^{ej}) after the collision rely upon the mass of the saltator, the mass of ejected particles as well as the impact speed of the saltator (Kok and Renno 2009). The speed of the ejected particles (V^{ej}) is generally half of the impact speed of the saltator (Rice et al. 1995). Therefore, some ejected particles are quickly deposited back in the surface while a fraction of them gain enough momentum by the wind and continue the saltating process by repeating the same cycle (Kok et al. 2012).

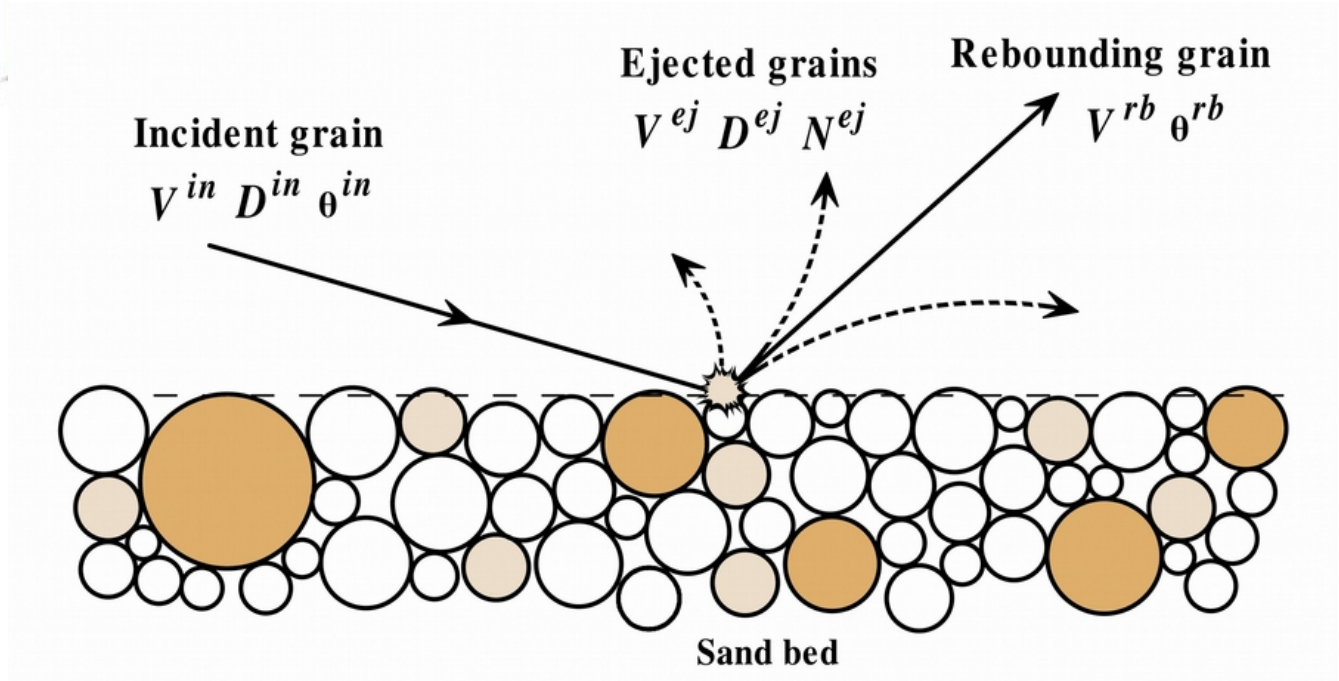

Figure 1.5. Illustration of a saltator (Incident grain) impacting the soil surface and its rebounding course (Rebounding grain). Where V, D, θ, N are the particles velocity, diameter, angle from the horizontal plain and number of the ejected particles respectively. The various trajectories of the ejected particles (Ejected grains) after the collisions are depicted with the dashed arrow lines. Source: Adapted from Li and Zhou (2007).

The wind velocity close to the surface, where saltation takes place, is modified by the presence of saltators. As their number increase so does their drag on the wind. Saltators consume a fraction of wind horizontal momentum, thus decreasing wind velocity in the saltation layer. The total kinetic energy remains the same, but it splits between wind and saltators momentum (Kok et al. 2012). The repeated cycle of emitted dust particles in the atmosphere and their drag on the wind momentum reaches an equilibrium when for every single particle leaving the soil surface there is one particle impacting the soil surface. This state is characterized in literature as steady state saltation.

1.2.2 Dust Transport

Dust emitted from the Sahara desert is transported over long distances. The vast majority of Saharan dust follows a southward path over the Sahel and the Gulf of Guinea (60%), a smaller portion of dust goes westward towards the Atlantic ocean (25%) while a northward and eastward route transports Saharan dust over Europe/Mediterranean (10%) and Middle East (5%) (Shao et al. 2011b). The almost permanent northeasterly winds over the eastern Sahara transports dust southward towards the southern border of the desert and the Sahel Dust Zone (SDZ) (Klose et al. 2010) followed by a westward path driven by the easterlies. All the above mentioned transport paths exhibit strong seasonal characteristics

driven by the periodic movement of the Inter Tropical Convergence Zone (ITCZ) (Ridley et al. 2012; Rodríguez et al. 2015), which affects the dust concentration in Sahel and acts a barrier that limits further southward transport of dust towards the equator due to intense wet deposition.

The small fraction of Saharan dust transported towards the Mediterranean and Europe in episodic events (11.4 $year^{-1}$) has also strong seasonal features and different sources (Israelevich et al. 2012; Gkikas et al. 2013). Eastern Mediterranean receives high amounts of dust in spring while western Mediterranean dust concentration peaks in summer. Dust reaches western Europe through a long path where dust is transported westward towards the Atlantic followed by a northward and an eastward flow, while central and eastern Europe receive high amounts of dust by a shorter direct northward path from Sahara towards Mediterranean and Europe (Israelevich et al. 2012).

The seasonality of dust events in Europe and Mediterranean can be linked to specific synoptic types of weather (Alpert et al. 2004b; Ganor et al. 2010). Annual cycle of dust in these regions can vary from year to year due to the changes in synoptic types of weather or changes in the dust production over the Sahara region (Marticorena and Bergametti 1996; Mbourou et al. 1997; Israelevich 2002). Sahara desert throughout summer and spring is constantly loaded with significant amount of dust (Israelevich 2002) and according to regional climate simulations studies the Dust Optical Depth (DOD) is permanently higher than 0.1 during these seasons (Tsikerdekis et al. 2017b).

Particles size distribution (PSD) changes significantly during transport (Knippertz 2014). Figure 1.6 shows the measured PSD retrieved from the ground-based AERONET station in Cape Verde (Dubovik et al. 2002), which is located at the eastern North Atlantic ocean where the long-range Trans-Atlantic dust transport occurs, and the PSD aircraft measurements from the FENEC 2011 campaign over the Sahara desert (Mali, Mauritania, Algeria) (Ryder et al. 2013). In the first case where dust is transported away from the dust source the particle size peak at 3-4μm while in the case of in-desert measurements PSD peaks between 20-30μm. Coarse particles have a short atmospheric life and the majority of them are deposited soon after their initial lift through gravitational settling. Hence, dry deposition of the coarse particles is mainly responsible for the shift towards lower particle size during transport.

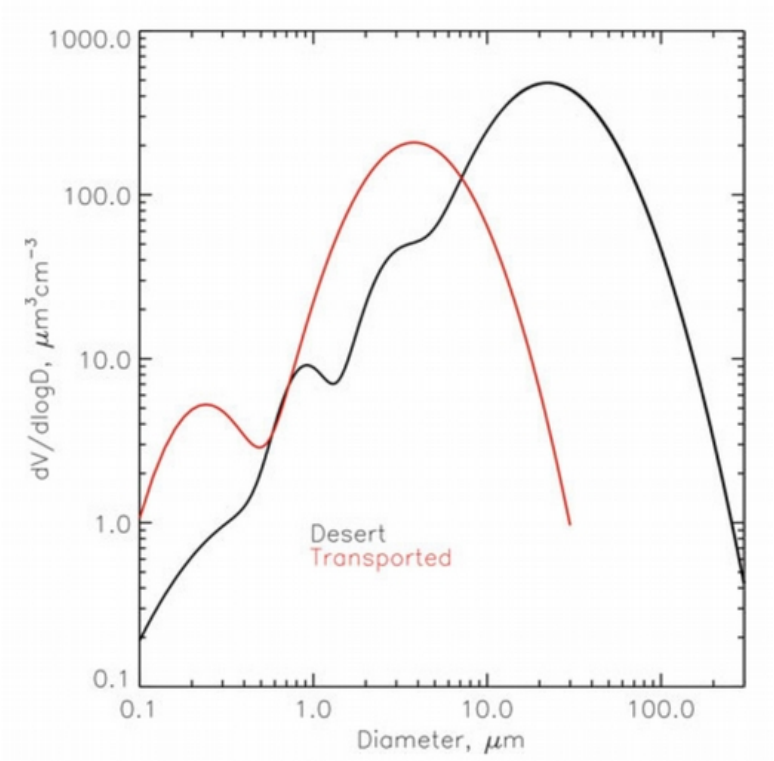

Figure 1.6. Dust Particle Size Distribution (PSD) of AERONET measurements over Cape Verde (red line; Dubovik et al., 2002) and aircraft measurements from the FENEC 2011 campaign which took place over the western Sahara (black line; Ryder et al., 2013). Source: Knippertz (2014)

1.2.3 Sedimentation

Mineral dust is consisted by particles of various shapes and sizes, which strongly influences particles sedimentation. The shape of dust particles affects their deposition rate and it can increase rapidly as particles deviate more from spherical shape (Cheng et al. 1988). For example, flat dust particles (e.g. spheroids) tend to have greater atmospheric lifetime and travel over longer distances in comparison to spherical shape dust particles (Knippertz 2014). The size of dust particle plays also a dominant role in dust dry deposition flux which shapes dust particle size distribution during transport. Fine particles (<2.5μm) can travel over intercontinental distances while the majority coarse particles (>10μm) are deposited hours or minutes after their initial ascend close to the source region.

Dust deposition can be separated into two distinct categories. The first one is dry deposition, which is associated mainly with the weight of the dust particles and the processes of gravitational settling, turbulent mixing and Brownian diffusion (Foret et al. 2006). The second category is wet deposition, which is related either with the in-cloud processes where dust particles act as a cloud condensation and ice nuclei (rainout) or processes where dust particles are located underneath a precipitated cloud

(washout). The relative importance of these processes is again highly dependable on particle size. Dry deposition dominates mainly on coarse particles close to the desert, while wet scavenging processes are equally important or in some cases more important that dry deposition in fine particles over the ocean (Figure 1.7). Thus, in climate dust simulation that includes long-range transport it is important to accurately simulate the spatiotemporal field of precipitation.

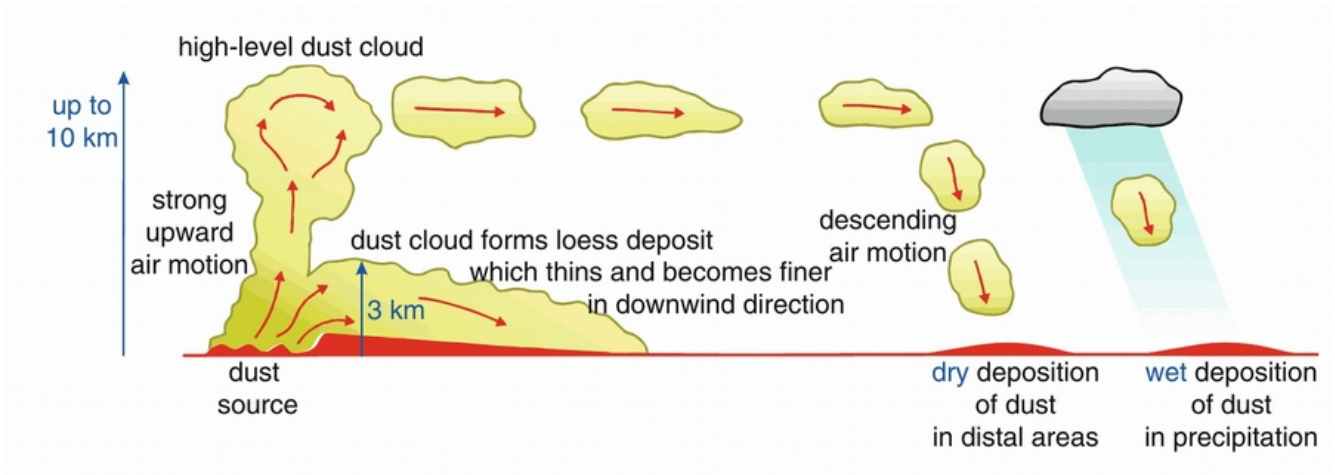

Figure 1.7. Schematic representation of dust transport and deposition mechanisms. Source: Knippertz (2014)

Dry deposition of dust in climate models is often simulated by considering two vertical layers (Slinn and Slinn 1980; Giorgi 1988). The first one is very close to the surface with a width of a few centimeters, where gravitational settling and Brownian diffusion regulates the sedimentation of coarse particles and fine particles respectively. The second layer over the first is called constant flux layer (Slinn and Slinn 1980), gravitational mixing and turbulent mixing through interception and impaction dominate.

The size dependent processes of dust deposition in respect to dust particle diameter were summarized in Foret et al. (2006) by using a simple one-box model with a detailed dry deposition scheme that simulates 1000 dust size bins. The Particle Size Distribution (PSD), Particle Number Distribution (PND) along with the dry deposition velocity, below-cloud scavenging coefficient and size specific extinction coefficient at 550nm are depicted in Figure 1.8. Number dust distribution peaks at ~0.7μm with a slight negative skewness while mass dust distribution reach its maximum value at ~12μm with a fairly positive skewness. Dry deposition velocity is quite low between 0.1μm and 2μm where the size independent turbulent mixing processes dominate since both Brownian diffusion and gravitational settling are limited in this size range. In very fine dust particles (<0.1μm) dry deposition velocity

increases mainly due to Brownian diffusion, while in coarser particles size range (>2μm) gravitational settling dominates. Below-cloud scavenging reaches its minimum value at the same size range as dry deposition velocity (0.1μm-2μm) and increases rapidly above 2μm since the probability to be impacted by the falling rain drops increases. Size specific extinction coefficient peaks at the same size range as the PND which highlights dust's high direct radiative effect efficiency.

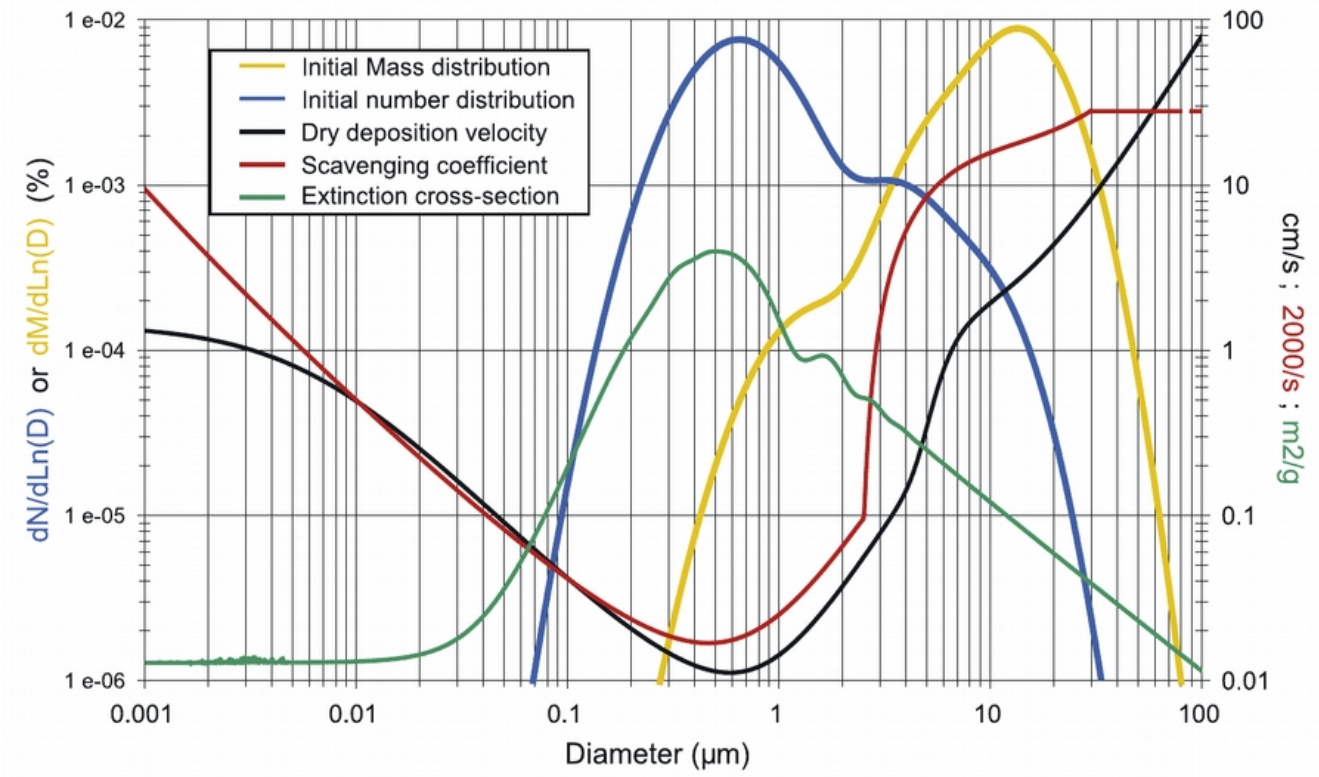

Figure 1.8. Dust mass distribution (yellow line), dust number distribution (blue line) , dry deposition velocity (black line), below-cloud scavenging coefficient (red line) and size specific extinction cross-section (green line) as a function of dust particles diameter from the experiment of Foret et al. 2006. Source: Foret et al. (2006).

1.2.4 Radiative effect of dust (Direct, Semi-direct, Indirect)

The Radiative Forcing (RF) is the energy balance change in the Earth system caused by forced perturbation (Boucher et al. 2013). In the recent IPCC 4th assessment report the RF of gaseous species and aerosols was defined as the downward net radiative flux change at the Top Of the Atmosphere (TOA) by holding the tropospheric variables constant while allowing the stratospheric temperature to reach a new radiative steady state. The Effective Radiative Forcing (ERF) allows the tropospheric and surface variables to change and re-adjust into a new radiative state while the variables that concern the ocean and sea ice remain constant. The ERF approach is considered a more realistic representation of

the atmosphere and is more useful for studying the direct and semi-direct radiative effect of aerosols (Boucher et al. 2013).

Radiative Forcing is calculated from the net radiation fluxes (I_{net}) in a layer. Typically, these layers are the Earth's surface (SRF) or the Top of the Atmosphere (TOA). The net radiation flux is defined as the difference between the downward ($I_{downward}$) and the upward (I_{upward}) irradiances in a layer:

$$I_{net} = I_{downward} - I_{upward} \quad \text{(Eq. 1.5)}$$

While the Radiative Forcing (RF) is defined as the difference between the net radiation fluxes in the presence ($I_{net + Aerosol}$) and absence ($I_{net + NoAerosol}$) of atmospheric aerosol in a specific surface:

$$RF = I_{net+Aerosol} - I_{net+NoAerosol} \quad \text{(Eq. 1.6)}$$

Dust is the most abundant atmospheric aerosol and aerosols in general still constitute a major uncertainty on climate change predictability (Myhre et al. 2013). In order to understand the impact of dust on Earth's climate, it is crucial to interpret the impact of dust on the positive-downward and negative-upward radiative transfer processes in the atmosphere. A conceptual visualization that categorizes the various ways where dust can alter the Earth's radiative budget (direct, semi-direct, indirect effect) is depicted in Figure 1.9.

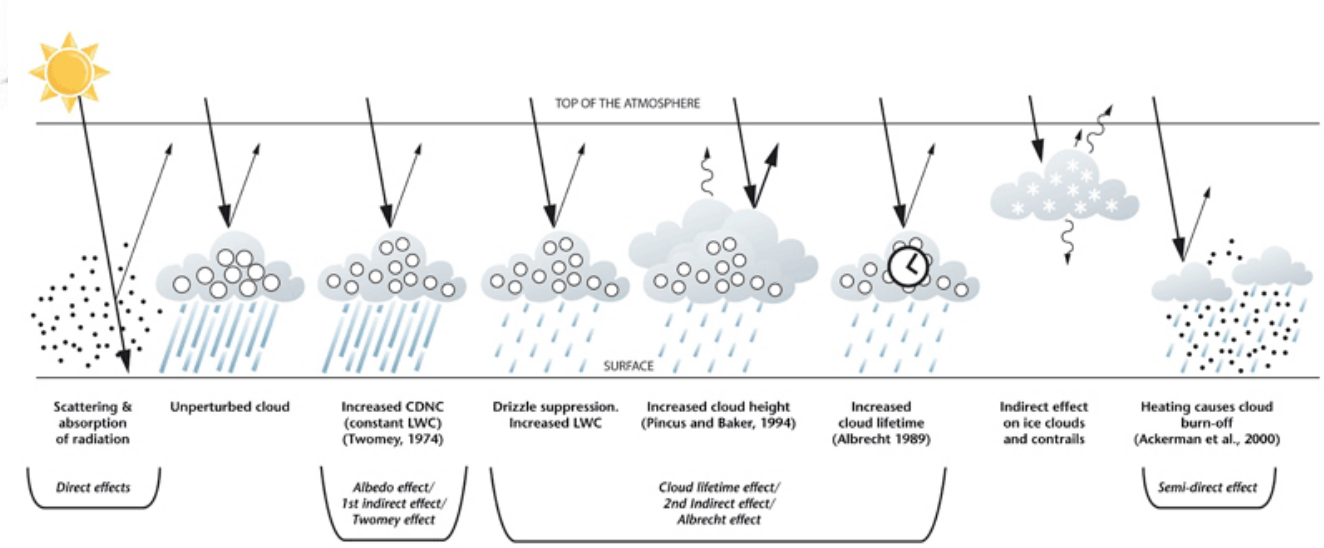

Figure 1.9. Illustration of the direct, semi-direct, first indirect and second indirect effect of aerosol on climate. Filled and open circles represent aerosol particles and cloud condensation nuclei respectively. Solid arrows depict the incident and reflected shortwave radiation while wavy arrows the emitted longwave radiation from Earth's surface and clouds. Source: http://www.metoffice.gov.uk/climate-guide/science/science-behind-climate-change/aerosols, adapted from IPCC Third Assessment report (2007).

Dust particles interact with both the shortwave (SW) and the longwave (LW) radiation, creating a dimming or a heating radiative effect (RE) on climate depending on their size, shape and mineral that compose their optical properties (Liao and Seinfeld 1998; Sokolik and Toon 1999). This RE is known as the dust direct radiative effect (DRE). In the shortwave spectrum (Figure 1.10), the DRE of dust is always negative at the surface (SRF), since the scattering and absorption from dust particles prevents a portion of the positive-downward incoming solar radiation to reach the ground (Choobari et al. 2014). On the other hand, at the top of the atmosphere (TOA) dust can significantly impact the DRE by increasing the surface albedo over dark forested regions and oceans or by decreasing the surface albedo over really bright desert covered areas (FigS 10 at Tsikerdekis et al., 2017) (Liao and Seinfeld 1998).

In the longwave spectrum (Figure 1.11), the DRE of dust is always positive and the radiative role of dust particles is similar to the role of greenhouse gases (Choobari et al. 2014). When dust is present, a portion of the upward Earth's longwave radiation is absorbed, mainly by the coarse dust particles, and remitted to all directions, including back towards the SRF and upward towards the space as longwave radiation. Hence, the longwave radiation leaving the TOA decreases and the arriving longwave flux to the SRF increases (Liao and Seinfeld 1998; Hansell et al. 2010). Hence, dust has a positive feedback effect on climate in the longwave spectrum since the total longwave radiation budget trapped in the atmosphere increases (FigureS 1). It is noted that the dust shortwave DRE cooling is more pronounce

than the dust longwave DRE warming at the surface (Choobari et al. 2014).

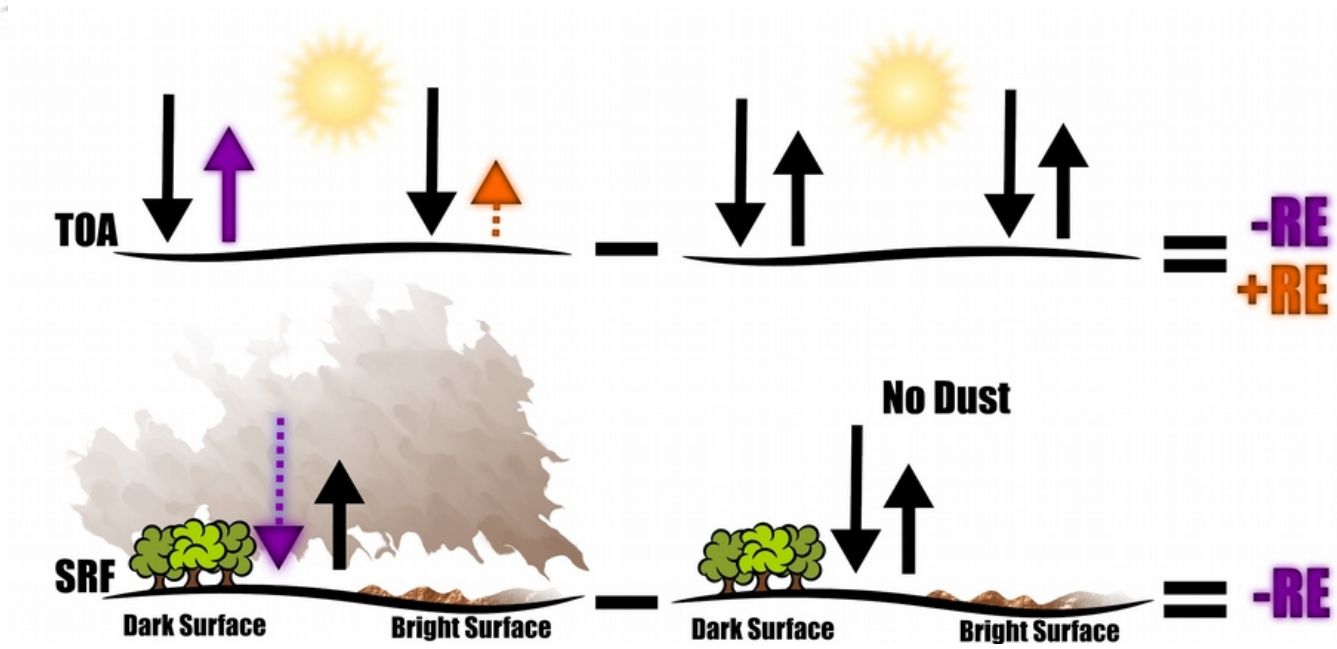

Figure 1.10. Illustration of the dust shortwave radiative effect (RE) at the surface (SRF) and at the top of the atmosphere (TOA). Left and right panel depicts a dust loaded and a dust free atmosphere respectively. Vectors indicate the downward and upward radiation. The purple and the orange colored vectors correspond to a negative and positive radiative effect of dust particles respectively.

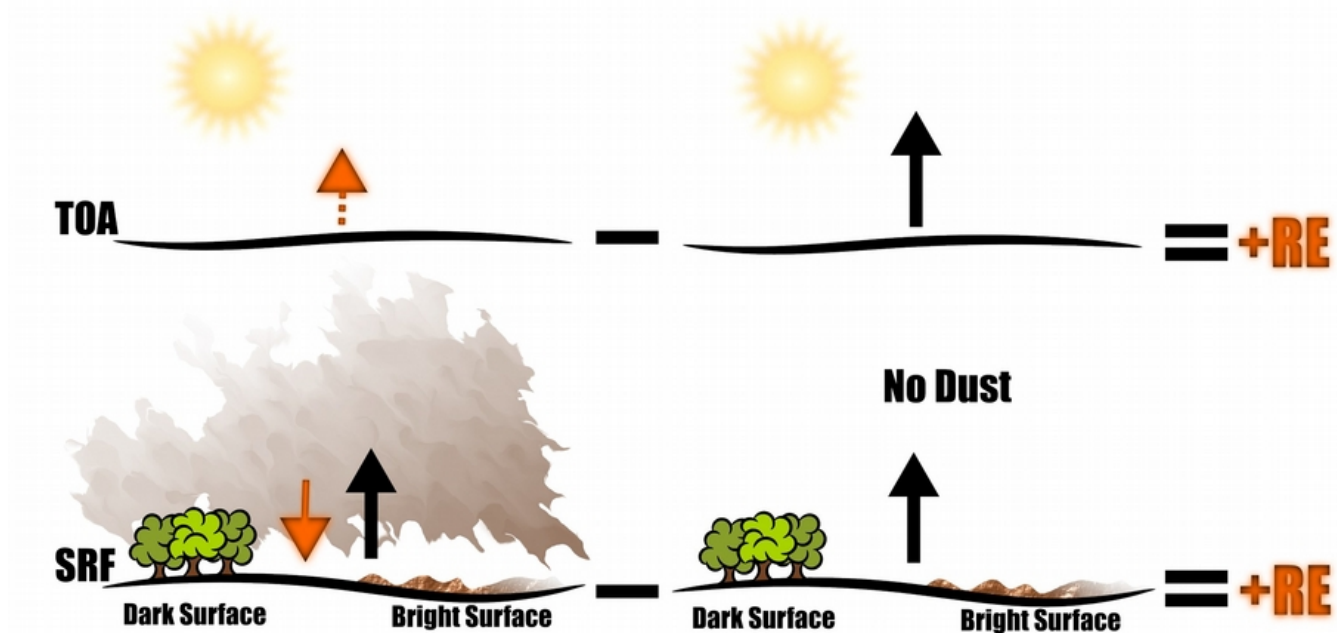

Figure 1.11. Illustration of the dust longwave radiative effect (RE) at the surface (SRF) and at the top of the atmosphere (TOA). Left and right panel depicts a dust loaded and a dust free atmosphere respectively. Vectors indicate the downward and upward radiation. The orange colored vectors correspond to a positive radiative effect of dust particles.

Dust radiative effect is not limited only on the direct scattering/absorbing of sunlight and emissivity in the longwave spectrum. Dust-radiation direct outcome, especially dust infrared emissivity, alters the thermodynamic state of the atmosphere which leads to cloud cover changes, a process known as semi-direct effect (SRE) of dust (Hansen et al. 1997). The SRE that represents the thermodynamic effect of dust on meteorological parameters (e.g. atmospheric pressure, temperature profile and cloudiness) that in turn affects the radiative balance in the atmosphere has not been examined extensively (specific dust events only: Helmert et al. (2007) or studied along with other aerosol types: Nabat et al. (2014)). Based on previous studies the authors in the review paper of Koch and Del Genio (2010) have built a theoretical model where they divided the positive/negative SRE of absorbing aerosols (mainly black carbon and dust) depending on particles placement relative to the clouds (Figure 1.12). When the absorbing aerosols are below clouds, they provide extra longwave heating that enhances upward convective vertical motion, which increases cloud cover causing a negative shortwave SRE. Absorbing aerosols above clouds can either limit shallow cumulus cloud vertical growth, due to temperature inversion atmospheric cap (positive shortwave SRE), or enhance cloud cover of stratocumulus clouds by the stabilization of the boundary layer (negative shortwave SRE) (Johnson et al. 2004; Brioude et al. 2009). The in-cloud or near-cloud absorbing aerosol heating promote cumulus cloud detrainment rate (Ackerman 2000) and reduce cloud height thickness (Hill and Dobbie 2008) causing a positive shortwave SRE. Nevertheless, under the right circumstances a dust layer within the low-mid level cloud can have a negative shortwave SRE. A noteworthy idealized experiment over land with a 2D model by Stephens et al. (2004) showed that the warming effect of a floating dust layer located between 850hPa and 500hPa can create a heat low pressure system in both dry and moist conditions, which creates a low level convergent/divergent below/above the dust layer and promotes convection and cloud formation. The complicated semi-direct effect can either promote or depress cloud formation relative to the vertical distribution of dust and clouds, making it a quite interesting subject of research in aerosol-climate studies, especially if we consider that in some localized cases the absolute value of dust SRE can be greater than the dust DRE.

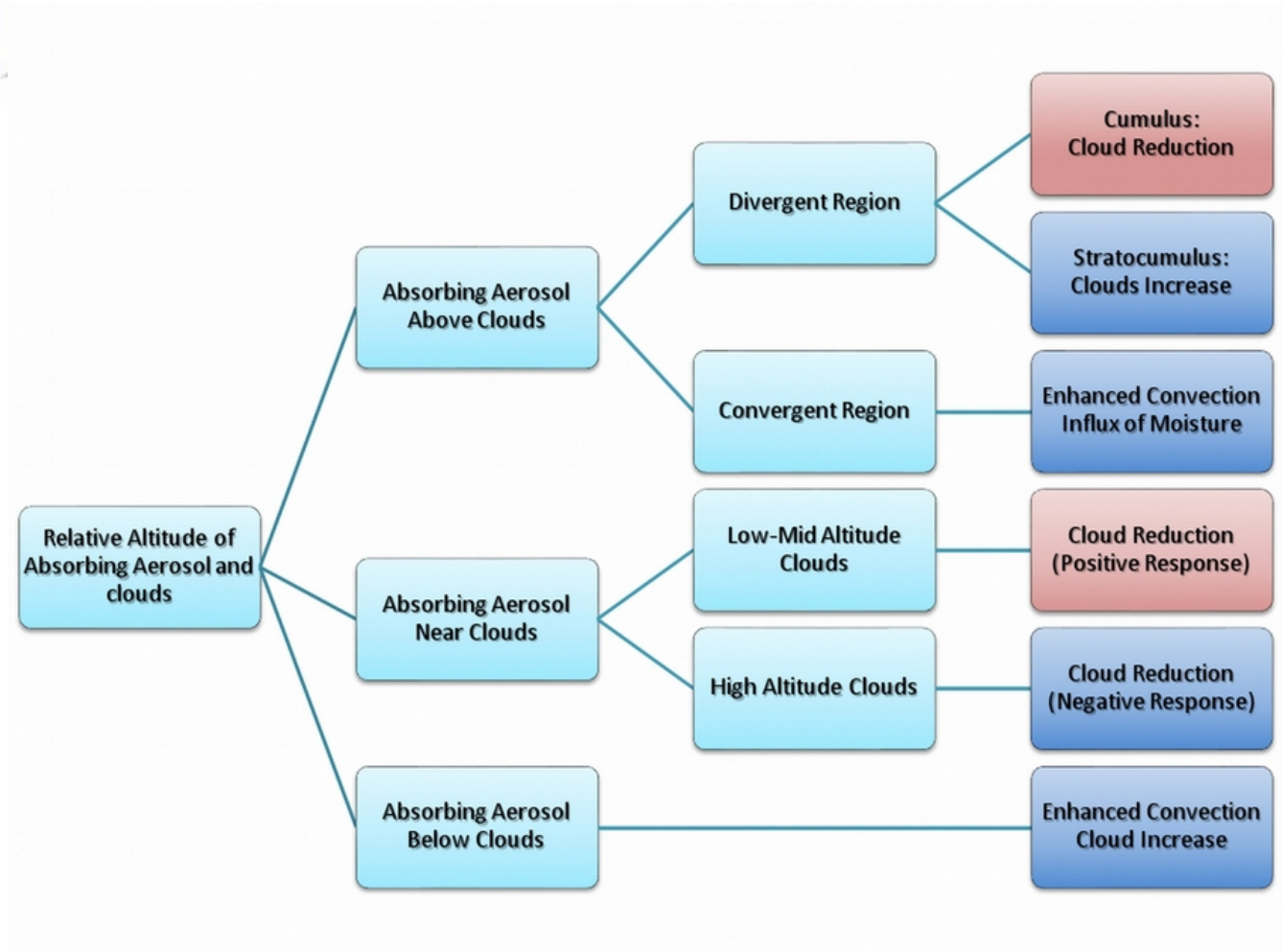

Figure 1.12. Semi-direct effect theoretical framework as proposed by Koch and Del Genio (2010). Red color represents positive and blue negative semi-direct effect of absorbing aerosols Source: Adapted from Koch and Del Genio (2010).

Based on the 4th assessment report of the intergovernmental panel on climate change (Forster et al. 2007), the indirect effect of aerosol can be separated in the “first indirect effect”, also known as “cloud albedo effect” or “Twomey effect” (Twomey 1977; Lohmann and Feichter 2004) and the “second indirect effect”, also known as “cloud lifetime effect” or the “Albrecht effect” (Albrecht 1989; Lohmann and Feichter 2004). The presence of aerosol particles in the first case alters cloud microphysical properties by increasing the in-cloud droplet number, decreasing their radius, keeping the liquid water path fixed and thus increasing cloud albedo and cloud longwave emissivity. The second case cloud microphysical properties are modified in a way that cloud height or lifetime is enhanced.

Dust alters Earth's climate system indirectly by changing the microphysical state and thus the lifetime,

albedo, height and overall the radiative properties of clouds. The size and the chemical composition of dust particles and in-cloud environment can determine if they can act effectively as Cloud Condensation Nuclei (CCN) and Ice Nuclei (IN). Dust particles volume, shape and physico-chemical composition changes during transport through coagulation with other types of aerosol, heterogeneous reactions with gas phase molecules and through in cloud processing (Yamashita et al. 2011). Hence, their optical properties, radiative effect, atmospheric lifetime as well as their CCN and IN capabilities are modified as they age (Sokolik et al. 2001; Karydis et al. 2011). The calcite content of dust particles plays a significant role in CCN efficiency (Gibson et al. 2006) while the kaolinite and illite amount enhances IN effectiveness (Zimmermann et al. 2008). Pure dust particle chemical composition is consisted mostly by a mixture of insoluble minerals (kaolinite, illite, quarts, hematite, goethite, dolomite) and a small fraction of semi-soluble, soluble minerals (gypsum, halite) (Sokolik and Toon 1999; Claquin et al. 1999; Sullivan et al. 2009). Hence, pure mineral dust particles, due to their initial mostly insoluble chemical composition, are considered hydrophobic and theoretically CCN inactive (Fan et al. 2004). But mineral dust is closely associated with nitrate (NO_3) and sulphate (SO_4) formation, due to heterogeneous reactions with sulfur dioxide (SO_2) or nitrogen oxides (NO). Thus, the insoluble minerals that form pure dust particles can progressively evolve into effective CCN in clouds, due to layers of soluble material (e.g. sulphate, nitrate) that formed upon their surface during transport (Knippertz 2014). Mineral dust was found to be the most effective ice-nucleating aerosol type in the planet, playing the role of IN in mixed-phase, stratus and cirrus clouds (Cziczo et al. 2013). It is noteworthy that ice-nucleation in the Amazon forest during the wet season was entirely composed by local emission of biological particles and transported dust particles from the Sahara (Prenni et al. 2009).

1.2.5 Optical properties of dust

The most important parameters to quantify the direct RE and aerosol optical properties are the size specific extinction coefficient, single scattering albedo and scattering phase function which they depend on wavelength, atmospheric humidity, aerosol concentration and size as well as the vertical and horizontal distribution of aerosol particles. The vast majority of chemistry-climate studies uses aerosol optical depth, also known as aerosol optical thickness ($\tau(\lambda)$), to quantify the radiative effect of aerosols and evaluate the output of climate models with satellite or ground-based measurements. Aerosol optical depth measures the extinction (scattered and absorbed) of solar irradiance by airborne particulate

matter. Aerosols block a fraction of the downward incoming solar radiation by absorbing or scattering light, thus preventing it from reaching the ground. It is a dimensionless number and describes the amount and the aerosol radiative effectiveness to scatter and absorb light for the whole vertical column of the atmosphere over a region. Dust optical depth depends on the wavelength (λ) and the optical properties of the airborne particulate matter (size, shape, refractive index, mineral composition), thus its calculation will contain some errors due to the required assumptions on the above-mentioned parameters. A common practice to describe the extinction of light by dust particles, is to define the size specific extinction coefficient ($\sigma_e(\lambda)$) using the Mie theory (Bohren and Huffman 1998) where it assumes that dust particles are spherical. Thus, dust optical depth can be approximately calculated as a function of the wavelength and size of the dust particles:

$$\tau(\lambda) = \sigma_e(\lambda) \cdot C \cdot h \qquad \text{(Eq. 1.7)}$$

where C is the mass concentration of dust and h is the thickness of layer where dust concentration is assumed to be homogeneous.

Several other optical properties are used to quantify the effect of dust on shortwave and longwave radiation. The percent transmission of direct sunlight (T) quantifies the amount of direct sunlight that reaches the surface after it was scattered and absorbed by aerosol particles and it is defined as a simple function of the aerosol optical depth (τ):

$$T = 100 \cdot \exp(-\tau) \qquad \text{(Eq. 1.8)}$$

Aerosol Single Scattering Albedo (SSA) is a measure of the effectiveness of scattering relative to the extinction of the light encountering the atmospheric aerosol particles. It is a dimensionless quantity ranging from 0 to 1 and can be expressed as the ratio of scattering optical depth ($\tau_{Scattered}$) to the total extinct optical depth (τ_{Total}):

$$SSA = \frac{\tau_{Scattered}}{\tau_{Total}} \qquad \text{(Eq. 1.9)}$$

Contrary the CO-Albedo (COA) described the fraction of absorbed radiation which will be remitted as longwave radiation and heat the surrounding environment:

$$COA = 1 - SSA \quad \text{(Eq. 1.10)}$$

Aerosol Phase Function (APF) denotes the angle beam of light relative to the incident beam and describes the angular distribution of scattered light by the aerosol particles. A simplified more commonly used quantity in climate models is the Asymmetry parameter (ASY). ASY is a measure of the preferred scattering direction. A value greater than ASY>1 indicate purely forward scattering (scattering angle>90°) while a value of ASY<-1 indicate completely backward scattering (scattering angle<90°).

1.3 Dust Modeling in RegCM4

1.3.1 Emission

The emission of dust particles is one of the most challenging processes to be implemented in atmospheric climate models, because it depends on various interlinked meteorological and surface properties (Textor et al. 2006; Huneeus et al. 2011). Furthermore, the lack of large scale spatio-temporal continuous emission measurements limits our ability for an accurate and quantifiable validation. Throughout the years a number of emission schemes were developed (Marticorena and Bergametti 1995; Zender et al. 2003; Shao et al. 2011a) in order to replicate the complex processes that control dust uplift from the desert. Although that all of them are based on the same wind friction velocity threshold assumption, they use different approaches on how physical processes and PSD ties with dust emission flux (Alfaro and Gomes 2001; Kok 2011b; Kang et al. 2011) as well as diverse surface characteristics and land schemes (Dickinson et al. 1993; Laurent et al. 2008; Oleson et al. 2013; Menut et al. 2013). The dust emission processes, that as of right now, are implemented in the regional climate model RegCM4 for the surface scheme BATS are discussed. Below there is a descriptive summary in order to organize better dust emission processes followed by a more detailed step by step presentation of the emission schemes of the model.

The model firstly checks if the dust scheme is enabled by the user in the description file (*.in). Then it initiates a loop for all the grid cells of the simulation checking if the landuse is defined as desert or semi-desert and preparing the soil aggregate size distribution for each grid cell. It calculates the wind friction velocity threshold velocity (Shao and Lu 2000) and the wind friction velocity accounting for surface roughness features (Marticorena and Bergametti 1995), soil moisture content (Fécan et al.

1999) and the changes of wind friction velocity profile due to the modification of surface roughness by the saltators (Gillette et al. 1998). Following a series of equations it calculates the emission fluxes for each of the three emission soil modes using the kinetic energy of the saltating particles (Alfaro and Gomes 2001) or for one emission mode following the fragmentation theory proposed by Kok (2011). Finally, it partitions the defined emission flux in 4 (Zakey et al. 2006) or 12 (Tsikerdekis et al. 2017b) distinct dust transport size bins. The majority of these processes are coded in the "mod_che_dust.F90" file under the "RegCM/main/chemlib" path.

The soil consists of a cumulation of various soil particle sizes. This soil mixture is characterized in literature as soil aggregate. The soil aggregate distribution is provided to the model according to 12 United States Department of Agriculture (USDA) textural classes defined using the classic clay/sand/silt triangle of texture composition (Figure 1.13; Hillel, 1982). The geographical distribution of global textural indices are originally defined every 10min in horizontal resolution and in each simulation a texture type characterizes each grid cell according to the dominant texture type within the grid cell (Zakey et al. 2006).

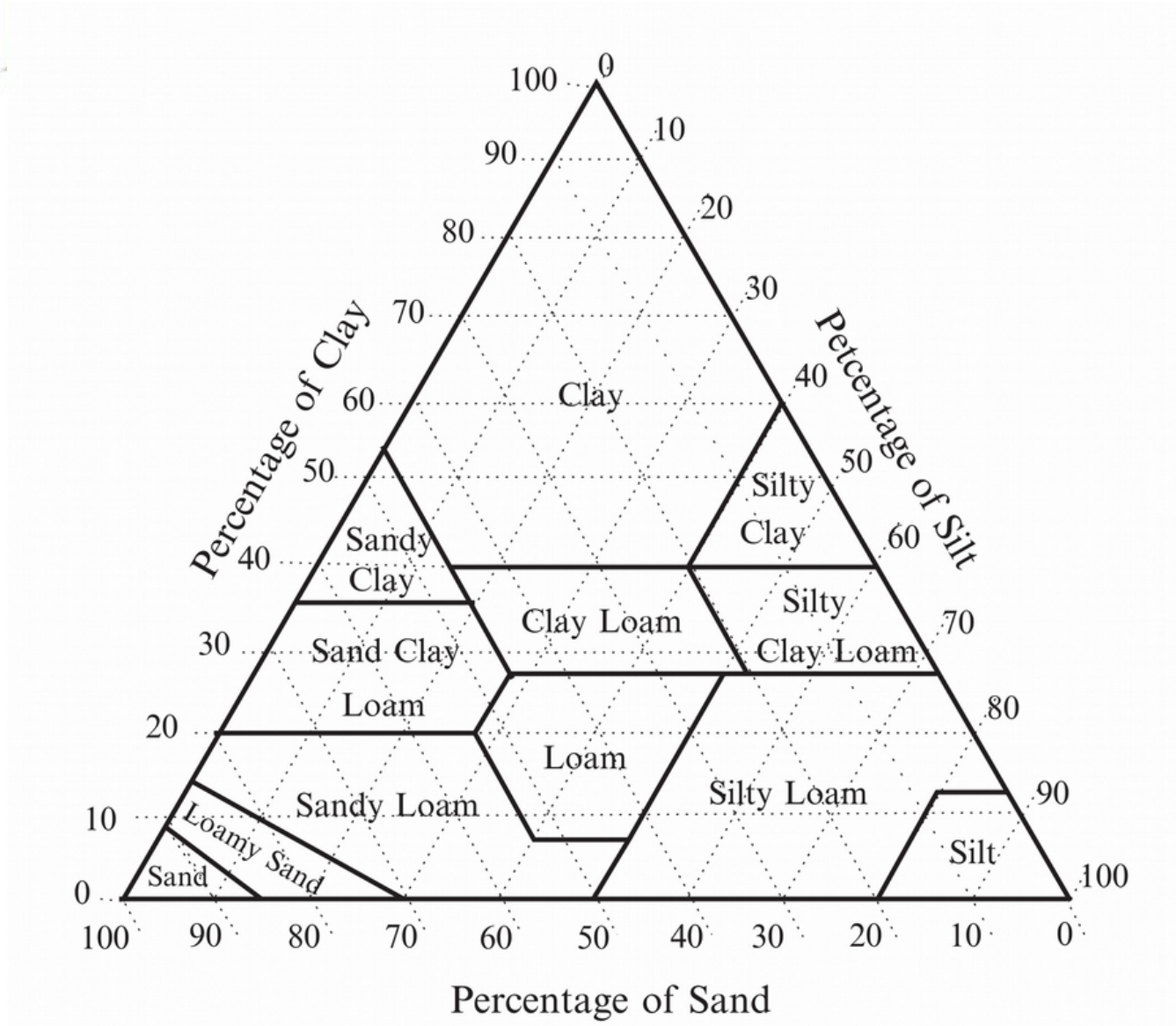

Figure 1.13. Soil texture type defined by the percentage of clay, silt and sand according to the United Stated Department of Agriculture (USDA). Source: Shao (2009).

Upon a desert or a semi-desert grid cell the ideal wind friction velocity (U_*) under a smooth and dry surface is calculated using the Eq. 1.3. This quantity does not take into account that wind friction velocity increases when the surface is irregular and decreases with increasing soil moisture. According to Marticorena and Bergametti (1995) the surface roughness correction factor or efficient factor (f_{eff}) is equal to:

$$f_{eff} = 1 - \left[\frac{\ln\left(\frac{z}{z_{0s}}\right)}{\ln\left(0.35 \cdot \left(\frac{10}{z_{0s}}\right)^{0.8}\right)} \right] \quad \text{(Eq. 1.11)}$$

where z_{0s} is the surface roughness of a smooth surface (10^{-3} cm) and z_m the effective roughness length ($5 \cdot 10^{-3}$ cm). The soil moisture content correction factor (f_w) Fécan et al. (1999) is defined by an empirical function as:

$$f_w = \left[1 + A \cdot (w - w')^B\right]^{0.5} when (w > w')$$
$$f_w = 1 \, when (w < w') \quad \text{(Eq. 1.12)}$$

where A=1.21, B=0.68 and w'=0.0015·(clay%)^2+0.17·(clay%) are based on measurements of wind friction velocity (U^*) for various soil moisture and texture. w is the soil moisture prognostically calculated by the surface scheme BATS.

When saltation initiates saltators increase the apparent region specific surface roughness, consequently wind friction velocity increases (Owen 1964). Therefore, the model includes a third correction based on Gillette et al. (1998) that accounts for the Owen effect adjusting the wind friction velocity under saltation conditions ($U_{*saltation}$) using the wind friction velocity under no saltation conditions ($U_{*no\_saltation}=U_*$), wind velocity at 10m ($U_{(10m)}$) and wind velocity threshold at 10m ($U_{t(10m)}$):

$$U_{*saltation} = U_{*no\_saltation} + 0.3 \cdot (U_{(10m)} - U_{t(10m)})^2 \quad \text{(Eq. 1.13)}$$

where $U_{*no\_saltation}$ and $U_{t(10m)}$ are acquired using the Eq. 3 multiplied by the corrections factors f_{eff} and f_w.

The wind friction velocity threshold is calculated by default according to (Eq. 1.4) defined by Shao and Lu (2000). Although there is a working alternative to calculate wind friction velocity threshold based on Iversen and White (1982).

For surface scheme BATS, the dust emission flux can be estimated following the Alfaro and Gomes (2001) approach where they proposed that increasing wind speed increases the kinetic energy (thus the impact speed) of the saltators which regulates the amount of dust emitted by the model. According to wind tunnel experiments for two completely different textural soil types Alfaro et al. (1998) concluded that the size distribution of aerosol particles released with saltation can be simulated with a three

lognormally distributed modes (i). In that case dust emission flux is calculated for three emission modes (i) associated to each textural type (Zakey et al. 2006) and for the corresponding textural type of the grid cell with the following equation:

$$EmFlux_{Dust}(i) = \frac{\pi}{6} \cdot \rho_p \cdot D_i^3 \cdot N_i \qquad \text{(Eq. 1.14)}$$

where ρ_p is the particles density, D_i is the median diameter associated with the i^{th} emission mode and N_i is the vertical dust particle number flux produced by the saltators integrated over the whole saltators size range. Practically N_i is the flux that shows the number of particles ejected in the atmosphere after the impact of saltators and is given from the function:

$$dN_i(D_p) = \beta \cdot E \cdot \frac{\rho_\alpha}{g} \cdot U_*^3 \cdot (1 + R(D_p)) \cdot (1 - R^2(D_p)) \cdot dSrel(D_p) \cdot \frac{\rho_i(D_p)}{e_i} \qquad \text{(Eq. 1.15)}$$

where β=16300cm·s^{-2}, E is the ratio between the potential erodible to the total surface, ρ_α is the surface air density, g the acceleration of gravity, U_* the wind friction velocity, R the ratio between the wind friction velocity (U_*) and the wind friction velocity threshold ($U_t^*(D_p)$), Srel is the relative surface of soil covered by saltators of diameter D_p to the total soil surface, e_i the binding energy attached to each emission mode and ρ_i the fraction of kinetic energy of the saltator that is used to eject dust particles upon impact with the ground. More details can be found in Marticorena and Bergametti (1995), Alfaro and Gomes (2001) and Zakey et al. (2006) studies.

Alternative dust emission flux can be calculated with the Kok (2011) theory in which he proposed that upon impact the soil surface disintegrates as brittle materials do and that the saltator impact speed does not depend on wind friction velocity (Kok 2011a). He found that the particle size distribution from various locations in the Sahara desert (d'Almeida and Schütz 1983) and in Utah (Goldstein et al. 2005) with a wide range of different soil textures were quite uniform. Thus, he established a theoretical expression of particle size distribution independent of wind friction velocity and soil texture, which is used in RegCM4 to calculate the dust emission flux in one emission mode.

The emission flux calculated either with the Alfaro and Gomes (2001) 3-mode or the Kok (2011) 1-mode aerosol size distribution parameterization originally were partitioned in 4 dust transport bins within the range of 0.01μm to 20μm. According to Foret et al. (2006), 4 size bins are not sufficient to reproduce accurately the transport and deposition of dust in the atmosphere. Thus, a 12 dust size bin

modification was implemented and tested in RegCM4 (Tsikerdekis et al. 2017b).

1.3.2 Transport

Following the calculation of the dust mass emission fluxes, the tracer transport equation (Qian et al. 2001) is applied for each transport bin (Solmon et al. 2006):

$$\frac{\partial \chi_{bin}}{\partial t} = -\bar{V}\cdot\nabla\chi_{bin} + T_{\mathrm{H,\,bin}} + T_{\mathrm{V,\,bin}} + C_{\mathrm{bin}} + E_{bin} + W_{\mathrm{LS,\,bin}} + W_{\mathrm{C,\,bin}} + D_{bin} + \sum\left(Q_{\mathrm{P,\,bin}} - Q_{\mathrm{L,\,bin}}\right) \qquad \text{(Eq. 1.16)}$$

where the terms on the right side of the equation represent advection, horizontal ($T_{H,\,bin}$) and vertical ($T_{V,\,bin}$) turbulent diffusion, vertical transport through cumulus convection (C_{bin}), surface emission (E_{bin}), wet deposition by large scale precipitation ($W_{LS,\,bin}$) and convective rain ($W_{C\,bin}$), dry deposition (D_{bin}) and production ($Q_{P,\,bin}$) and losses ($Q_{L,\,bin}$) due to physico-chemical transformations. Most of these terms are highly dependable on the implemented physical schemes of the model.

The vertical transport due to cumulus convection contains a simplified generic scheme where the tracer (in our case the dust) becomes well mixed between cloud base and cloud top (Kasibhatla et al. 1997). This simplified approach ascends dust from the lower parts of the cloud, where concentrations are higher, towards the top in order to homogenize the dust content throughout the cumulus cloud. This option is available in all convective schemes of the model (Tiedtke 1989; Kain and Fritsch 1990; Emanuel 1991; Grell 1993; Kain 2004). In addition, there is explicit convective transport for the Tiedtke and Emmanuel scheme.

The model can resolve either 4 or 12 transport dust size bins and the particles diameter ranges from 0.09μm to 63μm. A conceptual visualization of the two dust size method is presented in Figure 1.14. In the first case the size bins are separated with the “isolog” method, where the size range of each bin is calculated using an equal, logarithmic separation of the total size range of dust, using the diameter of dust particles (Zakey et al. 2006). In the second case each bin is defined according to the “isogradient” method, where the size range of each bin depends on the dry deposition velocity of dust particles (Foret et al. 2006). The model's sensitivity on the number and delimitation method of dust size bins has been thoroughly investigated and the results show that dust optical depth and total column burden increase by 10% and 4% respectively in the 12-bin approach (Tsikerdekis et al. 2017b). Dust particles in the model do not “age” and their optical properties and size remain the same throughout their atmospheric

life.

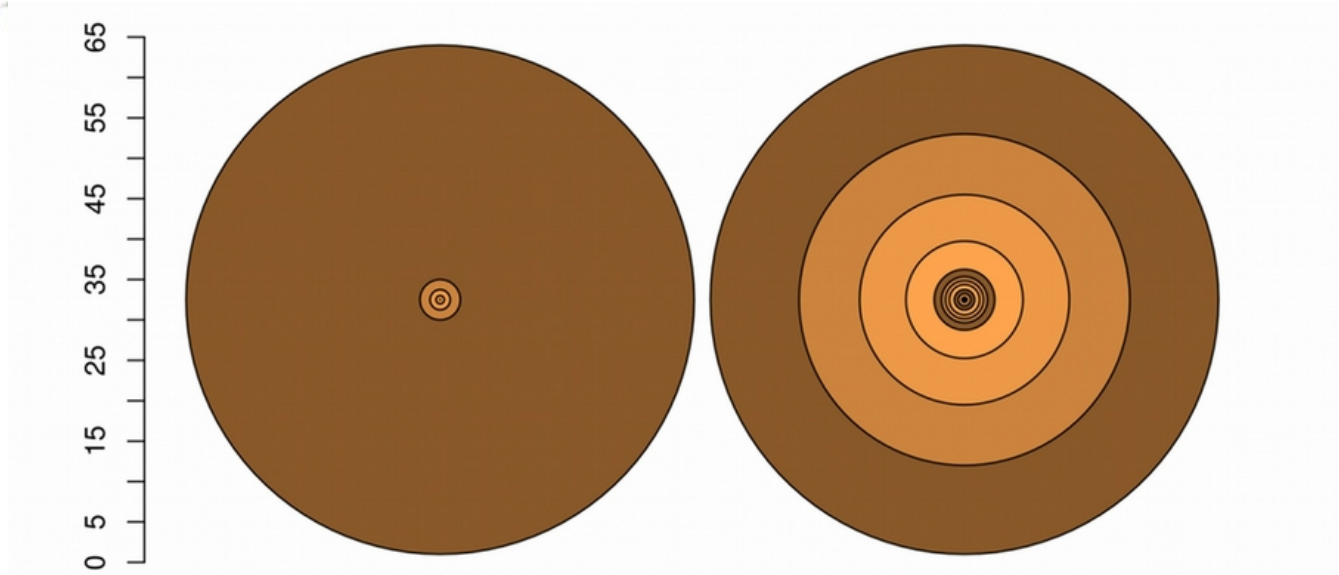

Figure 1.14. A visualization of the 4-bin isolog (left) and 12-bin isogradient (right) approach of dust in RegCM4. The units of the vertical axis is μm.

1.3.3 Deposition

Removal processes in RegCM4 include numerous dry deposition processes and the below-cloud scavenging (washout) wet deposition. Dry deposition scheme of the model includes the processes presented in Zhang (2001), which are based on Slinn (1982) model which was developed for forest canopies. It calculates gravitational settling with a modified version of the Stokes law, which is a function of particle diameter and density. Brownian diffusion acts mainly on small particles (<0.5μm) that are close to the ground. Particles that are larger that 5μm may rebound on the surface, while impaction and interception processes which are a function of land cover characteristics are also included.

Wet deposition processes for large-scale precipitation follow Giorgi (1989) and for convective precipitation Giorgi and Chameides (1986). Below-cloud scavenging include a size-dependent parameterization (Seinfeld and Pandis 1998; Gong 2003a). The detailed in-cloud processes where dust particles can act as CCN and be removed from the atmosphere through precipitation (rainout) is not yet implemented in the model. However a fraction of dust in each size bin is assumed to be incorporated in cloud droplets (Zakey et al. 2006). Dry deposition processes are coded in the “mod_che_drydep.F90” file and wet deposition processes are coded in the “mod_che_wetdep.F90”. Both files are under the “RegCM/main/chemlib” path.

1.3.4 Radiative Impact

The radiative transfer of the shortwave and the longwave can be calculated either with the default radiation scheme of Community Cloud Model (CCM3) or the Rapid Radiation Transfer Model (RRTM). The radiative effect of dust is calculated for each size bin and each the spectral bands of the radiation transfer scheme in use. In the case of the CCM3 scheme there are 9 shortwave and 9 longwave spectral bands ranging between 200-700nm and 700-4550nm respectively. The optical properties of dust are pre-calculated for every size bin and each spectral band of the radiation scheme in use (CCM3 or RRTM) using Mie theory. Due to the high nonlinearity of the Mie calculation, we calculated optical properties for each bin and each spectral band, based on a weighted average on size and wavelength assuming that the sub-size distribution follows Kok (2011a), consistent with the emission size distribution. Size specific dust extinction coefficient, asymmetry parameter and single scattering albedo of CCM3 bands are presented for the 4 and 12 bin methods in the appendix section. Dust extinction of each layer is calculated by multiplying the mixing ratio of each dust size bin and the corresponding size specific dust extinction coefficient for each vertical layer. Dust optical depth is derived by adding up the calculate dust extinctions for each grid. Aerosol optical depth from satellite and ground-based measurements is usually available in 550nm. Thus, the 350-640nm (CCM3) band is used for the evaluation of the model.

The dust Direct Radiative Effect (DRE) of the model is calculated through a double radiation call procedure for each timestep (typically 30 to 60 minutes) of a simulation in clear-sky conditions (cloud-free conditions). In the first call dust particles do not interact with radiation and the atmosphere is considered radiatively dust-free ($RFlux_{Call1}$), where in the second call dust particles reflect, scatter, absorb and re-emit radiation in the shortwave and the longwave spectrum ($RFlux_{Call2}$). By subtracting the radiation fluxes of the second from the first call, we come up with the DRE of dust:

$$DRE = RFlux_{Call2} - RFlux_{Call1} \quad \text{(Eq. 1.17)}$$

The model can optionally forward the changes in radiation due to the presence of dust particles as a temperature tendency in the next temporal timestep. Thus, the combined DSRE feedback on climate can be quantified by an inter-comparison of a radiatively dust-free run (Control) and a radiatively dust-loaded run (Feedback). By subtracting the radiation flux of the Control ($RFlux_{Control}$) from the radiation flux of the Feedback ($RFlux_{Feedback}$) simulation we get the DSRE. We can easily then isolate and

quantify the SRE of dust by subtracting the $DRE_{Feedback}$ from DSRE (Nabat et al. 2014):

$$DSRE = RFlux_{Feedback} - RFlux_{Control} \quad \text{(Eq. 1.18)}$$

$$SRE = DSRE - DRE_{Feedback} \quad \text{(Eq. 1.19)}$$

The model calculates the direct radiative effect of dust even if its effect will not be bypassed as temperature tendency in the next timestep. Thus, the dust run that accounts for the dust direct and semi-direct effect (*Feedback*) will have a slightly different direct radiative effect from the one where dust is just emitted and transported in a radiative dust-free atmosphere (*Control*). In reality, dust interacts with radiation affecting the meteorological parameters. In this manner is considered a more realistic representation of the atmosphere.

1.4 Overview

The manuscript consists of by three distinct result chapters followed by a conclusion chapter. The output of the model is evaluated with various observational dataset and analyzed in order to examine the role of dust on climate and its importance on terrestrial and marine ecosystems. Chapter 3 investigates two different dust size bin discretization methods in RegCM4 and quantifies their differences on dust optical depth, dust column burden and radiative effect. Chapter 4 explores the Trans-Atlantic transport of Saharan dust, its seasonal characteristics, the sensitivity of different convection schemes and their impact on precipitation and the deposition rates over the Atlantic ocean and the phosphorus-limited tropical forest of the Amazon basin. Chapter 5 studies dust direct and semi-direct effect on climate during the first and the last decade of the 21st century. Finally, in Chapter 6 the conclusions and the key remarks of this work are given.

2. Data and Methods

In this Chapter, a dust specific description of the regional climate model RegCM4 is given. Also the pros of using the LIVAS dust product as a reference for the evaluation of the model is analyzed. Finally, a quick overview of the reanalysis ERA-interim dataset and the Climate Research Unit (CRU), CERES, CMSAF and TRMM is provided.

2.1 RegCM4

The Regional Climate Model (RegCM) is a limited area numerical model developed at the National Center of Atmospheric Research (NCAR) and the Abdus Salam International Center for Theoretical Physics (ICTP). Notably, it was the first limited area model used for long-term climate simulations (Giorgi and Anyah 2012). Here we employ the RegCM4, which is described in detail in Giorgi et al. (2012). The hydrostatic core of the model, which is based on the fifth version of the Mesoscale Model (MM5) (Grell et al. 1994), restricts the minimum horizontal resolution of the model to 10km. Thus, the regional scale convective precipitation on RegCM4 is resolved through various convective scheme parameterizations (e.g. Tiedtke 1989; Kain and Fritsch 1990; Emanuel 1991; Grell 1993).The vertical computation of the atmosphere is applied on sigma levels. Land-Atmosphere interactions are analyzed with the Biosphere-Atmosphere Transfer Scheme (BATS) (Dickinson et al. 1993), while there is a recently implemented alternative option to use the Community Land Model (CLM4.5) (Oleson et al. 2013). The radiation transfer scheme used in RegCM4 is based on the NCAR Community Climate Model version 3 (CCM3) (Kiehl et al. 1996) with the additional option of the correlated-k Rapid Radiation Transfer Model (RRTM) (Mlawer and Clough 1997; Mlawer et al. 1997) to improve the model representation of the radiation processes in the longwave spectrum (Iacono et al. 2000). Resolved scale precipitation is parameterized with SUBEX scheme (Pal et al. 2000) and the processes in the Planetary Boundary Layer (PBL) can be parameterized either with the modified Holtslag scheme (Holtslag et al. 1990) or the UW-PBL scheme (Bretherton et al. 2004).

The chemical part of the model contains gas phase chemistry (Shalaby et al. 2012; Steiner et al. 2014) as well as natural and anthropogenic aerosols (Solmon et al. 2006; Zakey et al. 2006; Zakey et al. 2008). Most of the natural aerosols, such as dust and sea salt, are driven by RegCM4 meteorology, while all the anthropogenic aerosols, organic carbon, black carbon and pollen require emission datasets.

The dust emission scheme is activated in a grid cell when the friction velocity, resolved as a function of

RegCM4 simulated wind speed and surface roughness, is higher than the minimum friction velocity threshold. Dust saltation flux is calculated following Marticorena and Bergametti (1995) and Zakey et al. (2006), while the calculation of dust aerosol vertical flux from the saltation flux follows Laurent et al. (2008).

Particle size distribution (PSD) of the emitted dust and it's relation to surface wind conditions can be modelled using either Alfaro and Gomes, (2001) or Kok theory (2011a). The first theory, based on wind tunnel experiments, demonstrated that increasing wind speed close to the surface increases the portion of fine dust particles emitted (Alfaro et al. 1997). Based on these results Alfaro and Gomes (2001) suggested that the saltator kinetic energy increases with wind speed, thus the impact produces more fine particles and affects the PSD of dust. On the other hand Kok (2011a) represented the impact of saltator on the surface to act as the fragmentation of brittle materials and suggested that the saltator impact speed does not depend on wind friction speed (Kok 2011a). Using observational data he established a theoretical expression of particle size distribution independent of surface wind speed. Kok PSD theory shows a significant improvement of the simulated RegCM4 dust optical depth over the European and Northern African domain (Nabat et al. 2012), thus this parameterization was used in these simulations.

Surface roughness and soil moisture, which are essential for the calculation of threshold friction velocity and saltation fluxes, are provided by the surface scheme BATS (Zakey et al. 2006). The soil aggregate distribution used to determine threshold velocity and the saltation flux, differs from Zakey et al. (2006) and is taken from Menut et al. (2013), based on the FAO texture class and spatial distribution. Emission processes take place only over desert or semi-desert grid cells. RegCM4 also accounts for possible subgrid partial desert cover emissions on grid cells dominated by different types of soil and soil texture.

Following the calculation of the dust mass emission fluxes, the tracer transport equation is applied for each transported bin (Solmon et al. 2006). The equation includes transport of the tracers through resolvable winds, horizontal and vertical turbulent diffusion as well as vertical transport due to cumulus convection. The default number of dust size bins that are resolved for transportation in RegCM4 are four (Zakey et al., 2006) with the selection of each size bin defined according to the diameter of dust particles. The size range of each bin is calculated using an equal, logarithmic separation of the total size range of dust, using the diameter of dust particles. This method creates some biases that depend on how

representative the selected size bins are compared to the actual dust particle size distribution in each bin. Following the methodology of Foret et al. (2006), we have implemented a new dust size discretization scheme that resolves twelve dust transport size bins instead of four. The specification of each bin is linked to the gradient of dry deposition velocity as a function of particle diameter. When the change rate of dry deposition velocity to particle size is high, more bins are created on that specified size range, while the opposite happens when the rate changes are slower. The improved partitioning of dust size bins as well as the higher number of bins theoretically enhances the representation of physical removal processes during transport, the estimation of the effective radius of dust particles and the calculation of dust optical properties. Each transported bin is considered as a distinct tracer, which assumes that there is no mixing between the dust size bins.

Removal processes through dry deposition and wet deposition (washout) are included in the model. Dry deposition includes gravitational settling (a function of, particle size and density), brownian diffusion (acts mainly on small particles close to the ground) and turbulent transfer as well as impaction, interception and particle rebound (Zhang 2001). Wet deposition processes include a size dependent washout scavenging parameterization (Seinfeld and Pandis 1998; Gong 2003b) and occurs for a small fraction of dust (10%) considered as soluble.

The optical properties of dust are pre-calculated for every size bin and each spectral band of the radiation scheme in use (CCM3 or RRTM) using Mie theory. Due to the high non-linearity of the Mie calculation, we calculated optical properties for each bin and each spectral band, based on a weighted average on size and wavelength assuming that the sub-size distribution follows Kok (2011a), consistent with the emission size distribution. We ensure that the 12 and 4 bins options cover the exact same total size range and that the integrated optical properties over the whole distribution are conserved regardless of the number of bins. Figure 2.1 depicts the dust specific extinction coefficient, single scattering albedo and asymmetry parameter for both binning options. The differences for all the optical parameters are relatively small, because the calculations were performed for multiple effective particle radii within the range of each size bin and averaged in the end, instead of using the mean effective radius of each size bin (Figure 2.2). Using this method the optical properties between the two experiments are almost identical. The spectral band closer to 550nm (350-640nm in CCM3) is used for evaluation against most satellite derived aerosol optical depth and extinction products.

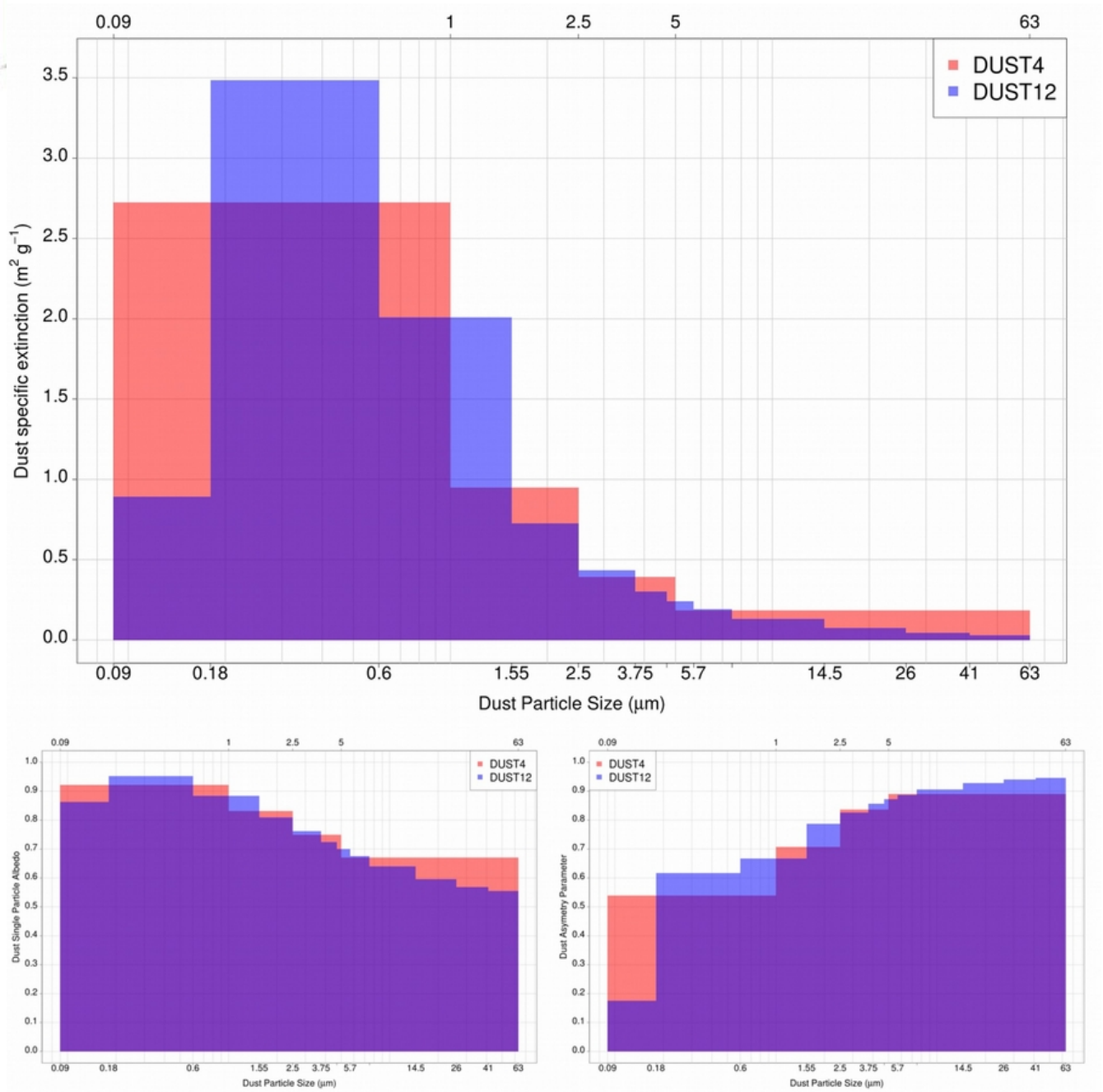

Figure 2.1. Dust bin specific extinction coefficient, single-scattering albedo (SSA) and particle asymmetry parameter on the 350–640 nm spectral band. Red coloring represents the 4-bin experiment and blue the 12-bin experiment. The top and bottom axes represent the dust article diameter limits of the 4 and 12 dust size bins, respectively.

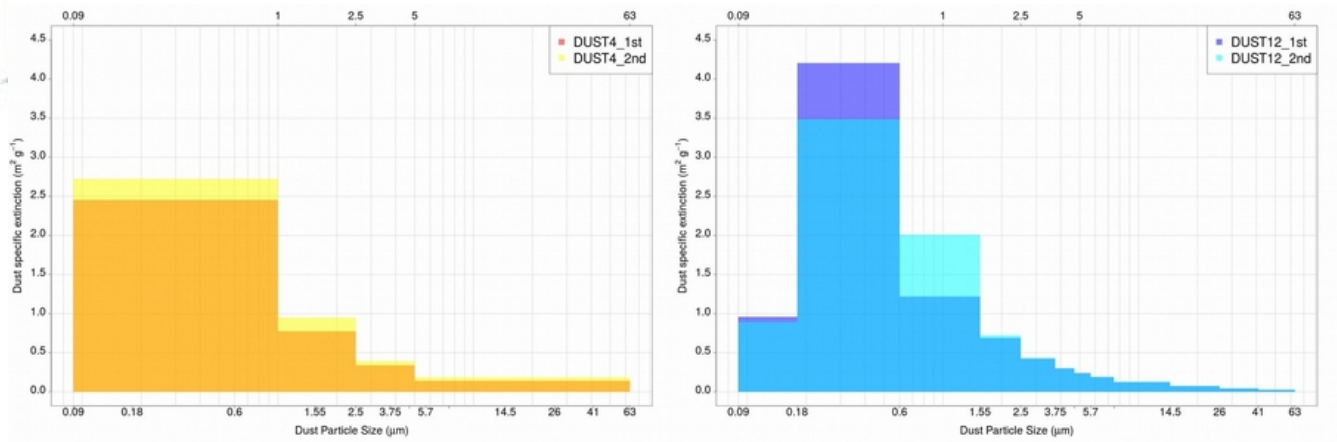

Figure 2.2. Dust bin specific coefficient for 4 and 12 dust size bins. The first method uses as effective particle radius the mean 5 diameter of each size bin in order to calculate the extinction coefficient, while the 2nd method calculates the extinction coefficient for multiple radii within the range of each size bin and average them in the end

In the simulation the default radiation scheme CCM3 is used to retain the same meteorological fields between the two binning experiments. In the current version of RegCM4, the RRTM scheme calculates cloud-radiation interaction using a Monte Carlo Integration of the Independent Column Approximation (McICA) (Pincus 2003). The McICA method, although it provides a more detailed and complicated perspective on the horizontal and vertical radiative structure of the clouds, it introduces a random generated noise even when simulating the exact same experiment. In his work, Pincus (2003) accurately highlights that this random generated noise can be significantly reduced to zero with enough ensemble members. But sensitivity tests with RegCM4 show that the changes in the radiative effect between the two dust bin partitioning methods are already small, thus the results can be significantly altered even with the small perturbation contained in an ensemble mean. A downside of the CCM3 scheme is the simplistic representation of the longwave spectrum as far as the dust particles. In Section 3.3 the relevant impact of the binning methods is discussed in the longwave radiative spectrum between the two radiative transfer schemes.

2.2 LIVAS

The “LIdar climatology of Vertical Aerosol Structure for space-based lidar simulation studies” (LIVAS;Amiridis et al., 2015), is a 3-dimensional global climatic dataset derived from CALIPSO measurements and funded by the European Space Agency (ESA). CALIPSO obtains high resolution profiles of the attenuated backscatter of aerosols and clouds at 532nm and 1064nm, and retrieves aerosol optical properties below optically thin clouds, in clear skies and above clouds (Winker et al.

2009). Thus, in regions with frequent optically thick clouds, aerosol measurements are limited. In regions with an absence of clouds like the Sahara desert, measurements of aerosols species (most likely dust) are available more frequently.

LIVAS utilizes Level 2 (Version 3) product of CALIOP measurements (Amiridis et al., 2015). The CALIPSO Level 2 database determines the vertical location of cloud/aerosol layers (Vaughan et al. 2009), distinguishes the clouds from the aerosol layers (Liu et al. 2009), identifies aerosol layers into six subcategories (dust, marine, smoke, polluted dust, polluted continental and clean continental; (Omar et al. 2009) and calculates the AOD for each selected layer (Young and Vaughan 2009).

The LIVAS extinction dust product is corrected for the Lidar Ratio (LR) based on multi-year measurements performed by the ground-based lidar stations of the EARLINET lidar network (https://www.earlinet.org) and intensive campaigns in different dust regions around the globe (Wandinger et al. 2010; Hänel et al. 2012; Baars et al. 2016). The LR of dust particles depends on their refractive index and may vary for aerosols of the same type. The refractive index values rely upon the composition of dust and most importantly on the relative proportion of clay-sized mineral illite in dust (Schuster et al. 2012). Thus, regions with different physiochemical dust characteristics leads to different LR values. The 0.3.1 version of LIVAS separates the globe into three regions, specified based on known dust sources and loadings with specific physio-chemical composition and LR for each region. The globally LR value 40sr used in CALIPSO retrieval algorithm (Omar et al. 2009) was replaced with region specific LRs of 40sr, 50sr and 55sr (Figure 2.3).

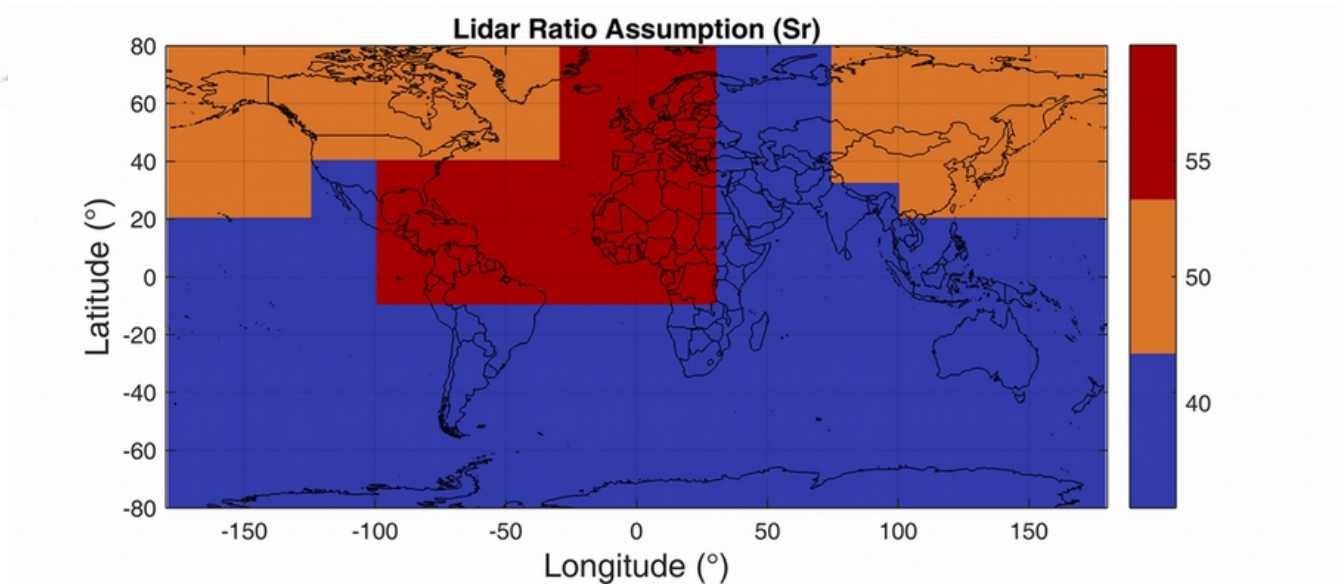

Figure 2.3. The region specific Lidar Ratio assumption used in LIVAS.

LIVAS has been evaluated against AERONET stations globally by Amiridis et al. (2015). The results show that the aerosol optical depth differences are between ±0.1 in most cases. Over the southwestern Sahara desert, LIVAS underestimates the AERONET AOD by -0.1, and this bias may be related with the dust underestimation of CALIPSO found in previous studies (Wandinger et al. 2010; Schuster et al. 2012; Tesche et al. 2013; Amiridis et al. 2013). Amiridis et al. (2013) showed that LIVAS correlates well with the Dark Target MODIS retrieval over sea, yet the correlation between MODIS Deep Blue (C5 version) and LIVAS over Sahara are weak (results not shown). The new version of MODIS Deep Blue (C6) improved its retrieval accuracy and spatial coverage globally (Sayer et al. 2014; Sayer et al. 2015) and the Mediterranean region (Georgoulias et al. 2016b) in comparison to AERONET. Thus, further research is needed to determine the correlation between LIVAS DOD and MODIS Deep Blue (C6) AOD. Furthermore, Georgoulias et al., 2016b showed that LIVAS correlates well with the high resolution TERRA MODIS and MACC dust optical depth over land covered regions in Eastern Mediterranean.

Monthly mean LIVAS data is available at a 1°x1° horizontal resolution with a vertical resolution ranging from 60 m (-0.5km and 21km) to 180 m (above 21km) (Amiridis et al., 2015). We concentrate on the troposphere where the vertical distribution of layers is constant. In our work we use the specialized LIVAS pure dust product which includes the extinction coefficient of pure dust calculated from the dust percentage of “dust” and “polluted dust” aerosol subcategories of CALIPSO (Amiridis et

al., 2013). Since CALIPSO is a non-geostationary satellite, the obtained mean monthly profiles are highly dependent on the date and time the measurements were taken. Thus, a spatiotemporal mask was produced according to the exact flight track of CALIPSO and applied to the nearest RegCM timestep prior to evaluation.

2.3 ERA-interim

ERA-interim is a state-of-the-art global atmospheric reanalysis product developed by the European Centre for Medium-Range Weather Forecasts (ECMWF) (Dee et al. 2011). The data assimilation system uses various types of observational data from ground-based stations, radiosondes, ships and satellites. Data availability starts from 1979 and it is extended forward in near-real time. Its assimilation scheme uses a 12 hour cycle, where observational data are combined with forecast information from the previous timestep in order to construct the global atmospheric conditions. ERA-interim reanalysis database is exceptionally useful over isolated areas like the Sahara desert, where meteorological measurements are limited. Wind velocity and direction, associated with dust emission and transport, were used to evaluate RegCM4 wind fields. ERA-interim is used also as boundary conditions in several regional climate models (e.g. RegCM4) for hindcast simulations. The spatial resolution of the reanalysis data is in 0.75x0.75 grid.

2.4 Climate Research Unit (CRU)

Climate Research Unit (CRU) data is a gridded global climate database of monthly meteorological measurements from ground-based stations (Harris et al. 2014). The dataset includes surface measurements of six meteorological variables, notably precipitation and temperature. Stations are interpolated into a 0.5x0.5 grid that covers all the land surface of the planet (except Antarctica). Data availability peaks between the period 1950-2000 and drops dramatically in the last decade. In places where the meteorological network of stations is sparse and stations are not available in certain grid boxes, infilling methods or the climate mean for the period 1960-1990 is used. It is noted that most of the continual measurements occur at stations close to the border of the desert, and station coverage is generally limited over the Sahara.

2.5 Tropical Rainfall Measuring Mission (TRMM)

Tropical Rainfall Measuring Mission was launched by National Aeronautics and Space Administration NASA and the Japan Aerospace Exploration Agency (JAXA) and it provides accurate rainfall data from

1998 to 2015 over land and ocean between 50º N-S latitude. In this study TRMM_3B42RT_v7 was used, where its horizontal resolution is 0.25ºx0.25º and temporal step is 3 hours (Huffman et al. 2016). Each timestep represents the three-hour period centered on the nominal file time.

2.6 CM SAF

Cloud fraction observations from the Satellite Application Facility on Climate Monitoring (CM SAF) have been used to evaluate simulated cloud fraction fields from the model. The data were obtained from the CM SAF web user interface (https://wui.cmsaf.eu/safira/action/viewProduktSearch). CM SAF cloud data from the CLAAS-1 record (Stengel et al. 2014) have been used in the past for the evaluation of RegCM4 simulations and satellite observations in the region (e.g. Alexandri et al. 2015; Alexandri et al. 2017). The data utilized in this work are part of the CLAAS-2 record that provides cloud properties such as cloud fractional coverage, thermodynamic phase, cloud top properties, cloud water path, cloud optical thickness and particle effective radius (Benas et al. 2017). Cloud products are available as instantaneous data (level 2) as well as daily and monthly averages (level 3) from the METEOSAT second generation satellites. An extensive evaluation of the CLAAS-2 dataset with data from active and passive satellite sensors such as CALIOP/CALIPSO and MODIS and observations from ground stations showing an overall good agreement (Benas et al. 2017). In our study monthly cloud fraction data (in %) from the Spinning Enhanced Visible and Infrared Imager (SEVIRI) optical imaging radiometer onboard the Meteosat Second Generation (MSG) set of satellites were used. The data are available in a regular 0.05ºx0.05º grid and cover the period from February 2004 to November 2009.

2.7 CERES

The CERES EBAF-TOA Ed4.0 cloud area fraction in a grid point is the ratio of the identified cloud pixel based on CERES-MODIS cloud mask algorithm to the total cloudy and clear sky number of pixels. The MODIS pixels can be either cloudy or clear. The cloud properties are derived from Terra-MODIS up until June 2002 and from then onward using the average retrieved measurements from Terra-MODIS and Aqua-MODIS (CERES EBAF Ed4.0, Data Quality Summary 2017). The pixel retrieved measurements are spatially averaged into a 1ºx1º grid and then averaged temporally into daily and monthly means. Additional information about the CERES product can be found in https://ceres.larc.nasa.gov and specifically for CERES top of the atmosphere fluxes in Loeb et al. (2009).

2.8 Other datasets (MODIS, MISR, GCMs)

Processed dust optical depth of MODIS v5.1 (Hsu et al. 2006; Levy et al. 2010), non-spherical aerosol optical depth from MISR (Kahn et al. 2010) and various dust parameters from 5 Global Climate Models (GCMs) (Kim et al. 2014) where used to discuss and inter-compare dust related precesses in RegCM4. Some key information about the 5 GCMs simulations is presented in the Table 1.

Table 1. Global climate simulations parameters used in Section 4.5 (Source: Kim et al. 2014).

Category/GCMs	GOCART	GISS-ModelE	SPRINTARS	ECHAM5-HAMMOZ	HadGEM2
Horizontal Resolution	2.5ºx2.0º	2.5ºx2.0º	1.125ºx1.125º	2.8ºx2.8º	1.875ºx1.25º
Vertical Layers	30	40	56	31	38
Meteorology Drive	GEOS4DAS	NCEP	NCEP	ECMWF	ECMWF
Number of size groups	5 bins	5 bins	6 bins	2 modes	6 bins
Size range diameter (μm)	0.1-10.0	0.1-16	0.1-10.0	0.05<rm<0.5 and 0.5<rm	0.0316-31.6

2.9 A new dust size particle discretization method

Dust tracers in climate models are usually represented by describing the size distribution with a specified number of bins defined according to the dust particle diameter (D). Increasing the number of transported dust size bins improves the representation of the physical properties and behavior of dust particles within same bin. However, the computational cost, especially in climate studies, generally limits the number of bins used to describe (dust). The transported size bins must be separated in an affordable number of bins and with a method that minimizes the numerical inaccuracies due to dust bin partitioning.

The isolog method, which partitions the dust bins in equal range of log D, is frequently used to specify the range of the dust size bins in climate models (Huneeus et al., 2011 and reference therein). An alternative partitioning method was introduced in (Foret et al., 2006), where they divide the total size range in each bin according to the changes of dry deposition velocity with size. Using a simple one-dimensional box model they simulated an experiment with a detailed particles size distribution that used 1000 size bins within the range of 0.001-100μm diameter. They used this experiment as a reference to evaluate the differences between the isolog and isogradient method. The error ratio

between the total dust particle mass (or number) simulated with the given particle size bin scheme (isolog or isogradient) and bin number (4-30bins), to the total dust particle mass (or number) simulated with the reference size distribution (1000bins), showed that for a given number of bins, isogradient scheme scored much better in terms of total dust mass, but isolog scheme produced somewhat better results in term of total dust particle number. The isogradient method yielded errors lower than 2% with regard to the total particle number and the representation of aerosol optical depth when using more than 8 dust bins (Foret et al., 2006).

Following the above results Menut et al. 2007 implemented the isogradient scheme into the 4D transport model CHIMERE-DUST and did several nested simulations over the Sahara region. To exclude any biases introduced by the emission, deposition and dynamics of the model they evaluated their results using a reference simulation that resolved 40 size bins. They concluded that the isogradient scheme reduced the errors by a factor of 2 compared to the isolog method and that 6 size bins are not sufficient to reproduce the correct concentration levels of dust even with the methodology proposed by Foret et al. 2006.

Both of these studies have shown that using a higher number of bins and the use of isogradient scheme improves the validity of the simulated results. However, they evaluate only the effect of dust bin partitioning on the size distribution dust emissions, either with a simple one-box model (Foret et al., 2006) or a three-dimensional dust transport model CHIMERE-DUST (Menut et al., 2007). In this manuscript, we take this research further by comparing the method and number of dust size bins with the RegCM4 results, and evaluate using observational data, account for biases introduced by the balance of production and loss processes, calculate optical properties of dust and evaluate these results with satellite products.

3. Dust size discretization: Impact on dust burden and dust radiative effect

Aerosols affect the energy budget of the planet through numerous feedback mechanisms. The direct aerosol climatic impact of -0.27W·m-2 at the surface and the indirect effect of -0.55W·m-2 was estimated in the most recent IPCC report, yet the radiative effect uncertainty remains the highest among all the other factors (Boucher et al. 2013). Aerosols strongly affect Earth's climate by scattering and absorbing the incoming solar radiation (direct effect), reduce low level clouds through longwave heating (semi-direct effect) or by producing brighter clouds (first indirect effect) with longer cloud lifetime (second indirect effect) (Hansen et al. 1997; Lohmann and Feichter 2001; Ramanathan et al. 2001; Tegen 2003; Karydis et al. 2011; Bangert et al. 2012; Nabat et al. 2014). Small particles can effectively scatter/reflect the incoming shortwave radiation while large particles can more effectively absorb and re-emit on the longwave part of the spectrum (Liao and Seinfeld 1998). Globally, dust is considered to have a slightly negative radiative effect -0.1W·m-2 (-0.3W·m-2 to 0.1W·m-2) on climate (Boucher et al. 2013). A recent detailed evaluation of RegCM4-CCM3 using satellite-based observations over the European domain highlighted that surface solar radiation bias can be attributed to an overestimation or underestimation of counteracting parameters, with cloud fractional cover, cloud optical thickness and aerosol optical depth being the most important (Alexandri et al. 2015). Since airborne dust plays a fairly significant role on the total aerosol optical depth, it is important to understand and improve the probable causes of dust optical depth biases.

Dust production begins when surface wind or wind at a certain height exceeds a threshold. In most studies, the threshold friction velocity is determined as the minimal wind velocity that is capable of sustaining particle movement (Iversen and White 1982). Practical threshold wind velocity is depents on soil particle size, inter-particle cohesion forces and surface roughness features. Assuming a constant particle density, soil particle size affects their weight. Thus, large particles require higher surface friction velocity to initiate dust movement. On the other hand the inter-particle forces (van der Waals, Capillary, Coulomb forces) acting upon small dust species, that depends on soil moisture and chemical composition, are higher compared to the larger particles and difficult to estimate (Shao and Lu 2000). Due to the opposite dependency of particles weight and inter-particle cohesion forces size particles with diameter 60μm was estimated to have the minimum wind erosion threshold (Knippertz 2014). Particles of this size have a higher probability to be emitted first and trigger the next stages of dust

emission (saltation and disaggregation).

Mineral dust is produced mainly in deserts. Its production depends on surface wind, precipitation and changes in the vegetation cover (Tegen et al. 2000). The Sahara desert is the most important source of aeolian soil dust on the planet (Prospero et al. 2002). Dust from the Sahara is transported northward in Europe and Mediterranean on episodic events quite frequently (11.4 year-1) (Gkikas et al. 2013). The dust burden in the Mediterranean region differs spatially and seasonally with the Eastern Mediterranean experiencing high dust load in spring and the Western Mediterranean reaching its peak in the summer and autumn (Moulin et al. 1998). The central Mediterranean can be considered a transition region where dust transport episodes can occur throughout spring to autumn (Israelevich et al. 2012). Depending on season and area of the Mediterranean, dust can originate from different places in the Sahara desert. Possible dust pathways have been identified for each season using the TOMS AI satellite data (Israelevich 2003). In spring for example, dust follows a long trajectory from the Bodélé depression to southern Algeria and then moves northward across the coast of northern Africa to reach Eastern Mediterranean. This long path affects the size of soil particles that reach the Mediterranean in spring in comparison with other seasons. Since dust particles have to travel for such a long distance, dry deposition through gravitational settling forces coarse particles to deposit. Thus, the size of dust particles across Mediterranean in the spring (1.5μm) is half compared to the particles during summer and autumn (3μm), which follow a shorter trajectory (Israelevich 2003).

The vertical dust distribution has remained uncertain in the past decade, because satellite measurements provided mainly the columnar aerosol optical depth and the stationary observations were spatially sparse. Modelling studies have shown different vertical dust distribution between the Mediterranean, the Atlantic and the Sahara desert (Alpert et al. 2004a), while after the launch of the CALIPSO satellite in 2006, our understanding on aerosol vertical distribution increased rapidly (Winker et al. 2009). The particle size distribution of dust changes over height with finer particles reaching higher in the atmosphere and therefore having a higher probability to be transported further because wind speed is also increasing with height. Considering that the fine particles scatter and reflect efficiently the incoming solar radiation, we can grasp the importance of the vertical dust distribution and its radiative effect.

An important component that affects the transport and the radiative properties of dust in climate modelling is the number of transport dust size bins. Small dust particles, due to their weight, can travel

over long distances and can efficiently reflect/backscatter the incoming shortwave solar radiation, while larger particles, with shorter atmospheric life, can effectively absorb and re-emit in the longwave spectrum. Thus, both the partitioning and the number of dust transport bins, used in atmospheric models, should carefully distinguish dust particles with contrasting radiative properties and transport characteristics. The number of dust bins and the size range resolved in global climate models varies between models, with most using 1-6 dust bins spanning a size range of 0.01-25μm (e.g. Huneeus et al., 2011 and reference there in; Kinne, 2003). Greater number of dust size bins improves particle dry deposition and thus allows to more accurately simulate both the atmospheric dust burden and the interaction with radiation (Foret et al. 2006; Menut et al. 2007). However, the high computational requirements of global climate models demands as few as possible dust size aggregates and consequently a low size range of aerosol species. Regional climate models with smaller domains of interest usually simulate between 4 to 12 dust size bins (e.g. (Zakey et al. 2006; Solmon et al. 2008; Basart et al. 2012; Giorgi et al. 2012; Solmon et al. 2012; Nabat et al. 2012; Spyrou et al. 2013; Alexandri et al. 2015), while dust transport models have conducted simulation experiments with up to 40 dust bins (Menut et al. 2007).

Dust particle size measurements in the Sahara desert from the Fennec 2011 aircraft campaign show that the dust coarse mode volume median diameter ranges between 5.8 and 45.3 μm (Ryder et al. 2013). Moving away from the dust source regions the mean/median size of dust particles drops dramatically. In the Mediterranean the mean diameter of dust particles ranges between 2-30μm (Goudie and Middleton, 2001 and reference therein). It is evident that particles with diameter >25μm possess a major role in the burden of dust close and in some cases away from the dust sources. Thus, Foret et al. (2006) proposed that dust size for the transported bins should range from 0.09μm to 63μm, considering both the total number and the mass distribution of soil particles.

This chapter presents new dust features in RegCM4, highlights the sensitivity of dust emission and deposition processes with various meteorological schemes, and analyzes the effect of size bin distribution on dust burden and radiative effect. Previous studies on dust size parameterization are discussed and explain how the present work expands these studies further in the previous Section 2.9. The regional climate model RegCM4 is evaluated using the dust product LIVAS, where high resolution vertical aerosol extinction coefficient measurements were made available and new techniques for the discrimination of pure dust were developed (Amiridis et al. 2013). The importance of the partitioning

method and the number of dust size bins is highlighted by comparing two simulations in terms of the dust column burden and dust optical depth. Finally, the effect of the two binning methods on the dust radiative effect is discussed both in the short and the longwave spectrum.

3.1 Simulations set-up

The key parameters of the RegCM4 simulations are presented in the Table 1. The simulation domain includes the Sahara desert and the largest part of the Arabian Peninsula (Figure 3.1), which captures the two main sources of dust in the Earth (Tegen, 2003). To reduce the contribution of dust from outside the domain requiring chemical lateral boundary conditions, the domain extends south of the Sahara desert. The simulated domain was separated into six distinct subregions: Sahel, Eastern Sahara (ESah), Western Sahara (WSah), Eastern Mediterranean (EMed), Central Mediterranean (CMed) and Western Mediterranean (WMed) (Figure 3.1b). Sahel was delimited using CRU precipitation for the period 2001-2014. The selected grid cells receive annual precipitation between 100mm and 600mm (Ali and Lebel 2009; Nicholson 2013) and are located in the southern border of Sahara. Eastern and Western Sahara were selected according to the desert and semi-desert landuse assigned by the model. Their southern borders were masked by the Sahel grid points. The three Mediterranean subregions contain only non-desert grid points and are separated according to their DOD seasonality (Israelevich et al. 2012). Two 8-yearly simulations (4 dust size bins and 12 dust size bins) were performed from September 2006 to November 2014, excluding in our analysis the initial 3 months as a spin-up time. The 4 dust bin experiment (DUST4) implements the isolog approach for the partitioning of the dust size bins, while the 12 dust bin experiment (DUST12) uses the isogradient method. Both experiments use the Kok (2011a) dust particle size distribution theory.

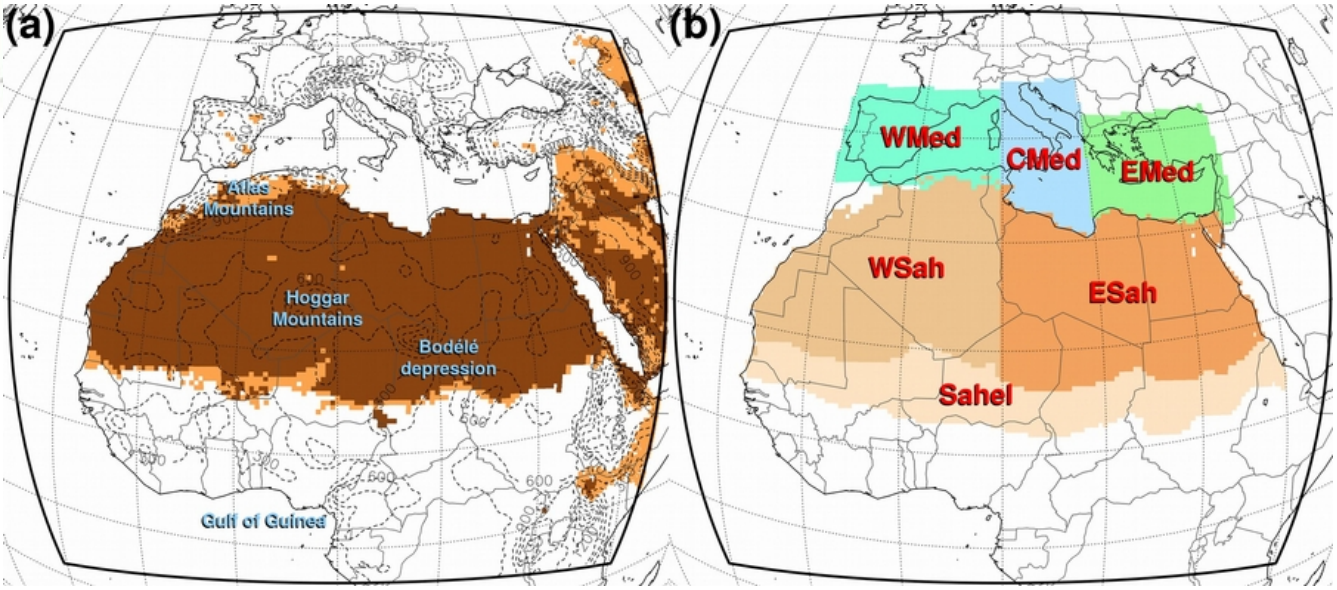

Figure 3.1. RegCM4 simulated domain (solid black contour) and the subregions selected for the analysis (blue contours). Background colors represent the desert (dark brown) and semidesert (light brown) grid cells assigned by the model. Dashed lines illustrate the topography used on RegCM4 in meters.

To ensure that the two experiments are identical in every way except the dust bin number and partitioning method, we have both distributions span the exact same total size range and conserve the integrated optical properties (over the whole distribution) whether we consider 4 or 12 bins. Furthermore, there is no interaction between the dust particles and the radiation fields (e.g. no direct aerosol feedback on climate) to ensure that there are no meteorologically driven changes between the two simulations. The radiative effect of dust is calculated using separate radiation calls during the simulation. Consequently, the meteorology of the two experiments is identical.

The initial and boundary conditions of the mean monthly dust burden were acquired from a global simulation (CAM + EC-EARTH), for the decades 2000-2009 and 2010-2019. Therefore, a constant static map was used as boundary conditions for each month. A certain degree of error is expected at the boundaries of our domain that will not capture individual dust events or strong inter-annual variability. However, our analysis shows that the boundary forcing in the examined sub-regions is negligible in the dust annual cycle column burden of fine and coarse particles (Section 3.2). Because the aerosol lateral boundary conditions used a 4-bin dust model, we modified the boundary conditions for the 12 bin experiment. The new bins were defined according to the ratio between the 4 and 12 bin size range and size limits. Multiplying this ratio by each month and atmospheric level we have created the necessary global boundary condition for the 12 bin dust scheme. This method assumes that the number of

particles is homogeneously distributed in each bin.

The dust size range of the boundary conditions dataset spans 0.01μm-20μm. Therefore, coarse dust size bins in both DUST4 and DUST12 scheme (e.g. that exceed the upper limit of the 20μm) are not influenced by boundary conditions. This does not introduce a significant bias in our results since large particles (> 20μm) have a short atmospheric lifetime and the main dust sources from outside the domain are located far from our simulation boundaries. The DUST12 experiment increased the computational cost by 66.8% in comparison to DUST4. However, we have to note that the computational cost difference between the two experiments may vary under other model physics options and domain size.

Table 2. Simulation options implemented in RegCM4.

Category/Experiments	DUST4	DUST12
Grid Dimensions	140 x 160, 18 sigma levels	
Horizontal Resolution	50km	
Top Layer Pressure	50hPa	
Meteorological Boundary Conditions	ERA-Interim (Dee et al., 2011)	
Surface Model	BATS (Dickinson et al., 1993)	
Chemical Boundary Conditions	CAM + EC-EARTH	
Cumulus Convection Scheme	Tiedtke (Tiedtke 1989)	
Transfer Radiation Scheme	CCM3 (Kiehl et al., 1996)	
Moisture Scheme	SUBEX (Pal et al., 2000)	
Planetary Boundary Layer Scheme	Modified Holtslag (Holtslag et al., 1990)	
Dust Tracers	(4bins, isolog)	(12bins, isogradient)
Dust Size Particle Distribution	Kok (Kok, 2011a)	

3.2 DUST4 vs LIVAS - Evaluation

The 4 bin simulation (DUST4) was evaluated against the climatological LIVAS Dust Optical Depth (DOD) (Figure 3.2). The high dust belt (DOD > 0.2) between 15º-25ºN in RegCM4 generally matches the observed DOD of LIVAS with some spatial inconsistencies. We discuss these differences for key regions (Figure 3.1) according to the mean bias, the lower (LCI) and upper (UCI) 95% confidence intervals of the mean and the percent bias (Pbias). RegCM4 underestimates DOD in a zone south of the Sahel around to 10ºN by about 0.05. Over the eastern Sahara (ESah), RegCM4 overestimates the

climatological DOD by 0.083 (LCI:0.078, UCI:0.088, PBias:63.1%), mainly in Chad and expanding to Libya, Egypt and northern Sudan. In western Sahara (WSah) where the DOD is higher, the model mean overestimation is 0.043 (LCI:0.039, UCI:0.047, PBias:26.2%). Over the Mediterranean all the grid points show a weak overestimation of DOD which for the three Mediterranean regions combined is 0.027 (LCI:0.026, UCI:0.029, PBias:54.7%).

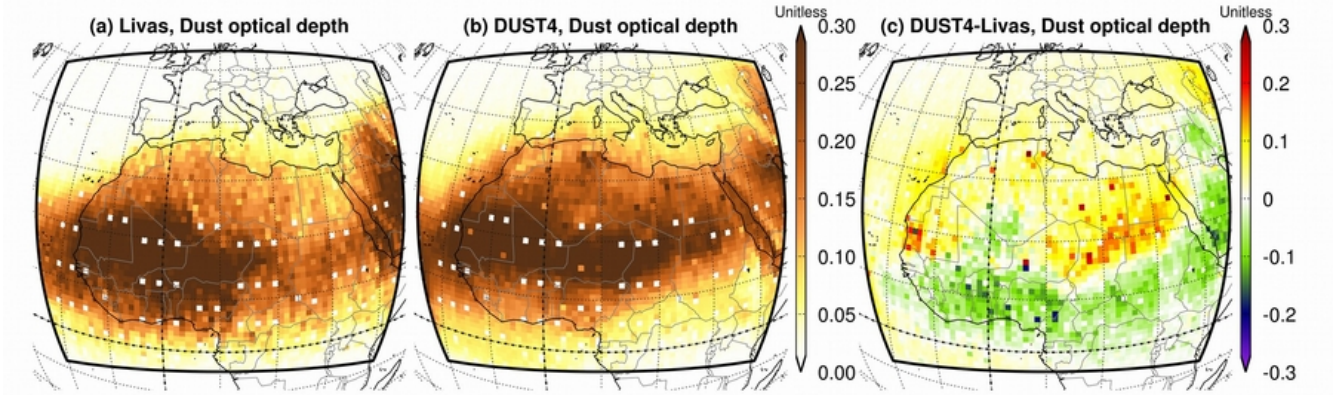

Figure 3.2. Dust optical depth of the DUST4 experiment and the LIVAS dust product for the period January 2007 to November 2014.

Figure 3.3 depicts the seasonal cycle of DOD in LIVAS observations and the DUST4 simulation for the six subregions depicted in Figure 3.1. In the Mediterranean the observed monthly mean DOD values are typically less than 0.1, with the RegCM4 maximum values reaching 0.15 in some months (Figure 3.3a-c). Although there is an almost constant overestimation of DOD for all Mediterranean regions, the observed annual cycle maximum and minimum values are simulated adequately and we note that generally, the monthly DOD values are relatively low. In the western Mediterranean DOD peaks in summer (Figure 3.3a) while the eastern Mediterranean peak is in spring (Figure 3.3c). Generally, DUST4 simulation overestimates DOD with a secondary annual maximum in spring and summer over the western and eastern Mediterranean, respectively. The central Mediterranean is the transition area that receives dust throughout the year from transport paths that affect both Eastern and Western Mediterranean (Israelevich et al. 2012). Therefore, it exhibits a broad maximum that peaks mainly in spring and remains until late summer (Figure 3.3b).

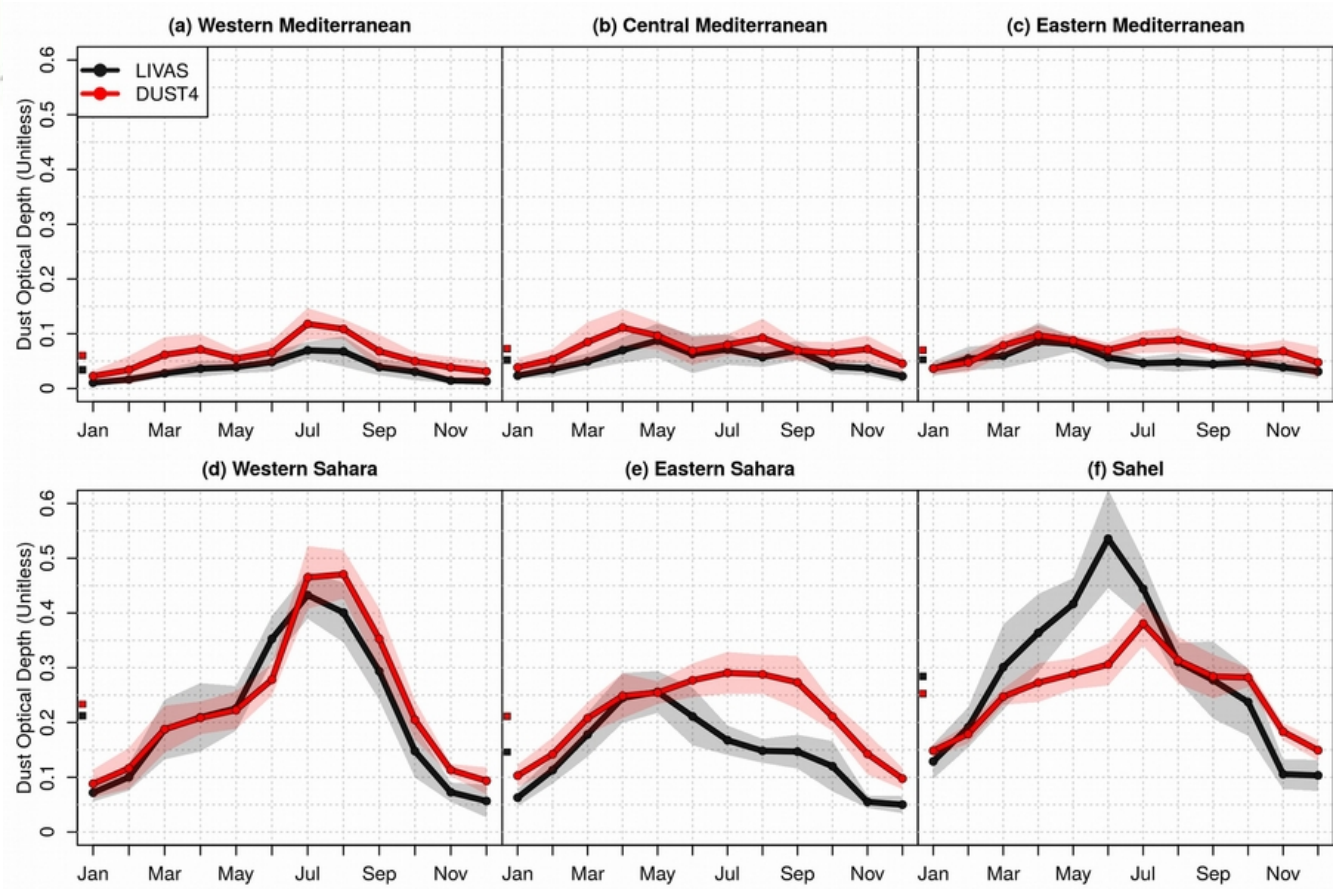

Figure 3.3. Dust optical depth annual cycle of LIVAS and DUST4 experiment for the period January 2007 to November 2014. Shaded areas display the 95 % confidence interval of the mean. The points at the edge of the vertical axis depict the average value of the dust optical depth annual cycle for each region.

The spatial distribution of wet deposition, dry deposition and surface emission fluxes is depicted for the fine and coarse particles in Figure 3.4. Over desert and semi-desert areas, DOD values are higher and show greater intra-annual variability and amplitude in comparison to the Mediterranean subregions (Figure 3.3d-f). Western Sahara DOD shows a strong summer maximum of 0.45 that is seven times higher than winter values (Figure 3.3d). RegCM4 simulates accurately the mean monthly values in the first six months and overestimates in the summer and autumn by 0.03-0.07. In the eastern Sahara, there is a significant overestimation of DOD during summer and autumn where the positive bias of the model is more than 0.1 in most months (Figure 3.3e). The Sahel annual cycle is affected by the southward transport of dust from Sahara and the seasonal movement of the Inter-Tropical Convergence Zone (ITCZ) (Ridley et al. 2012; Rodríguez et al. 2015). The local emission sources are activated mainly during winter (dry season) when soil moisture is low but DOD peaks in summer (Figure 3.3f), indicating that the dust annual cycle is strongly affected by the inflow of dust from the Sahara into the

Sahel. RegCM4 underestimates DOD during August-January and overestimates it during March-July (Figure 3.3f).

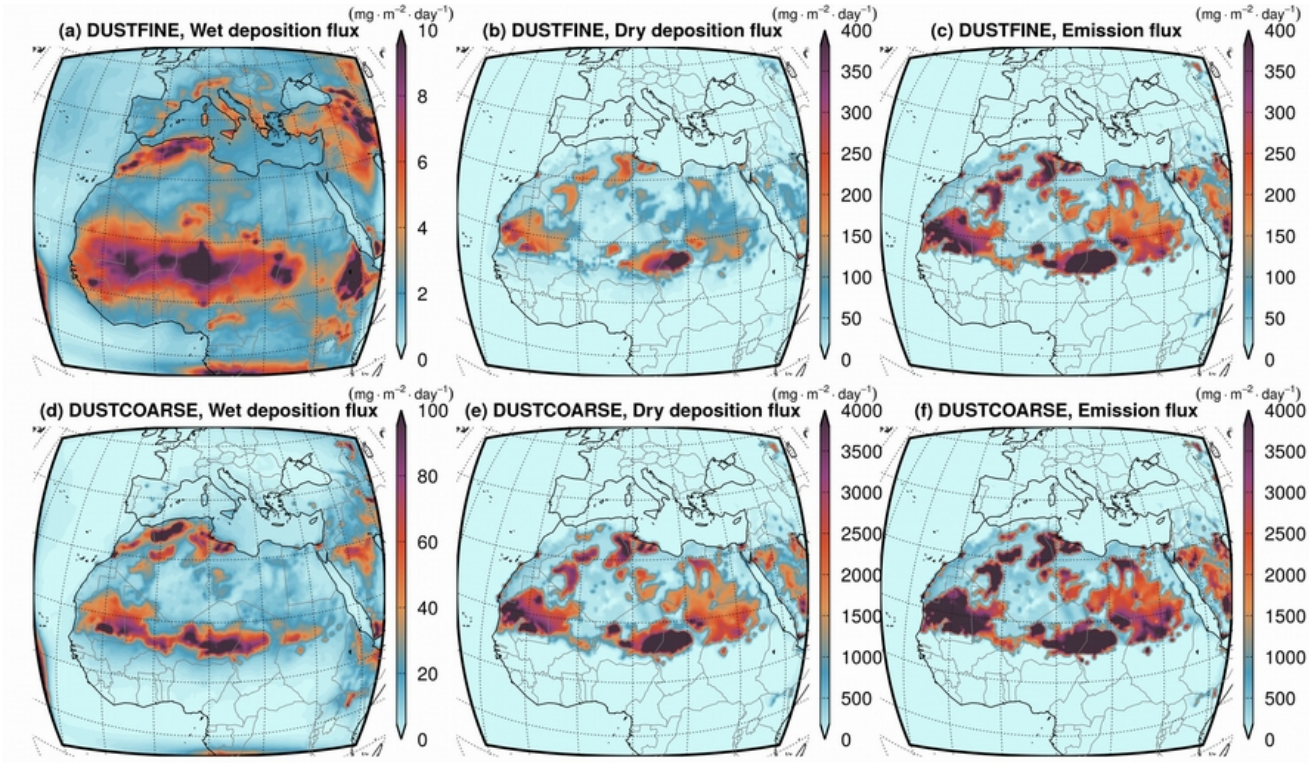

Figure 3.4. Wet deposition, dry deposition and surface emission fluxes of fine (a, b, c) and coarse (d, e, f) dust particles in DUST4 experiment for the period December 2006 to November 2014.

To understand the simulated processes of dust production-destruction-transport in the model and explain the discrepancies identified in the DOD annual cycle, we investigate the annual cycle of dust column burden for coarse-silt size (Dd > 2.5μm, Figure 3.5) and fine-clay size (Dd < 2.5μm, Figure 3.6) dust particles alongside the production/destruction column tendencies of dust. Fine particles dominate the annual cycle of the total column burden and control its seasonal variability, whereas coarse particles display a weak seasonal variability and its intra-annual amplitude is generally negligible in comparison to fine particles. The major tendencies that control the dust column burden in both fine and coarse particles is emission and sedimentation. Additionally, vertical turbulence, horizontal and vertical advection play a considerable role in the desert regions for fine particles. The fine column burden annual cycle is anti-correlated with the absolute values of production/destruction tendencies in the desert, e.g., during the warm season the absolute values of tendencies tend to be small and fine dust column burden high, with the opposite in the cold season. In most regions, fine and coarse

particles peak during the same month, enhancing the total column burden seasonal variability (e.g. western Sahara, Sahel; Figure 3.6e-f, Figure 3.5e-f respectively). However, in the eastern Sahara (Figure 3.5d and Figure 3.6d), fine and coarse annual cycles follow a completely different pattern. Coarse particles peak in spring while fine particles exhibit a broad spring-summer maximum that peaks during late summer. This indicates that fine particles are responsible for the overestimation of DOD in the Eastern Sahara as their burden and the size specific extinction coefficient (Figure 2.1) is higher in comparison to the coarse dust particles.

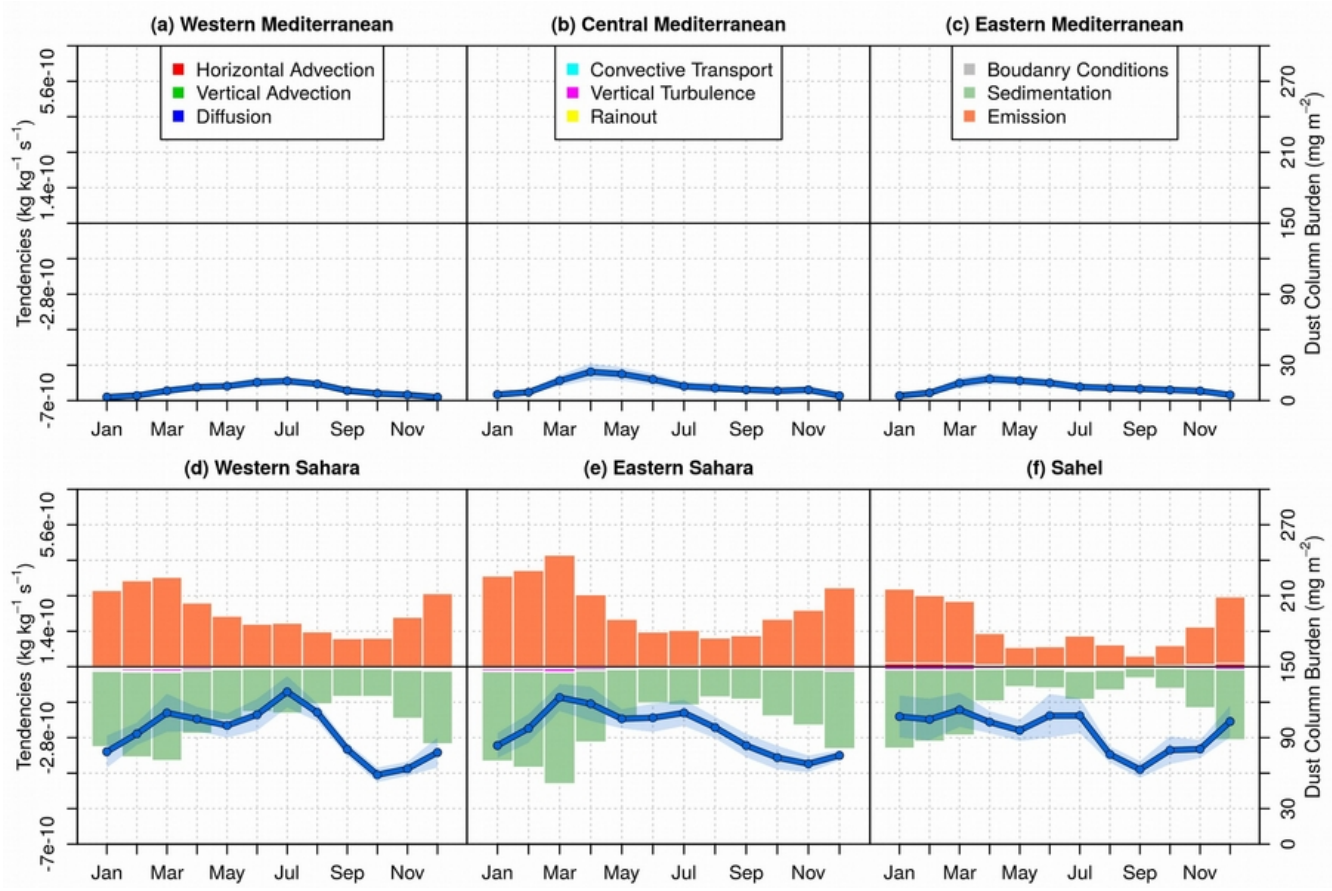

Figure 3.5. Coarse dust particle column burden of the DUST4 experiment (lines) alongside the production/destruction column tendencies(bars) averaged for the period December 2006 to November 2014. Shaded areas represent the 95 % confidence interval of the mean.

Over the Eastern and Western Sahara both emission and sedimentation fluxes display a distinct spring maximum in March (Figure 3.5d,e and Figure 3.6d,e), that does not explain the annual cycles of dust column burden. The ratio of emission to dry deposition flux is connected to the dust column burden, rather than the absolute values of emission and dry deposition flux. Values greater than 1 demonstrate periods where the emission dominates in comparison to dry deposition rate, while values smaller than 1

depicts the dominance of deposition. Coarse particles, due to their low atmospheric lifetime, are deposited close to their source region and shortly after emission, therefore exhibiting a very low seasonal variability. Fine particles on the other hand remain in the atmosphere for longer and can travel in long distances, affecting substantially the emission to dry deposition ratio.

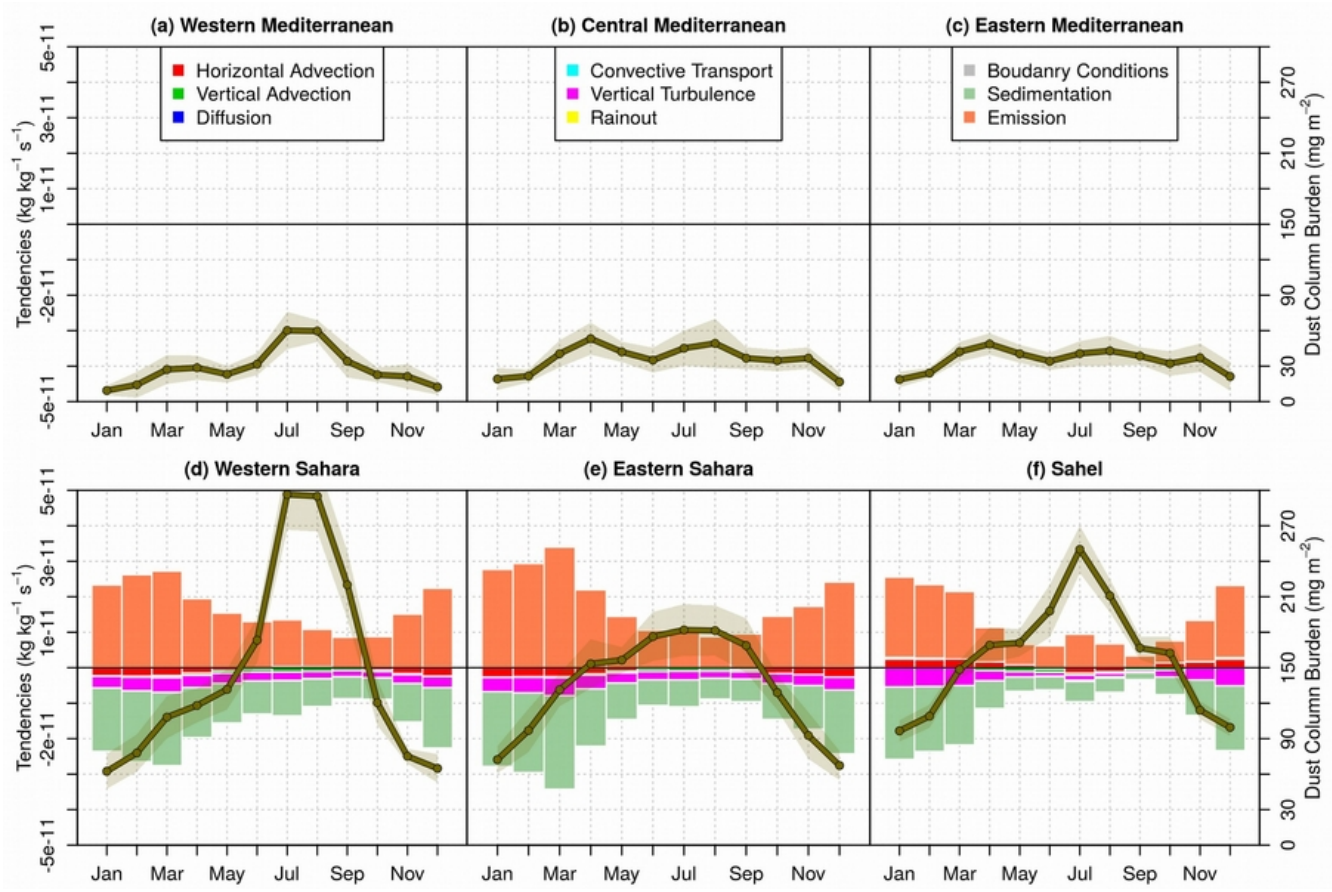

Figure 3.6. Fine dust particle column burden of the DUST4 experiment (lines) alongside production/destruction column tendencies (bars)averaged for the period December 2006 to November 2014. Shaded areas represent the 95 % confidence interval of the mean.

In the Western Sahara the fine particle emission to deposition ratio for the full simulation period is 1.46, which indicates that the model emits 46% more fine particles compared to its deposition. The coarse particle ratio is close to 1. In Eastern Sahara the emission to deposition ratio is much higher than in the Western Sahara, with values of 1.80 and 1.31 for fine and coarse particles, respectively. The strong yearly average annual NNE and NNW winds in the region transports dust away from the source region increasing the dust outflow of the Eastern Sahara (Figure 3.7). Thus, deposition in the Eastern Sahara decreases and the emission to deposition ratio rises. Furthermore, the fine particle emission to deposition ratio steadily increases from March to August, leading to an accumulation of fine dust

particles in the atmosphere that increases the column burden and the DOD. In the Sahel throughout the year, emissions are two times greater than the deposition for fine particles, with a mean ratio 2.26. As discussed later, RegCM4 exhibits some biases in the total precipitation annual cycle that influence this ratio.

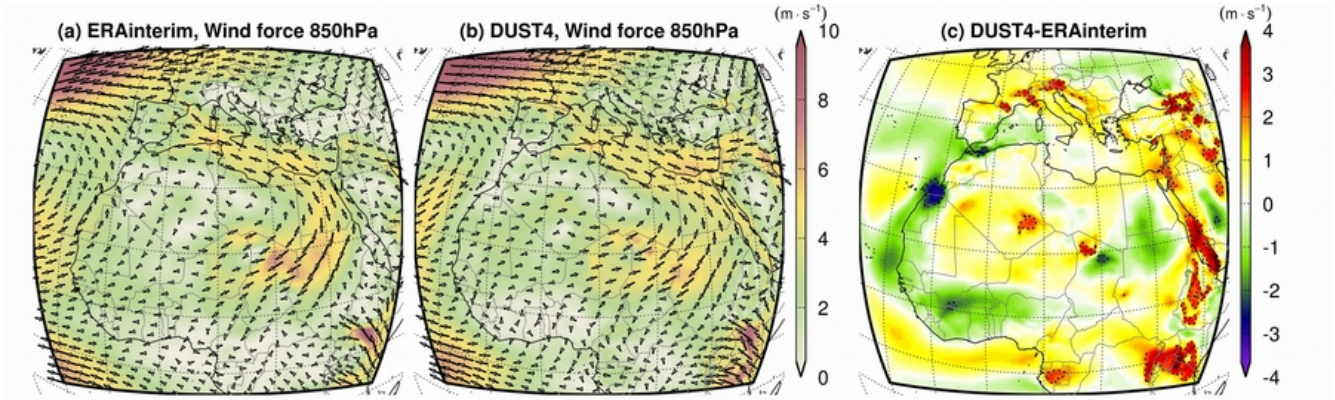

Figure 3.7. Wind velocity at 850hPa of the DUST4 experiment against the ERA-Interim reanalysis for the period December 2006 to November2014.

The column burden of dust can be affected by numerous meteorological variables that may alter the emission, deposition or the circulation and transport of dust. Thus, these variables were evaluated with the observational gridded and reanalysis data to explain the spatial biases observed in the DOD. The ERA-Interim was used for the evaluation of wind fields (surface, 925hPa and 850hPa) in order to have large spatial coverage and a long-term, continuous availability of data. The 10m wind velocity in RegCM, that constitutes the main driver of dust production through erosion, is comparable to ERA-Interim (Figure 3.8). We observe some positive and negative biases over the desert that generally are less than 1m·s-1.

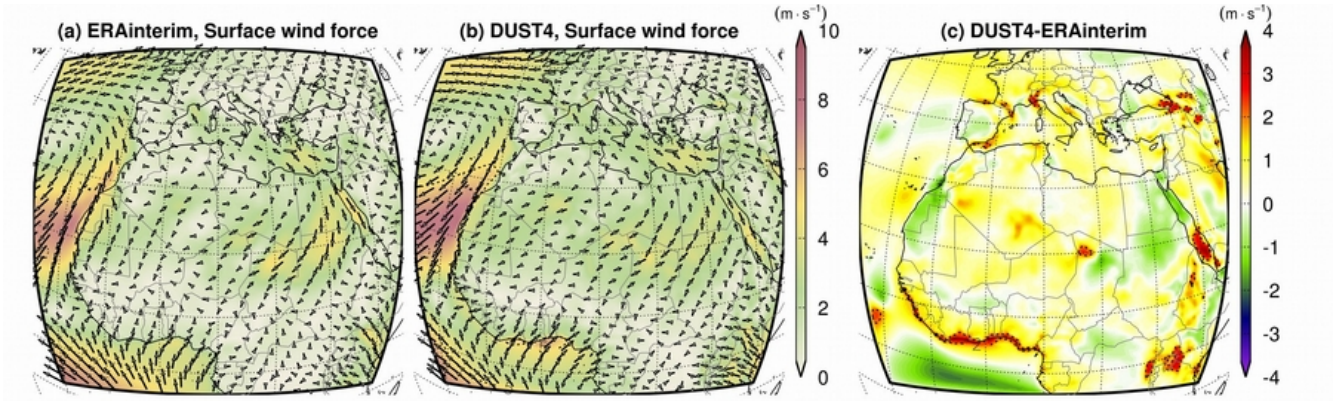

Figure 3.8. Wind velocity at the 10m of DUST4 experiment against the reanalysis ERA-interim for the period December 2006 to November 2014.

Although the mean wind velocity is linked with dust emission, wind gustiness and dust emission fluxes exhibit higher temporal and spatial correlation (Engelstaedter and Washington 2007). A wind gust is defined as a sudden increase of wind speed that last less than 20 seconds. In our simulations, wind speed is calculated within the internal timestep (120 seconds) of our model and wind gust is considered as the maximum value of wind velocity within the last output timestep (6 hours). Typically, this calculation method is applied in most climate models and reanalysis products with different internal and output timesteps. Therefore, it is difficult to draw conclusions when comparing the wind gust in RegCM and ERA-interim, because the wind gust was calculated in different time frames. Alternatively we calculated the mean field of the 6hourly timesteps that exceeded the 0.9 percentile value of wind velocity, averaged over the three desert subregions (Eastern Sahara, Western Sahara, Sahel) (Figure 3.9). The 0.9 percentile value of the averaged wind over the desert is 4.93m·s-1 and 5.92m·s-1 for ERA-interim and RegCM respectively. RegCM clearly overestimates locally high wind velocity over the desert by 1-3m·s-1, which indicates that the model potentially overestimates dust emission flux.

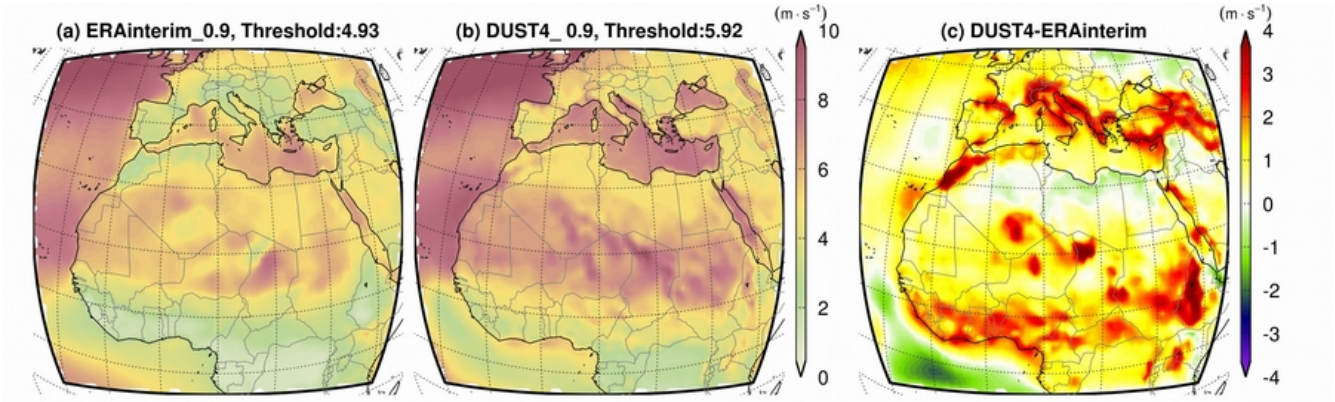

Figure 3.9. Wind velocity at the surface of the 0.9 percentile over the desert for the period December 2006 to November 2014.The 0.9 percentile threshold is depicted at the title of each dataset.

In Egypt and northern Sudan, the strong surface NNE winds depicted in ERA-interim is underestimated by RegCM, which may lower the simulated production of dust in the Eastern Sahara. But considering that the same wind pattern continues at both 925hPa and 850hPa and that the larger amount of dust is concentrated on these layers (Figure 3.7), it can also decrease its southward transport and the outflow of dust in Eastern Sahara. In Figure 3.10, the annual cycle of the meridional wind component confirms that during the summer (June-September) the southerly wind is underestimated by the model by more than 1m·s-1. Thus, a high load of dust remains stationary for longer period over Eastern Sahara that likely increases the modelled column burden and the DOD (Figure 3.3e).

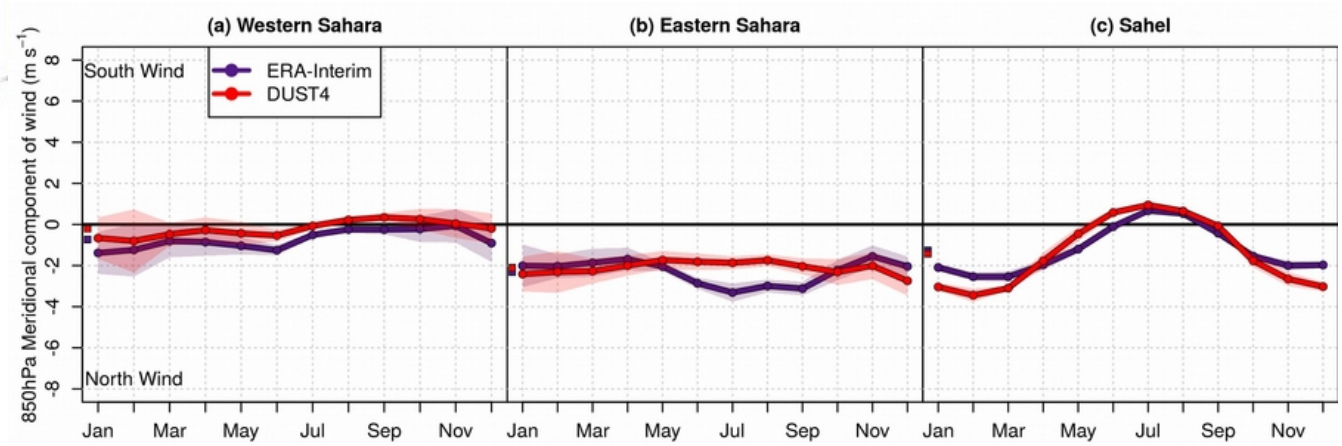

Figure 3.10. Annual cycle of the meridional wind component of ERA-Interim and DUST4 experiment for the period December 2006 to November 2014. Positive and negative values indicate south and north wind, respectively. Shaded areas represent the 95 % confidence interval of the mean. The points at the edge of the vertical axis depict the average value of annual cycle for each region.

Away from the Sahara region and especially in semi-arid environments, like the Sahel, precipitation can affect both emission and wet deposition processes. According to CRU database RegCM overestimates precipitation in the Sahel by 10-20 mm·month-1 (Figure 3.11) which increases wet deposition as well as soil moisture and vegetation (Engelstaedter et al. 2006). Consequently, more dust is deposited and less is emitted.

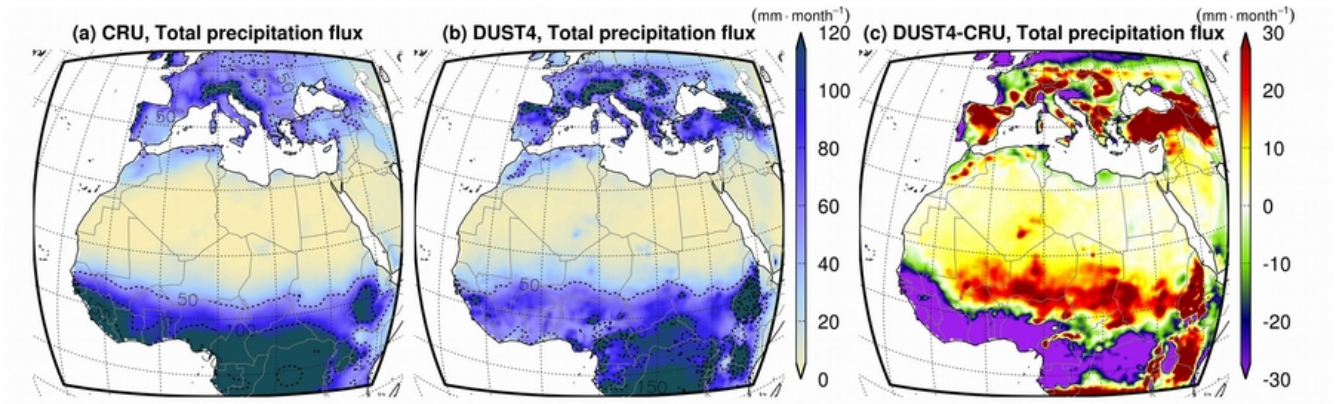

Figure 3.11. Total precipitation flux of DUST4 experiment against the reanalysis ERA-interim for the period December 2006 to November 2014.

According to the annual cycle of total precipitation (Figure 3.12) the overestimation of precipitation during April, May and June probably contributes into the underestimation of DOD (Figure 3.3f). The same process prevents the southward transport of dust to lower latitudes and is partly responsible for the strong underestimation of DOD close to the Gulf of Guinea.

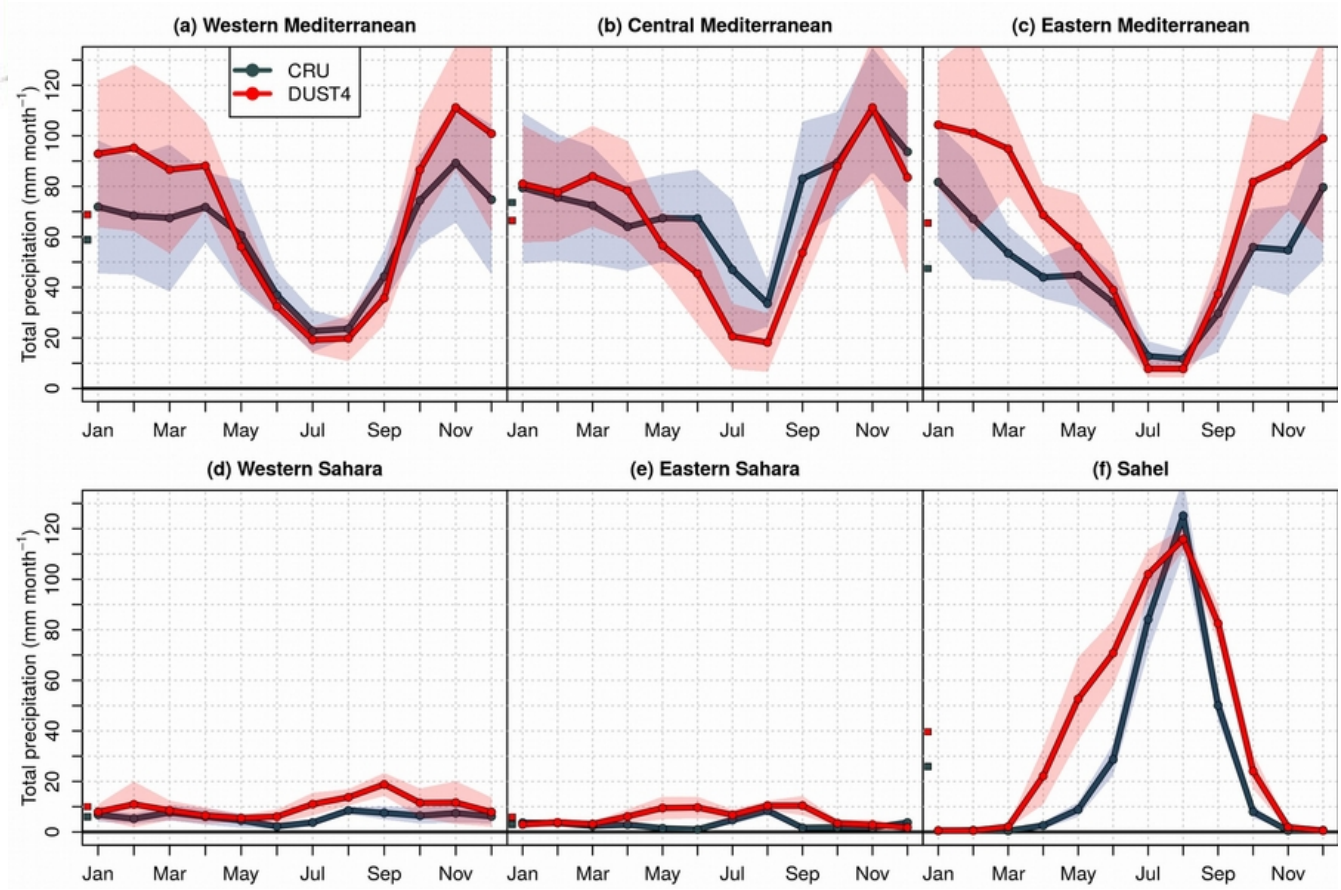

Figure 3.12. Total precipitation annual cycle of the ERA-Interim and DUST4 experiment for the period December 2006 to November 2014. The points at the edge of the vertical axis depict the average value of the annual cycle for each region.

The vertical distribution of dust is evaluated for the six subregions for vertical tendencies (advection, convective transport, vertical turbulence and sedimentation) in Figure 3.13. The first 200m of Dust Extinction (DEX) values were excluded from the analysis due to measurement restriction of LIVAS. The tendencies are illustrated in the plot as percentages for the layers 0.2-5km and 5-10km. DEX is overestimated by RegCM in all subregions in the middle and upper Troposphere. More than 95% of dust is located in the first 5km from the surface according to DEX measurements from LIVAS. However, RegCM places more dust at higher altitudes, with only 80-90% located between 0 to 5km. In Western Sahara and Sahel, DEX is underestimated by RegCM until the height of 5km (Figure 3.13d and f) and above that height there is a constant positive bias that decreases with altitude. The large observed DEX values between 3km and 5km over the Sahel indicates the high amount of fine dust particles that reach higher altitudes as compared to the Eastern and Western Sahara. In the Eastern Sahara the DEX is overestimated between 3-13km. At the western, central and eastern Mediterranean

regions, the DEX is overestimated above about 2-3km and underestimated below this height (Figure 3.13a-c).

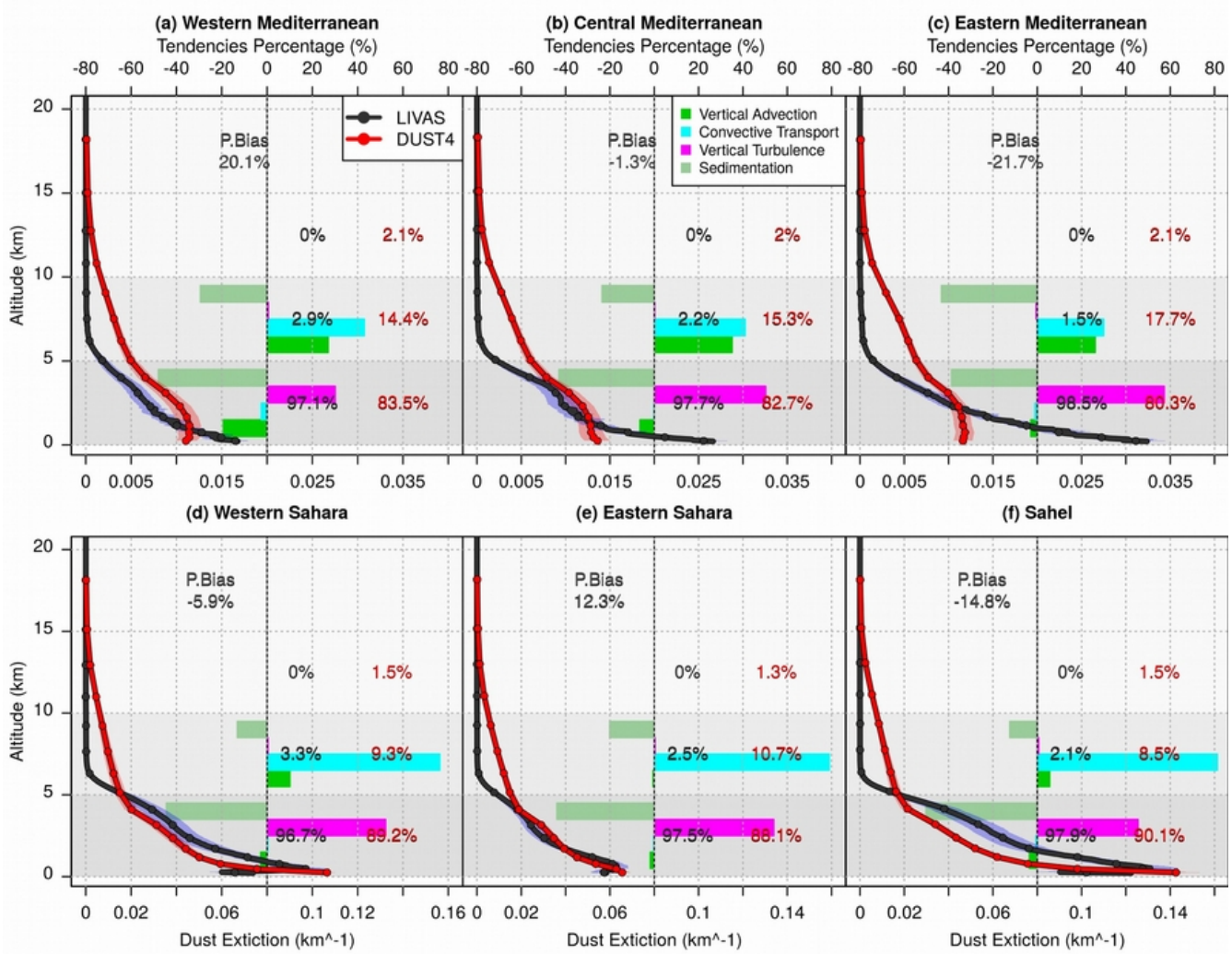

Figure 3.13. Dust extinction profiles of LIVAS and the DUST4 experiment. The percent bias (P.Bias) of dust extinction between 0.2 to 5, 5 to 10, and 10 to 20 km layer for each subregion is illustrated on the plots. The bars depict the percent of the vertical tendencies for 0.2-5 and5-10 km. The percentage along the yy' axis depict the amount of DEX located between the above-mentioned vertical layers.

In the model, the vertical transport of dust is controlled by four main processes: sedimentation, vertical turbulence, vertical advection and convective transport. The sedimentation tendency is always negative and equally important in all heights, whereas vertical turbulence plays a major role in the first couple kilometers of the atmosphere and vertical advection and convective transport, prevail in higher altitudes. As shown in Figure 3.13, in the first 5km of the atmosphere sedimentation exhibit negative values (contribution >-40%), which removes dust from the atmosphere. On the other hand, vertical

turbulence is the main force that raises dust upwards (contribution>50%). The planetary boundary layer (PBL) scheme based on Holtslag et al. (1990) produces high vertical turbulences in the first couple of kilometres in the atmosphere, and this may contribute to the underestimation or overestimation of the modelled DEX profile as compared to LIVAS measurements. We have simulated 2008 with the alternative PBL scheme option in RegCM4 based on (Bretherton et al. 2004), which suggests an improvement as far as the vertical distribution of dust in the PBL, although column DOD and DEX bias increases, especially over Eastern Sahara (Figure 3.14). The vertical advection and more importantly convective transport between 5 and 10km show positive values on average, which transports dust upward. Over the Mediterranean region vertical advection (>20%) and convective transport (>30%) contribution is equally important (Figure 3.13a-c), while in Sahara desert and Sahel convective transport is the most significant factor (>65%)(Figure 3.13d-f). Considering the overestimated DEX profile in this altitude range it suggests that the cumulus convection activity/convective transport mechanism is overactive in Tiedtke scheme (Tiedtke 1989) or another negative sign process (e.g. sedimentation) is not properly represented by the model. Discrepancies in the vertical distribution of dust can also be misinterpreted from possible local emission errors, the lack of simulated vertical levels or wet deposition biases. Further, research is needed in this regard to reduce the mean vertical distribution bias of dust in the model.

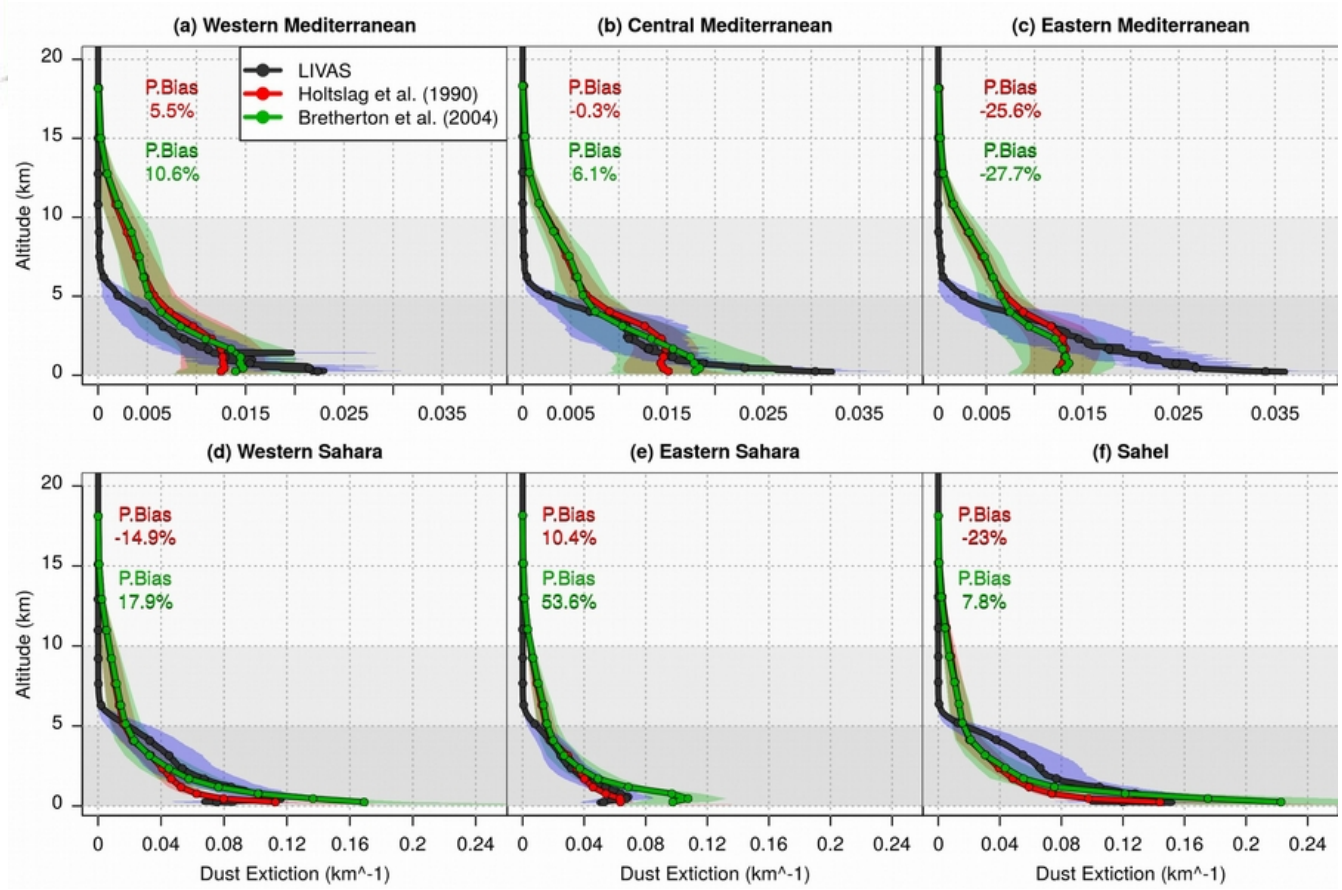

Figure 3.14. Dust extinction profiles of LIVAS and DUST4 using Holtslag et al. (1990) and Bretherton et al. (2004) PBL schemes for2008. P.Bias indicates the column percentage bias of DEX.

The model was evaluated also in terms of the surface net downward short wave and net upward longwave radiation flux against CERES satellite measurements (Figure 3.15). In the short wave spectrum radiation flux bias ranges between -10Wm-2 and 10Wm-2 above the desert and the Mediterranean, while in the longwave the differences are mostly positive (~10Wm-2).

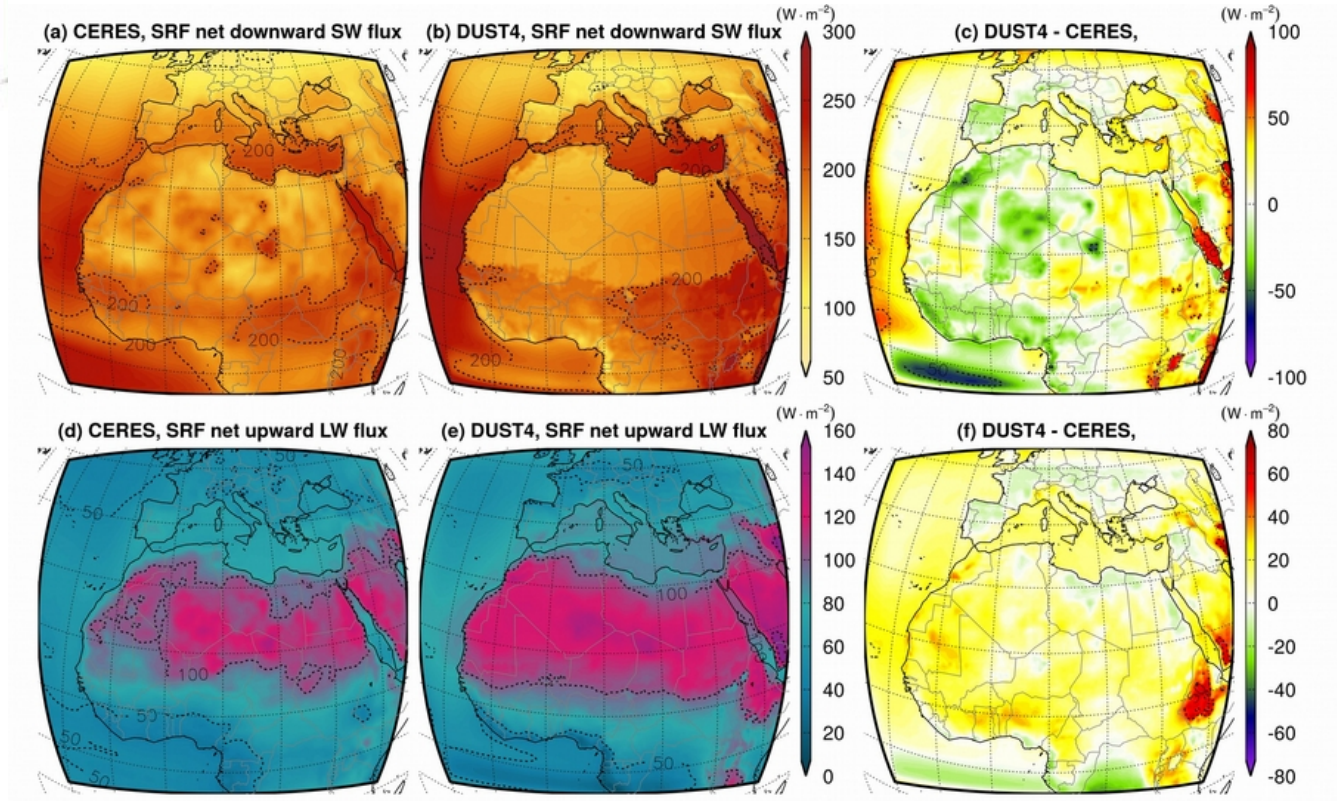

Figure 3.15. Net shortwave downward (a, b, c) and net longwave upward flux (d, e, f) in the surface of CERES and DUST4experiment for the period December 2006 to November 2014.

3.3 DUST4 vs DUST12 - Dust column burden and Dust optical Depth

The optical properties for the 4 and 12 dust size bins simulations were calculated using a Mie scattering code for each CCM3 radiation band. As noted above, the meteorological forcing between the two models is the same, therefore the emission fluxes which depend on the model's resolvable winds remain the same. Thus, the changes in column burden between the two experiments can only emerge from the new dust size discretization that theoretically improves dust transport and dry deposition processes, and the changes in DOD can only be attributed in changes related to transport and deposition.

Figure 3.16 compares the DOD coarse and fine column burden between the DUST4 and DUST12 for the full simulation period. The DOD percent increase is between 10.4% and 13% for all the subregions. Furthermore, there is a distinctive increase by 0.04 with the 12-bin model over the Sahara desert and especially along the Sahel region where the DOD values are higher (Figure 3.16c). In comparison with the DUST4 simulation the DUST12 simulation increases the deposition lifetime (column burden/total

deposition flux) by 3.5 hours and 2 minutes for fine and coarse particles respectively. Consequently, that increases the dust column burden of fine (+4%) and coarse (+3%) particles (Figure 3.16f,i). The changes in the fine particles correlates better with the changes in DOD, because dust extinction coefficient is much higher for fine particles (<2.5μm) (Figure 2.1). Over the Middle East and the northern part of the Arabian Peninsula we observe a distinct increase on the coarse dust column burden by 10mg·m-2. The differences of DOD and column burden between the two experiments, calculated from the monthly data for each grid, are statistically significant at the 95% confidence level according to a two-tailed paired t.test for almost all the grid points of the simulated domain.

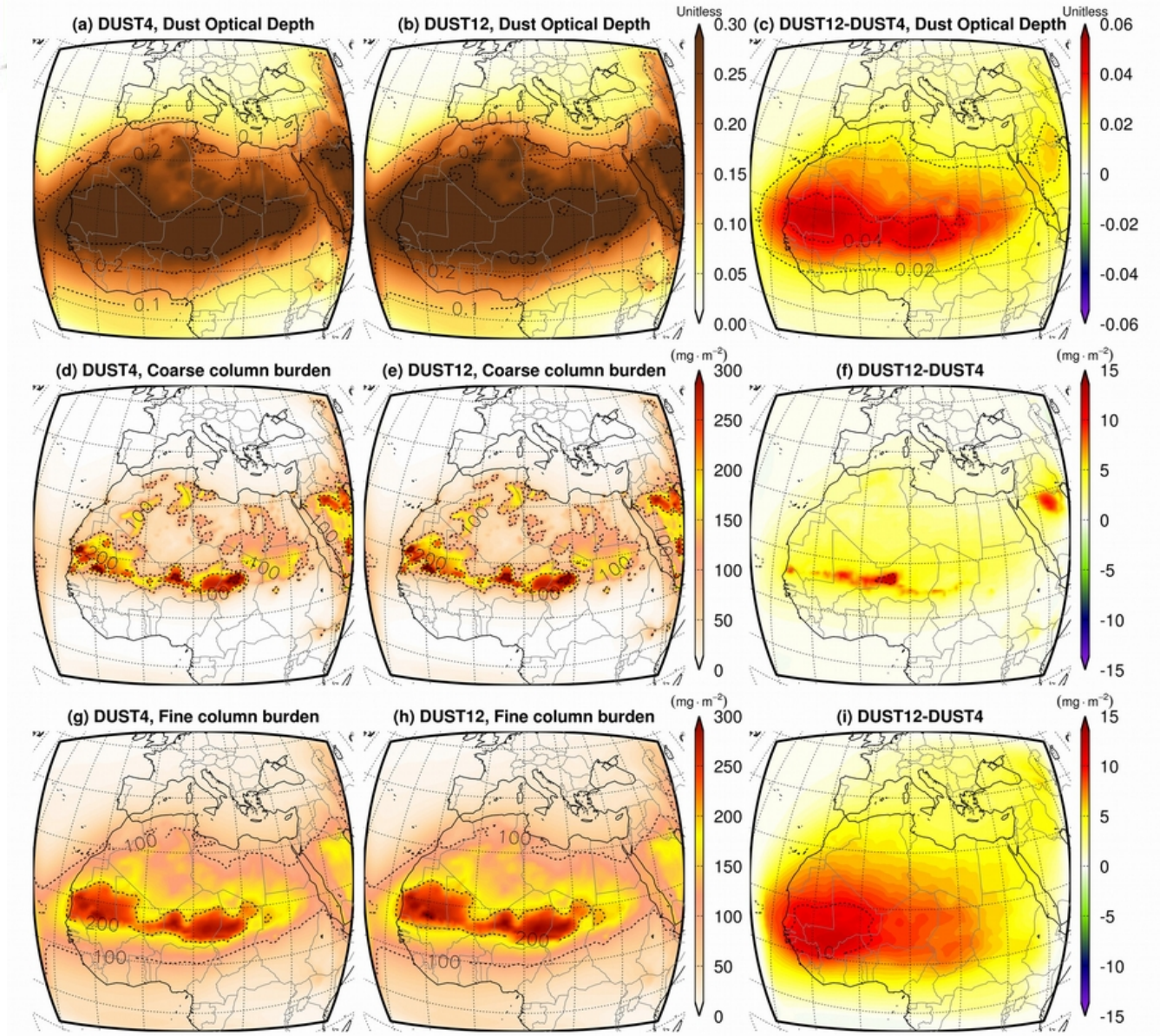

Figure 3.16. Dust optical depth and coarse (> 2.5 μm) and fine (< 2.5 μm) column burden of DUST4 and DUST12 experiments for the period December 2006 to November 2014.

The dust bin resolution also depends on the emission size distribution considered for the dust. In our study we use the Kok (2011a) dust Particles Size Distribution (PSD), which as already mentioned improves the DOD and the seasonality over the Sahara region (Nabat et al., 2012). But Kok (2011a) PSD drops very fast for large and small dust particles. Other typical dust size distributions (e.g. Alfaro et al., 1998; Zender et al., 2003) do not show such a sharp drop when increasing or decreasing the dust particle diameter (Kok, 2011a), thus they could be much more sensitive to the binning partitioning method and number which will generate bigger changes in dust column burden and DOD.

Figure 3.17 shows the annual cycle of DOD for LIVAS, DUST4 and DUST12 experiments. The monthly differences of the two experiments against LIVAS can be found in Figure 3.18. In all regions, the DUST12 experiment increases the DOD in comparison to DUST4. This is attributed to the increase of lifetime in fine and coarse dust particles in DUST12 with respect to DUST4 as also discussed earlier. Previous studies (Foret et al., 2006; Menut et al., 2007) revealed that the new approach in dust size bin partitioning and number (which is also adopted in our DUST12 experiment) more realistically simulates the transport and dry deposition of the dust size bins. This does not imply that the simulated biases will be reduced for all regions in the DUST12 experiment. The major factor that controls and potentially creates the first order biases in dust models is the balance between the emission and sedimentations terms (e.g. Figure 3.5 and Figure 3.6). As discussed in Section 3.2, some positive DOD biases (e.g. Eastern Sahara) might be due to an underestimation of the outflow of dust or a local overestimation of the emission flux from surface wind velocity errors. Therefore, although the new dust size parameterization theoretically improves dry deposition, it does not necessarily regulate or improve the biases that originate from other processes.

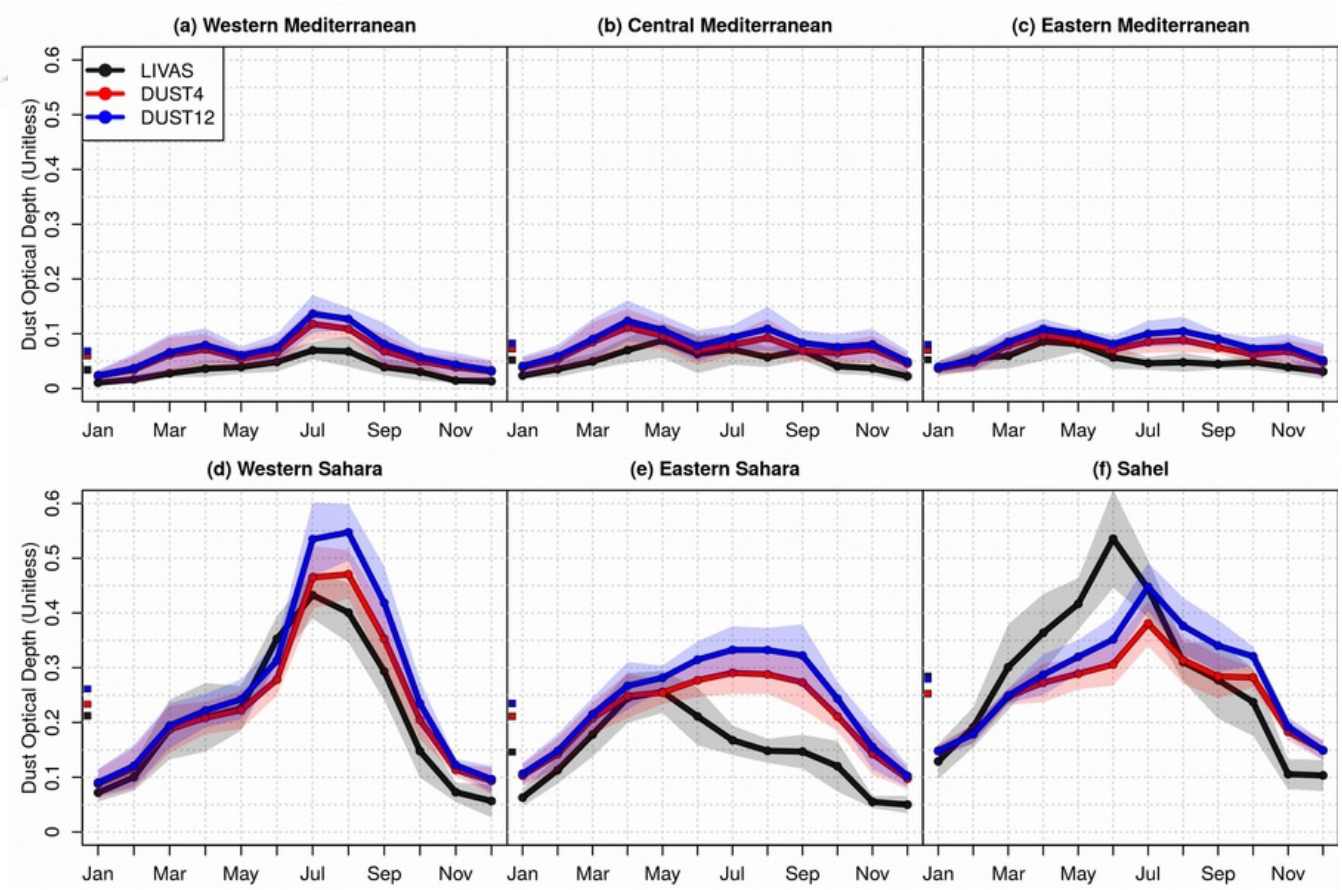

Figure 3.17. Annual cycle of dust optical depth of LIVAS, DUST4 and DUST12 experiments for the period December 2006 to November2014.

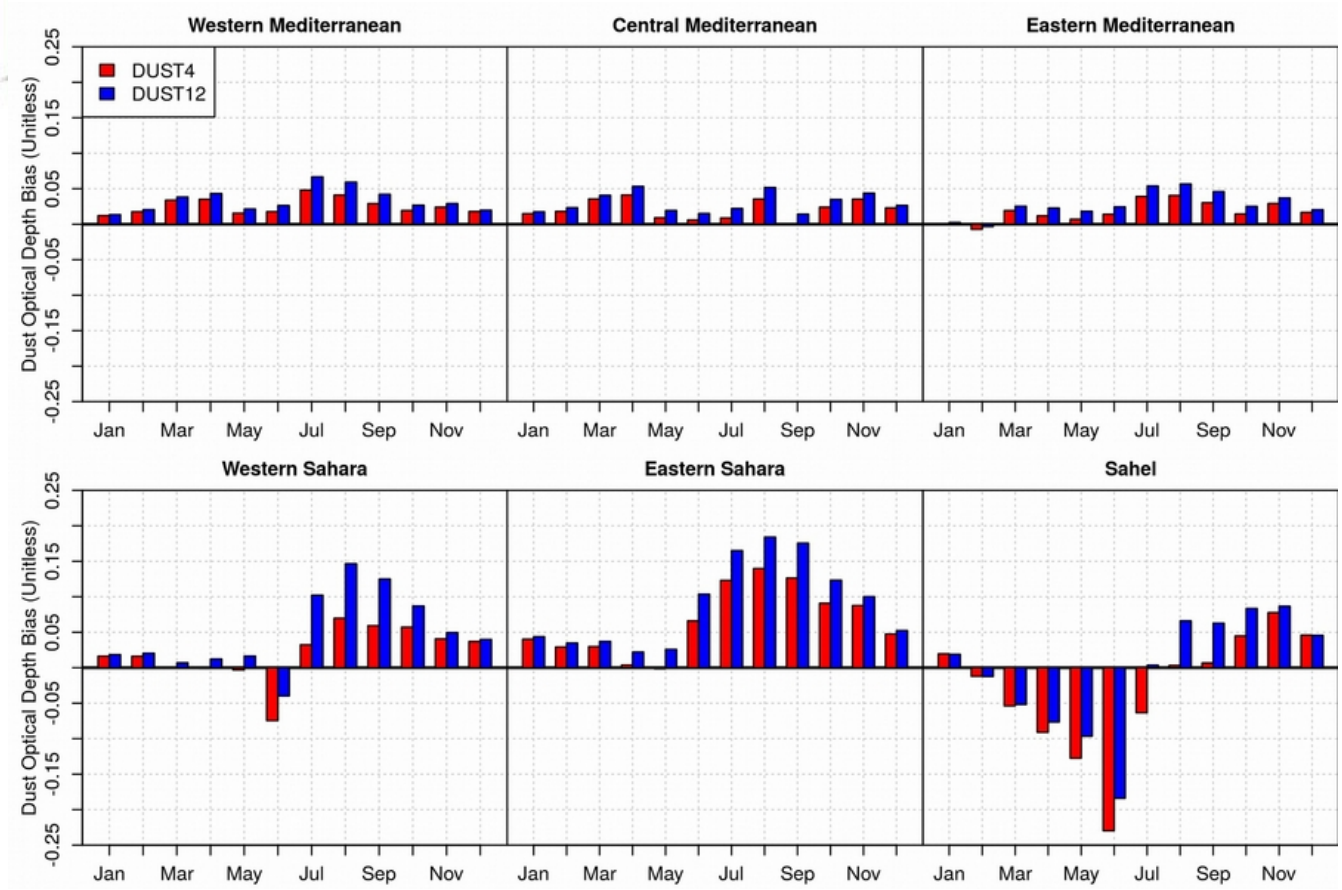

Figure 3.18. Monthly biases of DUST4 and DUST12 experiment in comparison to the LIVAS dust product for the period December2006 to November 2014.

3.4 DUST4 vs DUST12 - Radiative Effect

Dust particles can interact both with the shortwave and the longwave radiation, creating a dimming or a heating radiative effect on climate (Liao and Seinfeld 1998). According to the model the dust radiative effect over the Sahel and the North Atlantic ocean is greater than -5W·m-2 (Figure 3.19a,b). The albedo on the desert areas is already very high and in most cases, surface albedo does not change from the suspended dust. However, close to the high emission dust source of Bodélé depression we can observe positive RE values. In the model dust aloft decreases the already high albedo of the desert and creates a positive RE at the TOA. In the Bodélé depression, sediments were deposited during the Holocene in the bed of the Megachad paleolake and the large diatomite sediments formed there have high albedo values that are visible in satellite images (Bristow et al. 2010). It is interesting that RegCM4 simulates a positive radiative response caused by the combination of high surface albedo values and high emission fluxes on that area, and the change to DUST12 decreases this positive response (Figure 3.19c). The

DUST12 experiment enhances the negative radiative effect in the central and eastern Mediterranean by -0.24W·m^{-2} (10.5%) and in eastern by -0.18W·m^{-2} (8.7%). The highest absolute changes are located over the Sahel where the negative radiative effect strengthens by -0.41W·m^{-2} (12.1%).

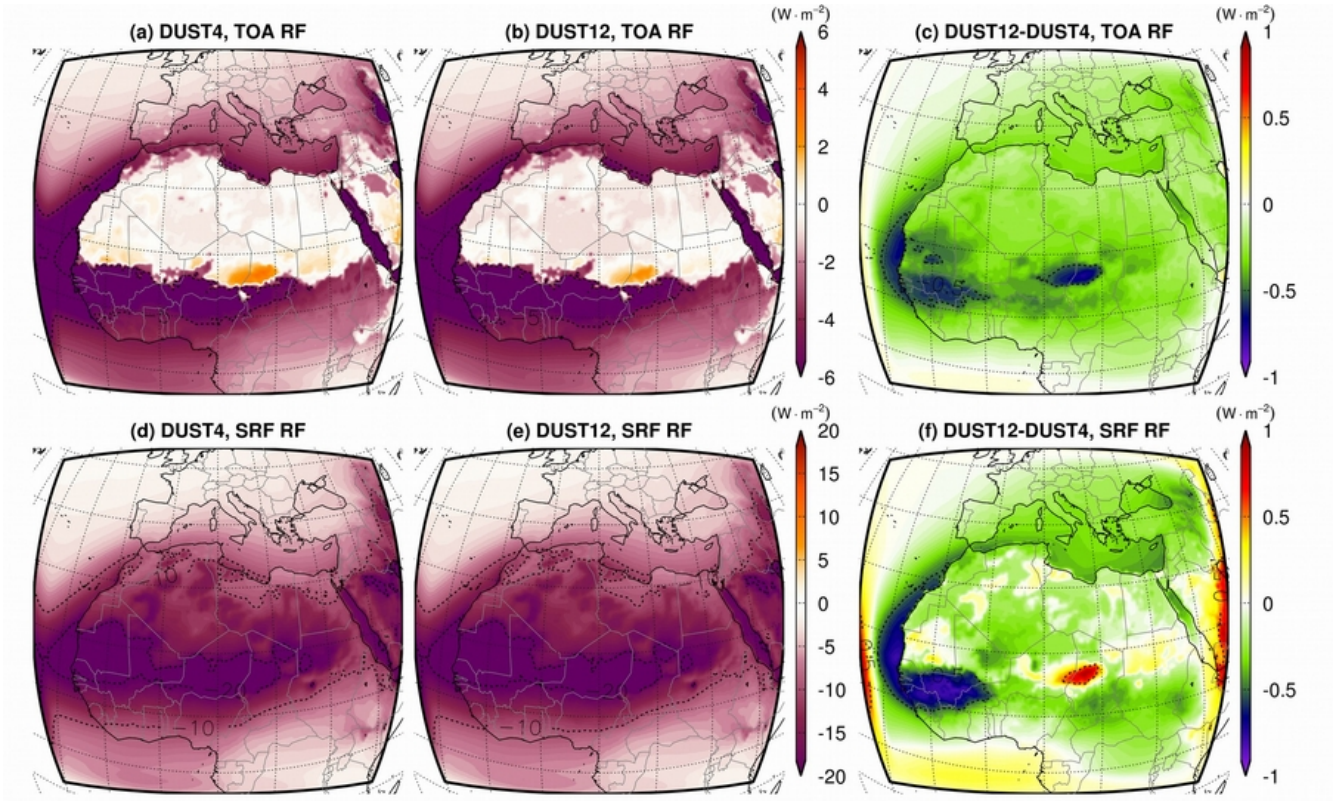

Figure 3.19. Top-of-the-atmosphere (top) and surface (bottom) radiative effect in the shortwave spectrum for the period December 2006 to November 2014.

The radiative process that backscatters and reflects the incoming solar radiation is the dominant global mechanism that affects climate. As shown in Figure 3.19d and Figure 3.19e, dust prevents more than 20W·m^{-2} of incoming solar radiation from reaching the surface on the desert and 5-10W·m^{-2} on the Mediterranean. The highest absolute differences between the two experiments are located on the western part of Africa between 15º-20ºN, where the highest fine dust burden differences between DUST4 and DUST12 were noted (Figure 3.16i). These negative changes are located in the region with the most persistent dust concentrations (Figure 3.16g,h) and changes in the dust size bins might have a bigger effect over the long range Trans-Atlantic transport than local dust radiative effect. It is worth discussing the source of the surface positive radiative effect differences between the DUST12-DUST4 experiment (Figure 3.19f), which is related to the TOA discussion. The positive RE at the TOA over the Bodélé depression is reduced in the DUST12 experiment, allowing less downward shortwave radiation

to reach the surface. Consequently, there is less available downward radiation to be scattered and reflected on these areas, and the negative radiative effect in DUST12 is smaller than DUST4. As a result the difference (DUST12-DUST4) is positive. The simulated shortwave radiative effect by the 4-bin isolog method is to some extent numerically efficient and acceptable. Nevertheless, this work emphasizes that the simplified representation of the 4-bin approach underestimates the direct radiative effect of dust by 13.7% (-0.29 $W \cdot m^{-2}$) and the SW SRF radiative effect by 1.8% (-0.23 $W \cdot m^{-2}$).

On the longwave spectrum, the RE is always positive. Coarse dust particles in the atmosphere absorb the upward longwave Earth's radiation and remit it either towards the surface or upwards to space. A part of the Earth's longwave radiation is absorbed by dust and limits the portion of upward longwave radiation that reaches the TOA, making the RE positive (Figure 3.20a,b). A fraction of the absorbed longwave radiation is remitted back towards the Earth and increases the downward longwave radiation on the surface, creating a positive RE (Figure 3.20d,e). In both cases the DUST12 experiment enhances the positive RE by $0.1W \cdot m^{-2}$ in a large portion over the Sahara desert, the northern part of the Arabian peninsula and the middle east (Figure 3.20c,f). More specifically at the TOA the positive radiative effect enhances over the eastern and western Sahara by $0.08W \cdot m^{-2}$ (6.9%) and $0.07W \cdot m^{-2}$ (5.9%) while in western, central and eastern Mediterranean increases by $0.02W \cdot m^{-2}$ (7.8%), $0.03W \cdot m^{-2}$ (7.8%) and $0.04W \cdot m^{-2}$ (8.3%) (Figure 3.20c). Similarly, at the surface the positive radiative effect rises by $0.08W \cdot m^{-2}$ (3.0%) and $0.09W \cdot m^{-2}$ (2.7%) in eastern and western Sahara and $0.9W \cdot m^{-2}$ (6.3%), $0.08W \cdot m^{-2}$ (4.8%) and $0.9W \cdot m^{-2}$ (6.5%) in western, central and eastern Mediterranean (Figure 3.20f). The shortwave and longwave radiative effect differences between the two experiments, calculated from the monthly data for each grid, are statistically significant at the 95% confidence level according to a two-tailed paired t.test for almost all the grid points of the simulated domain.

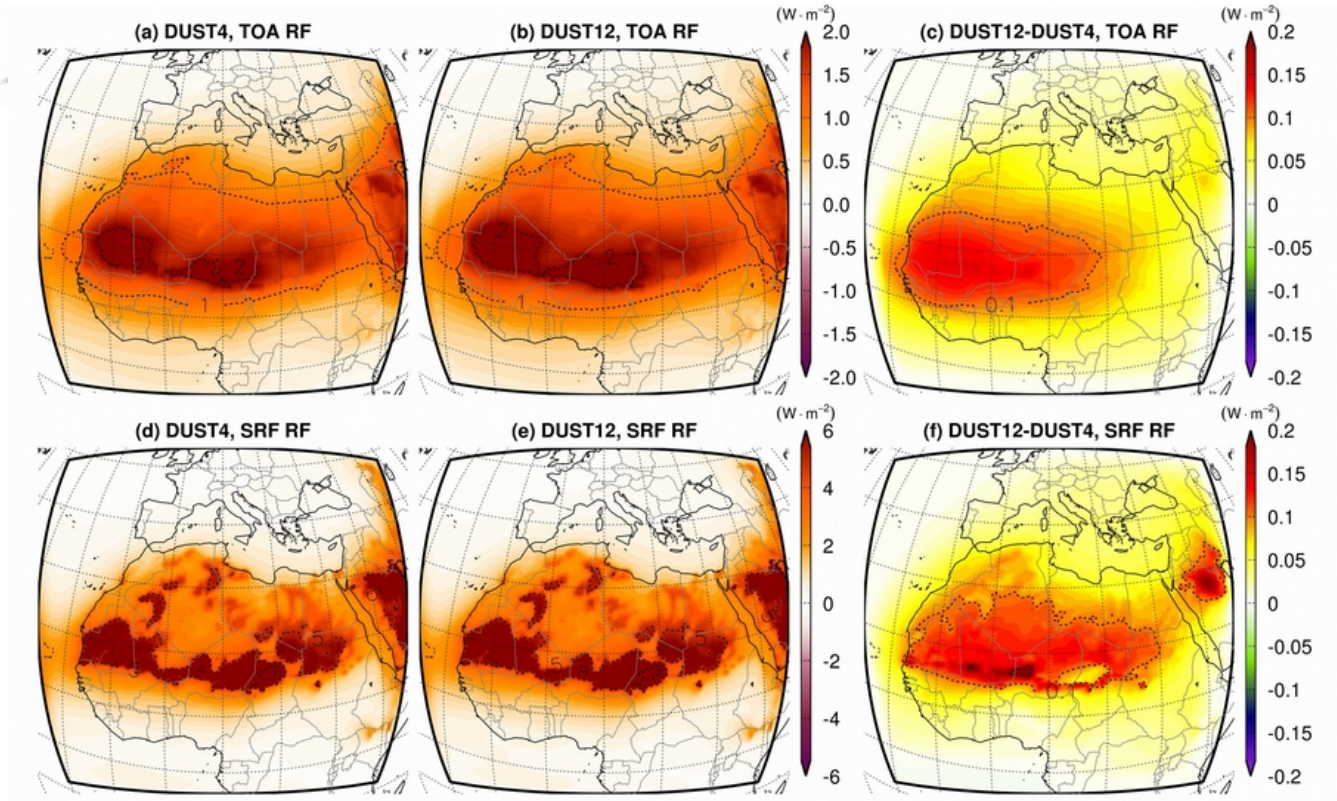

Figure 3.20. Top-of-the-atmosphere (top) and surface (bottom) radiative effect in the longwave spectrum for the period December 2006 to November 2014.

However, the current treatment of the optical properties of dust in the longwave spectrum of CCM3 scheme is limited and does not account for specific absorption coefficients for each dust size bin. Furthermore, the CCM3 longwave bands are concentrated on the absorption of H_2O and CO_2 and they do not integrate in detail the absorbing aerosol component part of the longwave. Therefore, we have conducted two similar dust experiments for June 2008 using the radiation transfer scheme RRTM, which is known for its detailed longwave calculation. It is noted again that the current version of RRTM (+McICA) produces a random generated noise on radiation fields, therefore the dust emission fluxes are not identical between the DUST4 and DUST12 experiments. The preliminary simulations using the RRTM scheme (Figure 3.22), have shown notably lower longwave dust RE over the desert in comparison to CCM3 (Figure 3.21) for the same period and roughly the same DOD levels and spatial patterns. More specifically, the DOD and the longwave radiative effect averaged above the Sahara for the CCM3_DUST4 experiment is DOD=0.31, SRF=3.5W·m^{-2} and TOA=2.1W·m^{-2}, While the related values for the RRTM_DUST4 experiment is DOD=0.29, SRF=1.9W·m^{-2} and TOA=0.6W·m^{-2}. Although DOD increases in the 12 bin experiment in both radiation schemes (Figure 3.21c, Figure 3.22c), the

longwave RE changes display a striking difference. With the CCM3 radiation scheme, the longwave radiation linearly increases with higher DOD and dust burden values (Figure 3.16f,i). In comparison, the RRTM scheme uses specific absorption coefficient for each dust size bin, taking into account the fine/coarse dust burden changes. Thus, it exhibits local increases or decreases of the longwave RE (Figure 3.22f,i), according to the changes of fine to coarse dust burden. Overall the total longwave RE increase in RRTM is smaller compared to CCM3 when spatially averaged over the Sahara desert.

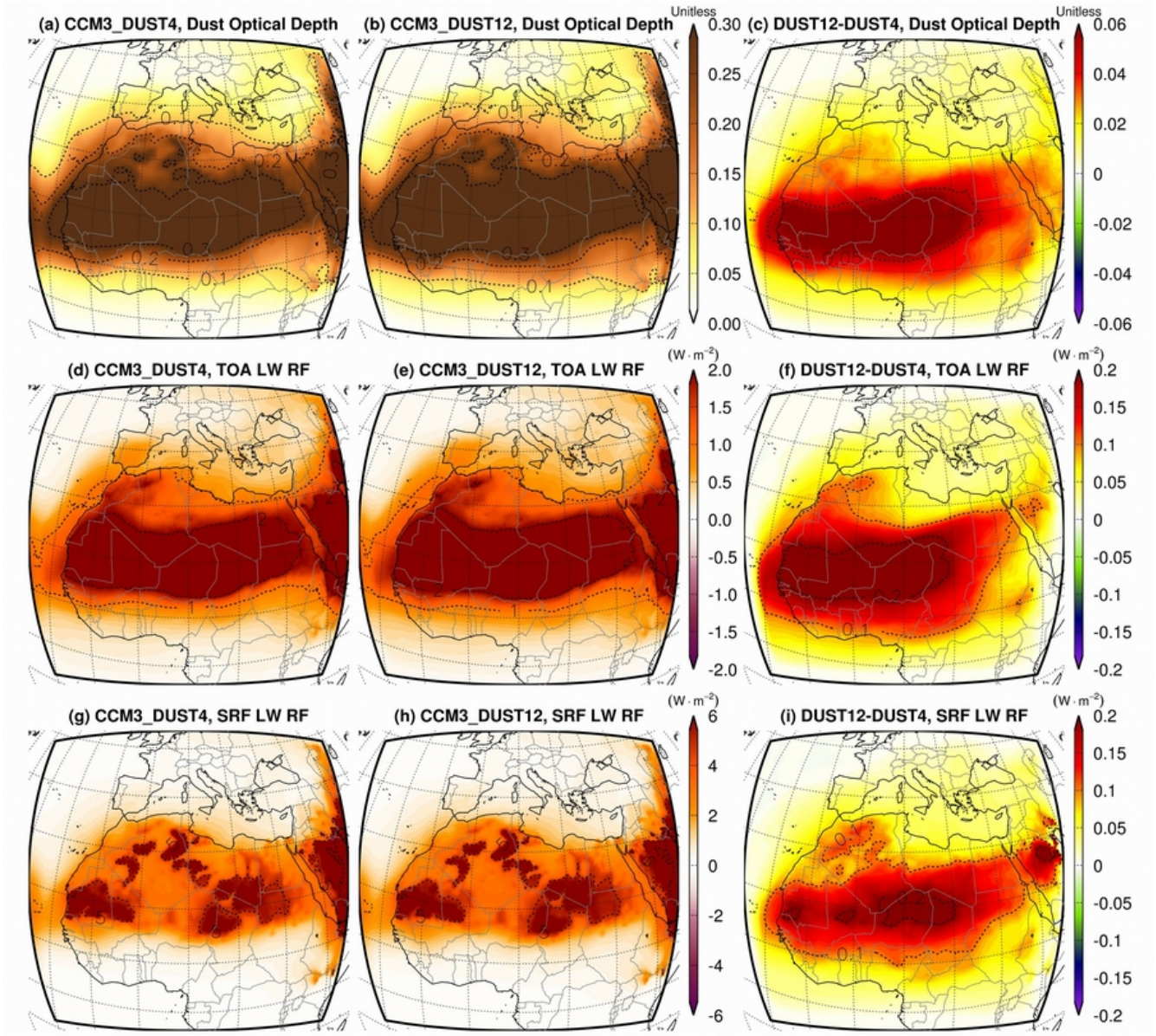

Figure 3.21. Dust optical depth, top of the atmosphere (TOA) and surface (SRF) radiative effect on the longwave spectrum using the Community Climate Model 3 (CCM3) radiation transfer scheme for June 2008.

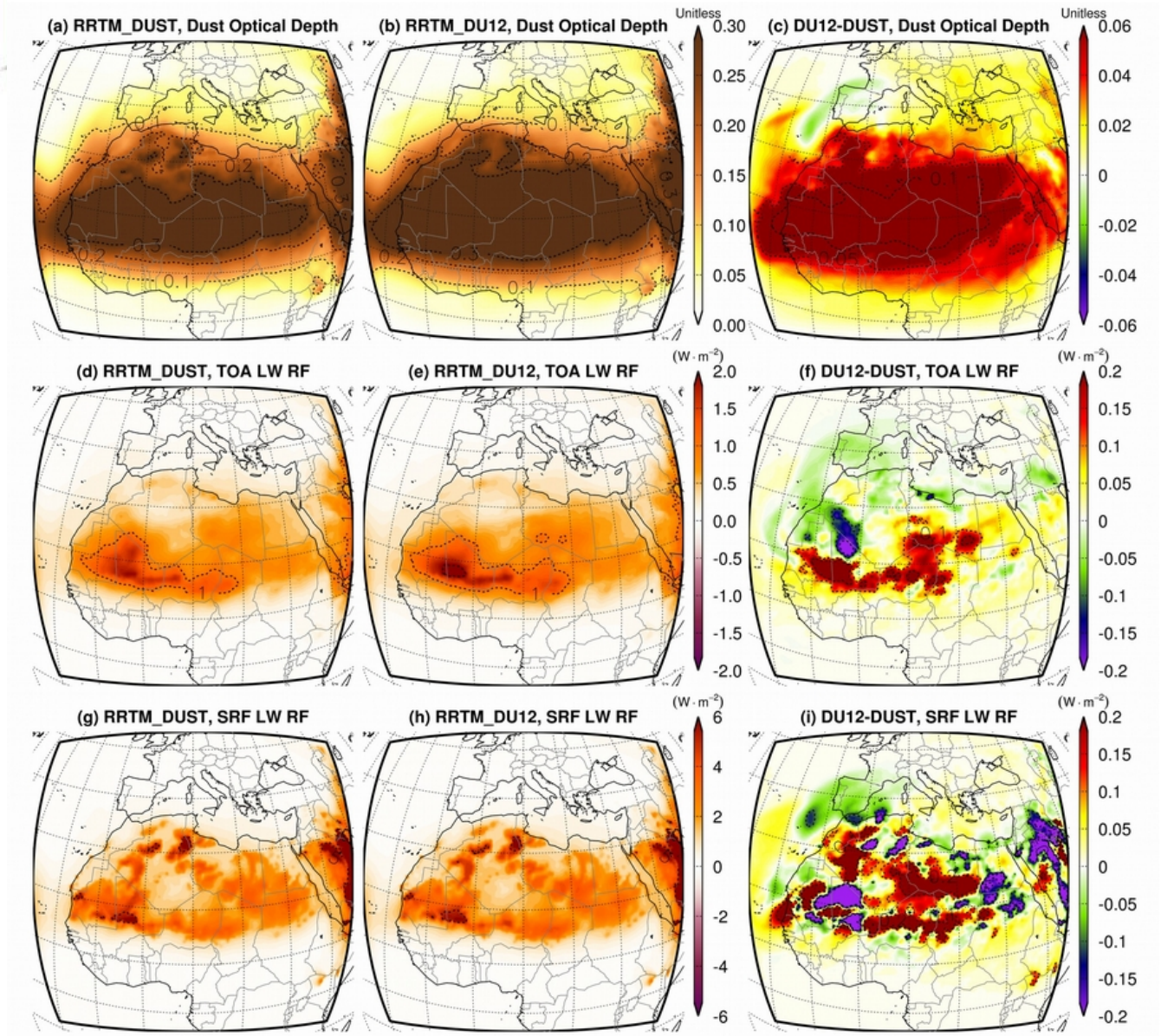

Figure 3.22. Dust optical depth, top of the atmosphere (TOA) and surface (SRF) radiative effect on the longwave spectrum using as radiation transfer scheme the Rapid Radiation Transfer Model (RRTM) for June 2008.

3.5 Summary

In this Chapter the role of the modelled particle size distribution on DOD, total column burden and radiative effect of dust is investigated using a regional climate model. The published version of these results can be found in Tsikerdekis et al. (2017) at the Atmospheric Chemistry and Physics Journal and the proceedings of the 13th International Conference on Meteorology, Climatology and Atmospheric Physics (COMECAP 2016) (Tsikerdekis et al. 2017a). A fraction of these results have also been presented in American Geophysical Union 2015 fall meeting (AGU 2015) (Tsikerdekis et al. 2015) and

the Mediterranean Climate Variability and Predictability conference 2016 (MEDCLIVAR 2016) (Tsikerdekis et al. 2016a).

The regional climate model RegCM4 dust optical depth and dust extinction is evaluated with the LIVAS dust product to understand potential model biases and link these with size-dependent emission and atmospheric processes. Generally, RegCM4 overestimates dust optical depth over important source regions such as the eastern and western Sahara by 0.083 (Pbias:63.1%) and 0.043 (PBias:26.2%) respectively and in Mediterranean by 0.027 (PBias:54.7%).

The dust optical depth annual cycle of LIVAS correlates with RegCM4 adequately in most regions. In the western Mediterranean, RegCM shows an annual cycle with a summer maximum similarly to LIVAS and in eastern Mediterranean, RegCM captures the spring maximum observed in LIVAS but additionally it illustrates a secondary maximum in summer. In the western Sahara, the RegCM DOD annual cycle correlates with LIVAS, although there is a constant overestimation during summer and autumn while in the eastern Sahara RegCM shows a broad spring-summer maximum while the observations show a clear spring maximum. In the Sahel, the model captures the observed DOD summer maximum.

The modelled emission and sedimentation terms are analyzed, as these are the most important factors for the production and deposition of dust. Additionally, vertical turbulence, horizontal and vertical advection pose a considerable negative tendency for the fine dust particles (Dd < 2.5μm). According to the annual cycle of the meridional wind component in ERA-interim, the model underestimates the southerly wind in eastern Sahara and probably decreases the outflow of dust in the area. Furthermore, the 0.9 percentile value of the averaged wind over the desert is 4.93m·s-1 and 5.92m·s-1 for RegCM and ERA-interim respectively, which indicates that the model potentially overestimates dust emission flux. At the Sahel during April, May and June the total precipitation is overestimated by the model in comparison with the CRU database. Thus, wet deposition is enhanced and emission flux is decreased since the ground has higher moisture. Overall, this process-level analysis suggests that meteorological drivers such as wind and precipitation may explain some model biases with observations.

These changes in the physical processes then link to the radiative properties that affect climate. We evaluate the Dust Extinction (DEX) from the model with LIVAS observations, and find the RegCM overestimates DEX in all subregions in the middle and upper troposphere, that can be either attributed

to an overestimation of dust convective transport or to an underestimation of some other deposition process (e.g. sedimentation). In the Western Sahara and Sahel, DEX is underestimated by RegCM below 5km, suggesting that the emissions and deposition processes are not well-balanced in the model. Our one year sensitivity study showed that the PBL mixing scheme (e.g., changing from Holtslag et al. (1990) to Bretherton et al. (2004)) can potentially improve the dust vertical distribution in the boundary layer by reducing overactive mixing.

The effect of the two different approaches on the number and the partitioning method of dust size bins was investigated in the model with two experiments: a 4 size bin simulation based on the isolog approach (DUST4) and a 12 size bin simulation based on the isogradient approach (DUST12). The DUST12 experiment increases the deposition lifetime by 3.5 hours and 2 minutes for fine and coarse particles respectively in comparison to DUST4. Consequently, the dust column burden increases by 4% (fine) and 3% (coarse) that boosts DOD by approximately 10% over the desert and the Mediterranean.

The negative surface radiative effect of DUST12 experiment in the shortwave spectrum is regionally enhanced by -0.5W·m-2 while the top of the atmosphere radiative effect is intensified by almost -1W·m-2 (10%). The negative changes in the surface dust RE are concentrated in the western part of Africa and extend over the Eastern Atlantic, where the near-constant annual dust plume is located. On the longwave spectrum DUST12 experiment enhances the positive dust RE at the surface and TOA by 0.1W·m-2 (3% and 7% respectively) in a large portion of the Sahara desert, the northern part of the Arabian Peninsula and the middle east. The radiation transfer scheme RRTM, known for its detailed integration on the longwave spectrum, revealed that these longwave dust RE changes can be also locally negative and therefore smaller when spatially averaged over the Sahara desert.

Overall, this study highlights that the DOD, dust column burden and radiative effect differences between the two dust size bin treatments are relatively small. The 12-bin isogradient method represents more realistically the physical processes such as deposition and optical properties of dust, nevertheless the 4-bin isolog method is numerically efficient and can be useful for long term regional climate simulations. We have to note that other typical size distributions (e.g. Alfaro et al. 1998; Zender et al. 2003) could be much more sensitivity to the binning partitioning method and number which could generate bigger changes in dust column burden DOD and dust RE.

4. Modeling the Trans-Atlantic transport of Saharan dust

Mineral dust is the most abundant atmospheric aerosol in the atmosphere, accounting for the 70% of global aerosol volume and almost 25% of the total aerosol optical depth in 550nm (Kinne et al. 2006). Natural dust is emitted in episodic events over arid and semi-arid areas that are concentrated between 15º-30º latitude in both hemispheres. The largest source of mineral dust is the Sahara desert (Tegen 2003), a vast arid region in the Northern Africa that receives less than 200 $mm \cdot yr^{-1}$ of precipitation (Engelstaedter et al. 2006). Between the zone 40ºN-10ºS latitude, dust is transported by the easterly trade winds though the Atlantic ocean to the American continent affecting the radiation budget of the planet with numerous direct (Liao and Seinfeld 1998) and indirect mechanisms (Bangert et al. 2012). A fraction of Saharan dust, which is rich in phosphorus (Hudson-Edwards et al. 2014) and iron (Jickells 2005), is deposited in the Atlantic and the Amazon forest providing crucial nutrients that are essential for marine (Mahowald et al. 2005b) and forest ecosystem (Bristow et al. 2010). Dust may also affect the growth and intensity of strong tropical synoptic systems, known as easterly waves, that eventually may evolve into tropical cyclones (Zipser et al. 2009).

Dust particles size in the atmosphere ranges from 0.01μm to 100μm (Knippertz 2014). The atmospheric lifetime of dust particles controls the evolution of dust size distribution as they move downwind (Mahowald et al. 2014). Large particles, due to their size and weight, are concentrated close to the ground and they are quickly removed from the atmosphere through dry deposition processes. Since they have such a short atmospheric life, they are located mainly close to the source regions. However recent studies have found coarse dust particles (4μm to 32μm) deposited over long distances into the Atlantic (Van Der Does et al. 2016). On the other hand, small particles, usually smaller than 2.5μm, can be uplifted and remain in the atmosphere while they are being transported for thousands kilometers away from their source regions. Although size and density of dust particles are the key factors that force sedimentation, particle shape can have a big impact both on their deposition velocity and optical properties (Formenti et al. 2011). The number of the simulated dust size bins and their partitioning method can affect the dust optical depth by up to 10%, both close to the dust sources (Sahara) and away from them (Mediterranean) (Tsikerdekis et al. 2017b).

Previous researches have highlighted the almost constant dust plume that begins on the western coast

of Sahara and floats over the North Atlantic ocean reaching the South-Central America (Carlson and Prospero 1972; Prospero et al. 1981; Karyampudi and Carlson 1988; Kallos et al. 2006; Ridley et al. 2012; Chin et al. 2014; Kim et al. 2014; Yu et al. 2015; Tsikerdekis et al. 2016b). Although the dust plume covers the largest part of the North Atlantic ocean all year long, it has some spatial-seasonal characteristics. Backscattering measurements of dust from the satellite instrument CALIOP showed that the dust transport peaks at summer and weakens in autumn. In both of these seasons dust concentration reaches its highest value between 10ºN-20ºN latitude. Contrary in winter and spring dust transport shifts southward close to the equator between 0º to 10ºN latitude. These seasonal differences extent also on the vertical distributions of dust that looms over the North Atlantic (Yu et al. 2015). CALIOP measurements indicated that most of the global models underestimate dust extinction (DEX) in lower levels close to the sources and overestimate it on higher altitudes above Atlantic (Koffi et al. 2012). The Inter-Tropical Convergence Zone (ITCZ) correlates with the western Africa monsoon in this area. The ITCZ controls the seasonal precipitation rates over the semi-arid Sahel area and more importantly the changes in large-scale wind patterns. Both of these factors affect dust productivity and long-range transport (Engelstaedter et al. 2006; Engelstaedter and Washington 2007; Williams 2008). A simulation of an offline dust model that uses the re-analysis database ERA-40 and ground-based measurements for several soil characteristics in Sahara, showed that dust emission flux follows a marked seasonal cycle that peaks in spring over the eastern part of the desert and in summer on the western (Laurent et al. 2008).

During the trans-Atlantic transfer Million tons (Tg) of dust are emitted from Sahara and deposited over the North Atlantic and the South and Central America every year. The exact number of the deposited dust for these regions it is still debated (Kaufman et al. 2005; Koren et al. 2006; Ridley et al. 2012), partly because satellite products do not measure directly deposition fluxes but aerosol optical depth and the ground-based station network that actually measure dust deposition is spatially sparse, especially over the ocean. Using the Advanced Very High Resolution Radiometer data, Swap et al. (1992) showed that about 13 $Tg \cdot yr^{-1}$ of dust are deposited into the Amazon Basin mainly by wet deposition during intense rainfall episodes, but highlighted that more than 50 $Tg \cdot yr^{-1}$ of dust are necessary to adequately fertilize the Amazon Tropical forest. Kaufman et al. (2005) has calculated using the MODIS (Terra/Aqua) measurements that dust deposited in the tropical Amazon forest can reach up to 50 $Tg \cdot yr^{-1}$. The dust Tran-Atlantic transport intensifies during summer, although its southward shift takes place

during winter and spring, where dust emissions in Bodele are high. Koren et al. (2006) concentrated over the rich-in-phosphorus soil over the Bodele depression in Sahara (Hudson-Edwards et al. 2014). They argued using MODIS that about 40±13 $Tg \cdot yr^{-1}$ arrive at South America and that most of this dust comes from this single source. The GEOS-Chem model showed that 17±5 $Tg \cdot yr^{-1}$ are deposited in the Amazon forest, which is considerably lower than MODIS studies have estimated (Ridley et al. 2012) and noted that the satellite approximation is probably a maximum estimate.

Regional and global climate models can help us quantify the amount of dust deposited in the Amazon or in any other place in the globe. Although as mentioned in Huneeus et al. (2011) that studied 14 global climate dust simulations, the relative standard deviation of both global emission (61%) and deposition fluxes (59%) is quite large, while the dust column burden and dust optical depth at 550nm relative standard deviation is lower (39% and 37% respectively). A similar study which is focused over the Sahara highlighted that the emitted dust from the desert greatly differs between models by a factor of five (from 422 to 2025 $Tg \cdot yr^{-1}$) with a relative standard deviation 57.1%, considerably affecting dry (59.1%) and wet (60.8%) deposition flux too (Kim et al. 2014). Simulating dust emission becomes even more challenging if we consider that soil surface particle distribution does not reflect the respective emitted aerosol dust distribution (Okin et al. 2011). Thus, dust climate model results should be treated with caution when quantifying deposition processes and always should be evaluated with the available ground-based and especially broad spatially available satellite products.

The processes involved in the Trans-Atlantic transport of dust over the Atlantic is explored and assessed using the regional climate model RegCM4. In Section 4.1 the simulated domain and the six experiments conducted are presented. Five distinct Sections of the results follow: (i) evaluating the dust optical depth column/profile of the model and exploring the intra-annual characteristics governing the Trans-Atlantic dust transport, (ii) investigating the role of cumulus convection in the Trans-Atlantic dust transport, (iii) expanding the work of Tsikerdekis et al. (2017) by searching the role of dust size number/method discretization during long-range dust transport, (iv) comparing RegCM4 dust related processes with the multi-model study of Kim et al. (2014) and (v) quantifying the amounts of dust deposited in North Atlantic, the Amazon basin and the Caribbean based our RegCM4 simulations. Section 4.7 summarizes our results and proposes possible improvements and ideas for future research.

4.1 Simulation set-up

One long 8-year simulation, one 4-year simulation and four yearly simulations for 2012 have been conducted with the regional climate model RegCM v4.5.0. To comprehensively study the dust Trans-Atlantic related processes, the domain includes the Sahara desert, a large portion of the north and south Atlantic ocean, the Caribbean and the Amazon forest basin (Figure 4.1). The domain was divided in six subregions according to dust optical depth spatio-temporal characteristics. Sahara was selected based on the desert grid points assigned by the model. The semi-desert region of Sahel, which is located southern of the Sahara, was isolated by selecting the grid cells that receive annual precipitation between 100mm to 600mm (Ali and Lebel 2009; Nicholson 2013) using the CRU dataset for the period 2001 to 2014. The South and North Atlantic subregions were separated by taking into account the year-long dust plume over the Atlantic ocean and its inter-annual variability upon ocean grid cells only. The Amazon basin delimitation used the "Evergreen broadleaf tree" grid cell type over South America which characterizes the vegetation in the tropical band. The Caribbean region was selected using longitude and latitude limits.

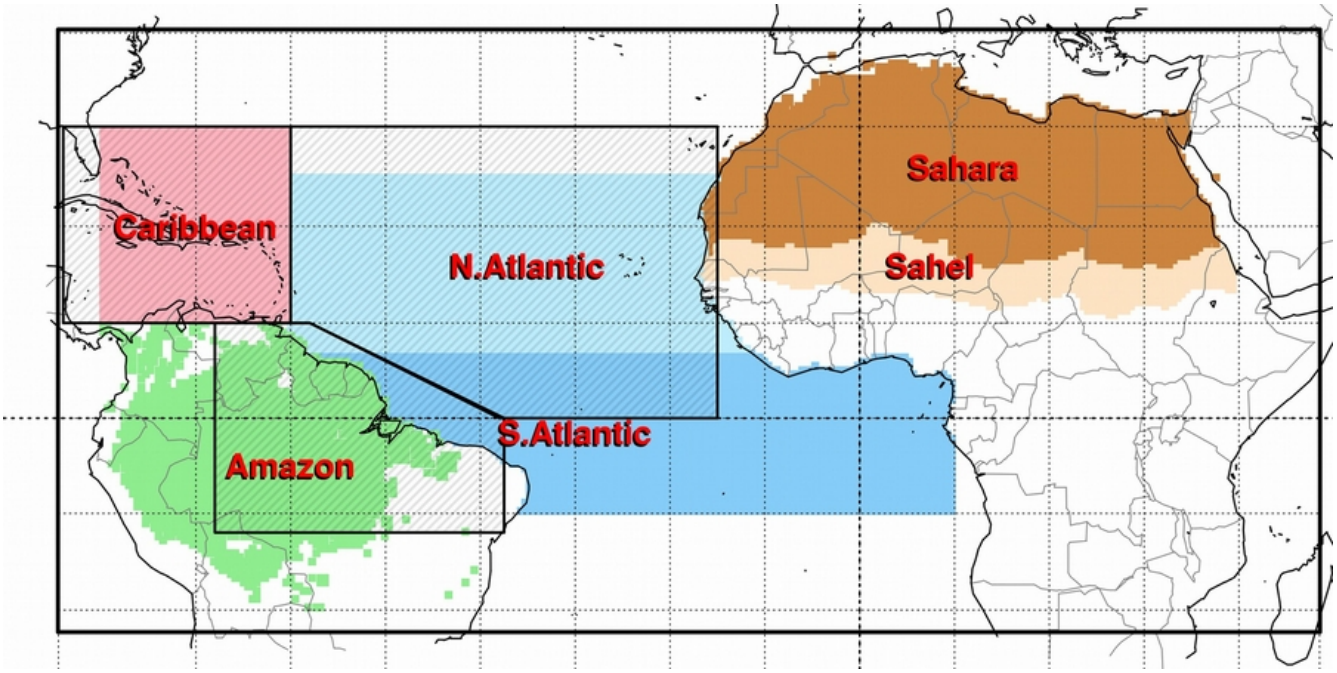

Figure 4.1. The domain used for all the simulations is depicted with the outer solid black line. The six subregions that were used in the statistical analysis are depicted as colored grid cells. The delimitation of each region is described in the text. The hatched filled polygons depict the regions defined by Ridley et al (2012). The equator and prime meridian are depicted with bold dashed lines while the rest parallels and meridians are drawn every 10° with dashed lines.

The first two experiments (TRANS4 and TRANS12) cover the period from December 2006 to

November 2014 and their set-up is similar to DUST4 and DUST12 of 3. TRANS4 and TRANS12 inter-comparison is aiming to quantify the importance of dust bin discretization method and number on dust optical depth and dust radiative effect, during the long-range Tran-Atlantic course. More information about the bin discretization method and number can be found in Foret et al. (2006) and Tsikerdekis et al. (2017). Four cumulus convection combinations with Emanuel, Grell and Tiedtke schemes over land and ocean have been conducted (TRANS-E, TRANS-EG, TRANS-T, TRANS-TG). The objective of these experiments is to highlight the influence of convective scheme on dust load, wet deposition and vertical distribution. After analyzing the LIVAS dataset, 2012 was proven to be an intense dust Trans-Atlantic year, thus it was selected for these short-term experiments. A detailed description with the options of all the experiments is available at Table 3.

Table 3. A summary of the simulations and the options selected in RegCM4. ICBC stands for Initial and Boundary Conditions, PBL stands for Planetary Boundary Layer and PSD stand for Particle Size Distribution.

Category/Experiment	**TRANS4**	**TRANS12**	**TRANS-E**	**TRANS-EG**	**TRANS-T**	**TRANS-TG**
Grid Dimensions	300 x 150, 18 sigma levels					
Horizontal Resolution	50km					
Period	2006-12-01 2014-11-30	2006-12-01 2010-11-30	2012-01-01 - 2012-12-31			
Meteorological ICBC	ERA-interim					
Chemical ICBC	EC-EARTH + CAM					
Cumulus over Ocean	Tiedtke		Emanuel		Tiedtke	
Cumulus over Land	Tiedtke		Emanuel	Grell	Tiedtke	Grell
Radiation Scheme	CCM3 (Kiehl et al., 1996)					
Moisture Scheme	SUBEX (Pal et al., 2000)					
PBL Scheme	Modified Holtslag (Holtslag et al., 1990)					
Dust Tracers	4 bins	12 bins	4 bins			
Dust PSD	Kok (Kok, 2011a)					

4.2 Trans-Atlantic dust evaluation and spatio-temporal characteristics

Dust Optical Depth (DOD) and Dust EXtinction coefficient (DEX) for each layer of TRANS4 experiment was assessed using the LIVAS dust product. Since those two datasets were produced based on different spatiotemporal considerations, some necessary pre-processing steps were required before the evaluation. The simulated spatial fields were firstly interpolated into the 1ºx1º grid of LIVAS in order to calculate directly the differences between the two datasets. Furthermore, since LIVAS was produced using the attenuated backscatter measurements of the CALIOP instrument upon the non-geostationary satellite CALIPSO, the spatial-temporal fields are not consecutive. Dust optical measurements were available only when the satellite orbit and the cloud vertical distribution in the atmosphere were favorable. Thus, a spatiotemporal mask was produced using the exact UTC time and grid cell location specified in LIVAS. The UTC times specified in the metadata of LIVAS were interpolated to the closest timestep of the model. The spatial-temporal mask of LIVAS was applied in the 6-hourly RegCM4 data and thereafter the monthly, seasonal and yearly means were calculated.

The DOD of LIVAS and TRANS4 experiments for the period 2007 January to 2014 November is depicted in Figure 4.2. Overall the model simulates the DOD level over the Sahara adequately and captures the extended dust plume from the western part of the desert towards the North Atlantic Ocean. The differences of the two datasets are fairly small ranging from 0.1 to -0.1. The western and eastern Sahara display a negative and positive bias respectively. The possible source of those discrepancies is thoroughly discussed in Tsikerdekis et al. 2017. The apparent negative bias over the Arabian peninsula is produced partially because the region lies close to the boundaries of the simulation and more importantly by the Lidar Ratio used in LIVAS, which is calibrated for the physicochemical characteristics of Saharan dust only (Amiridis et al. 2013). Over the Atlantic ocean the model slightly overestimates DOD in a zone between 0º and 10º which extends also over the northern part of South America and slightly underestimates DOD between 10º and 30º. These biases, averaged for the whole 8-year period, intensify when we analyze our datasets in a monthly basis. The Modified Normalized Mean Bias (MNMB) and the Fractional Gross Error (FGE) (equations in the Appendix) for the six subregions presented in Figure 4.1 is presented in the Table 4. The Amazon basin shows the highest positive MNMB (90%) and FGE (91%), which is mostly produced by an overestimation of dust in mid

and upper Troposphere as discussed later on in Figure 4.4.

Table 4. Dust optical depth basic validation metrics of LIVAS and TRANS4 experiment for 6 subregions. MNMB stands for Modified Normalized Mean Bias and FGE stands for Fractional Gross Error.

Region	LIVAS DOD	TRANS4 DOD	MNMB	FGE
Caribbean	0.033	0.036	7%	32%
N.Atlantic	0.12	0.128	4%	19%
Sahara	0.18	0.197	11%	25%
Amazon	0.012	0.035	**90%**	**91%**
S.Atlantic	0.05	0.058	28%	44%
Sahel	0.276	0.274	-3%	21%
All	0.102	0.113	23%	38%

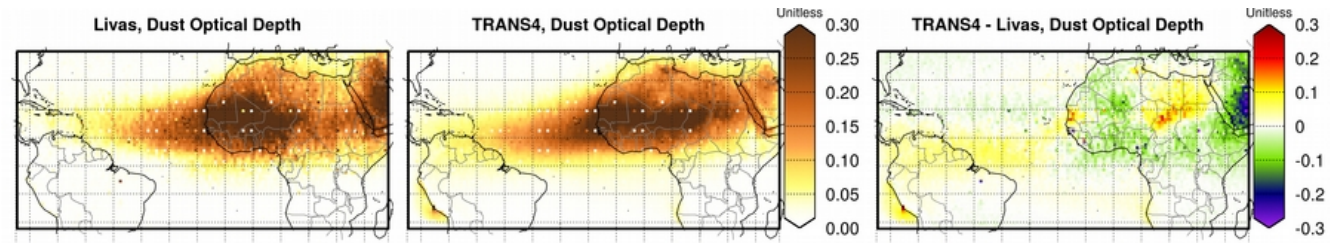

Figure 4.2. Dust optical depth of LIVAS and TRANS4 experiment for the period January 2007 to November 2014.

The annual cycle of dust optical depth is depicted in Figure 4.3 for the six subregions presented in Figure 4.1. In all subregions and especially in Sahara and Sahel ((Figure 4.3c,f) the inter-annual amplitude of the model is smaller in comparison to LIVAS (except the Amazon). Over the Sahara the combined overestimation and underestimations of the eastern and western Sahara creates an almost zero bias over the desert. DOD is overestimated from October to February and underestimated during the warm period of the year (March-September). Similar behavior is observed in Sahel (Figure 4.3f), although in that case the DOD overestimation during spring and summer is quite higher that the one observed in Sahara. As we move westward away from the dust sources towards the N.Atlantic (Figure 4.3b) and the Caribbean (Figure 4.3a), the DOD annual cycle preserves its shape with an evident June-July-August maximum. The model underestimates DOD and the inter-annual standard deviation in both cases, but it adequately captures the summer DOD maximum. In South Atlantic (Figure 4.3e) and the

Amazon basin (Figure 4.3d) the model does not capture the December-April peak and simulates a flat (constant) DOD annual cycle throughout the year. During winter and especially spring, the Atlantic dust plume moves southward (Yu et al. 2015) closer to the equator, but most of the global/regional climate models cannot accurately simulate that change (Prospero et al. 2014). Although RegCM4 shows a slight southward transfer in winter-spring across the Atlantic compared to summer-autumn, it is not enough to accurately simulate the observed spatial pattern of LIVAS. Like most of the models, RegCM4 simulates the trans-Atlantic transport better during summer than in winter (Huneeus et al. 2011).

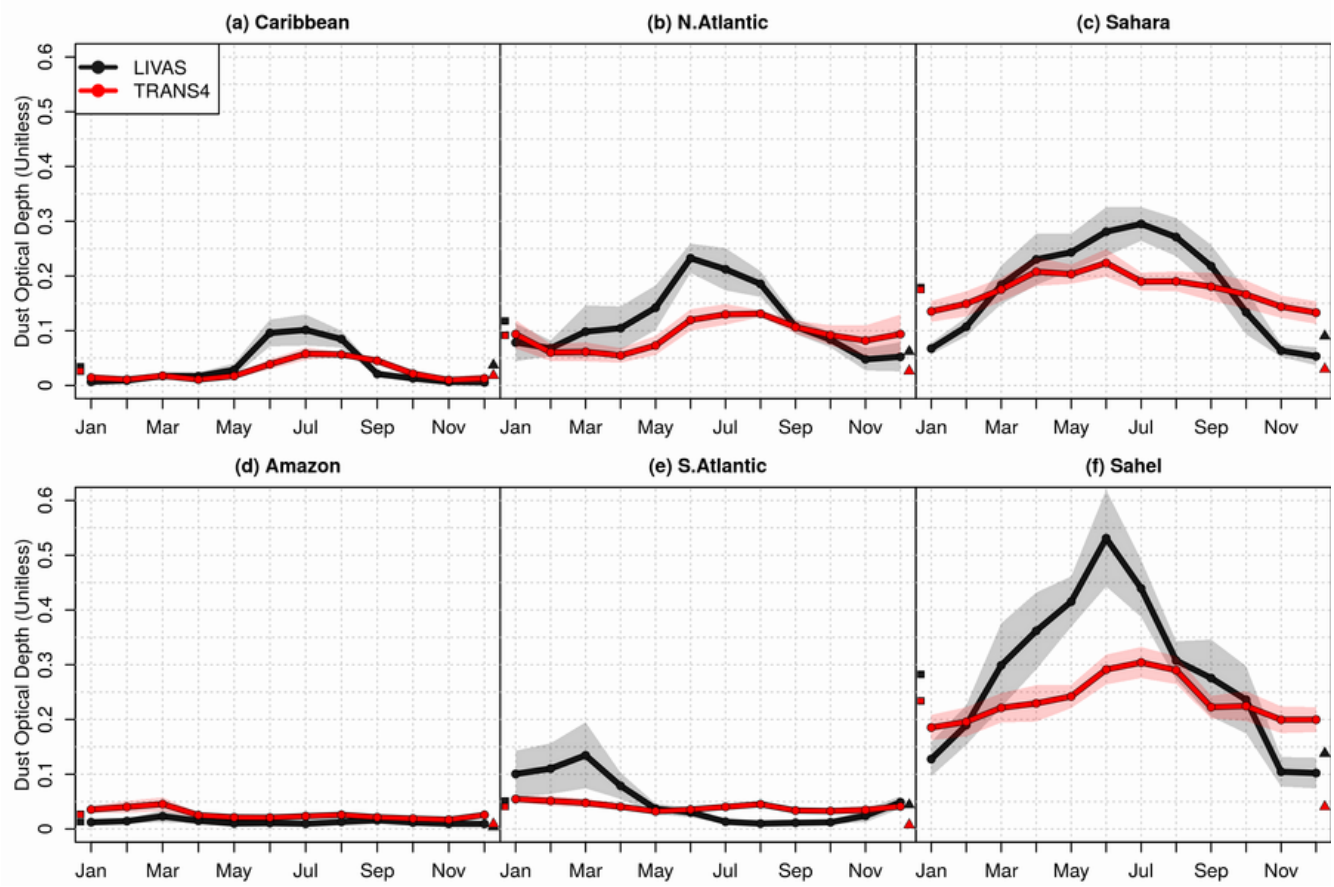

Figure 4.3. The annual cycles of dust optical depth for six sub-regions. The shaded areas show the 95% confidence level of monthly means. The squares and triangles along the yy' axis indicate the annual mean and standard deviation for each region.

The vertical profile of DEX is depicted for the same six subregions in Figure 4.4. The profiles where created for two distinct warm (May-September) and cold (December-April) periods by taking into account the (i) annual cycle presented in Figure 4.3 and the (ii) results of previous studies that highlight the seasonal changes in dust height and trajectory over the Atlantic. These seasonal changes are

strongly related to the Inter-Tropical Convergence Zone (ITCZ) advancement or retreat (Yu et al. 2015). During the warm period, TRANS4 underestimates DEX in 5km of the atmosphere in Sahara, Sahel, N.Atlantic and Caribbean (Figure 4.4a,b,c,f) and overestimates it in all cases above 5km. The mid-upper Troposphere positive bias is created by the simplistic method of dust vertical transport when cumulus convection initiates in a grid cell (more on section 4.3). The model captures the DEX profile more efficiently in the cold period, except the South Atlantic Figure 4.4e whereas the December-April peak is not captured by the model (Figure 4.3e). Over North Atlantic (Figure 4.4b), where the dust Trans-Atlantic transport is more evident during warm period, dust peaks at 3-4km according to LIVAS while TRANS4 peaks slightly lower at 3km. On the other in South Atlantic (Figure 4.4e), where dust is evidently more present in the cold period, dust is transported over lower altitudes closer to the surface (0-3 km) according to LIVAS. The model shows the same low-altitude “peak” but strongly underestimated. Over the Amazon (Figure 4.4d) TRANS4 greatly overestimates the DEX above 1-2km in the cold period but adequately captures the DEX in the lower levels close to the ground. Thus, the models dry deposition flux estimations can be considered quite accurate for the Amazon. The same cannot be stated for wet deposition flux, due to the underestimation of precipitation over the same region as shown in Figure 4.5. Previous multi-model studies showed that the Aerosol Extinction profile of CALIOP instrument is overestimated over Sahara and Middle East by the majority of the GCMs models while over North Atlantic and South America the effective dust height is underestimated (Koffi et al. 2012). Similar behavior is observed for Dust Extinction profile by RegCM4 in the non-dust source regions, but not over desert where DEX profile is again underestimated, especially in summer. The inter-annual variability of MODIS AOD for the period 2000 to 2003 is 12% (Kaufman et al. 2005), while the inter-annual ratio of standard deviation to the mean DOD for LIVAS and TRANS4 is 10% and 4% respectively.

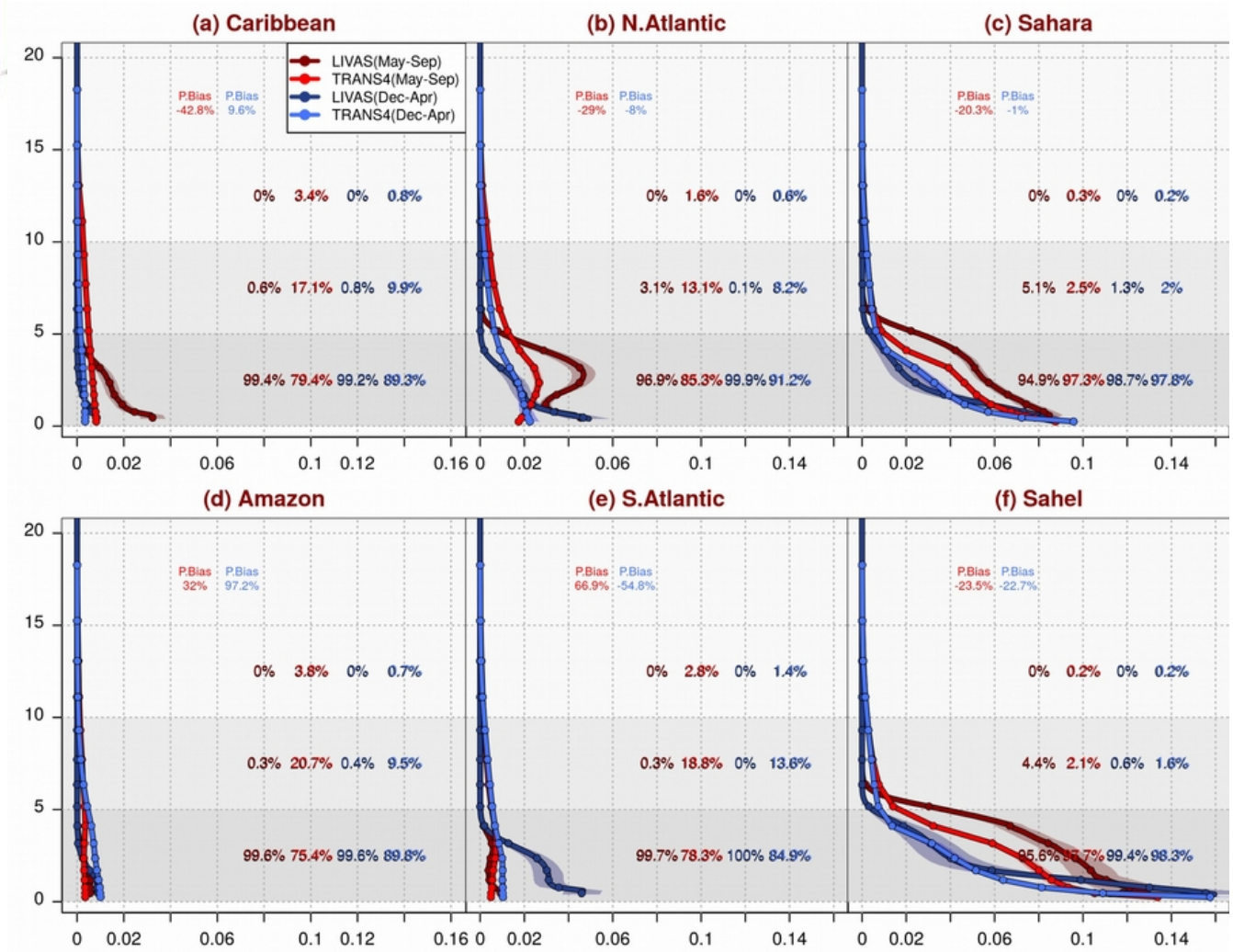

Figure 4.4. The DEX profiles of LIVAS and TRANS4 from the period January 2007 to December 2014. The red and blue colors depict May-September and December-April profiles. The percent bias (P.Bias) for the whole DEX column as well as the percent of DEX between 0-5km, 5-10km and 10-20km for each case is depicted on the plot.

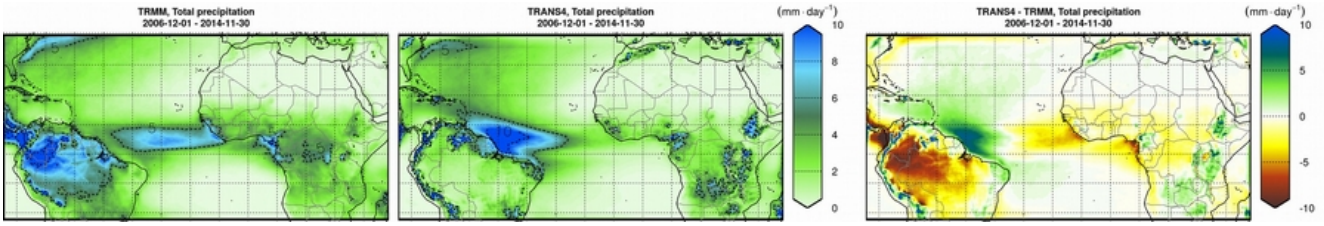

Figure 4.5. Total precipitation of TRMM and TRANS4 experiment for the period 2006-12-01 to 2014-11-30.

4.3 Trans-Atlantic dust and the role of cumulus convection

Cumulus convection can significantly enhance or depress dust column burden over the Sahara and north Atlantic. One mechanism is by changing the precipitation pattern over the desert which can affect the surface humidity of the erodable surface, increase the inter-particle cohesion forces between the

dust particles and decrease the potential dust emission flux. Precipitation can also alter the dust column burden and dust particles atmospheric lifetimes, mostly away from the emission sources, through wet deposition processes. Furthermore, dust vertical distribution and consequently its horizontal transport and distribution in the atmosphere can be affected by the vertical transport of dust particles due to cumulus convection.

On this Section four yearly RegCM4 simulations parameterized under different convective scheme combinations over ocean and land are evaluated. The Grell (Grell 1993) convective scheme accounts for dust vertical transport when cumulus convection initiates with a simplistic assumption, where dust concentration becomes homogeneous from clouds top to base, due to turbulence and the well-mixed air within the cloud. This simplistic method usually has a positive effect on dust load that increases dust atmospheric lifetime, since low altitude rich-in-dust layers are averaged with dust-free higher altitude layers. The Emanuel (Emanuel 1991) and Tiedtke (Tiedtke 1993) schemes account for dust transport in a cumulus convection cloud using the simplistic and a more detailed explicit approach. In the explicit method the calculated upward-downward fluxes of the scheme are used to vertically transport dust. Thus, it can have a positive or a negative effect on dust load and dust atmospheric lifetime.

Precipitation of the four experiments is plotted against the satellite observations of TRMM, the station based dataset CRU (over land only) and the reanalysis product ERA-interim. TRMM was chosen for the differences plots, since it is quite reliable for precipitation around the tropics and includes precipitation over ocean (Huffman et al. 2016). Figure 4.6 depicts the total precipitation of 2012 for the four sensitivity experiments along with the three observational/reanalysis datasets. In comparison to TRMM (Figure 4.6a), ERA-interim (Figure 4.6c) shows increased precipitation along the tropics and especially over the Amazon forest and the northwest Atlantic ocean, while CRU (Figure 4.6b) displays similar amounts of precipitation over land in Africa and South America. The four RegCM4 experiments show similarities on the range of total precipitation and similar dry/wet patterns when compared with TRMM. The first two experiments (Figure 4.6d,e), driven by Emanuel/Grell (TRANS-EG) and Emanuel/Emanuel (TRANS-E), ocean/land respectively, are dry over the Gulf of Guinea and the eastern part of the North Atlantic (Figure 4.6h,i). The TRANS-E experiment slightly overestimates the total precipitation over the Sahara and Sahel, which can potentially affect dust emission, but has a relative small bias over South America, which can aid on a more realistic representation of dust deposition in the Amazon forest. The second group of experiments (Figure 4.6f,g), driven by

Tiedtke/Tiedtke (TRANS-T) and Tiedtke/Grell (TRANS-TG), ocean/land respectively, display a similar dry bias over South America and the eastern part of the North Atlantic (Figure 4.6k,l) as the previous two experiments. TRANS-T experiment has a fairly good performance over the desert (close to zero bias) and the western part of the Atlantic. Furthermore, the dry bias over the Amazon forest is improved in comparison to the TRANS-TG experiment. The MNMB and FGE for the six subregions and the four sensitivity experiments is shown in Table 5. The TRANS-EG experiment has the lowest averaged MNMB for all subregions (1%) and the TRANS-E experiment has the lowest FGE (68%). Which means that the Emanuel over land and ocean displays the lowest error among the other experiments in terms of precipitation.

The cloud cover fraction for the four experiments is evaluated against the CERES satellite dataset in Figure 4.7. All the experiments show similar inconsistencies in comparison to CERES. There is an underestimation of total cloud fraction over the ocean by 20% in the TRANS-EG and TRANS-E experiments and about 10% in the TRANS-T and TRANS-TG experiments. All the experiments overestimate cloud fraction over the desert by 10%, which are mostly not precipitable clouds since total precipitation bias is quite small Figure 4.6. The increased cloud fraction cover in the model can potentially affect incoming shortwave radiation and the stability of the atmosphere over the desert, affecting the atmospheric lifetime of dust.

Table 5. Total precipitation basic validation metrics of TRMM and the four convective scheme experiments. MNMB stands for Modified Normalized Mean Bias and FGE stands for Fractional Gross Error.

Region	MNMB				FGE			
	TRANS EG	**TRANS E**	**TRANS TG**	**TRANS T**	**TRANS EG**	**TRANS E**	**TRANS TG**	**TRANS T**
Caribbean	19%	25%	**-12%**	-21%	39%	40%	**36%**	41%
N.Atlantic	30%	16%	**-2%**	-34%	65%	55%	**48%**	55%
Sahara	54%	122%	**37%**	95%	82%	126%	**79%**	112%
Amazon	-97%	**-35%**	-101%	-66%	104%	**40%**	105%	68%
S.Atlantic	**-2%**	-7%	-32%	-48%	76%	**64%**	77%	81%
Sahel	-61%	36%	-63%	**-8%**	74%	48%	77%	**44%**
All	**1%**	29%	-20%	-10%	75%	**68%**	71%	73%

The effect of precipitation on Trans-Atlantic dust transport can be indirectly quantified using indices related to wet deposition, total deposition and total dust column burden. The wet to total deposition fraction (FWET) and the deposition lifetimes (DL), along with the 50km land/ocean mask used by in RegCM4, are depicted for the four simulations in Figure 4.8. All the experiments show that the dust total column burden over the coast of South America is about 40 $mg \cdot m^{-2}$ and FWET almost one. Close to dust sources the FWET values is close to zero due to the combined effect of low precipitation and dominant dry deposition fluxes of coarse dust particles. Wet deposition starts to become equally important to total deposition (FWET=0.5) in the middle of the Atlantic ocean, while it dominates over the tropics starting from the gulf of Guinea and extending all the way to the Amazon river delta. In TRANS-EG and TRANS-TG experiments (Grell scheme over land), wet deposition accounts for only ~20% of the total deposition over the Amazon forest (Figure 4.8b,d), since as already discussed Grell scheme is quite dry over South America (Figure 4.6k,h) (-97% and -101% MNMB respectively). Contrary both TRANS-E and TRANS-T experiments wet deposition is equally or even more important than dry deposition (FW>=0.5) over the Amazon forest (Figure 4.8c,e). The quite low FWET values over the Southeastern part of the Atlantic is caused by the emittance/dry deposition of dust from the Namib desert that stretches along the Atlantic coast of Angola and Namibia. DL (day) is the ratio of total column burden ($mg \cdot m^{-2}$) to total deposition flux ($mg \cdot m^{-2} \cdot day^{-1}$). High DL indicate regions where dust particles can stay in the atmosphere for longer periods. One of these key regions, that it seems to be highlighted by all the experiments, is located over the gulf of Guinea and the equatorial Atlantic ocean. DL over there ranges from 40 to 60 days and it is probably produced by the combined effect of the constant easterly trade winds and the low simulated precipitation that extends the atmospheric lifetime of dust particles. Respective to the FWET behavior, DL averages to ~25days, over the Amazon basin for the Grell driven experiments (Figure 4.8f,h), while for the non-Grell driven experiments, DL is quite lower ~10days (Figure 4.8g,i).

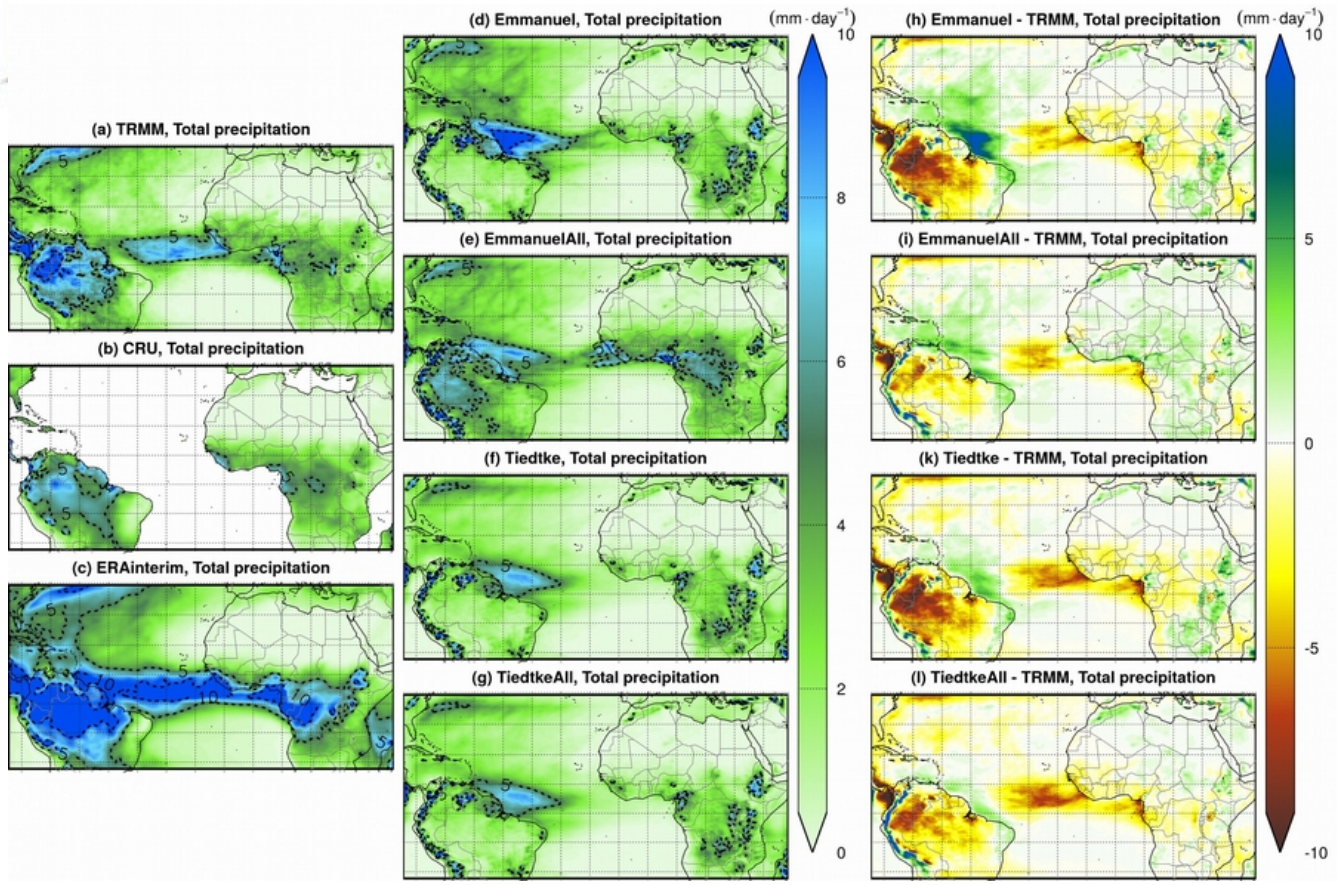

Figure 4.6. Total precipitation of TRMM, CRU, ERA-interim and the four RegCM4 convective scheme sensitivity experiments. The simulations cover the period from 2012-01-01 to 2012-12-31. The differences were calculated using the TRMM dataset.

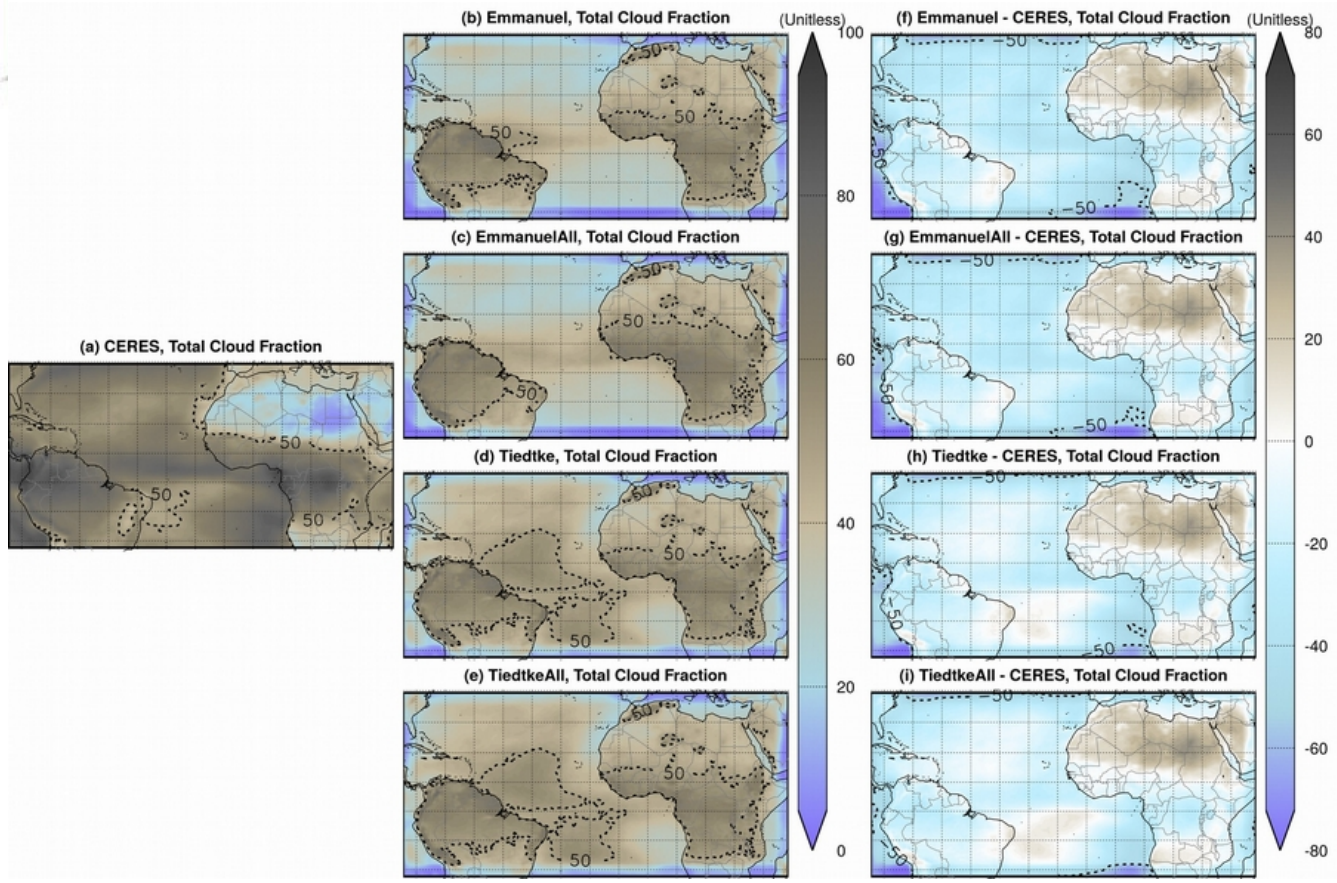

Figure 4.7. Total cloud cover fraction of CERES and the four RegCM4 convective scheme sensitivity experiments. The simulations cover the period from 2012-01-01 to 2012-12-31.

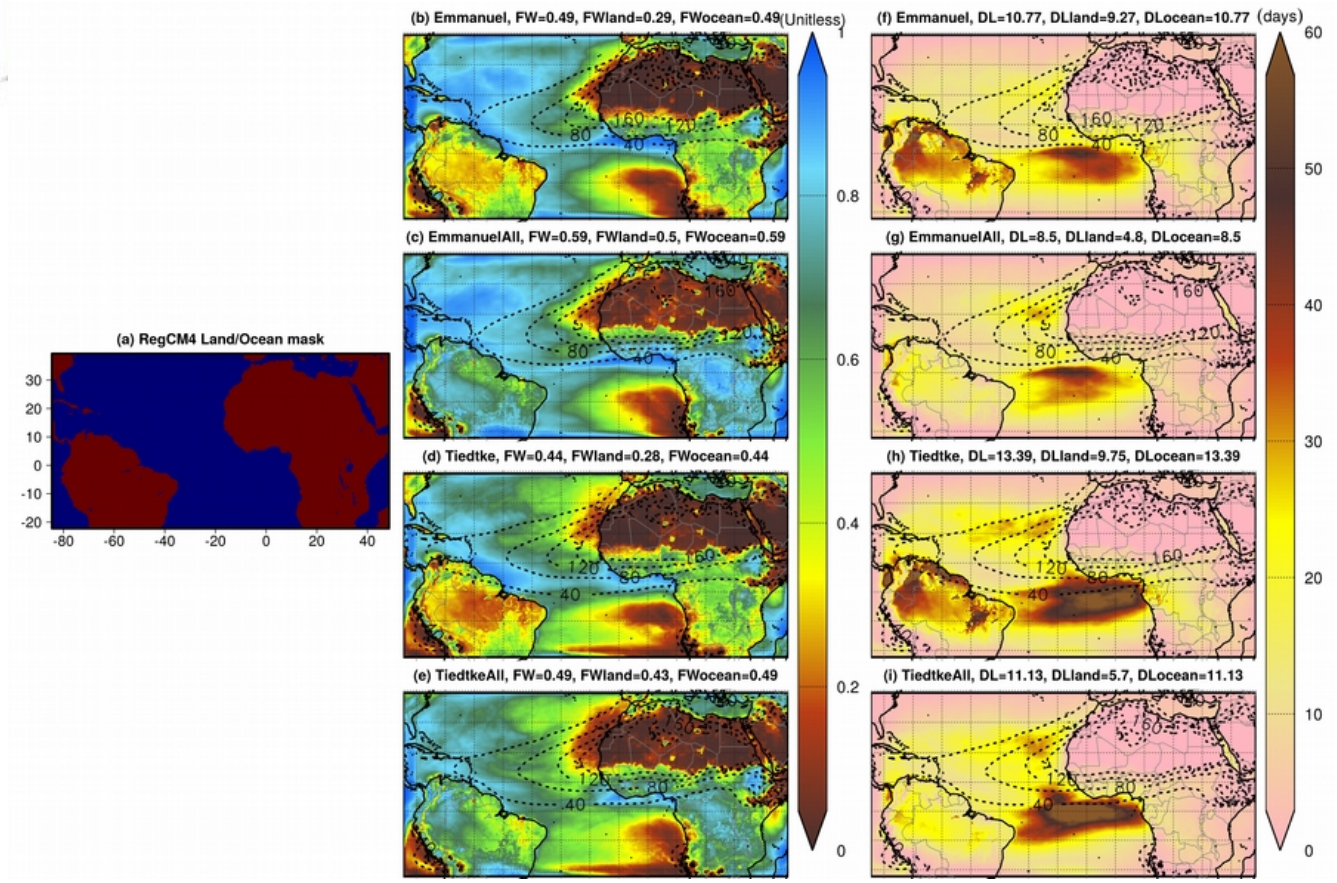

Figure 4.8. (a) The Land/Ocean mask used in all simulations. (b,c,d,e) Wet deposition Fraction (FW) and (f,g,h,i) Deposition Lifetimes (DL) for the four convective scheme sensitivity experiments using RegCM4. The simulations cover the period 2012-01-01 to 2012-12-31. Contour lines depict the dust column burden (mg·m^{-2}).

Dust optical depth (DOD) and dust extinction (DEX) profile are evaluated using as a reference the LIVAS dust product. Prior to the evaluation, all the experiments have been spatially and temporally collocated with the exact flybys of CALIPSO satellite measurements used in LIVAS (method in Tsikerdekis et al., 2017). Overall all the experiments simulate the Trans-Atlantic transport of Saharan dust adequately when compared to LIVAS measurements (Figure 4.9). DOD over the eastern part of North Atlantic reaches up to 0.3 and gradually decreases towards the west reaching 0.1 at the coast of South America. All convective scheme experiments display a positive bias over the eastern Sahara and negative bias over the southern part of Sahara and Sahel. The possible sources of these discrepancies has been discussed extensively for a smaller domain in Tsikerdekis et al. (2017). TRANS-E, TRANS-EG and TRANS-TG experiments illustrate comparable negative DOD biases over the eastern North Atlantic and positive over the western part of the ocean (Figure 4.9f,g,i). DOD in TRANS-T experiment is slightly higher than the other experiments creating a mostly positive bias throughout the

North Atlantic ocean (Figure 4.9h).

The DEX profile for Sahara+Sahel, the Atlantic and the Amazon forest is depicted in Figure 4.10. Over the desert (Figure 4.10c), the four experiment overestimate dust concentration, mainly due to the positive bias over the eastern Sahara. Over the Atlantic (Figure 4.10b) ocean the underestimation of DEX in the first 4 kilometers is combined with the DEX overestimation in the mid and upper Troposphere that leads to an almost zero DOD bias. An almost identical behavior is observed over the Amazon forest (Figure 4.10a), only this time the DEX values are quite smaller for the simulations and the observational dataset.

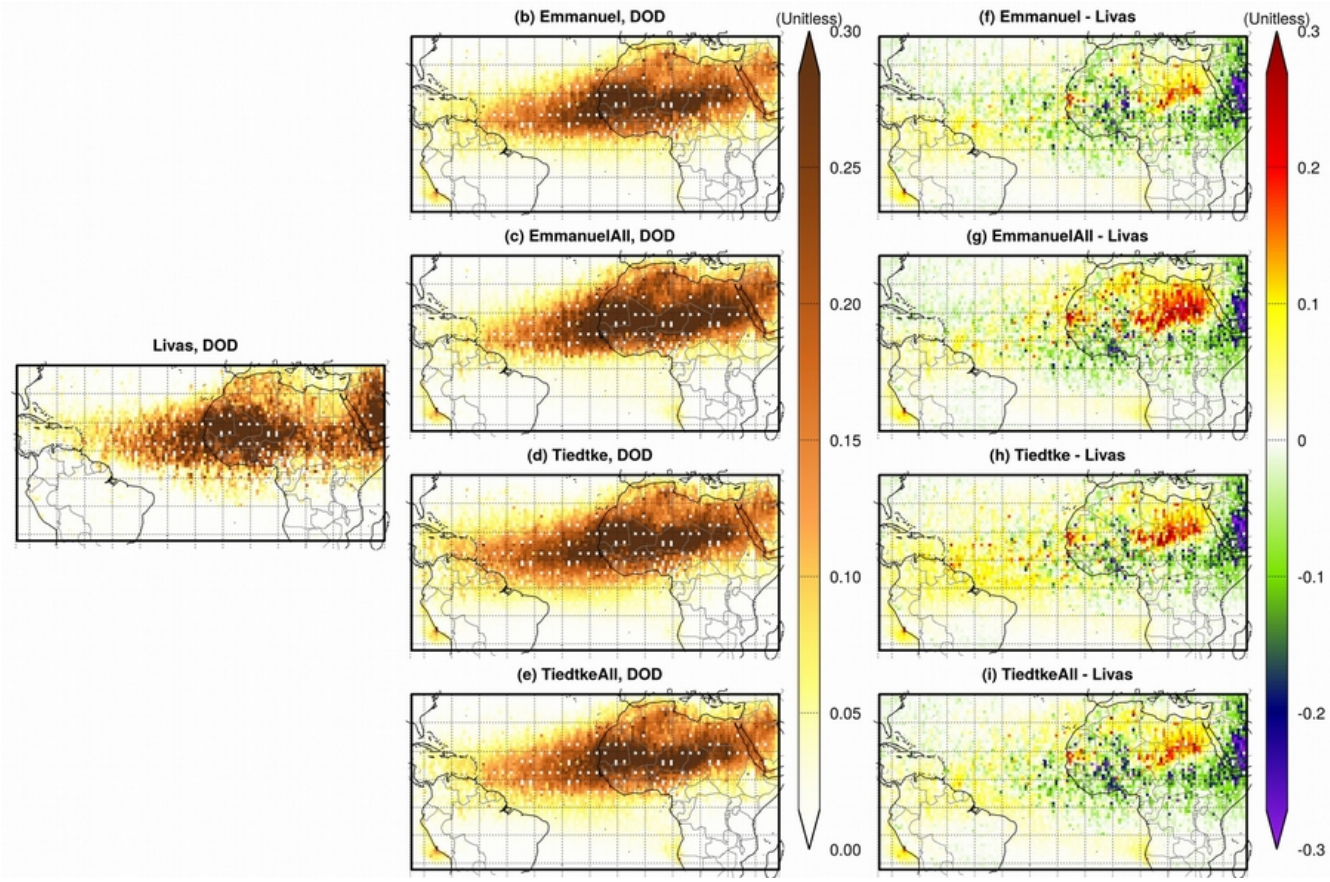

Figure 4.9. Dust optical depth close to 550nm for LIVAS and the four convective scheme sensitivity experiments using RegCM4. The dust optical depth differences of each experiment with LIVAS is shown in the 3rd column.

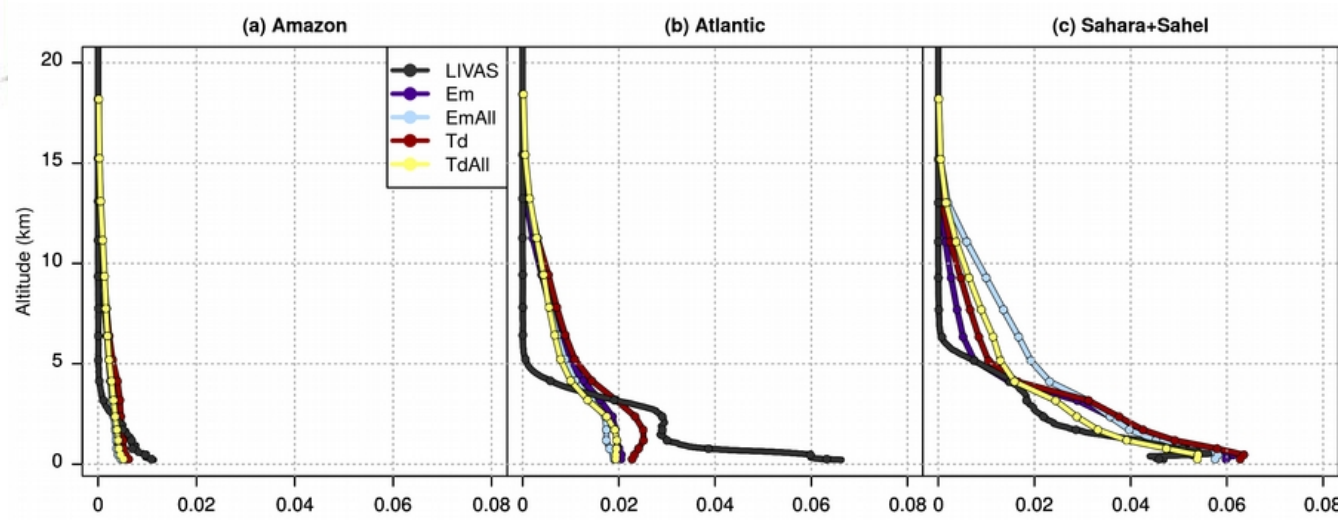

Figure 4.10. Dust extinction profile of LIVAS and the our convective scheme sensitivity experiments for (a) Amazon, (b) Atlantic and (c) Sahara+Sahel subregions.

4.4 Trans-Atlantic dust and the role of dust size discretization

In this Section we explore the impact of dust size discretization number and method on dust optical depth (DOD) and radiative effect (RE) during the long-range Trans-Atlantic transport of dust. Figure 4.11 depicts the DOD of TRANS4 and TRANS12 experiments along with the TRANS12-TRANS4 difference. The averaged DOD over all subregions depicted in Figure 4.1, is higher in the TRANS12 experiment by 0.03 (32%), which is similar to the 0.05 (10%) increase presented in Tsikerdekis et al. (2017) for a smaller domain. The actual differences averaged for each subregion range between 0.01 and 0.05. Subregions close to dust sources like Sahel and Sahara depict a moderate percentage increase 18-19% (Table 6). As dust moves westward over the Atlantic the percentage increase of TRANS12 experiment accumulates. Over north Atlantic DOD increases by 28%, while over South Atlantic and the Amazon basin DOD increase by 44% and 33% respectively. The increasing DOD behaviour when increasing the number of dust size bins was expected from our previous results (Tsikerdekis et al. 2017), but the percentage enhancement of that increase towards the southern dust Trans-Atlantic path is a new finding. High positive differences over the Arabian Peninsula and the Mediterranean are too close to the boundaries of the simulation to consider them trustworthy.

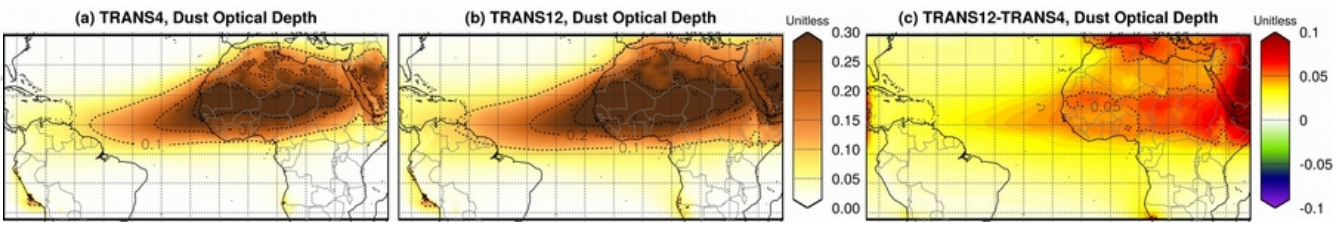

Figure 4.11. Dust optical depth of TRANS4 and TRANS12 experiments along with the TRANS12-TRANS4 difference for the period December 2006 to November 2010.

Table 6. Dust optical depth average value of the TRANS4 and TRANS12 experiments for the period December 2006 to November 2010. The percentage difference of the two experiments is presented in the form of Modified Normalized Mean Bias (MNMB).

Region	TRANS4	TRANS12	MNMB
Caribbean	0.04	0.06	50%
N.Atlantic	0.13	0.16	28%
Sahara	0.24	0.29	19%
Amazon	0.04	0.05	33%
S.Atlantic	0.06	0.09	44%
Sahel	0.32	0.37	18%
All	0.13	0.16	32%

The RE on the shortwave and longwave spectrum are depicted in Figure 4.12 and Figure 4.13 respectively for both experiments. Since DOD increases in TRANS12 experiment, the respective changes in RE tend to go one way. Thus, the typically negative shortwave RE is enhanced and the positive longwave RE increases. More specifically the top of the atmosphere (TOA) RE is high where surface albedo is low, such as over forest and ocean. The averaged TOA RE enhances by 0.7 $W \cdot m^{-2}$ (59%) and for the larger part of the Atlantic by more than $1W \cdot m^{-2}$ in the TRANS12 experiment (Table 7). South and North Atlantic depicts the greatest enhancement of TOA RE by $0.9W \cdot m^{-2}$ (40%) and 1 $W \cdot m^{-2}$ (25%) respectively. The surface (SRF) RE is related to dust extinction/backscattering of solar radiation and is highly correlated with the distribution of fine dust particles. It is enhanced over all regions by $-1.3W \cdot m^{-2}$ (25%). The greatest changes between the two experiments are again observed in South and North Atlantic where SRF RE enhances by $1.6W \cdot m^{-2}$ (37% and 22% respectively).

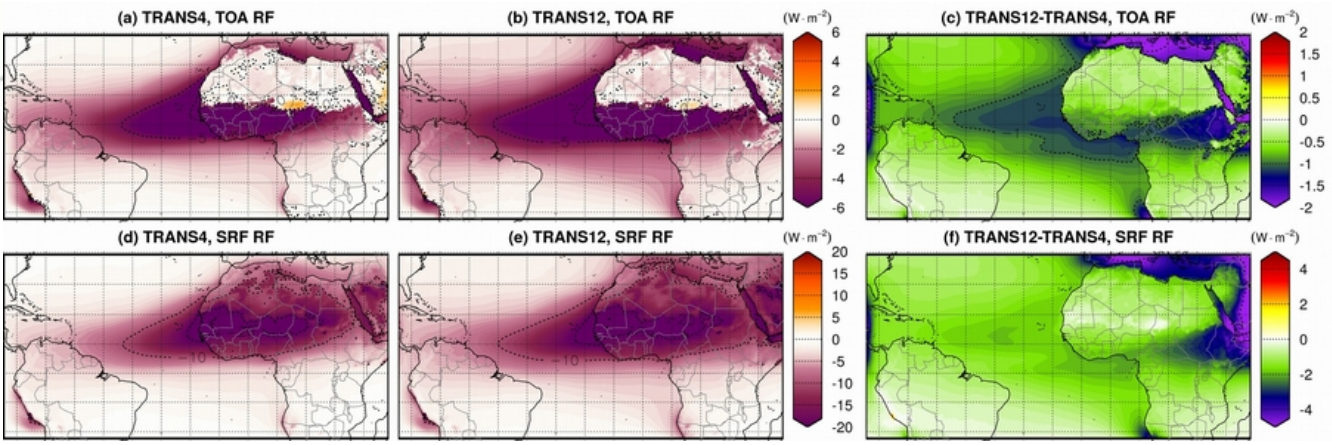

Figure 4.12. Radiative effect on the shortwave spectrum of the model for TRANS4 and TRANS12 experiments along with the TRANS12-TRANS4 difference for the period December 2006 to November 2010. First and second row depicts the top of the atmosphere and the surface radiative effect respectively.

Table 7. Top of the atmosphere and surface shortwave Radiative Effect (RE) average value of the TRANS4 and TRANS12 experiments for the period December 2006 to November 2010. The percentage difference of the two experiments is presented in the form of Modified Normalized Mean Bias (MNMB).

Region	Top of the Atmosphere Shortwave RF			Surface Shortwave RF		
	TRANS4	TRANS12	MNMB	TRANS4	TRANS12	MNMB
Caribbean	-1.4	-2.1	48%	-2.7	-4.0	45%
N.Atlantic	-4.5	-5.5	25%	-9.1	-10.7	22%
Sahara	-0.5	-0.8	56%	-12.9	-14	10%
Amazon	-1.3	-1.6	29%	-2.6	-3.3	25%
S.Atlantic	-2.2	-3.1	40%	-4.4	-6.0	37%
Sahel	-3.7	-4.4	39%	-18.9	-20.2	8%
All	-2.2	-2.9	59%	-7.9	-9.2	25%

On the longwave spectrum (Figure 4.13), both the TOA and the SRF RE is enhanced where the coarse dust particles column burden is high. On the TOA the averaged increase is approximately 0.1W·m^{-2} (33%), while over the Sahara and the Sahel is 0.2W·m^{-2} (21% and 19% respectively) (Table 8). Similar small changes are observed in the SRF RF, where the average increase is equal to 0.1W·m^{-2} (29%) and the respective values for Sahara and Sahel are 0.2W·m^{-2} (10%) and 0.2W·m^{-2} (9%). We have to note that longwave RE values are calculated using the spectrum bands of the radiative transfer scheme

CCM3, which focuses on the absorbing greenhouse gases (H_2O, CO_2) longwave spectrum.

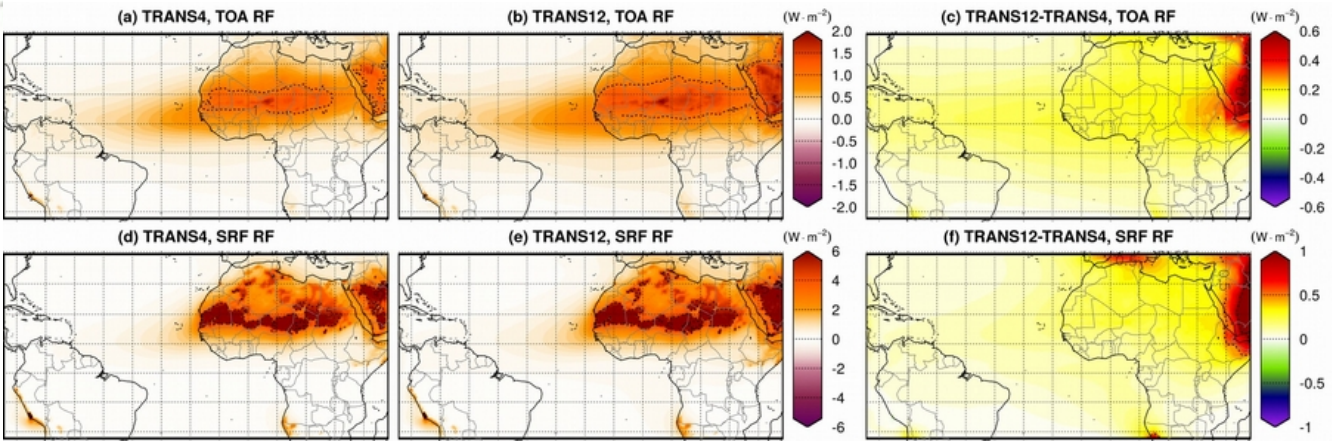

Figure 4.13. Radiative effect on the shortwave spectrum of the model for TRANS4 and TRANS12 experiments along with the TRANS12-TRANS4 difference for the period December 2006 to November 2010. First and second row depicts the top of the atmosphere and the surface radiative effect respectively.

Table 8. Top of the atmosphere and surface longwave Radiative Effect (RE) average value of the TRANS4 and TRANS12 experiments for the period December 2006 to November 2010. The percentage difference of the two experiments is presented in the form of Modified Normalized Mean Bias (MNMB).

Region	Top of the Atmosphere Longwave RF			Surface Longwave RF		
	TRANS4	TRANS12	MNMB	TRANS4	TRANS12	MNMB
Caribbean	0.1	0.2	47%	0.1	0.2	49%
N.Atlantic	0.4	0.5	30%	0.6	0.7	25%
Sahara	0.7	0.9	21%	3.5	3.7	10%
Amazon	0.1	0.2	36%	0.1	0.2	35%
S.Atlantic	0.2	0.3	41%	0.2	0.3	42%
Sahel	1.0	1.2	19%	4.1	4.3	9%
All	0.4	0.5	33%	1.3	1.4	29%

4.5 Trans-Atlantic dust - A multi-model inter-comparison

Simulating the long-range transport of dust over the Atlantic is a challenging task since various counteractive processes may affect the amount of dust emitted from the desert or the height of the dust layer over the Atlantic or even the wet deposition rate during transport. Climate models results may converge in variables such as the dust optical depth column, but display distinct discrepancies when

analyzing emission/deposition fluxes or the optical efficiency of the simulated dust particles. The multi-model study of Kim et al. (2014) investigated the Trans-Atlantic transport of Saharan dust as well dust sink and source regions using 5 simulations of the global climate models GOCART, GISS-ModelE, SPRINTARS, ECHAM5-HAMMOZ and HadGEM2 for the period 2000-2005. A quick description of these global climate simulations is available in Section 2.8. For a more detailed information refer to Kim et al. (2014). The dust optical depth (DOD), emission flux (EMI), loss frequency (LF), wet to total deposition fraction (FWET) and mass extinction efficiency of the TRANS4 experiment is plotted along with the five global simulations, satellite measurements (MODIS, MISR) and ground based observations (AERONET). TRANS4 experiments refer to a different time period (December 2006 to November 2014). This analysis is not focused on the exact quantification of the differences between RegCM4 and these global simulations, but investigates the generic diversities and similarities of dust processes of the models over the North Atlantic.

Figure 4.14 depicts MODIS DOD, the MISR non-spherical AOD, the DOD of seven climate simulations and the coarse particle AOD of numerous ground-based AERONET stations. The two satellite-derived optical depths are adequately similar, while the higher values of AERONET AOD over the Eastern North Atlantic can be partially explained by the coarse-mode sea salt contribution (Kim et al. 2014). The total and over land DOD of TRANS4 simulation (0.13, 0.20) lies between the range of the 5 global simulations, with the lowest being HadGEM2 (0.04, 0.06) and the highest being GOCART (0.17, 0.33). Over ocean the MODIS and MISR averaged value is 0.12 and 0.10 respectively. All the models underestimate these values, although RegCM4, GISS and GOCART are most effective on simulating the Trans-Atlantic DOD (0.07, 0.07, 0.09 respectively). RegCM4 dust plume spatial pattern over the North Atlantic is quite similar to the satellite datasets, which initiates with values between 0.2-0.3 from the west coast of North Africa and reaches the northeastern coast of South America with about 0.05-0.1.

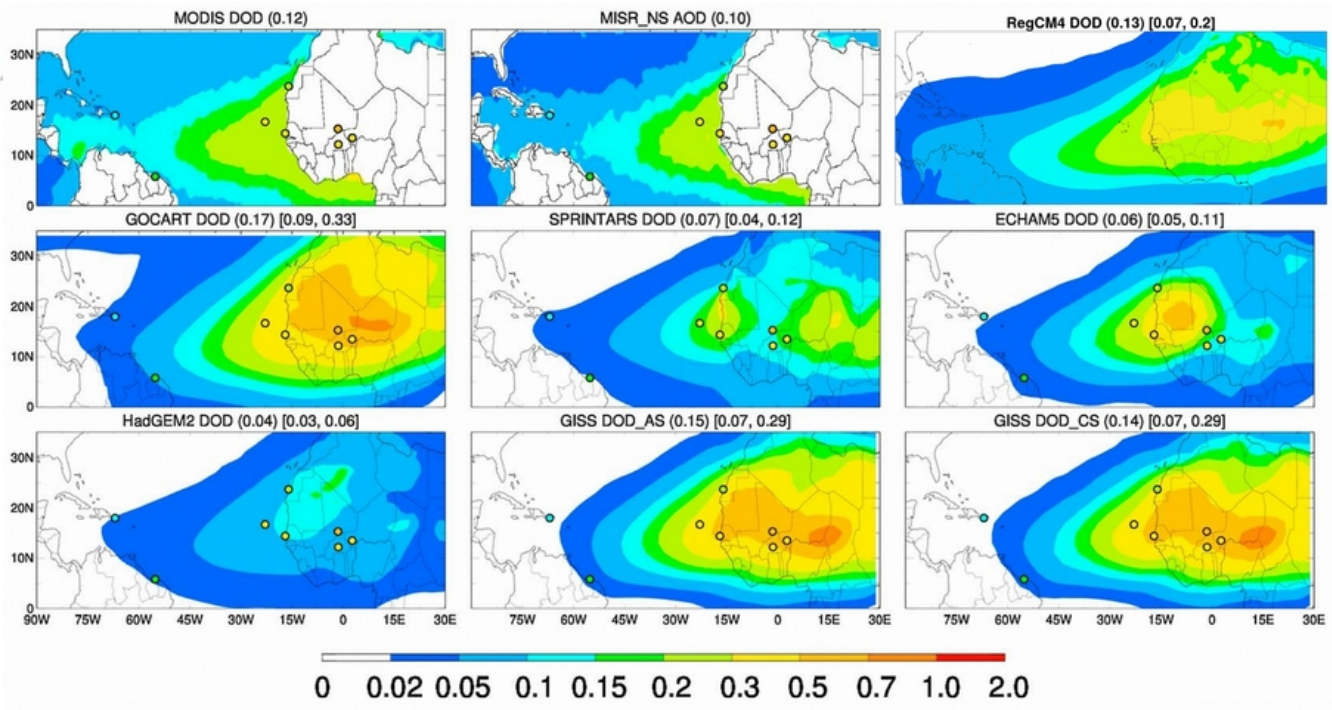

Figure 4.14. MODIS dust optical depth, MISR aerosol optical depth of non-spherical aerosol which serves as dust optical depth and dust optical depth of of six global models for the period 2000 to 2005. The superimposed points represent the coarse particles aerosol optical depth of AERONET stations for the same period. In the upper right corner TRANS4 dust optical depth is depicted for the period December 2006 to November 2014. The parenthesis in the title indicate the averaged value for the whole domain and the brackets the respective ocean and land averaged values. Source: Kim et al. (2014), slightly modified by adding RegCM4.

The dust emission flux of the 5 GCMs and the TRANS4 experiment is presented in Figure 4.15. The total dust emission flux per year for the period 2000-2005 differs by a factor of five between the GCMs, with the lowest being ECHAM5 (422 $Tg \cdot yr^{-1}$) and GOCART being the highest (2025 $Tg \cdot yr^{-1}$) (Kim et al. 2014). RegCM4 emission flux is quite higher (8097 $Tg \cdot yr^{-1}$) making also its deposition flux very high, especially close to the sources. RegCM4 higher emission flux can be partially explained by the higher emitted dust size range (0.09-63μm). All the GCMs models detects the main dust sources over Sahara, like Bodélé depression and over western Africa. RegCM4 more detailed horizontal resolution (50x50km) is able to simulate in finer detail the orographic landscape over the desert, creating a sharper overview of dust emission sources.

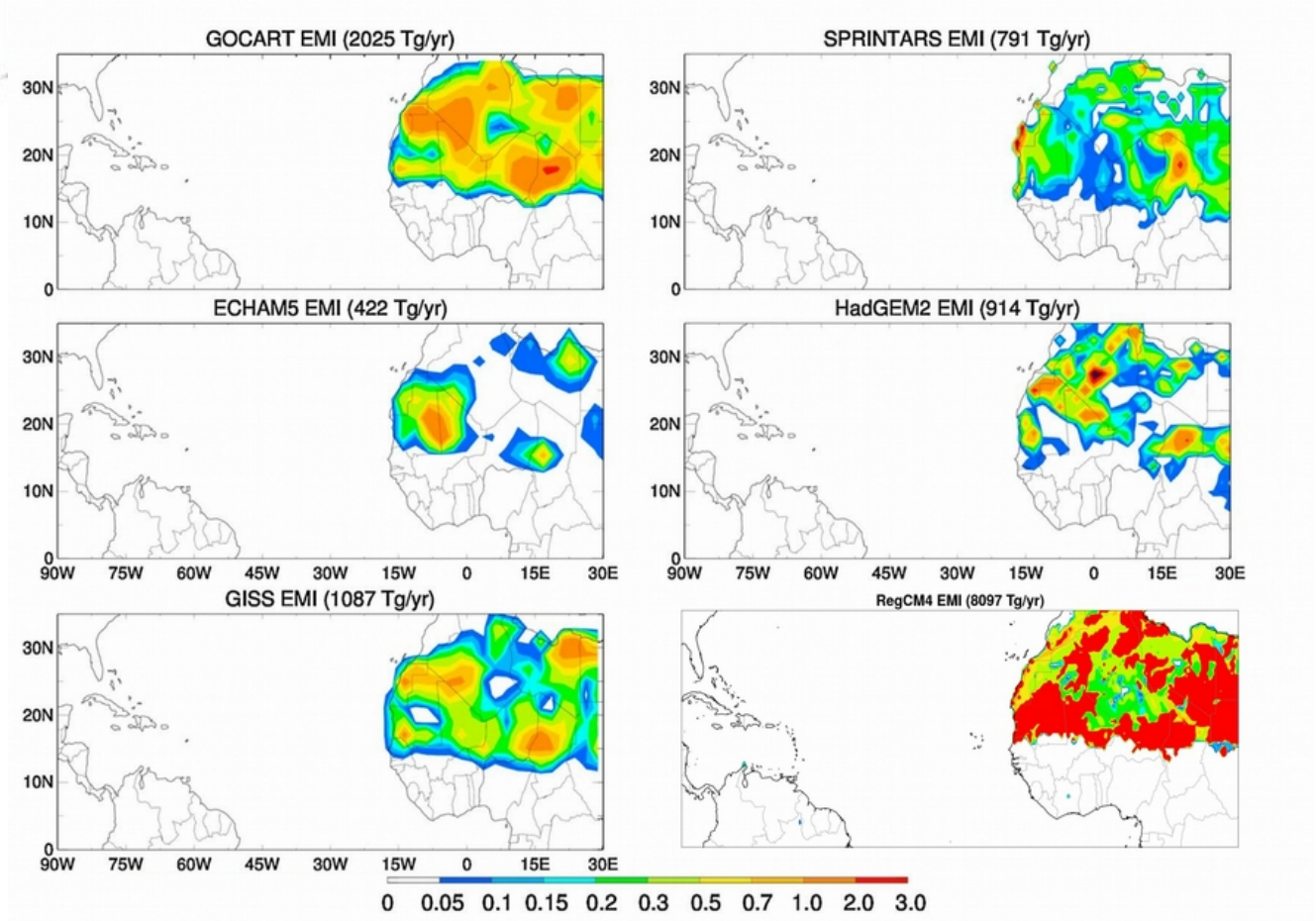

Figure 4.15: Emission flux of five global climate simulations for the period 2000-2005 along with the dust emission flux of the RegCM4 simulation (TRANS4) for the period December 2006 to November 2014. Source: Kim et al. (2014), slightly modified by adding RegCM4.

Figure 4.16 illustrates LF, FWET and MEE of the 5 global dust simulations and the TRANS4 experiment (last row). The LF (day^{-1}), being the reverse quantity of DL (day), is the ratio of total (dry+wet) dust deposition flux ($mg \cdot m^{-2} \cdot day^{-1}$) to the dust column burden ($mg \cdot m^{-2}$). During the long-range Trans-Atlantic transport of dust LF changes according to the changes of advection and deposition (Kim et al. 2014). The LF of RegCM4 is 3 to 4 times greater in comparison to the other models. High values are observed over the desert (>3 day^{-1}) and lower away from the dust sources (<0.2 day^{-1}). It is noted that RegCM4 dust particle upper size limit goes up to 63μm, which is way higher than the respective upper limit of GCMs (10μm to 31.6μm). Thus, the high LF gradient is probably related to dry deposition of coarse dust particles over the Sahara with short atmospheric lifetimes that increase the total deposition flux but do not increase sufficiently the dust total column burden. SPRINTARS and HadGEM2 indicate the same behavior, with high values close to sources and decreasing values over the

Atlantic ocean.

The FWET (Unitless) spatial pattern and range of values between the GCMs and RegCM4 are quite similar. FWET has close to zero values near dust sources, since gravitational settling through dry deposition dominates, and increasing values over the ocean, where wet deposition becomes important. Over the Atlantic all the models display FWET that ranges from 0.4 to 0.8, except SPRINTARS where over the westward expanding dust plume upon Atlantic wet deposition account for only 20-30% of total deposition. The average FWET value for the whole domain ranges from 0.36 (SPRINTARS) to 0.63 (GISS), with RegCM4 value (0.54) laying well between these bounds.

Several hypotheses and approximations concerning the physical (density, shape, size distribution) chemical (color, composition) and optical (refractive index) properties of dust particles are adopted by dust models in order to calculate the dust radiation interactions (Sokolik and Toon 1999; Foret et al. 2006). The MEE (m^{-2}·mg) expresses the efficiency of dust particles to extinct shortwave radiation and it is calculated from the ratio of dust optical depth at 550nm to the dust column burden ($mg \cdot m^{-2}$). In a way MEE is a measure of the effectiveness of the dust direct radiative effect in a model and thus correlates well with the particle size distribution of dust. High MEE values are found where small size dust particles dominate and lower values where coarse-mode particles are more (Kim et al. 2014). The GCMs average MEE value for the whole domain ranges from 0.56 (ECHAM5) to 1.05 (SPRINTARS), while RegCM4 MEE is almost 2-3 times greater (1.75) than that. High MEE values in RegCM4 can be partially explained by the overestimation of dust extinction profile, even close to the dust sources, which makes fine size particles presence evident everywhere, without increasing the column burden much.

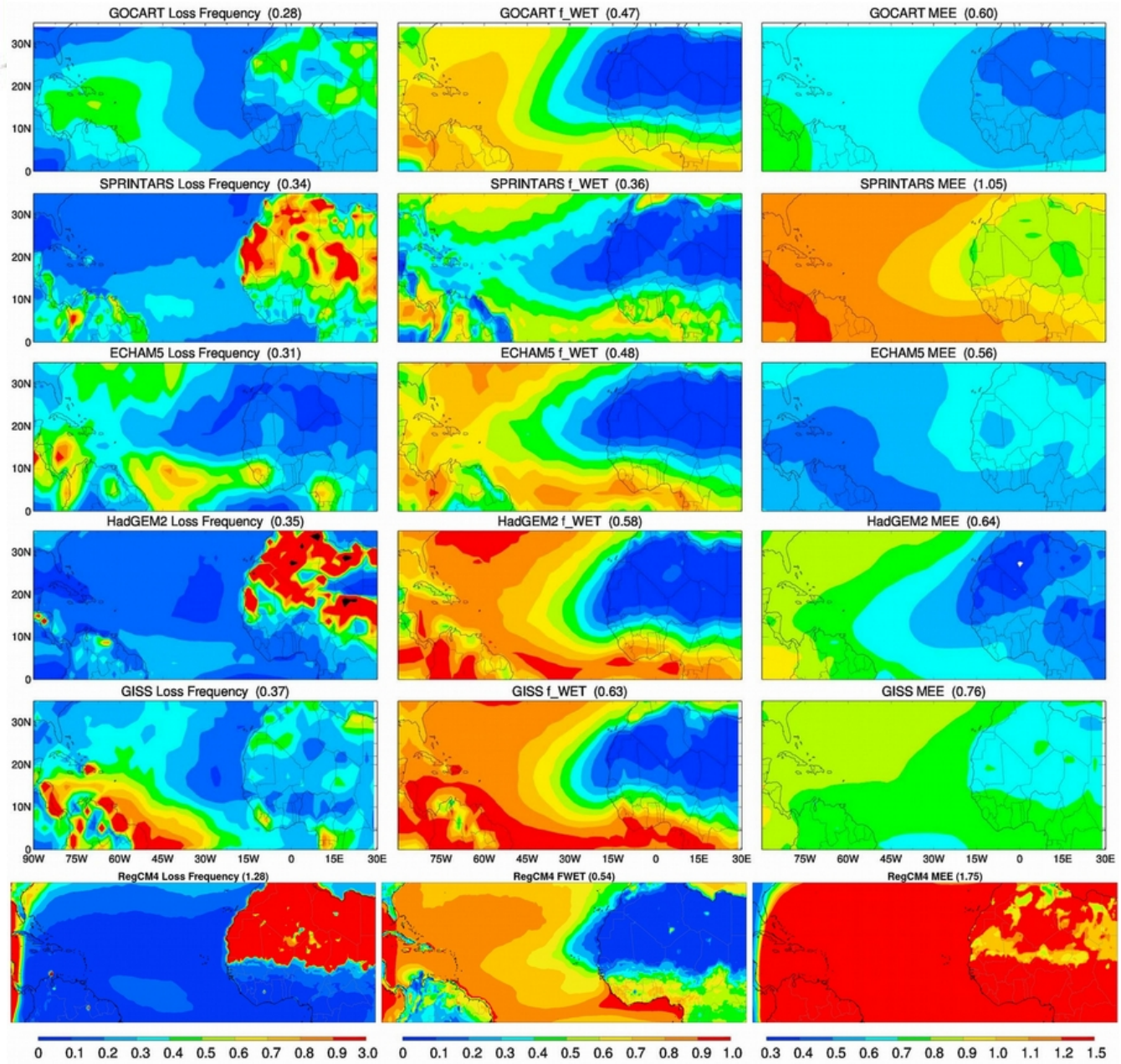

Figure 4.16. Dust Loss Frequency (day^{-1}), Fraction of Wet deposition in comparison to total deposition (Unitless) and Mass Extinction Efficiency at 550nm (m^2 g^{-1}) of four global models presented in Kim et al. (2014) along with the TRANS4 experiment. The four global model refer to the period 2000-2005 while the RegCM4 simulations is for the period December 2006 to November 2014. The averaged value for the whole domain for each variable is depicted on the title of each plot. Source: Kim et al. (2014), slightly modified by adding RegCM4.

4.6 Trans-Atlantic dust and its deposition role

Chemical composition of dust and especially its Phosphors (P) and Iron (Fe) concentration can significantly impact nutrient adequacy of marine (Fasham 2003; Mahowald et al. 2005b) and terrestrial (Okin et al. 2004; Bristow et al. 2010) ecosystems. Chemical measurements over Bodele depression,

which is the world's most active dust emission source (Koren et al. 2006), showed that rich amounts of phosphorus (28-60%) is contained in its soils (Hudson-Edwards et al. 2014). Most likely the source of this phosphorus rich (780mg/g) diatomite sediments of Bodele depression were formed during the existence of the paleolake Megachad (Bristow et al. 2010). In order to estimate the deposited phosphorus through aerosol dust several studies assumed that Saharan dust consist 700μg/g of phosphorus (Chadwick et al. 1999; Mahowald et al. 2005a; Ridley et al. 2012). Significant amounts of deposited Saharan/Sahel dust (50Tg) were estimated to be crucial for the phosphorus limited Amazon forest nutrient fertilization (Swap et al. 1992), although the exact number of the deposited dust in the Amazon basin ranges from 17.5-50 $Tg \cdot yr^{-1}$ (Swap et al. 1992; Kaufman et al. 2005; Koren et al. 2006; Ridley et al. 2012).

In marine ecosystems, the soluble bio-avaliable iron contained within dust act as a micronutricient sources for the photosynthetic efficiency of oceanic phytoplankton. The potentially soluble iron form, hematite and goethite, found in sand sediment of desert environments (Claquin et al. 1999) is insoluble in ocean waters. Thus, a number of proposed mechanisms have been proposed that describe the mobilization of Fe in aerosol dust particles, like hematite dissolution or acid mobilization (Meskhidze et al. 2003). Based on previous studies the soluble dissolved iron fraction of dust ranges from 0.01% to 80% (Gao et al. 2003; Baker et al. 2006; Baker and Jickells 2006; Journet et al. 2008). This range is a function of size as well as chemical composition of aerosol dust particles, which makes iron solubility of dust an inverse function of dust concentration (Baker and Jickells 2006; Journet et al. 2008). Since iron solubility change over time and space, the bio-avaliable iron approximation should be online calculated within climate models. Despite the uncertainties related to the dissolved iron fraction, the Saharan dust deposition flux into the Atlantic ocean can still be useful for studying the desert-ocean bio-chemical relation.

In this Section the TRANS4 experiments is used to quantify the mean annual dust deposited over three delimited subregions as defined by Ridley et al. (2012) (illustrated in Figure 1.2). Table 9 depicts the inter-annual variability of all-size dust particle deposition ($Tg \cdot yr^{-1}$) and the average amount of dust deposited every year in each subregion. For the Amazon, the total amount of all-size dust particle deposited and its uncertainty is somewhat smaller than the respective amounts calculated with GEOS-Chem in Ridley et al. (2012) and even lower than the satellite approximation calculated in Kaufman et al. (2005). According to TRANS4 simulation 4.3 ± 0.4 $Tg \cdot yr^{-1}$ of dust are deposited in and close to the

Amazon basin which is lower than the 17±5 Tg·yr^{-1} estimate from the GEOS-Chem model (Ridley et al. 2012) and significantly lower than the satellite estimate using MODIS (Terra/Aqua) 50 Tg·yr^{-1} (Kaufman et al. 2005). Over the Atlantic and the Caribbean 154.5±10.7 Tg·yr^{-1} and 10.3±0.6 Tg·yr^{-1} of dust are deposited each year, which are too lower than the corresponding estimates of 218±48 Tg·yr^{-1} 26±5 Tg·yr^{-1} determined by GEOS-Chem, but at least for the Atlantic it matches the satellite estimate of 140±40 Tg·yr^{-1}. TRANS4 reduced dust deposition in comparison to previous studies can partially be explained by the lack of wet deposition due to the possible underestimation of convective precipitation over the Amazon basin, where Grell scheme is active (Figure 1.6). The respective inter-annual deposition of Phosphorus (Gg·yr^{-1}), assuming that 700 milligram of phosphorus are contained in one gram of dust, based on Table 9 is depicted in Table 10.

Tables 11, 13 and 12 summarize the intra-annual and dry/wet estimates of dust deposition (Tg yr^{-1}) for all-size dust particles, fine dust particles and coarse dust particles respectively of the TRANS4 simulation. Fine dust particles correspond to the sum of the two small dust size bins of the model (0.09-2.5μm) and coarse particles the sum of the larger two size bins (2.5-63μm). In all-size Table 11, gravitational settling due to the weight of dust particles (dry column), is the major mechanism that deposits dust over the Amazon (2.9 Tg·yr^{-1}, 67.4%) and the Atlantic (137.3 Tg·yr^{-1}, 88.9%). Contrary over Caribbean rain washout (8.8 Tg·yr^{-1}, 85.4%) is the main process that deposits dust in the ground. The seasonal deposition analysis shows that over the Atlantic and the Caribbean the maximum dust deposition occurs during summer (30.3% and 39.8% respectively), which coincides with the fact that during that period the dust plume over the Atlantic is at its peak. According to TRANS4 dust deposition is highest during summer-autumn (30.2%) over the Amazon basin, although previous researches indicate that maximum deposition occurs in Spring. Note that fine dust particle deposition over the Amazon indeed peak during Spring (33.3%) (Table 12), but coarse particles culminate during autumn (42.9%) (Table 13). Over the Amazon the fine and coarse particle contribute the same amount of total dust deposition (2.1 Tg·yr^{-1}), while over the Atlantic and the Caribbean coarse particles are the major contributor of dust deposition (132.2 Tg·yr^{-1} and 8.3 Tg·yr^{-1} respectively). Table 14 depicts the all-size total dust deposition for the 4 1-year experiments. Total dust deposition diverse by 26.1% in the Amazon basin and 22.4% in the Caribbean.

Table 9. All-size dust particle (0.09-63μm) deposition (Tg yr^{-1}) of the TRANS4 experiments for three delimited subregions as defined by Ridley et al. (2012). Diversity of the inter-annual deposition of the model is calculated as the ratio of standard deviation to the mean of a subregion following Textor et al. (2006) and is used to quantify the uncertainty in column Total.

Regions	2007	2008	2009	2010	2011	2012	2013	2014	Diversity	Total
Amazon	4.2	3.7	4.4	4.0	3.9	4.5	4.7	5.0	10.1%	4.3±0.4
Atlantic	162.1	160.6	154.2	129.8	159.7	161.4	157.2	152.2	6.9%	154.5±10.7
Caribbean	11.3	10.1	9.6	11.2	10.0	10.8	10.2	10.0	6.0%	10.3±0.6

Table 10. Phosphorus deposition (Gg yr^{-1}) of the TRANS4 experiments for three delimited subregions as defined by Ridley et al. (2012). Diversity of the inter-annual deposition of the model is calculated as the ratio of standard deviation to the mean of a subregion following Textor et al. (2006) and is used to quantify the uncertainty in column Total.

Regions	2007	2008	2009	2010	2011	2012	2013	2014	Diversity	Total
Amazon	3.0	2.6	3.1	2.8	2.7	3.2	3.3	3.5	10.3%	3.0±0.3
Atlantic	113.5	112.4	107.9	90.9	111.8	113	110	106.5	6.9%	107.0±7.4
Caribbean	7.9	7.1	6.7	7.9	7.0	7.6	7.2	7.0	6.1%	6.7±0.4

Table 11. All-size dust particle (0.09-63μm) deposition (Tg yr^{-1}) of the TRANS4 experiments for three delimited subregions as defined by Ridley et al. (2012). The percentage depicted reflect the relative importance of the deposition mechanism (dry or wet) and the seasonal variability (Winter, Spring, Summer, Autumn) of dust deposition.

Regions	Dry	Wet	Winter	Spring	Summer	Autumn	Total
Amazon	2.9 (67.4%)	1.4 (32.6%)	0.8 (18.6%)	0.9 (20.9%)	1.3 (30.2%)	1.3 (30.2%)	4.3
Atlantic	137.3 (88.9%)	17.2 (11.1%)	36.4 (23.6%)	43.5 (28.2%)	46.8 (30.3%)	28.0 (18.1%)	154.5
Caribbean	1.5 (14.6%)	8.8 (85.4%)	0.9 (8.7%)	3.0 (29.1%)	4.1 (39.8%)	2.4 (23.3%)	10.3

Table 12. Fine dust particle (0.09-2.5μm) deposition (Tg yr^{-1}) of the TRANS4 experiments for three delimited subregions as defined by Ridley et al. (2012). The percentage depicted reflect the relative importance of the deposition mechanism (dry or wet) and the seasonal variability (Winter, Spring, Summer, Autumn) of dust deposition.

Regions	Dry	Wet	Winter	Spring	Summer	Autumn	Total
Amazon	1.1 (47.6%)	1.1 (52.4%)	0.5 (23.8%)	0.7 (33.3%)	0.5 (23.8%)	0.4 (19%)	2.1
Atlantic	11.1 (49.8%)	11.2 (50.2%)	5.1 (22.9%)	4.3 (19.3%)	6.7 (30%)	6.3 (28.3%)	22.3
Caribbean	0.5 (23.8%)	1.6 (76.2%)	0.2 (9.5%)	0.3 (14.3%)	1.1 (52.4%)	0.5 (23.8%)	2.1

Table 13. Coarse dust particle (2.5-63μm) deposition (Tg yr^{-1}) of the TRANS4 experiments for three delimited subregions as defined by Ridley et al. (2012). The percentage depicted reflect the relative importance of the deposition mechanism (dry or wet) and the seasonal variability (Winter, Spring, Summer, Autumn) of dust deposition.

Regions	Dry	Wet	Winter	Spring	Summer	Autumn	Total
Amazon	1.9 (90.5%)	0.2 (9.5%)	0.3 (14.3%)	0.2 (9.5%)	0.7 (33.3%)	0.9 (42.9%)	2.1
Atlantic	126.2 (95.5%)	6.0 (4.5%)	31.3 (23.7%)	39.2 (29.7%)	40.1 (30.3%)	21.7 (16.4%)	132.2
Caribbean	1.1 (13.3%)	7.2 (86.7%)	0.7 (8.4%)	2.7 (32.5%)	3.0 (36.1%)	1.9 (22.9%)	8.3

Table 14. All-size dust particle (0.09-63μm) deposition (Tg yr^{-1}) for the year 2012 of the TRANS-E, TRANS-EG, TRANS-T and TRANS-TG experiments for three delimited subregions as defined by Ridley et al. (2012). Diversity is calculated as the ratio of standard deviation to the mean of a subregion following Textor et al. (2006).

Regions	TRANS-E	TRANS-EG	TRANS-T	TRANS-TG	Diversity
Amazon	7.4	4.3	7.2	5.0	26.1%
Atlantic	164.1	167.6	159.9	166.8	2.1%
Caribbean	14.0	10.8	9.5	8.5	22.4%

4.7 Summary

Various simulations under different convective schemes were conducted with the regional climate model RegCM4 for an extended domain that includes large parts of Africa, the Atlantic as well as Central and South America. The temporal range of the experiments spans between December 2006 and November 2014. The goal was to simulate the Trans-Atlantic transport of Saharan dust, validate its seasonal characteristics, evaluate the output of the model with satellite-derived measurements and quantify dust deposition flux in the North Atlantic and the phosphorus-limited ecosystem of the tropical Amazon forest. A fraction of these results is already published in the Proceeding of the 14th International Congress of the Geological Society of Greece (Tsikerdekis et al. 2016b) and there is a manuscript in preparation for submission in a peer-review journal under the title “The role of cumulus convection on Trans-Atlantic transport and deposition of Saharan dust”.

In comparison to LIVAS climatology, the model overestimates DOD by 23% and displays a moderate overestimation in Eastern Sahara (<0.1), which was discussed thoroughly in Tsikerdekis et al. (2017), a weak underestimation in western Sahara and Sahel (<0.05), and a slight overestimation along the South Atlantic. The model captures the summer DOD June-July peak in North Atlantic and Caribbean but it underestimates it by ~0.1 and ~0.05 respectively. The South Atlantic winter maximum is not captured and the annual cycle in the same region is flat, almost constant throughout the year. In the Amazon

DOD is slightly overestimated in all months. Generally the mean annual cycle of the model exhibits lower standard deviation in comparison to LIVAS dataset over all regions, except Amazon. The dust vertical distribution in the warm (May-September) and the cold (December-April) period showed that the model tends to perform better at the northern part of the ocean rather than the southern part. The model underestimates dust extinction in the first 5km and overestimates between 5-10km. The processes that are responsible for these biases (cumulus convective transport, sedimentation, horizontal and vertical advection) have been discussed in Tsikerdekis et al. (2017).

In terms of precipitation the model displays a limited range of FGE (68%-75%) under four combinations of land-ocean convective scheme. The best convective scheme combination in term of the MNMB is Emmanuel over sea and Grell over land (TRANS-EG). There is an underestimation of total cloud fraction over the ocean by 20% when Emanuel scheme is used over sea (TRANS-EG and TRANS-E) and about 10% with Tiedtke scheme over sea (TRANS-T and TRANS-TG). All the experiments show that the dust total column burden over the coast of South America is about 40 mg and FWET almost one over the Atlantic ITCZ path, which indicates the dominating role of wet deposition due to heavy precipitation over that area.

The size discretization experiments (TRANS4 and TRANS12) depicted that the averaged DOD over all subregions depicted in Figure 3.1, is higher in the TRANS12 experiment by 0.03 (32%), which is similar to the 0.05 (10%) increase presented in Tsikerdekis et al. (2017) for a smaller domain. The actual differences averaged for each subregion range between 0.01 and 0.05. Subregions close to dust sources display moderate percentage increase 18-19% while as dust moves westward over the Atlantic the percentage increase of TRANS12 experiment accumulates. The averaged, over all regions, TOA and surface RE enhances by $0.7 W \cdot m^{-2}$ (59%) and $-1.3 W \cdot m^{-2}$ (25%) respectively. The weaker longwave RE enhances by $0.1 W \cdot m^{-2}$ in TOA and surface (33% and 29%).

The dust global climate multi-model inter-comparison by Kim et al. (2014) and the TRANS4 experiment were used to investigate the generic diversities and similarities of dust processes over the North Atlantic. The total and over land DOD of TRANS4 simulation (0.13, 0.20) lies between the range of the 5 global simulations, with the lower being HadGEM2 (0.04, 0.06) and the higher being GOCART (0.17, 0.33). RegCM4 emission flux is quite higher making the loss frequency (day^{-1}) 3 to 4 times greater in comparison to the other models. Over the Atlantic all the models display FWET that ranges from 0.4 to 0.8, with RegCM4 value (0.54) laying well between these bounds. RegCM4 MEE is

almost 2-3 times greater (1.75) than that. High MEE values in RegCM4 can be partially explained by the overestimation of dust extinction profile, even close to the dust sources, which makes fine size particles presence evident everywhere, without increasing the column burden much.

The total, dry and wet dust as well as the analogous phosphorus deposition were calculated using the 8-year TRANS4 simulation and the spatial delimitation of the Amazon, Caribbean and Amazon based on Ridley et al. (2012). According to TRANS4 simulation 4.3±0.4 $Tg \cdot yr^{-1}$ of dust are deposited in and close to the Amazon basin which is lower than the 17±5 $Tg \cdot yr^{-1}$ estimate from the GEOS-Chem model (Ridley et al. 2012) and significantly lower than the satellite estimate using MODIS (Terra/Aqua) 50 $Tg \cdot yr^{-1}$ (Kaufman et al. 2005) which can be can partially explained by the lack of wet deposition due to the underestimation of convective precipitation over the Amazon basin, when Grell scheme is active. Gravitational settling due to the weight of dust particles (dry column), is the major mechanism that deposits dust over the Amazon (2.9 Tg·yr-1, 67.4%) and the Atlantic (137.3 Tg·yr-1, 88.9%), contrary to the Caribbean where rain washout dominates (8.8 Tg·yr-1, 85.4%). Over the Amazon the fine and coarse particle contribute the same amount of total dust deposition (2.1 $Tg \cdot yr^{-1}$), while over the Atlantic and the Caribbean coarse particles are the major contributor of dust deposition (132.2 $Tg \cdot yr^{-1}$ and 8.3 $Tg \cdot yr^{-1}$ respectively). Dust deposition can diverse by more than 20% in the Amazon basin and the Caribbean depending on the cumulus convective scheme in use.

5. Assess the radiative effects of dust in present and future climate

Numerous dust simulations have been carried out in the past with either global (e.g. Huneeus et al., 2011; Kinne, 2003; Miller et al., 2006; Woodage et al., 2010) or regional (e.g. Basart et al., 2012; Helmert et al., 2007; Nabat et al., 2012; Solmon et al., 2012; Spyrou et al., 2013; Tegen et al., 2013; Tsikerdekis et al., 2017; Zakey et al., 2006) climate models for historical periods. Global dust model inter-comparison in AEROCOM phase I (Huneeus et al., 2011, and reference therein) showed that between 14 dust simulations, parameterized under different set of dust schemes and meteorological driven data, provided a broad spectrum of dust emission flux (from 664 $Tg \cdot yr^{-1}$ to 4313 $Tg \cdot yr^{-1}$, SD=1141 $Tg \cdot yr^{-1}$), deposition flux (from 676 $Tg \cdot yr^{-1}$ to 4359 $Tg \cdot yr^{-1}$, SD=1118 $Tg \cdot yr^{-1}$) and dust load (from 6.8 $Tg \cdot yr^{-1}$ to 29.5 $Tg \cdot yr^{-1}$, SD=6.9 $Tg \cdot yr^{-1}$). Miller et al. (2006) demonstrated that even under the same model (ModelE AGCM), 13 simulations with slightly altered parameterization can lead to large deviation in emission fluxes (from 682 $Tg \cdot yr^{-1}$ to 4214 $Tg \cdot yr^{-1}$, SD=989 $Tg \cdot yr^{-1}$), which highlights the current challenges around accurate dust modeling.

Future projections of dust bare even higher uncertainty, since various feedback mechanisms can affect dust emission and atmospheric lifetime. Depending on the focused feedback mechanism (changes in wind, precipitation, vegetation cover, aerosol climate feedback), the dust emission rates and burden can give a wide range of results. Tegen et al. (2004) showed that over eastern and central Sahara dust emission is expected to increase in the decade 2040-2050 by 11% (ECHAM4+BIOME4 simulation) mainly due to higher wind speeds or decrease slightly by 4% (HADCM3+BIOME4 simulation) as a result of the increased monsoon precipitation that will increase the vegetation covered.

Woodward et al. (2005) considered both the vegetation cover changes and the dust radiative feedback on climate and found that dust loading can be three times greater globally in the future decade 2090-2100 due to the desertification of several regions in the southern hemisphere. However when considering only the effect of climate change and dust climate feedback dust loading was increased by a small amount (+10%). Land cover changes can be a major factor for future dust emission rates if we consider that the expected global warming in the future is expected to enhance the Hadley circulation, which will intensify the precipitation along the InterTropical Convection Zone (ITCZ), reduce it along the subtropics and lead into drier conditions over the Mediterranean and Sahel (Hansen 2005). The

potential desertification of these areas can alter the emission fluxes and the dust concentration in the planet.

Other simulations showed that under increased CO_2 concentration conditions stomatal conductance decreases, which increases the water use efficiency of plants making them more adaptable in arid and semi-arid environments. Thus, CO_2 fertilization can potentially increase vegetation in deserts and decrease dust emission and burden by up to 60% in the future (Mahowald and Luo 2003; Mahowald et al. 2006). Future climate forcing and loading of dust bares high uncertainty, especially in studies where vegetation and land cover are taken into account. Thus, in our future projection we consider only the atmospheric climate change and not the vegetation alteration it might cause.

Although dust accurate simulation in climate models is hard to achieve, in both historical and future periods, dust modeling is an essential tool to quantify and enhance our knowledge about the physical process governing dust emission, transport and deposition as well as the direct and indirect radiative impact of dust on climate.

5.1 Simulation set-up

In order to study the feedback effect of dust on climate, both the historical and the future period contain a set of simulations. In the first experiment (ControlRun) dust exists in the model but it does not interact with radiation. In the second experiment (FeedbackRun) dust is radiatively active, scattering and absorbing shortwave and longwave radiation, and forwarding its effect as a temperature tendency in the next timestep. This process continuously slightly changes the simulated meteorology due to the radiative direct and semi-direct effect of dust. A schematic representation of the key differences between the two experiments is shown in Figure 5.1.

The domain includes the Mediterranean, north Africa as well as a large portion of Europe and of the Arabian desert (Figure 5.2). Four experiments have been conducted using the RegCM4, two for the historical decade (*ControlHindcast14*, *FeedbackHindcast14*) ranging from 2000 to 2009 and two for the future decade (*ControlFuture14*, *FeedbackFuture14*) ranging from 2090 to 2099. All the experiments include eleven months as spin-up time, starting from January 1999 and January 2089 for the historical and future set of simulations respectively. The simulations conducted in this study range over a decade which is not considered a “climate experiment” with the strict sense of that term, which requires more than 30 years. Nevertheless, decadal regional and global simulations are often used in

many chemistry-climate interaction studies (Mahowald and Luo 2003; Zanis et al. 2012a; Zanis et al. 2012b).

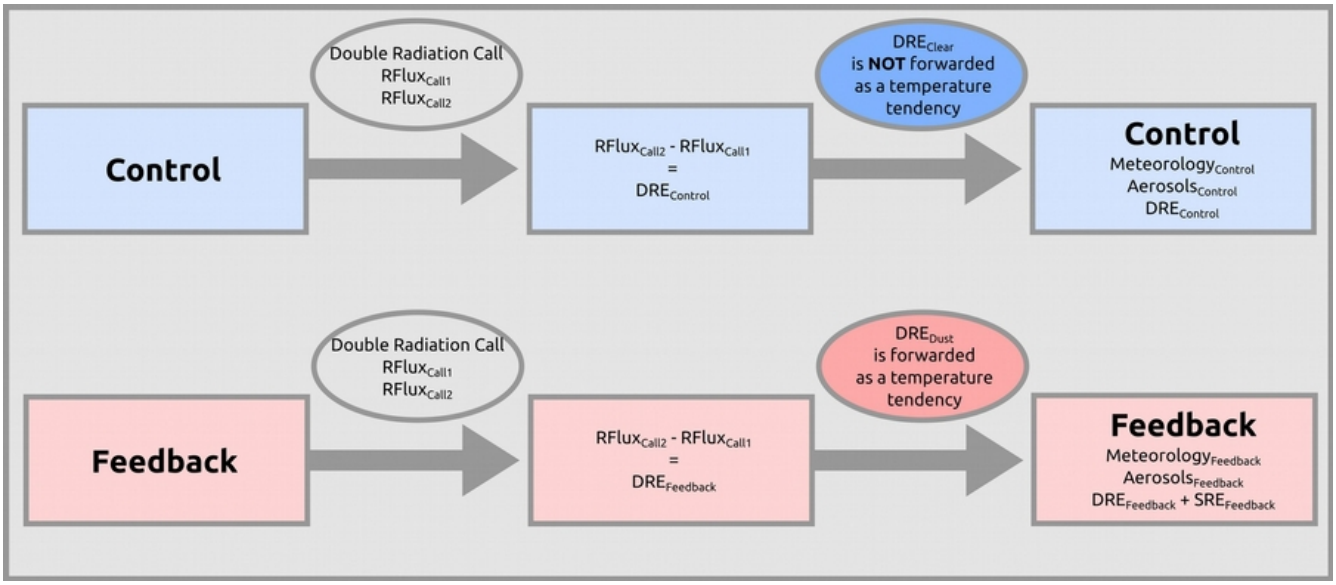

Figure 5.1. Schematic representation of the radiation logic in ControlRun and FeedbackRun in RegCM-CHEM4.

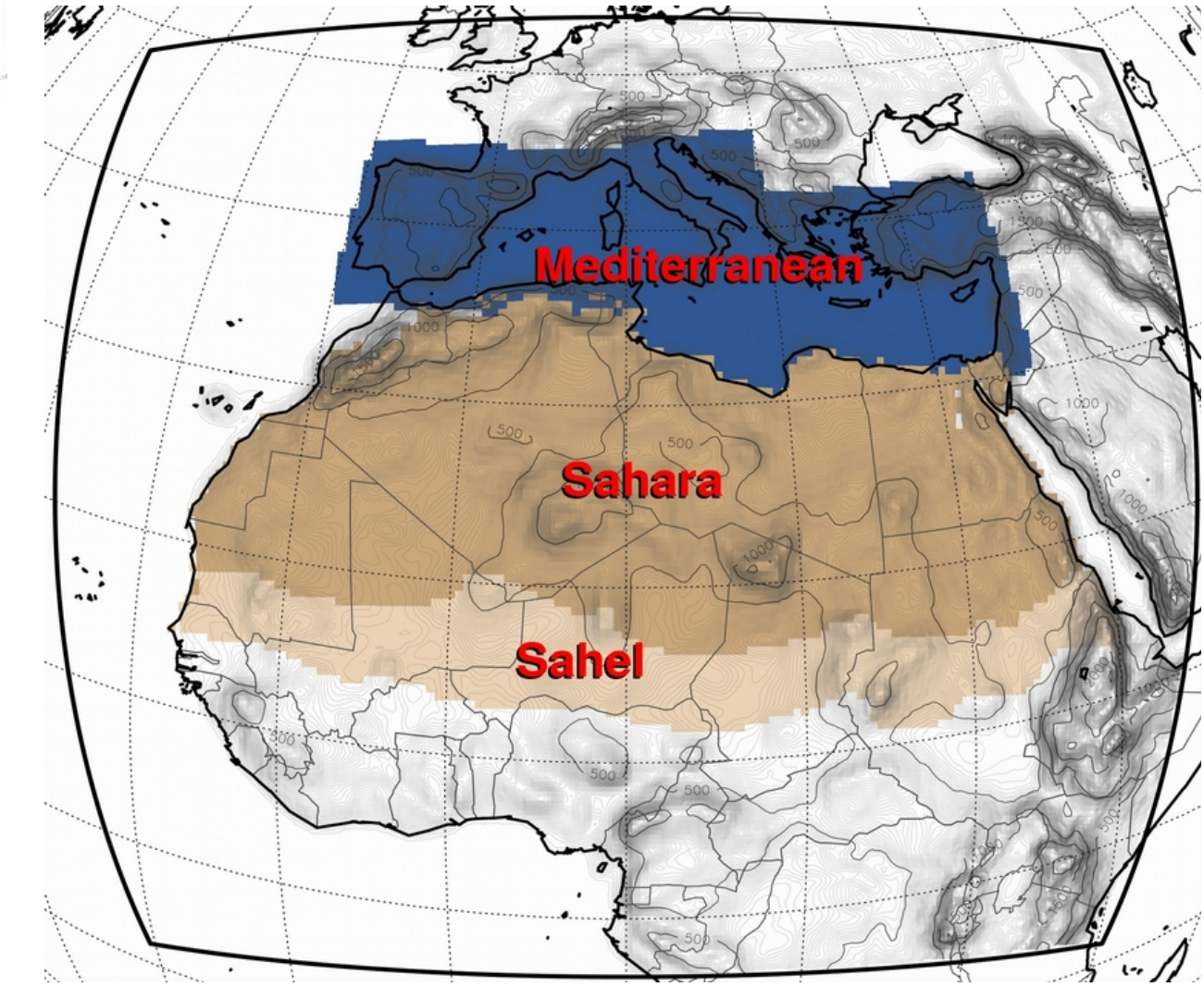

Figure 5.2. RegCM4 simulated domain (outer black polygon) and the subregions selected for the analysis. The topography of the simulation is superimposed in 500m contour lines.

The meteorological initial and boundary conditions for the simulations are provided in 6 hours intervals and were acquired from a simulation of the global model EC-EARTH. The respective chemical initial and boundary conditions of the dust mixing ratio ($kg \cdot kg^{-1}$) were obtained by the same global simulation of EC-EARTH (1.125ºx1.125º) coupled with CAM in mean monthly time intervals for the decades 2000-2009 and 2090-2099. A summary of the simulations options for this Chapter is depicted in Table 15.

Table 15. A summary of the decade simulations and the options selected in RegCM4. GHG stands for GreenHouse Gases, ICBC stands for Initial and Boundary Conditions, PBL stands for Planetary Boundary Layer and PSD stand for Particle Size Distribution.

Category/Experiment	**ControlHistorical14 (CH14)**	**FeedbackHindcast14 (FH14)**	**ControlFuture14 (CF14)**	**FeedbackFuture14 (FF14)**
Grid Dimensions	140 x 160, 18 sigma levels			
Horizontal Resolution	50km			
Period	1999-01-01 to 2009-11-30		2089-01-01 to 2099-11-30	
GHG Scenario	-		RCP45 (Thomson et al. 2011)	
Meteorological ICBC	EC-EARTH			
Chemical ICBC	EC-EARTH + CAM			
Cumulus Scheme	Tiedtke (Tiedtke, 1989)			
Radiation Scheme	CCM3 (Kiehl et al., 1996)			
Moisture Scheme	SUBEX (Pal et al., 2000)			
PBL Scheme	Modified Holtslag (Holtslag et al., 1990)			
Dust Tracers	4bins, isolog			
Dust PSD	Kok (Kok 2011b)			
Dust Feedback	OFF	ON	OFF	ON

The future projection simulations are driven by a moderate greenhouse gas emission scenario RCP4.5 (Thomson et al. 2011). The Representative Concentration Pathway (RCP) 4.5 sets as a goal the stabilization of the global radiative forcing at 4.5 $W \cdot m^{-2}$ (equivalent to 650ppm CO2) without ever exceeding that value until the year 2100. RCP4.5 is designed to be cost-efficient to reach the radiative forcing target. It assumes technological advancements by combining bioenergy production along with CO2 capture and geologic storage (CCS), that will resolve to an extent the energy requirement of the planet efficiently.

Prior to the decade simulation for the historical and the future period, multiple 3-year simulations have been conducted for the period January 2007 to December 2009 to improve the model dust performance

(Table 16). The basic simulation options of these experiments are identical to ControlHistorical14 (Table 15). In each 3-year simulation Dust Optical Depth (DOD) column and Dust EXtinction (DEX) profile have been evaluated against the LIVAS dust product (Amiridis et al. 2013). The Tiedtke scheme in RegCM4 calculates the dust cumulus transport explicitly using the in cloud updraft/downdraft fluxes and the simplistic dust convective transport in which dust becomes well-mixed between the layers of a cumulus cloud top and bottom (Kasibhatla et al. 1997; Solmon et al. 2006). The vertical tendency and DEX analysis in Chapter 3 showed that the model overestimated DEX in the mid and upper Troposphere (5-10km), most probably due to the vertical dust transport from cumulus convection (Tsikerdekis et al. 2017b). Thus, we have conducted an experiment that takes into account the explicit cumulus convection transport (CH) and an experiment where both the explicit and simplistic dust convective transport are active (CHESC). To further improve the DEX profile in our simulations, two additional experiments have been conducted similar to CH, where dust emission flux was linearly increased by adjusting the soil erodibility factor, that makes the surface features over desert and semi-desert grids more easily erodable, from the default value 1 to 1.4 (CH14) and 1.8 (CH18).

Table 16.A summary of the 3-year simulation distinct options.

Category/Experiment	ControlHistorical (CH)	ControlHistoricalESC (CHESC)	ControlHistorical14 (CH14)	ControlHistorical18 (CH18)
Period	2007-01-01 to 2009-11-30			
Soil Erodibility	1	1	1.4	1.8
Dust Cumulus Transport	Explicit	Simplistic+Explicit	Explicit	Explicit

5.2 Calibrating RegCM4 dust optical depth

The results of the 3-year experiments (Table 16) have been evaluated with the dust product LIVAS. Prior to the evaluation a spatio-temporal mask was applied to the model, according to the flybys of the CALIPSO satellite (More info in Section 2.2). Figure 5.3 depicts the DOD of LIVAS, CH, CHESC, CH14 and CH18 experiments for the period January 2007 to November 2009. Overall, all the experiments display an overestimation of DOD over the eastern Sahara and an underestimation over Sahel. The CH and CH18 experiments Modified Normalized Mean Bias (MNMB) over all subregions is -16% and 32% respectively and they can be considered the negative and the positive extremes among

the set of our experiments. The DOD spatial differences of CHESC and CH14 against LIVAS look almost identical (16% and 11% MNMB respectively) and they can be considered the best two candidates for conducting our long term simulations.

Although the DOD bias against LIVAS is similar between the CHESC and CH14 experiments, the vertical distribution of dust in the atmosphere is quite different. The results presented in Figure 5.4 show that the CHESC experiment clearly underestimates DEX values over 4-5km depending on the region, while the CH14 overestimate DEX in the first couple kilometers. Although the absolute value of the percent bias in DEX over Sahara is smaller in the CHESC experiment (-4.8%) in comparison to CH14 experiment (6.1%), the DEX overestimation of CHESC in the mid and upper Troposphere affects both dust transport and its radiative impact on the model physics. Thus, CH14 is considered the best candidate among these 4 experiments for simulating both DOD and DEX and its set-up was used for our longterm decade simulations.

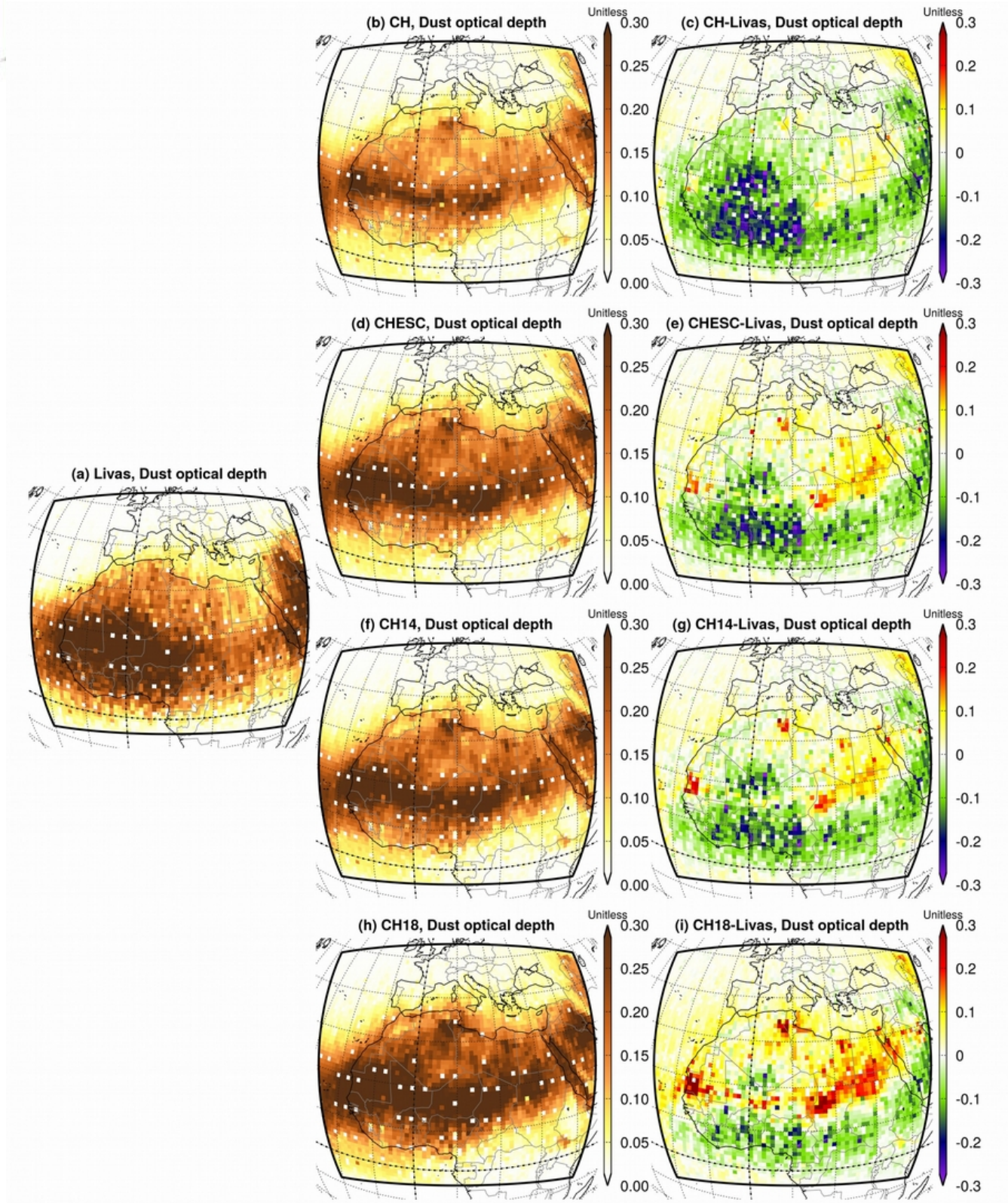

Figure 5.3. Dust optical depth of LIVAS, ControlHistorical (CH;erodibility-factor=1), ControlHistoricalESC that enables both explicit and simplistic dust cumulus convection transport (CHESC;erodibility-factor=1), ControlHistorical14 (CH14;erodibility-factor=1.4) and ControlHistorical18 (CH18;erodibility-factor=1.8) for the period January 2007 to

Table 17. Dust optical depth basic validation metrics of LIVAS (Obs), ControlHistorical (CH;erodibility-factor=1), ControlHistoricalESC that enables both explicit and simplistic dust cumulus convection transport (CHESC;erodibility-factor=1), ControlHistorical14 (CH14;erodibility-factor=1.4) and ControlHistorical18 (CH18;erodibility-factor=1.8) for the period January 2007 to November 2009. (Equation in Appendix)

CH	ObsMean	ModMean	MNMB	FGE	R	MaxBias	MinBias	UPCIBias	MeanBias	LWCIBias	PercentBias	RMSE	NRMSE	obsSD	modSD	RatioSD
Mediterranean	0.05	0.05	-4%	31%	0.76	0.09	-0.08	0.00	0.00	0.00	-6.2%	0.02	68.3%	0.03	0.03	0.93
Sahara	0.18	0.15	-15%	32%	0.55	0.13	-0.37	-0.03	-0.03	-0.04	-18.6%	0.07	92.3%	0.08	0.05	0.58
Sahel	0.29	0.19	-42%	44%	0.64	0.15	-0.33	-0.08	-0.09	-0.10	-32.6%	0.12	133%	0.09	0.08	0.93
All	0.15	0.12	-16%	34%	0.82	0.15	-0.37	-0.03	-0.03	-0.04	-21.7%	0.07	66.2%	0.11	0.08	0.69
CHESC	**ObsMean**	**ModMean**	**MNMB**	**FGE**	**R**	**MaxBias**	**MinBias**	**UPCIBias**	**MeanBias**	**LWCIBias**	**PercentBias**	**RMSE**	**NRMSE**	**obsSD**	**modSD**	**RatioSD**
Mediterranean	0.05	0.07	32%	41%	0.75	0.19	-0.06	0.02	0.02	0.02	37%	0.03	109%	0.03	0.04	1.30
Sahara	0.18	0.21	16%	28%	0.62	0.23	-0.28	0.03	0.02	0.02	13%	0.07	85%	0.08	0.06	0.79
Sahel	0.29	0.25	-18%	29%	0.65	0.20	-0.32	-0.03	-0.04	-0.05	-13%	0.09	102%	0.09	0.11	1.19
All	0.15	0.17	16%	33%	0.82	0.23	-0.32	0.01	0.01	0.01	8%	0.06	58%	0.11	0.10	0.90
CH14	**ObsMean**	**ModMean**	**MNMB**	**FGE**	**R**	**MaxBias**	**MinBias**	**UPCIBias**	**MeanBias**	**LWCIBias**	**PercentBias**	**RMSE**	**NRMSE**	**obsSD**	**modSD**	**RatioSD**
Mediterranean	0.05	0.06	22%	36%	0.76	0.15	-0.06	0.01	0.01	0.01	25%	0.03	96%	0.03	0.04	1.28
Sahara	0.18	0.20	13%	28%	0.58	0.33	-0.29	0.02	0.02	0.01	10%	0.07	87%	0.08	0.07	0.82
Sahel	0.29	0.26	-14%	28%	0.65	0.30	-0.29	-0.01	-0.03	-0.04	-9%	0.09	103%	0.09	0.12	1.29
All	0.15	0.16	11%	31%	0.82	0.33	-0.29	0.01	0.01	0.01	6%	0.06	58%	0.11	0.10	0.94
CH18	**ObsMean**	**ModMean**	**MNMB**	**FGE**	**R**	**MaxBias**	**MinBias**	**UPCIBias**	**MeanBias**	**LWCIBias**	**PercentBias**	**RMSE**	**NRMSE**	**obsSD**	**modSD**	**RatioSD**
Mediterranean	0.05	0.08	42%	48%	0.76	0.20	-0.05	0.03	0.03	0.03	56%	0.04	150%	0.03	0.04	1.64
Sahara	0.18	0.25	34%	39%	0.58	0.48	-0.24	0.08	0.07	0.07	39%	0.10	127%	0.08	0.08	1.04
Sahel	0.29	0.33	8%	27%	0.65	0.47	-0.24	0.06	0.04	0.03	16%	0.12	136%	0.09	0.15	1.67
All	0.15	0.21	32%	40%	0.82	0.48	-0.24	0.06	0.05	0.05	33%	0.09	83%	0.11	0.13	1.21

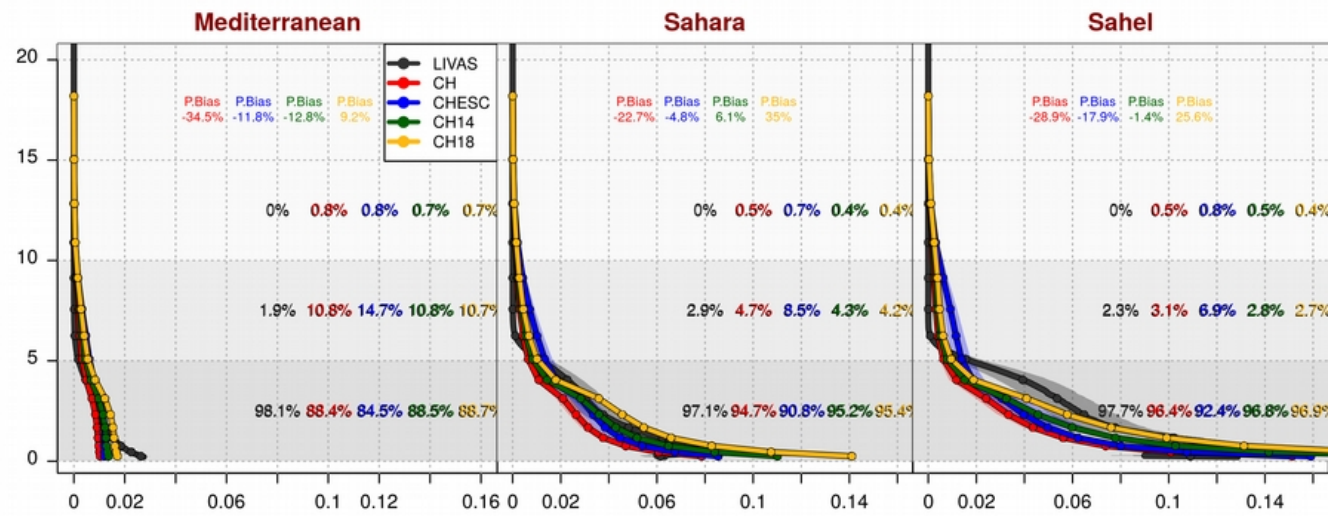

Figure 5.4. Dust extinction profile for three subregions of LIVAS, ControlHistorical (CH;erodibility-factor=1), ControlHistoricalESC that enables both explicit and simplistic dust cumulus convection transport (CHESC;erodibility-factor=1), ControlHistorical14 (CH14;erodibility-factor=1.4) and ControlHistorical18 (CH18;erodibility-factor=1.8). The percent bias (P.Bias) for the whole DEX column as well as the percent of DEX between 0-5km, 5-10km and 10-20km for each dataset is depicted upon the plot.

5.3 Evaluation

Our work investigates the future dust changes as well as the temperature and cloud fraction adjustments due to climate change and dust radiative effect. Thus, an evaluation of the near surface temperature and the cloud fraction for the period December 1999 to November 2009 was conducted using the CRU and the period February 2004 to November 2009 for the CMSAF datasets. Prior to evaluation, CRU 0.5x0.5 grid was interpolated into CH14 50kmX50km grid and the non-available ocean values of CRU were also omitted from the model. Figure 5.5 depicts the near surface (2m) temperature of the CRU dataset and the CH14 experiment for winter (DJF) and summer (JJA). In both seasons CH14 underestimates near surface temperature over Sahara and Sahel. During winter there is a small positive tendency by the model which generates a slight overestimation of temperature by 0.2°C, while in summer temperature in Mediterranean is underestimated by 1°C. The underestimation of near surface temperature over the Sahara correlates well with the deserts orography. Thus, part of the negative error might be due to the limited observations over the desert and especially over the desert's mountains.

The simulated climate in a Regional Climate Model (RCM), like RegCM4, is created following the internal physics of the model, but is also driven to an extent by the boundary forcing of the Global Climate Model (GCM) used. Thus, if the driver GCM climatology underestimates a variable, so will the climatology of the RCM. In our experiments we use as Initial and Boundary Conditions (ICBCs) data from the GCM EC-EARTH. The respective near surface temperature evaluation plot for EC-EARTH and CRU is depicted in Figure 5.6. EC-EARTH tends to be quite cold over Sahel, Sahara and Mediterranean during summer (Figure 5.6f) and slightly warm in Sahara and Mediterranean in winter (Figure 5.6c). Although EC-EARTH and CH14 biases do not complete agree, there is a clear tendency to underestimate near surface temperature in both cases.

Other RCM simulations from the Coordinated Regional Downscaling Experiment (CORDEX) research program, that used EC-EARTH as ICBCs have been proven to be quite cold. For example in Figure 5.7a shows that the RCM RACMO22E (highlighted line) simulation which is driven by the GCM EC-EARTH is quite colder in historical and future period in comparison too the other RCM simulations. Nevertheless, RACMO22E (EC-EARTH) is able to simulate the expected rise of near surface temperature at the course of the 21st century, agreeing fairly well with the other RCM simulations and the ensemble mean (Figure 5.7b).

Clouds and their vertical distribution in the atmosphere play an essential role in the overall albedo of the planet as well as the semi-direct effect of aerosols (Koch and Del Genio 2010). Thus, an evaluation of total, low, middle and high cloud fraction follows for CH14 using the CMSAF satellite measurements. Overall a distinct underestimation of all cloud fraction is observed in Mediterranean and generally over the Atlantic ocean (Figure 5.8c). An overestimation of low-cloud fraction is also evident during summer over the gulf of Guinea and Sierra Leone (Figure 5.9f). The limited CMSAF all cloud fraction over the Sahara during winter (23%) is underestimated by CH14 by 9% (Figure 5.8c) which originates mainly from the underestimation of high cloud fraction over the same region (Figure 5.11c). The same applies for the Mediterranean and the largest part of Europe where all-cloud and high-cloud fraction are underestimated by CH14 experiment by 25% and 10% respectively. In terms of the averaged MNMB over the three examined subregions, the all-cloud fraction is underestimated by 41% and 31%, the middle-cloud fraction by 9% and 6% and the high-cloud by 83% and 76% (respective values for winter and summer).

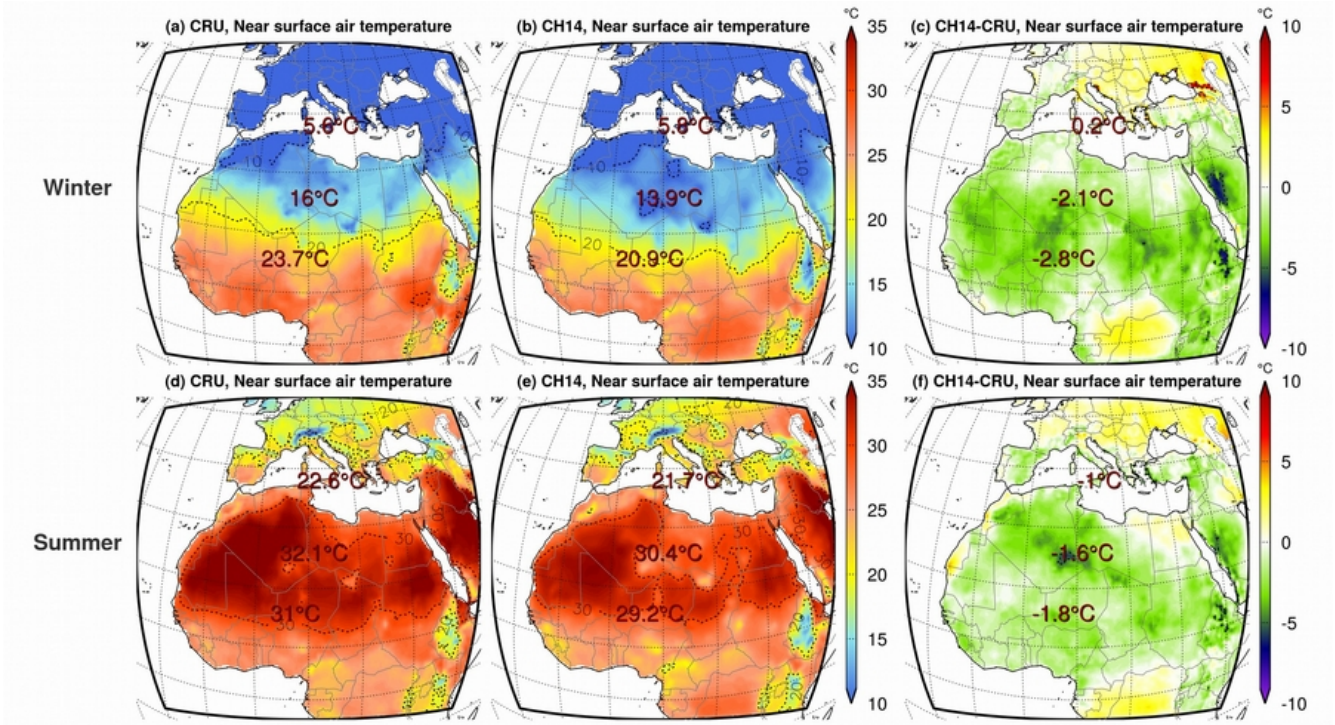

Figure 5.5. Near surface air temperature (°C) of CRU (a, d), ControlHistorical14 (b, e) and their difference (c, f) for the period February 2004 to November 2009. The first and second rows of plots depict winter (DJF) and summer (JJA) respectively. The numbers depict the average near surfance temperature values for Mediterranean, Sahara and Sahel.

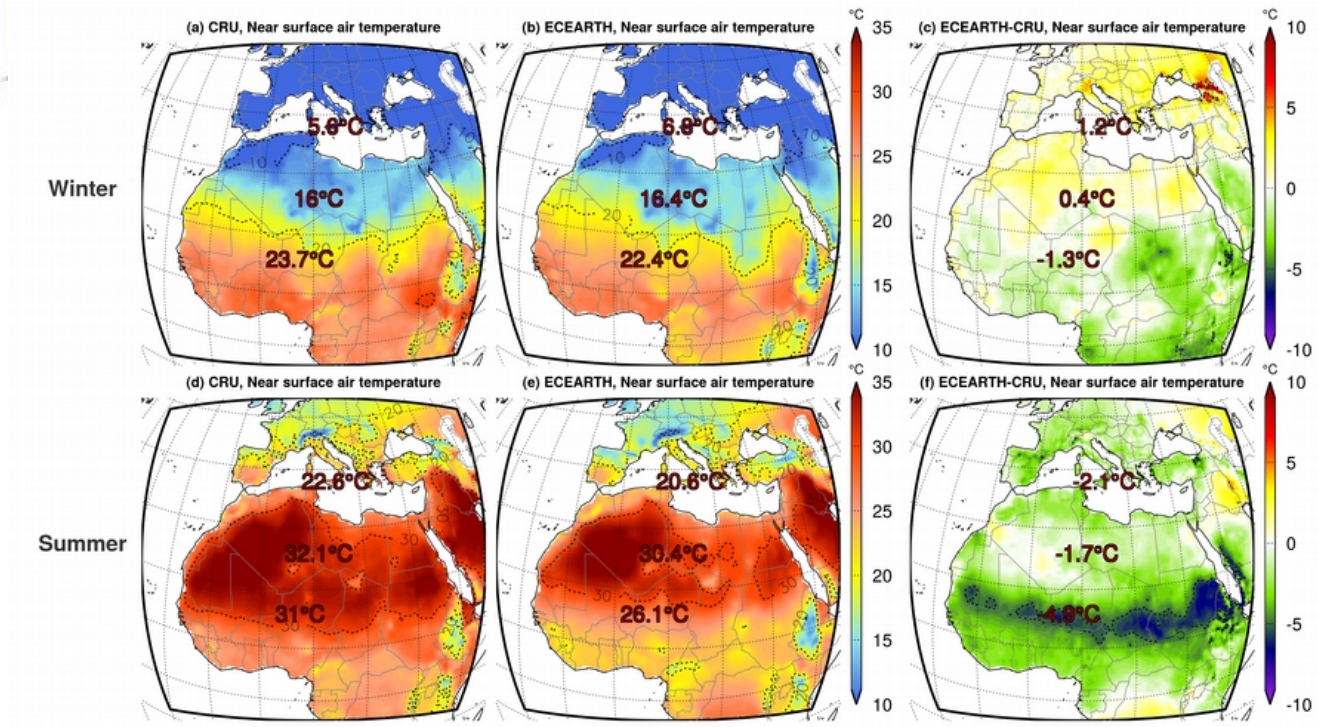

Figure 5.6. Near surface air temperature (°C) of CRU (a, d), EC-EARTH (b, e) and their difference (c, f) for the period February 2004 to November 2009. The first and second rows of plots depict winter (DJF) and summer (JJA) respectively. The numbers depict the average near surfance temperature values for Mediterranean, Sahara and Sahel.

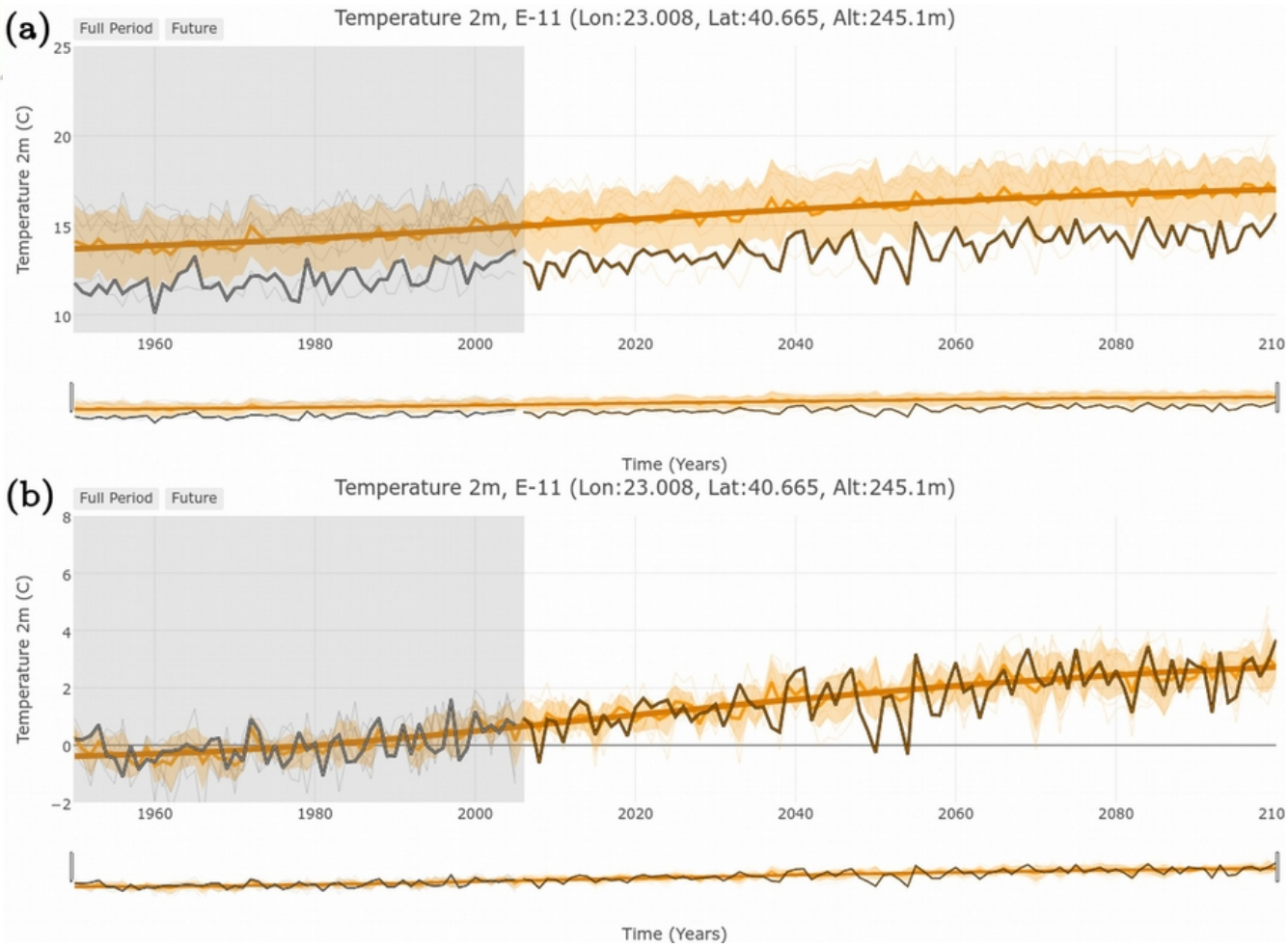

Figure 5.7. Yearly near surface temperature of 8 RCMs for the period 1950-2100 over Thessaloniki. Panel (a) illustrates the actual near surface temperature and panel (b) the near surface temperature after the historical mean was subtracted from each year. The shaded gray area depicts the historical period, while the white area, that starts in 2006, depict the future period where the models are forced by the greenhouse emission scenario RCP4.5. The bold yellow timeseries depict the ensemble mean of all the RCMs, while the highlighted golden timeseries illustrates the RCM RACMO22E simulation driven by the GCM EC-EARTH. All the models are a part of the Coordinated Regional Downscaling Experiment (CORDEX) research program. The plot was created by the climate-projection application at http://meteo.geo.auth.gr:3838/.

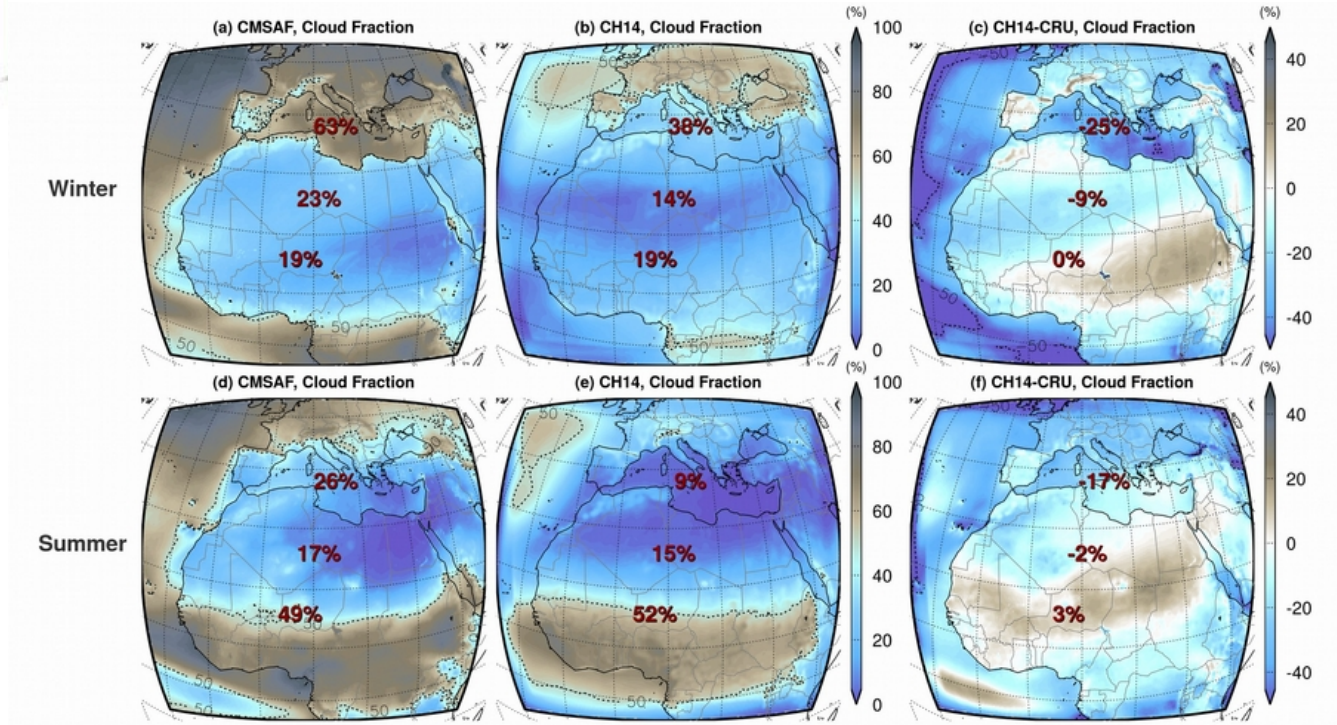

Figure 5.8. All cloud fraction (%) of CMSAF (a, d), ControlHistorical14 (b, e) and their difference (c, f) for the period February 2004 to November 2009. The first and second rows of plots depict winter (DJF) and summer (JJA) respectively. Percentages depict the average cloud fraction values for Mediterranean, Sahara and Sahel.

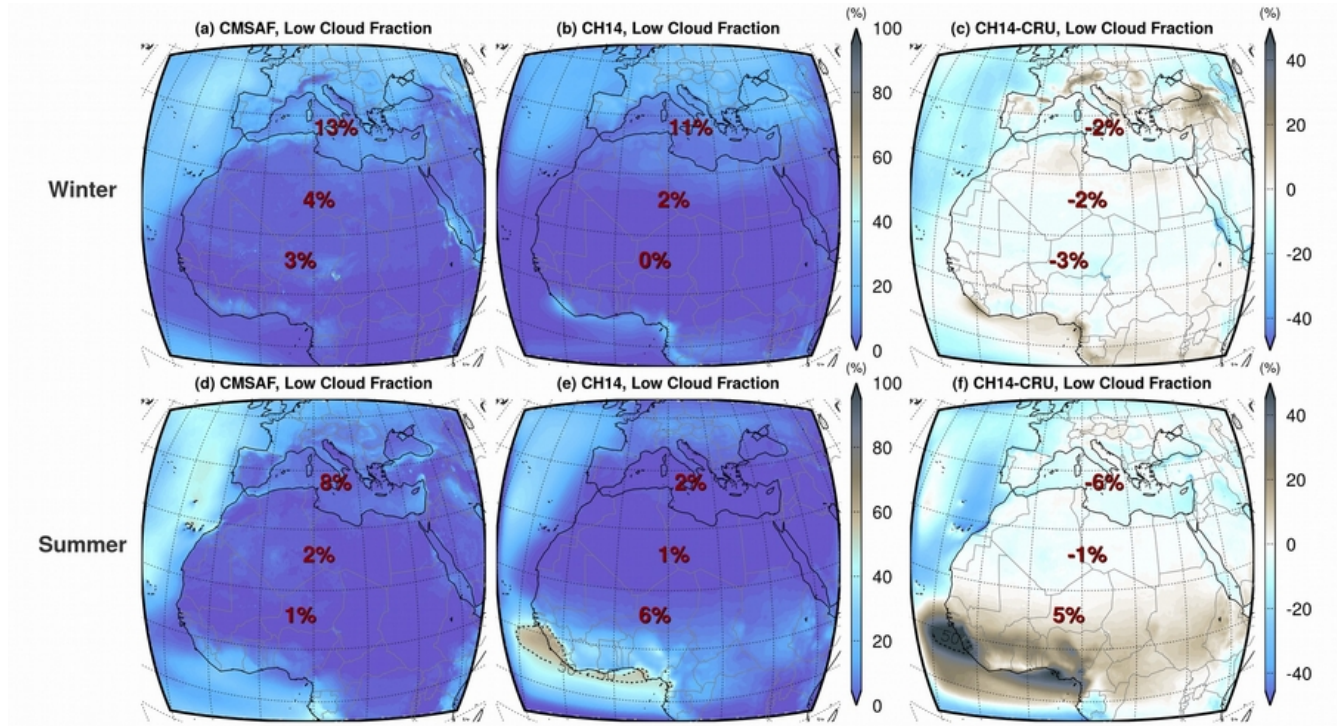

Figure 5.9. Low cloud fraction (%) of CMSAF (a, d), ControlHistorical14 (b, e) and their difference (c, f) for the period February 2004 to November 2009. The first and second rows of plots depict winter (DJF) and summer (JJA) respectively. Percentages depict the average cloud fraction values for Mediterranean, Sahara and Sahel.

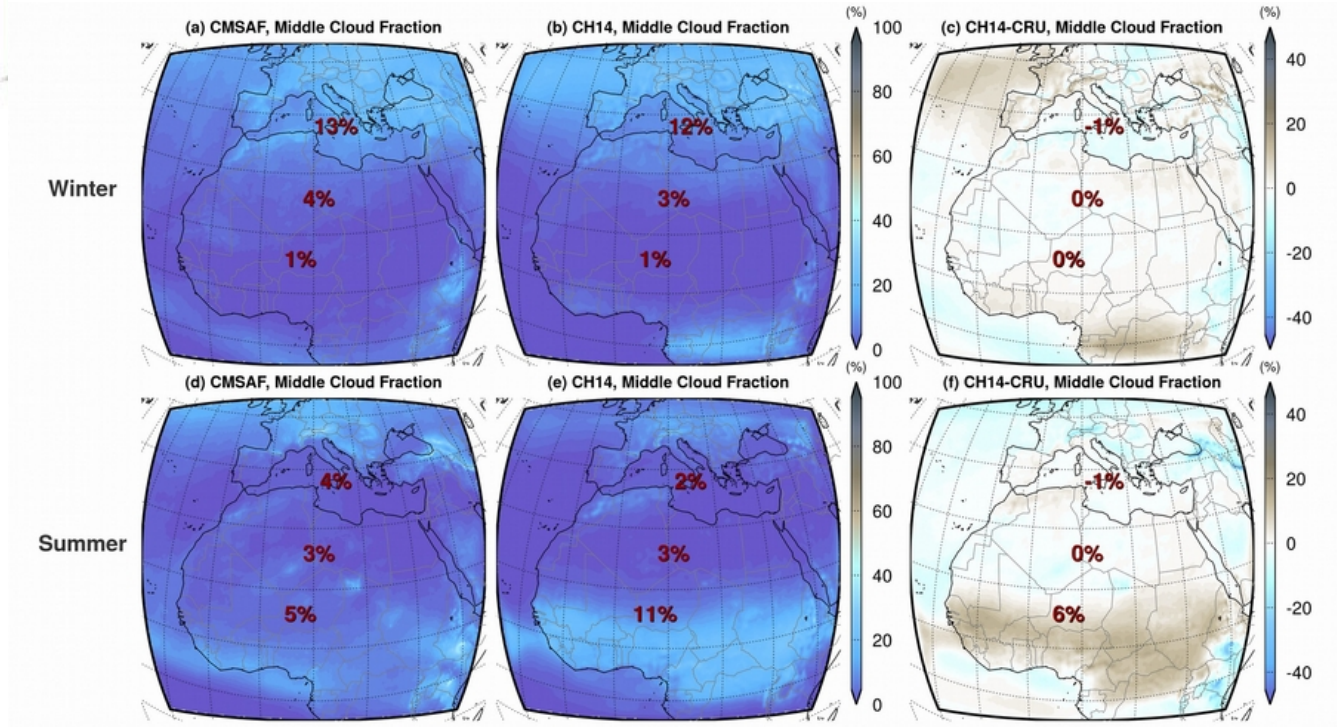

Figure 5.10. Middle cloud fraction (%) of CMSAF (a, d), ControlHistorical14 (b, e) and their difference (c, f) for the period February 2004 to November 2009. The first and second rows of plots depict winter (DJF) and summer (JJA) respectively. Percentages depict the average cloud fraction values for Mediterranean, Sahara and Sahel.

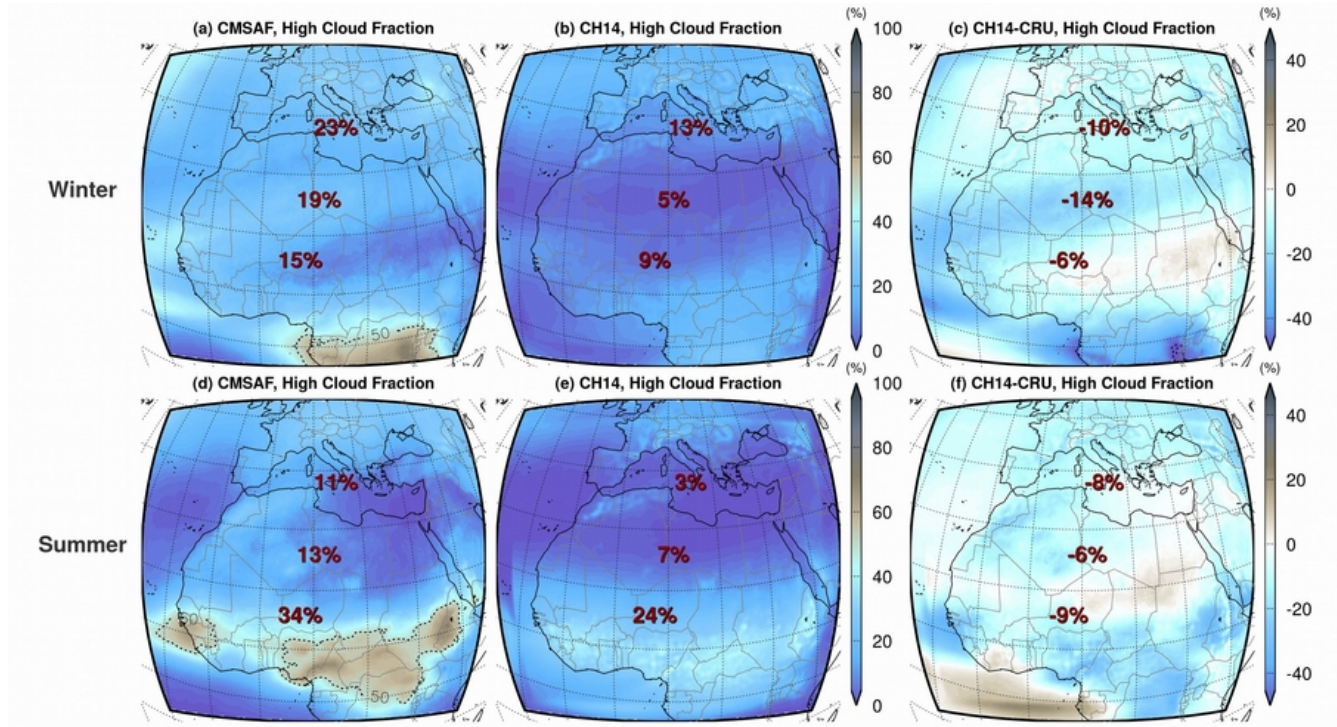

Figure 5.11. High cloud fraction (%) of CMSAF (a, d), ControlHistorical14 (b, e) and their difference (c, f) for the period February 2004 to November 2009. The first and second rows of plots depict winter (DJF) and summer (JJA) respectively. Percentages depict the average cloud fraction values for Mediterranean, Sahara and Sahel.

5.4 Dust radiative effect on climate - Historical Period

The dust DRE and SRE on climate are examined in this Section for the historical period (December 1999 - November 2009) using the ControlHistorical14 (CH14) and the FeedbackHistorical14 (FH14) experiments.

Dust optical depth, near surface wind field, fine dust particle (0.09-2.5μm) and coarse dust particle (2.5-63μm) column burden are shown in Figure 5.18. Dust optical depth in winter is lower over all the examined subregions in comparison to summer. The vast amounts of coarse dust particles are limited close to the dust sources, especially between the 15°N to 25°N zone (Figure 5.18c). In winter, large amounts of fine dust are transported southward towards the equator (Figure 5.18a,b). The northward movement of ITCZ during summer, which associated with high precipitation and dust wet deposition, acts as a barrier for the southward transport of dust. (Figure 5.18d,e). In summer the average dust optical depth values for Sahel and Sahara are 0.38 and 0.32, while some Mediterranean islands like Malta and Pantelleria exhibit low dust optical depth of the order of 0.1 (Figure 5.18d). Over the Mediterranean both the fine and the coarse particle concentrations are greater in summer (43kg·m^{-2} and 19kg·m^{-2} respectively) in comparison to winter (Figure 5.18f).

Typically, the RE is reported for the Earth's surface and at the top of the atmosphere. Here the dust DRE, SRE and DSRE of the FH14 experiment is depicted in Figure 5.13 for the surface. During summer the DRE (Figure 5.13d) is -14.9W·m^{-2} for the Sahara, -19.3W·m^{-2} for the Sahel and -3.9 W·m^{-2} for the Mediterranean. The SRE is mostly positive above the Sahara and Sahel and more enhanced in winter (Figure 5.13b,e). In the Mediterranean the same effect is positive but smaller in both winter and summer (0.8W·m^{-2} and 0.6W·m^{-2} respectively). The combined effect of the DRE and SRE (Figure 5.13c,f) decreases the net shortwave radiation (not shown) on the surface by about 6% to 10% over the Sahara and the Sahel and by 2% over the Mediterranean. The SRE over the Sahel is positive and accounts for a small fraction (10-20%) of DSRE in both winter and summer.

On the longwave spectrum the DRE (Figure 5.14a,d), which is highly correlated with the coarse dust particle concentration (Figure 5.12c,f), is high over the south Sahara and the Sahel (~5W·m^{-2}), while over the Mediterranean is close to zero, since large particles remain close to the emission source. In winter the longwave SRE signal (Figure 5.14b) is weaker than the DRE (Figure 5.14a) since cloud changes are very limited between the two experiments (Figure 5.12a). On the contrary in summer the

longwave SRE signal is quite prominent (Figure 5.14e) and comparable to the longwave DRE (Figure 5.14d). The mostly positive SRE reach up to 2.0W·m^{-2} in Sahara and 3.6W·m^{-2} in Sahel, while in Mediterranean is practically close to zero. The high values of longwave SRE over the Sahel and Sahara correlate with the enhanced total cloud fraction over the same regions (Figure 5.12c). Overall the combined longwave DSRE increases the surface downward longwave radiation over the Sahara and Sahel by 5% and 6% respectively, mainly due to the presence of coarse dust particles. In summer the longwave DSRE contribution is higher over the Sahara and the Sahel (7% and 12% respectively) by the combined effect of the coarse dust particles and the increase of total cloud fraction.

The respective differences of total cloud fraction between the two historical experiments are depicted in Figure 5.15. The shaded areas in Figure 5.15a,b depict the statistical significance of the monthly difference with 90% confidence using the 2-tailed paired t.test (see Katragkou et al. 2015 for a detailed description of the t-test). The total cloud fraction does not change significantly in winter (Figure 5.15a), while during summer there is a stronger statistically significant increase of clouds up to 0.03 which stretches across the eastern and mostly a part of the western Sahara (WS) desert (Figure 5.15b). To further understand what drives the cloud changes over the WS region the vertical profile of several meteorological parameters was created (Figure 5.15c). In the first couple kilometers from the surface there is a steady increase of wind from the Atlantic towards the desert. This process increases the specific and relative humidity. The dust DSRE creates a negative temperature profile in the first 2.5km from the surface and a positive up until 12km due to the heating rate of dust particles (Choobari et al. 2014). The positive temperature anomaly in the middle and upper Troposphere initiates a steady updraft flow by -0.58hPa per day, which generates more clouds that peak between 10km to 14km. Similar ascending circulation due to the “elevated heat pump” mechanism of dust has been observed in previous studies for the same region (Solmon et al. 2008) and for India (Lau and Kim 2006). The increase of total cloud fraction over WS region and mainly north of 17°N is mainly produced by the increase of high altitude clouds rich in cloud ice water content (Figure 5.16), in contrast to the limited increase of total cloud fraction under 17°N where cloud liquid water content increases (Solmon et al. 2008).

The 2-meter temperature, maximum daily temperature and minimum daily temperature differences between the FH14 and the CH14 experiments for summer and winter are depicted in Figure 5.17. The dominant dust radiative process is the reflectance-backscattering of the shortwave incoming solar

radiation back to space (DRE=~15W·m^{-2} in the desert), which reduces the energy that reaches the ground (Figure 5.13a,d). Thus, in all cases and in the majority of the grid points, temperature is lower in the FH14 experiment. The maximum reduction may reach up to 1.5°C in the 2-meter maximum daily temperature (Figure 5.17e). In both seasons the highest daily mean near surface air temperature differences are observed in the southern part of the western Sahara and in the Sahel where dust higher concentration prevail. During summer, the statistically significant reduction of temperature is concentrated over the Sahel (0.4°C), which is partially due to the increase of total cloud fraction during the same season (Figure 5.12c). In contrast, the local decline of temperature in winter is lower and scatters across all the Sahara and Sahel (0.2°C). The daily maximum air temperature reduction is spatially similar to the daily mean temperature but more pronounced, with an average decrease of temperature by 0.6°C over the Sahel during summer (Figure 5.17e) and by 0.2°C to 0.3°C over the desert during winter (Figure 5.17b). The minimum temperature is more frequently observed just before dawn when there is no shortwave radiation to interact with fine dust particles. Thus, near surface temperature is regulated by the net longwave radiation of the Earth's surface. Coarse dust particles and clouds absorb longwave emissivity and remit towards the ground, thus postponing the nocturnal cooling and increasing the daily minimum temperature (Hansell et al. 2010). During summer the daily minimum near surface temperature, over the regions where the longwave DSRE is about 8W·m^{-2} over the desert (Figure 5.14f), increases the minimum air temperature by more that 0.5°C locally (Figure 5.17f).

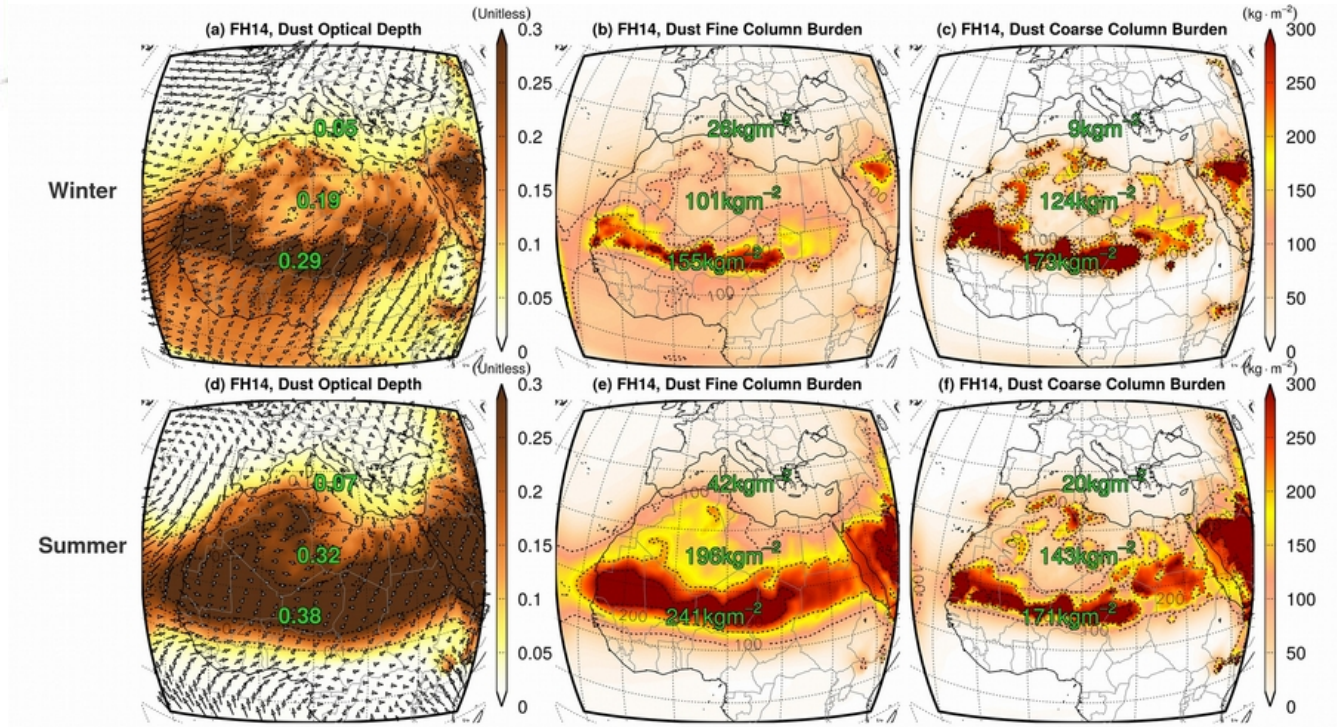

Figure 5.12: Dust optical depth (a, d), dust fine column burden (b, e) and dust coarse column burden (c, f) of FH14 experiment for the period 1999-12-01 to 2009-11-30. The first and second rows of plots depict winter (DJF) and summer (JJA) respectively. The near surface wind field is superimposed in panel a and d.

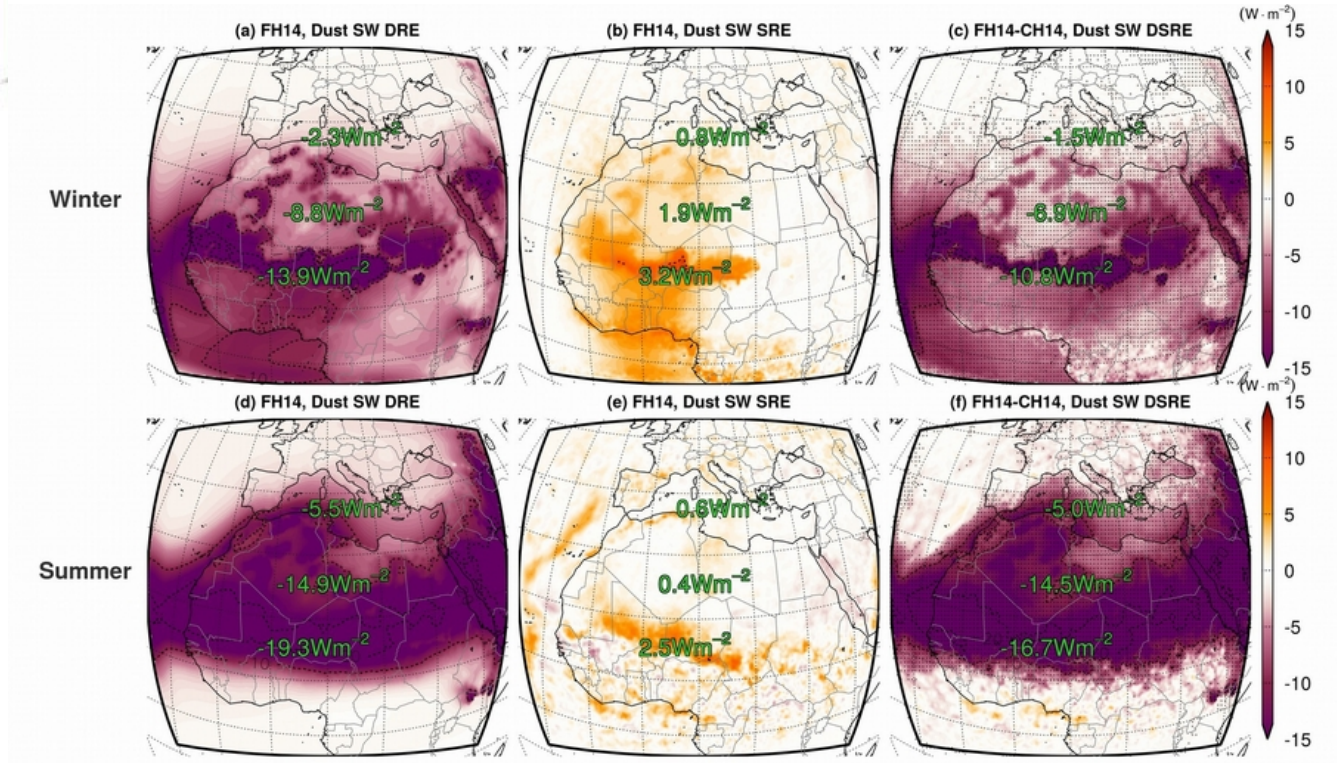

Figure 5.13: Dust shortwave DRE (a, d), SRE (b, e) and DSRE (c, f) of FH14 experiment for the period 1999-12-01 to 2009-11-30. The first and second rows of plots depict winter (DJF) and summer (JJA) respectively.

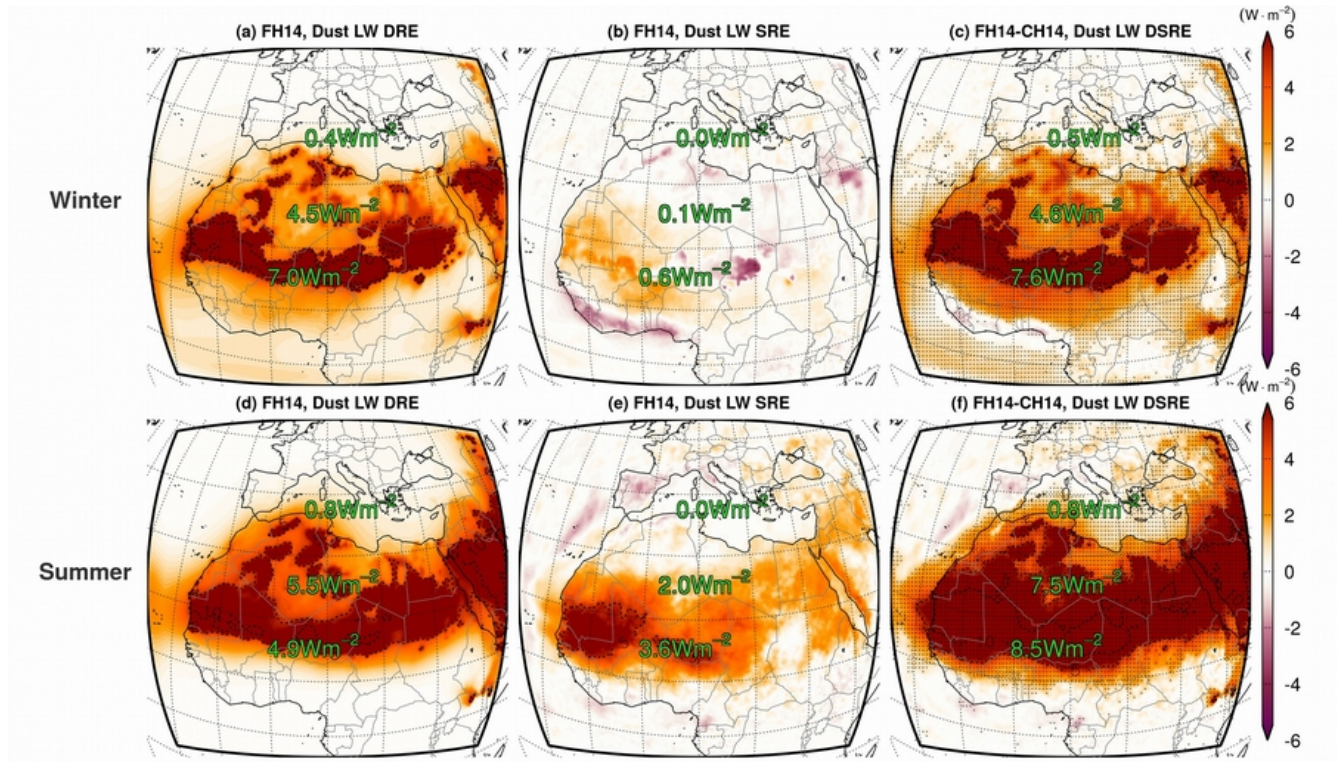

Figure 5.14: Dust longwave DRE (a, d), SRE (b, e) and the DSRE (c, f) FH14 experiment for the period 1999-12-01 to 2009-11-30. The first and second rows of plots depict winter (DJF) and summer (JJA) respectively.

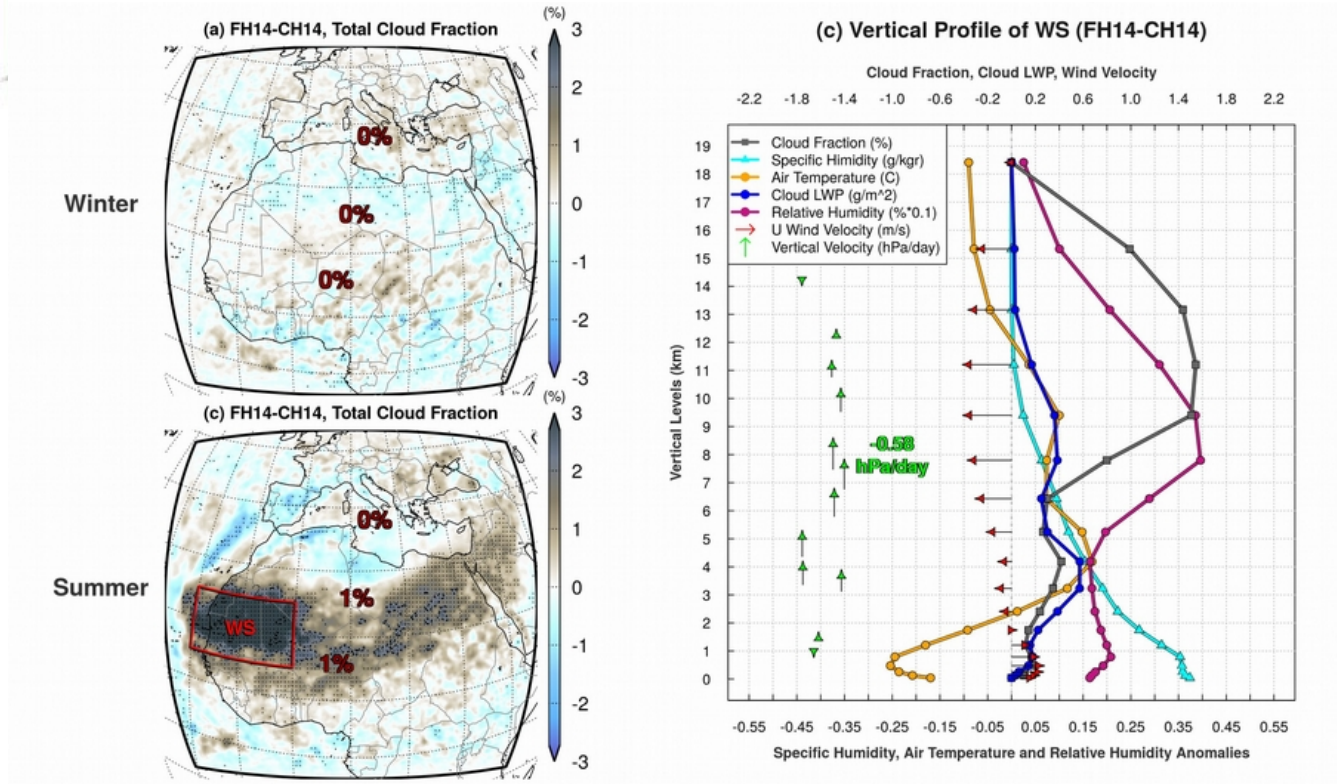

Figure 5.15: Differences of total cloud fraction (a, b) between the FH14 and the CH14 experiments for the period 1999-12-01 to 2009-11-30. In panel c the vertical profile of several meteorological variables during summer is depicted for region WS.

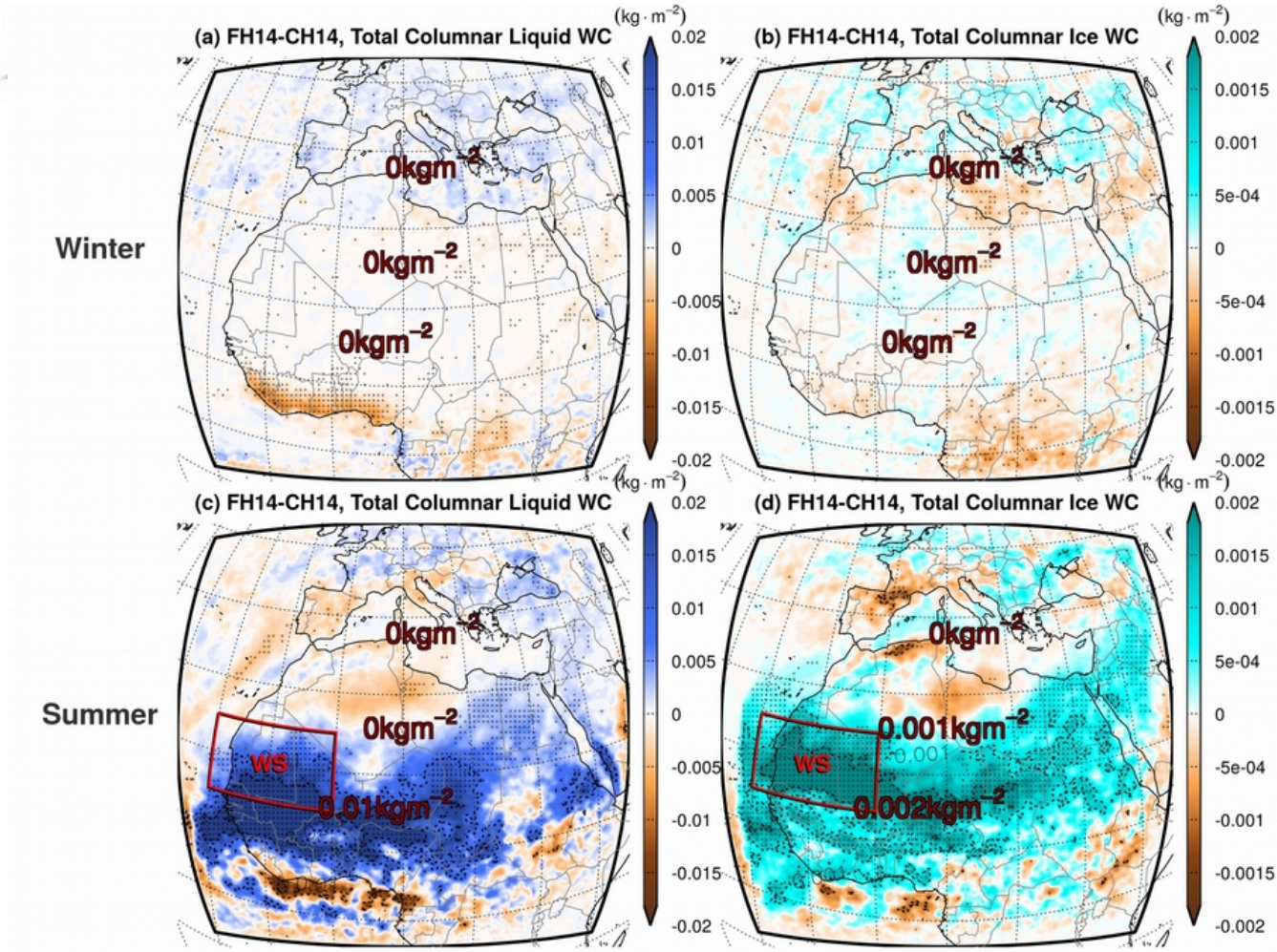

Figure 5.16. Differences of total columnar liquid water content of clouds (a, c) and total columnar ice water content of clouds (b, d) between the FH14 and the CH14 experiments for the period 1999-12-01 to 2009-11-30.

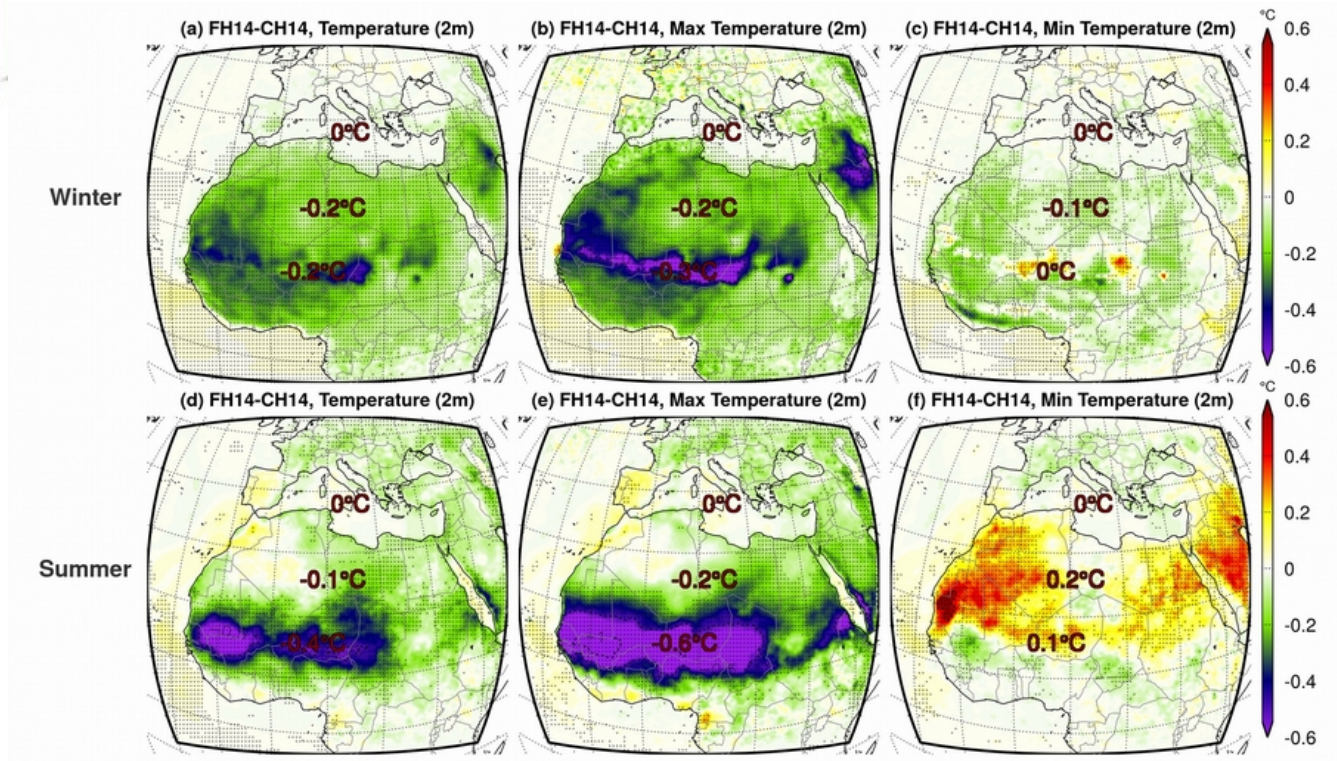

Figure 5.17. Differences of average (a, d), minimum (b, e) and maximum daily 2-meter temperature (c, f) between the FH14 and CH14 experiments for the period 1999-12-01 to 2009-11-30. The first and second rows of plots depict winter (DJF) and summer (JJA) respectively.

5.5 Dust radiative effect on climate - Future Period

Respectively to the previous Section, the DRE and SRE on climate are analyzed for the future period (December 2089 - November 2099) using the ControlFuture14 (CF14) and the FeedbackFuture14 (FF14) experiments. Dust burden, its RE and the meteorological changes in the future period are driven only by the greenhouse concentration path scenario RCP4.5. Landuse changes (e.g. desertification) are not taken into account, thus the following plots depict the future dust conditions driven only by the meteorological forcing of climate change.

Dust optical depth, near surface wind field, fine dust particle (0.09-2.5μm) and coarse dust particle (2.5-63μm) column burden are depicted in Figure 5.18. In winter the dust optical depth and burden are again less in comparison to summer and the vast amount of coarse dust particles are limited between the 15°N to 25°N zone, which indicates that the wind pattern, transport paths and dust sources remain almost the same in the future. Dust concentration of both fine and coarse particle increases in most cases in comparison to the historical period. Fine dust particle concentration in summer averaged for the Mediterranean, Sahara and Sahel are 45kg·m^{-2}, 205kg·m^{-2} and 252kg·m^{-2} respectively (Figure 5.18d), which is slightly higher (+4% to +8%) than the corresponding values in the historical period.

In the future period, the dust DRE and SRE keep almost the same spatial distribution in respect (Figure 5.19) to the historical period (Figure 5.13). In winter the negative DRE (Figure 5.19a) is counter-balanced by the positive SRE (Figure 5.19b), which sums up to a fairly weak negative DSRE (Figure 5.19c) over the Mediterranean (-1.3W·m^{-2}) Sahara (-8.8W·m^{-2}) and Sahel (-11.5W·m^{-2}). Consequently, the net shortwave radiation on the surface is reduced by 1%, 6% and 7% respectively. In summer the fine dust particles expand towards northern latitude, enhancing the DRE over the Mediterranean (-5.8W·m^{-2}), Sahara (-15.4W·m^{-2}) and Sahel (-20.7W·m^{-2}) (Figure 5.19d). The SRE in summer is almost negligible (Figure 5.19e) in comparison to the DRE and has no significant effect to the combined DSRE (Figure 5.19f). The mostly negative total DSRE over the Mediterranean is reducing the net radiation on the surface by 2% in the Mediterranean and by 8% and 12% in the Sahara and Sahel respectively (Figure 5.19f).

Since the model does not take into account the landuse changes due to climate change and the potential desertification of some regions over north Africa and Mediterranean (Kosmas and Danalatos 1994; de Wrachien et al. 2006; Skibba 2016), the location of the high column burden coarse dust particle

remains the same. Thus, the future decadal longwave DRE in both seasons (Figure 5.20a,d) is similar to the historical period (Figure 5.14a,d). The summer SRE spatial pattern remains also the same, but it is more intense as the increase of the cloud fraction (Figure 5.21b) is greater in comparison to the historical period (Figure 5.12a,c). In winter the longwave SRE is mostly positive and fairly small (Figure 5.20b), while in summer is mostly positive and more prominent over Sahara ($2.8 W \cdot m^{-2}$) and Sahel ($6.5 W \cdot m^{-2}$) where clouds increase. The longwave DSRE in winter is positive over the desert, mostly due to the DRE of the coarse dust particles. In summer DSRE is mostly positive over Sahara and the eastern/central Mediterranean due to the combined effect of coarse dust particles (DRE) and the increase of the total cloud fraction (SRE). The DSRE in summer contributes by more than 17% of the total downward longwave radiation in Sahel.

During winter no significant total cloud fraction changes occur (Figure 5.21a). Nevertheless, the total cloud fraction in summer increases by 0.02-0.03 over the desert (Figure 5.21b) due to the radiative effect of dust, which consequently decreases the downward shortwave radiation in the surface and the near surface air temperature (Figure 5.23d). The vertical profile of WS during summer (Figure 5.21c) shows that the increase of total cloud fraction is enhanced in comparison to the historical period (Figure 5.15c). The profile of temperature anomaly along with the specific and relative humidity intensify too. The updraft created in the future decade is somewhat weaker (-0.15hPa per day) in comparison to the historical period (-0.58hPa per day). The main increase of total cloud fraction can mainly be attributed to high clouds which are mainly formed by ice crystals (Figure 5.22).

Figure 5.23 is equivalent to Figure 5.17, with the difference that the displayed temperature changes regard the future period. Figure 5.23e depicts an averaged 0.9°C decrease of daily maximum temperature over Sahel in summer and a smaller broader reduction across all the desert in winter (Figure 5.23b). Analogous pattern are observed in the average temperature (Figure 5.23a,d). Similar to the historical period the minimum temperature is not altered considerably in winter (Figure 5.23c), but it increases by up to 0.6 in the Sahara desert and the Arabian peninsula. Most of the positive or negative differences over the desert are statistically significant. Over Europe the temperature differences are small and statistically insignificant almost everywhere.

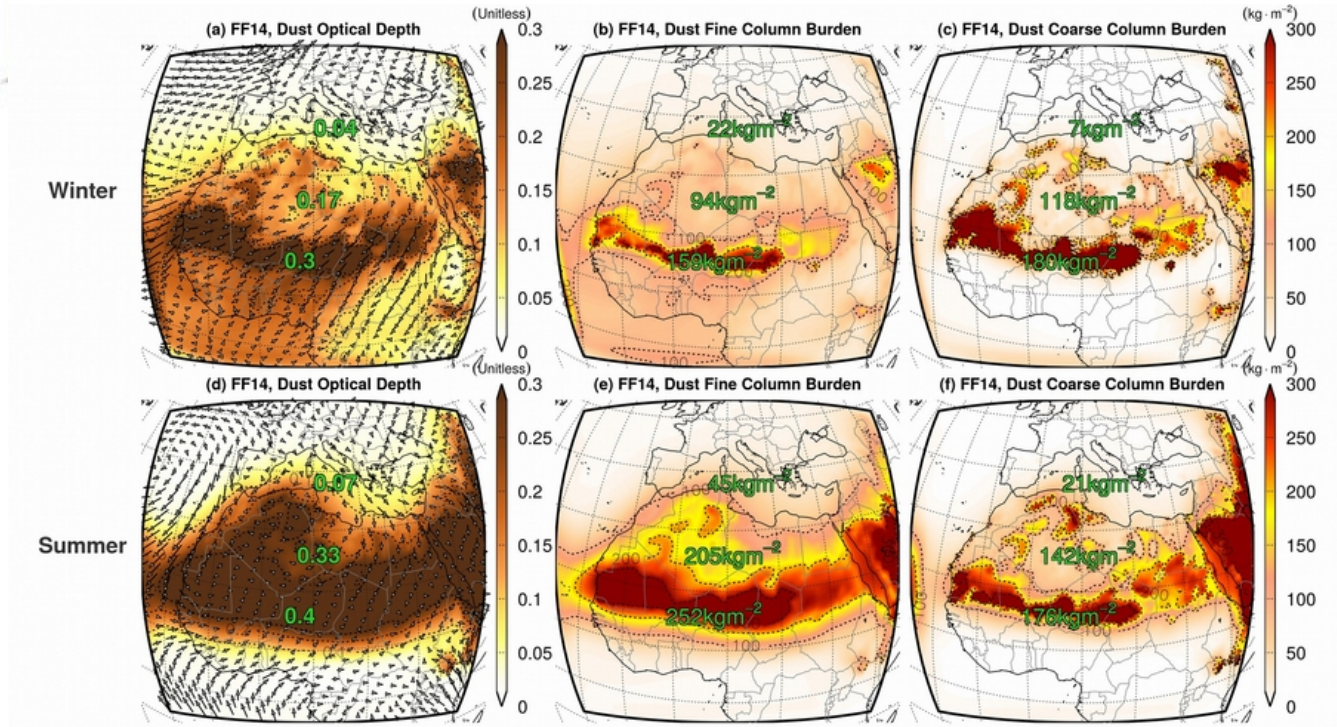

Figure 5.18: Dust optical depth (a, d), dust fine column burden (b, e) and dust coarse column burden (c, f) of FF14 experiment for the period 2089-12-01 to 2099-11-30. The first and second rows of plots depict winter (DJF) and summer (JJA) respectively. The near surface wind field is superimposed in panel a and d.

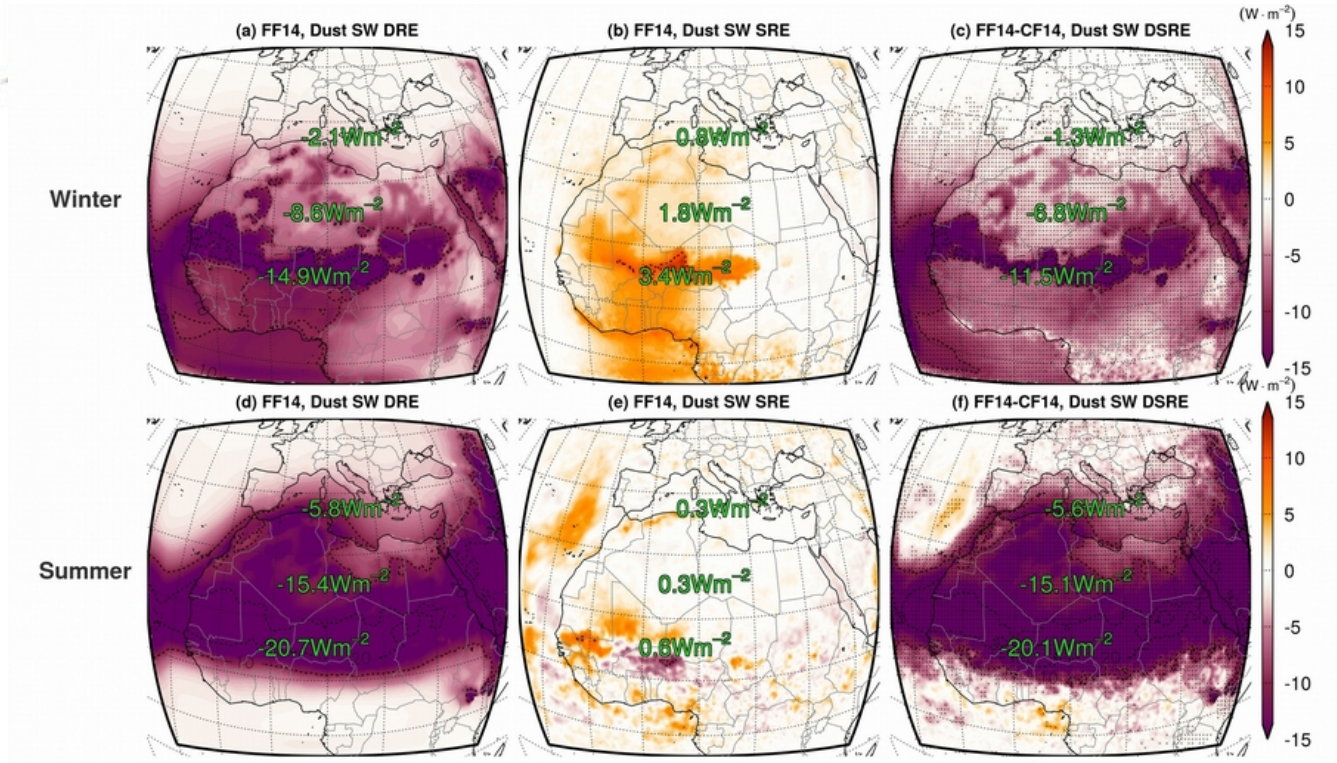

Figure 5.19: Dust shortwave DRE (a, d), SRE (b, e) and DSRE (c, f) of FF14 experiment for the period 2089-12-01 to 2099-11-30. The first and second rows of plots depict winter (DJF) and summer (JJA) respectively.

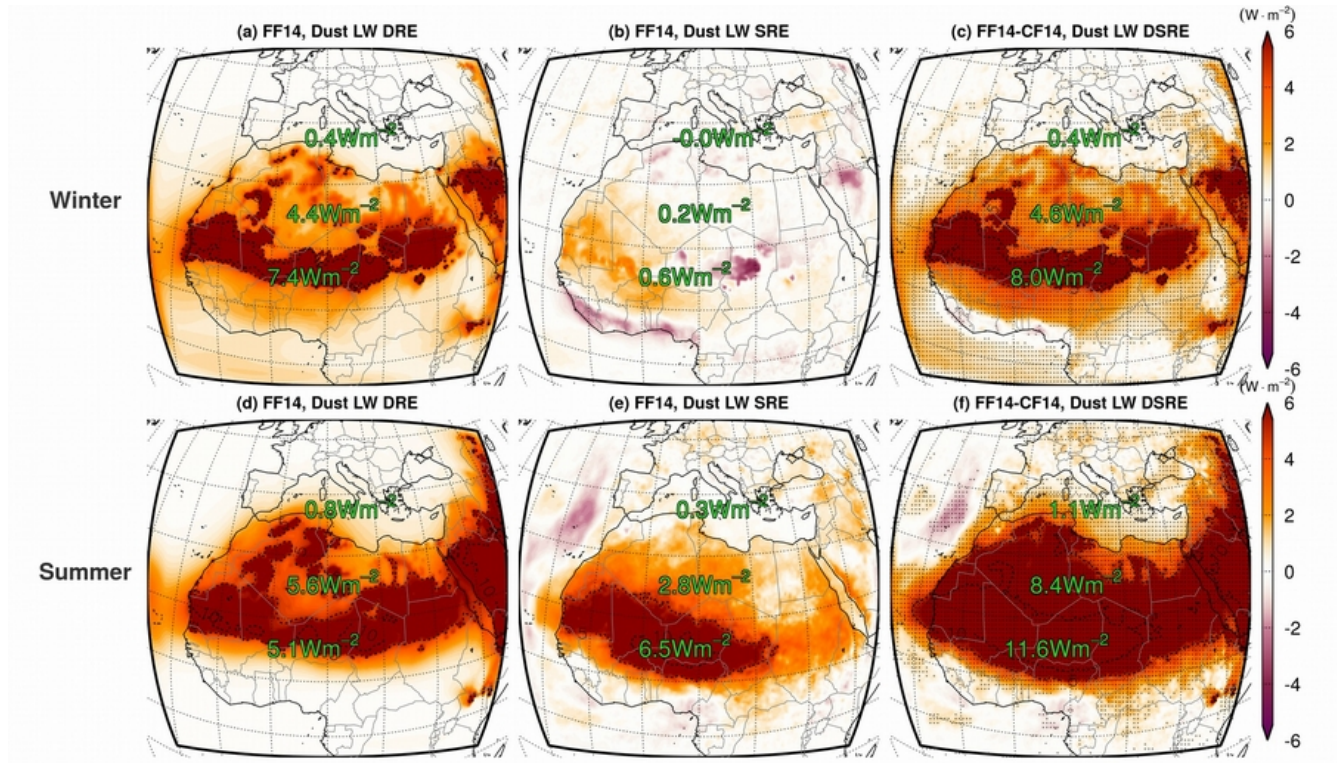

Figure 5.20: Dust longwave DRE (a, d), SRE (b, e) and the DSRE (c, f) FF14 experiment for the period 2089-12-01 to 2099-11-30. The first and second rows of plots depict winter (DJF) and summer (JJA) respectively.

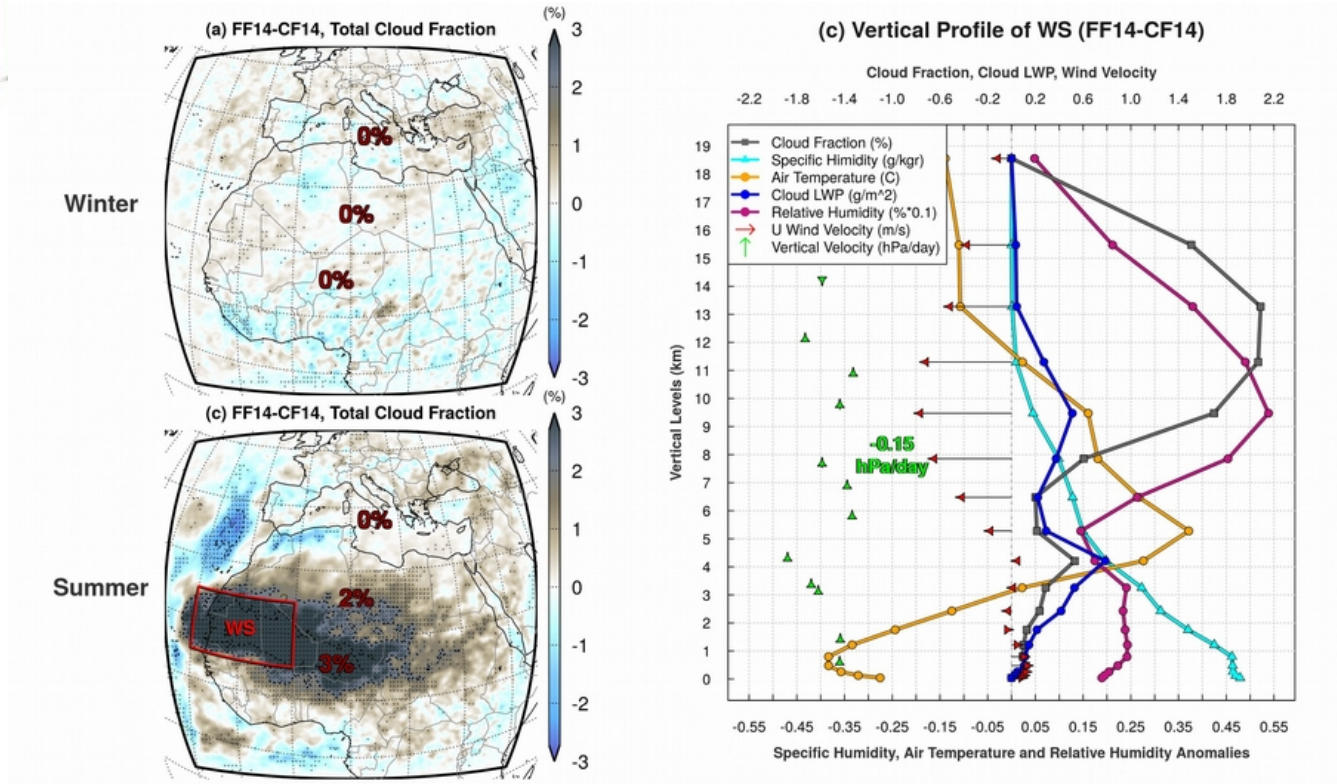

Figure 5.21: Differences of total cloud fraction (a, b) between the FF14 and the CF14 experiments for the period 2089-12-01 to 2099-11-30. In panel c the vertical profile of several meteorological variables during summer is depicted for region WS.

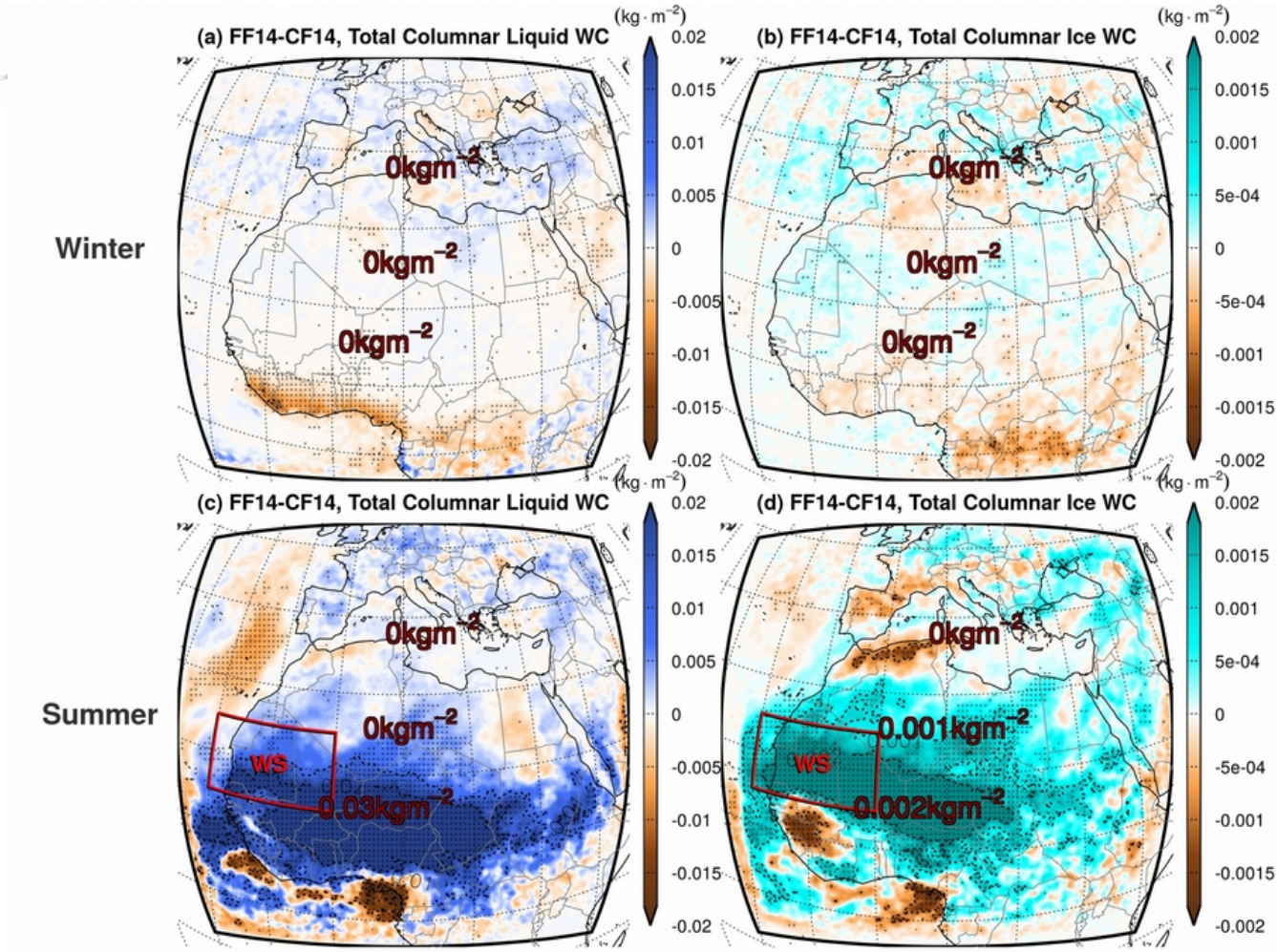

Figure 5.22. Differences of total columnar liquid water content of clouds (a, c) and total columnar ice water content of clouds (b, d) between the FH14 and the CH14 experiments for the period 2089-12-01 to 2099-11-30.

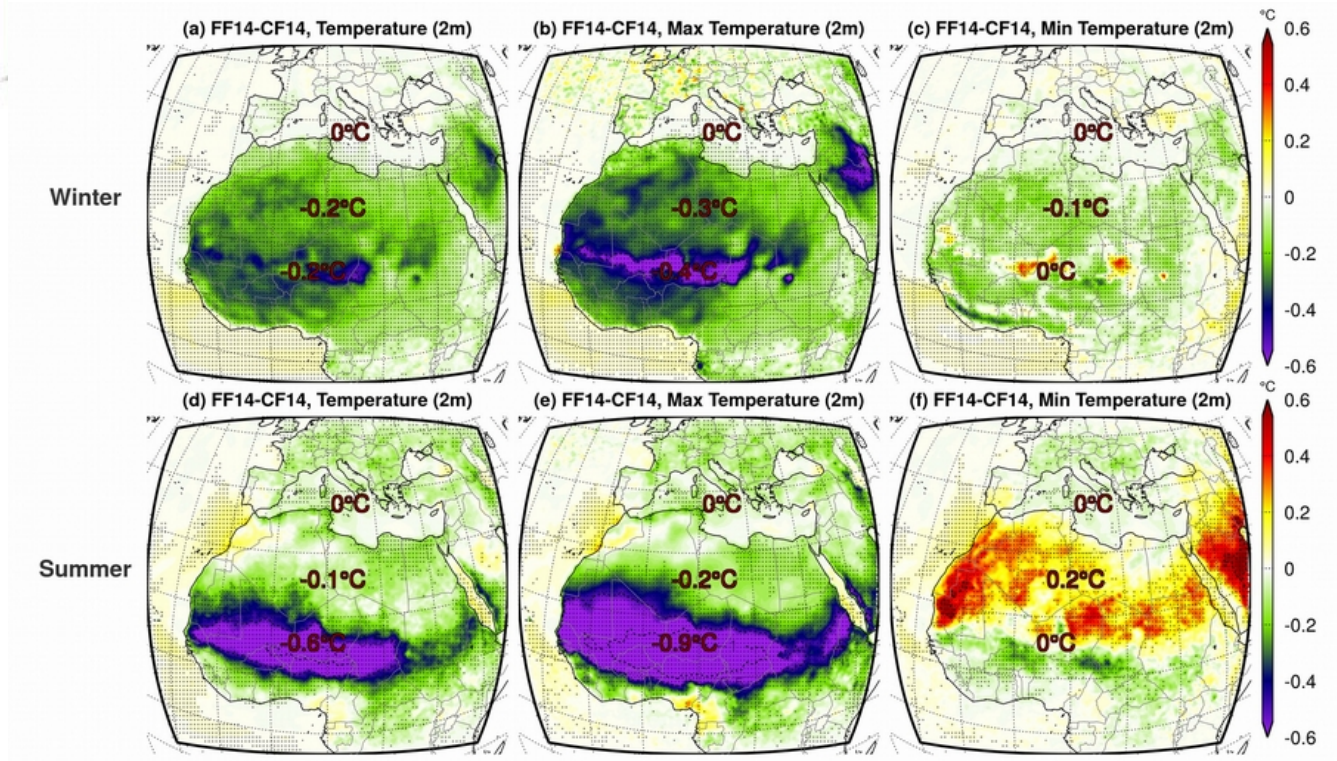

Figure 5.23. Differences of average (a, d), minimum (b, e) and maximum daily 2-meter temperature (c, f) between the FF14 and CF14 experiments for the period 2089-12-01 to 2099-11-30. The first and second rows of plots depict winter (DJF) and summer (JJA) respectively.

5.6 The role of dust radiative effect on future climate projections

In the future decade (2089-2099), the energy budget of the planet in our simulations is driven according to the RCP4.5 scenario. The continuous increase of greenhouse gases radiative effect in the atmosphere (up to 4.5W·m^{-2} by the year 2100 in comparison to the preindustrial era), alters the climate state of future simulations in comparison to the historical simulations (1999-2009). Temperature is expected to steadily increase on average in the future, as is strongly linked to the increase of anthropogenic greenhouse gases radiative forcing (Intergovernmental Panel on Climate Change 2014). Other variables, like total cloud fraction, total precipitation or dust column burden have a more complex behavior, including multiple feedbacks and dependences with local and regional patterns, thus their evolution in the future climate is difficult to be estimated accurately and bares high uncertainty.

The difference between the “future” (FF14 and CF14) and “historical” (FH14 and CH14) simulations in this work, represents the climate change caused by the continuous increase of the greenhouse gases concentration based on the RCP4.5 scenario for the 21st century. In the “feedback” (FF14 and FH14) simulations the dust radiative feedback on climate is taken into account, while in the “control” (CF14 and CH14) simulations include dust as an inactive radiative tracer, participating only in physical processes (advection, transport, sedimentation). We derive the impact of the direct and semi-direct dust radiative effect on future climate projections by comparing the “control” and “feedback” spatial fields.

The 2-meter maximum daily temperature differences between those experiments is presented in Figure 5.24. The average temperature over continental Europe in both winter and summer rises up to 2°C locally, while over the Sahara desert temperature increases locally by more than 2.5°C (Figure 5.24a,d). Over the Mediterranean Basin (land+ocean grid points) the average increase of maximum air temperature is about 1.5°C for both seasons while the highest maximum temperature increase in the future is observed during summer in Sahel (~2.8°C). When including the dust feedback on climate, the robust daily maximum temperature increase (Figure 5.24d) over the Sahel is reduced by 0.3°C (Figure 5.24f) while a further increase by about 0.2°C is observed over eastern Sahara. A similar spatial pattern is detected in the changes of the mean daily and minimum daily temperature (Figure 5.25, Figure 5.26). Overall we can conclude that the feedback effect of dust on future climate changes of mean, maximum and minimum daily temperature is small over the Sahara and the Sahel and insignificant for the Mediterranean Basin.

Dust optical depth changes in the future period can increase or decrease depending on various meteorological parameters that alter emission, transport and deposition of dust particles (wind velocity, transport paths, soil humidity, precipitation etc.). According to the FF14-FH14 differences, dust optical depth is expected to decrease by 25% in Mediterranean, remain fairly the same in the Sahara desert and decrease by 7% in the Sahel during winter (Figure 5.27b). In summer the changes are mostly concentrated over the desert with a 2% increase in the Sahara and an 8% increase in the Sahel (Figure 5.27e). When the feedback effect of dust on climate is included, dust optical depth decreases in all subregions by 0.01 during summer and remains the same during winter.

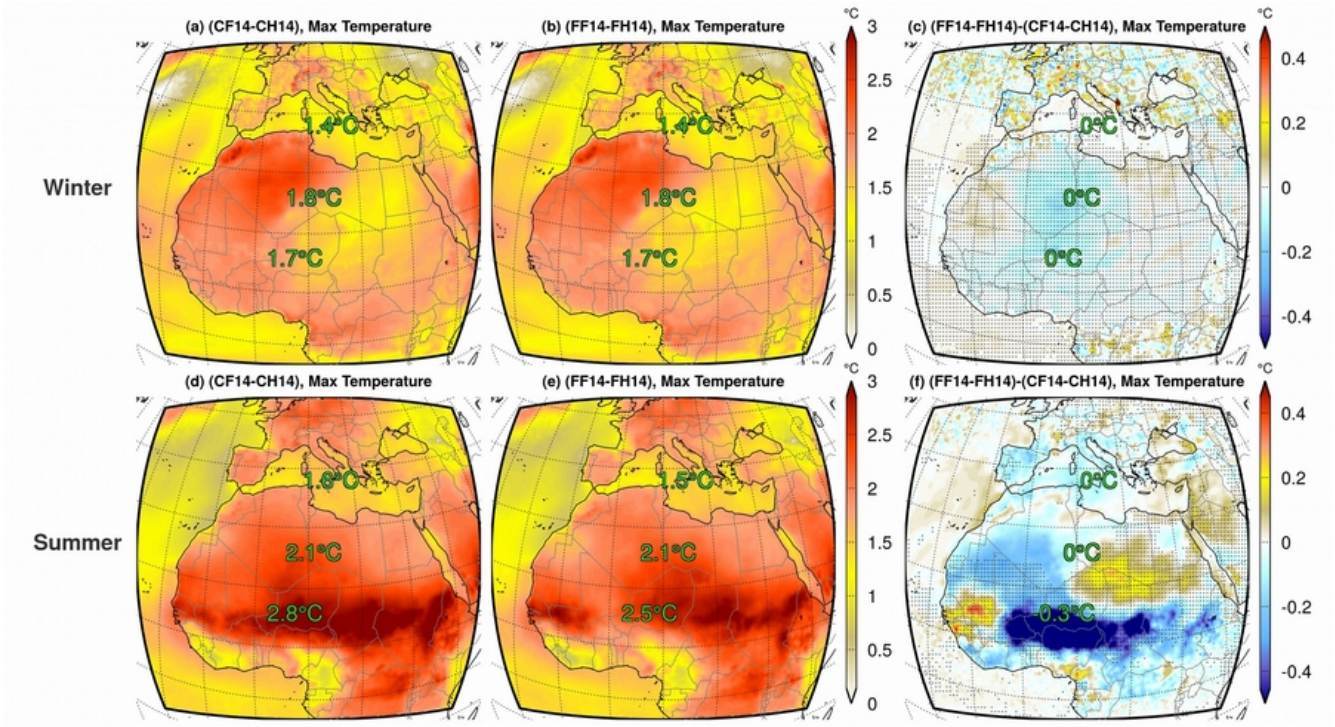

Figure 5.24: Differences of 2-meter daily maximum temperature between the CF14 and CH14 experiments (a, d), the FF14 and FH14 experiment (b, e) and their combined difference (FF14-FH14)-(CF14-CH14) (c, f) for the periods 2000-2009 and 2090-2099.

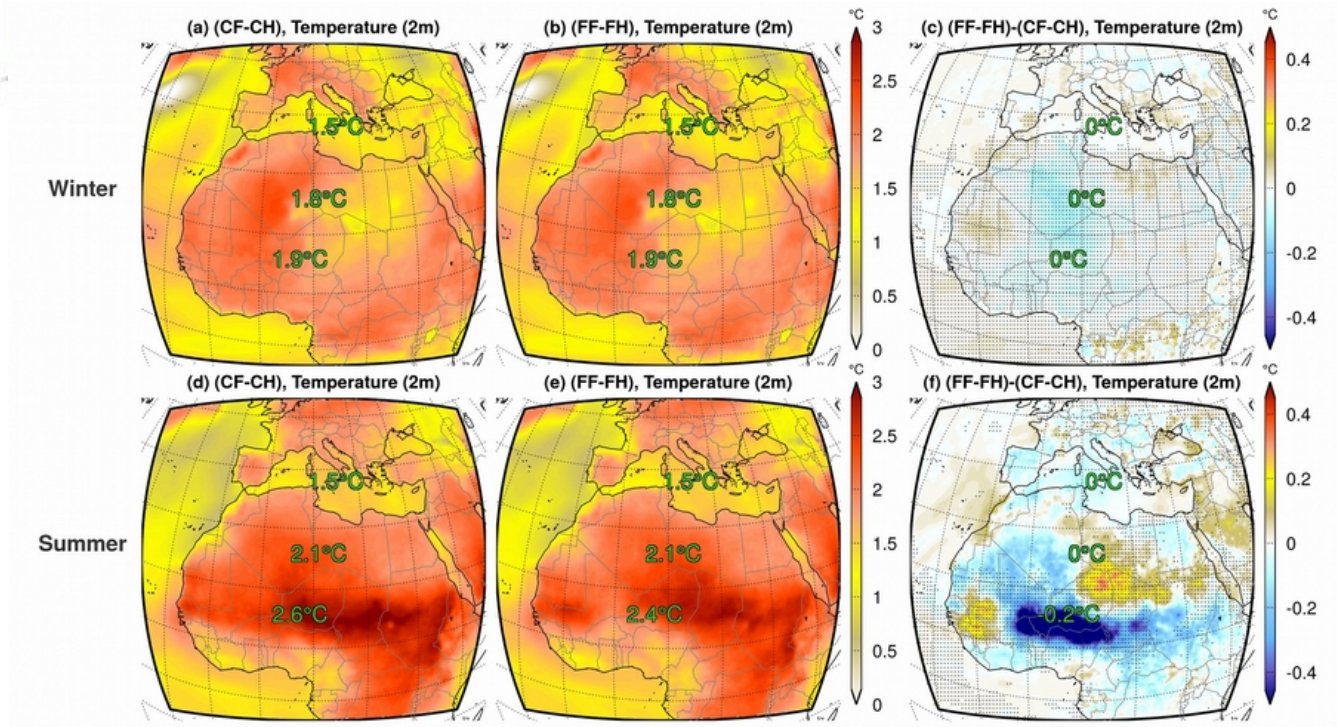

Figure 5.25. Differences of 2-meter daily mean temperature between the ControlFuture14 (CF14) and ControlHindcast14 (CH14) experiments (a, d), the FeedbackFuture (FF14) and FeedbackHindcast (FH14) experiment (b, e) and their combined difference (FF-FH)-(CF-CH) (c, f) for the periods 2000-2009 and 2090-2099. The shaded areas indicate the statistical significance of the difference with 90% confidence using the 2-tailed paired t.test.

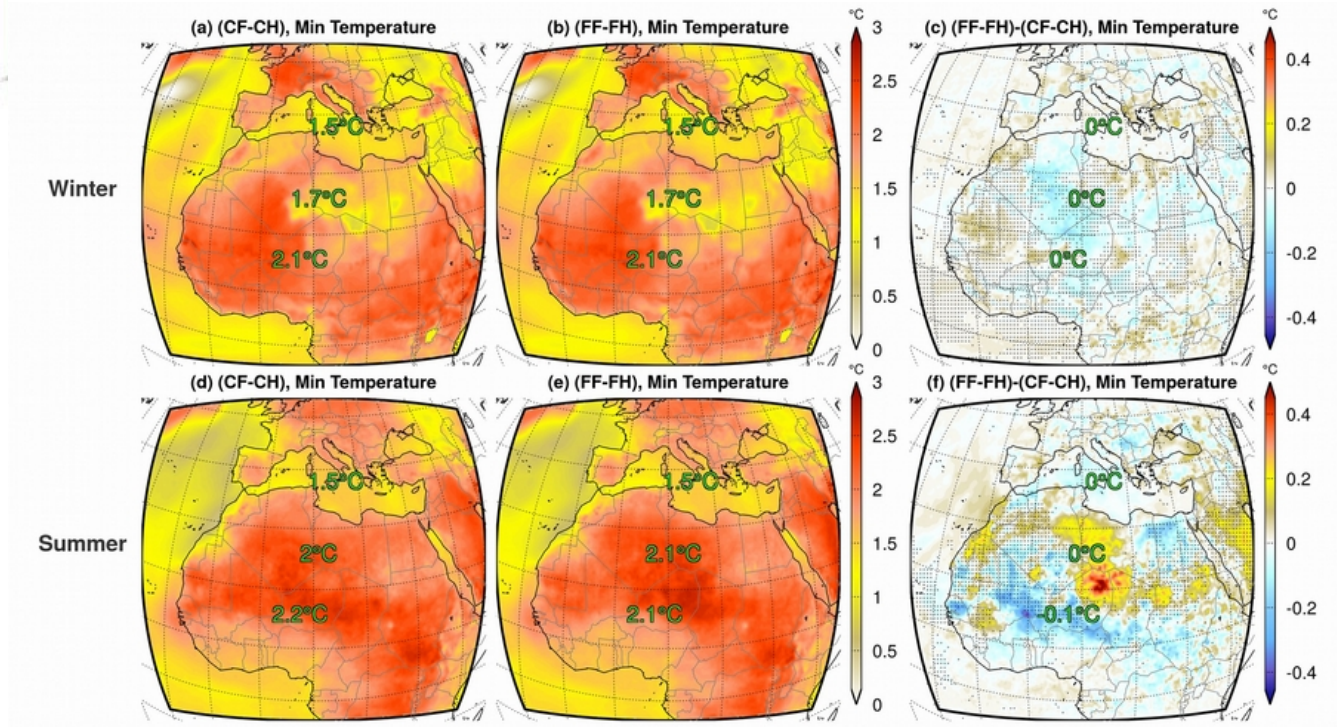

Figure 5.26. Differences of 2-meter daily minimum temperature between the ControlFuture14 (CF14) and ControlHindcast14 (CH14) experiments (a, d), the FeedbackFuture (FF14) and FeedbackHindcast (FH14) experiment (b, e) and their combined difference (FF-FH)-(CF-CH) (c, f) for the periods 2000-2009 and 2090-2099. The shaded areas indicate the statistical significance of the difference with 90% confidence using the 2-tailed paired t.test.

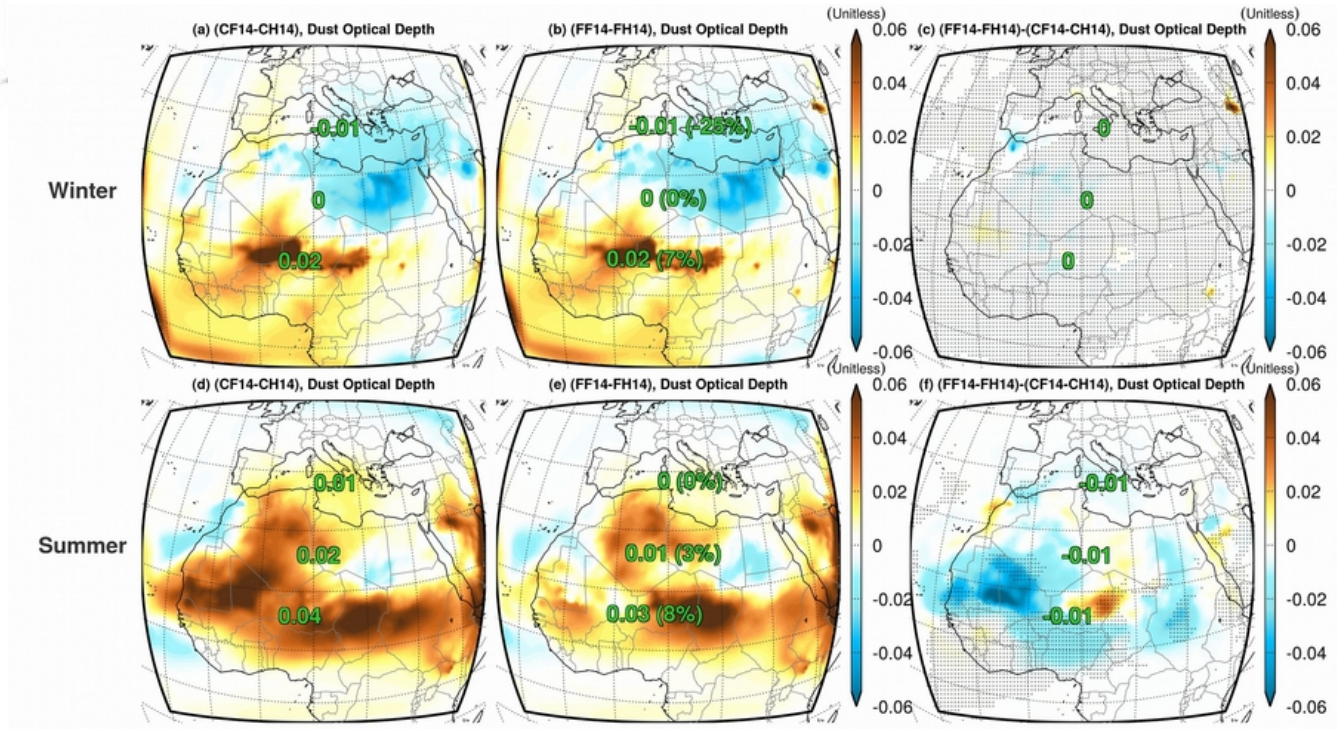

Figure 5.27. Differences of dust optical depth between the CF14 and CH14 experiments (a, d), the FF14 and FH14 experiment (b, e) and their combined difference (FF14-FH14)-(CF14-CH14) (c, f) for the periods 2000-2009 and 2090-2099. The number in the parenthesis (b,e) represents the percentage change of dust optical depth in comparison to the historical period.

5.7 Summary

In this Chapter the direct and semi-direct effect of dust on the historical (1999-2009) and future (2089-2099) climate is explored using the regional climate model RegCM4. The future simulations account for the climate change following the Representative Concentration Pathways 4.5 (RCP4.5). The climate change forcing affects only the state of the troposphere and it is not coupled with the land surface model. A manuscript with the results of this chapter is in preparation for a peer-review journal with the title "Assessing the radiative effects of North African dust in present and future climate".

Before the decade dust simulations for the historical and future period, 3-yearly (2007 to 2009) experiments were conducted to calibrate the DOD in respect to LIVAS dust product. CH14 experiment displayed the most promising results, in which the soil erodibility factor was raised to 1.4 and the default simplistic dust vertical convective transport was deactivated. The simulation still contained a slight underestimation over the Sahel (Bias:-0.03, MNMB=-14%, FGE=28%) and a minor overestimation over the Sahara (Bias=0.02, MNMB=13%, FGE=28%) and the Mediterranean

(Bias=0.01, MNMB=22%, FGE=36%). The experimental set up of this experiment was used to create the decadal Control and Feedback simulations for the historical and future period.

The decade CH14 simulation was evaluated in terms of the mean daily near surface temperature over land as well as for its total-cloud, high-cloud, middle-cloud and low-cloud fraction using the gridded ground-based CRU and the satellite-derived CMSAF observational dataset respectively. Near surface daily temperature is underestimated in both winter and summer over Sahel and Sahara (1.6 to 2.8°C) and slightly overestimated during summer in Mediterranean by about 1°C. Overall a distinct underestimation of all cloud fraction is observed in Mediterranean and generally over the Atlantic ocean. The averaged absolute differences of the three subregion between CM SAF and ControlHistorical14 simulation is lower that 25% in all cases (total, low, middle, hight clouds).

The subtraction of FH14 from the CH14 shows the dust direct and semi-direct radiative effect on climate during the historical period and the changes caused on total cloud fraction as well as mean, maximum and minimum near surface daily temperature. The winter's dust optical depth, fine and coarse column burden is lower in all examined subregions in comparison to summer. Thus, the shortwave and longwave direct effect is more prominent in summer. The combined effect of the direct and semi-direct effect decreases the net downward shortwave radiation on the surface by about 6% to 10% over the Sahara and Sahel and by 2% over the Mediterranean. The LW semi-direct effect is quite important in summer where it contributes about 7% and 12% to the surface downward LW radiation. During the same season there is noteworthy statistical significant increase of clouds that reaches up to 0.03 and stretches across the eastern and western Sahara desert. Also, the near surface mean daily temperature drops by about 0.4°C in Sahel, which is partially due to the increase of total cloud fraction. In contrast, the local decline of temperature in winter is lower and scatter across all the Sahara and Sahel (0.2°C). In summer the combined LW direct and semi-direct RE increases the downward LW radiation by $8 W \cdot m^{-2}$ which increases locally the near surface minimum air temperature by more that 0.5°C over the desert.

The dust direct and semi-direct outcome can be quantified by differentiating the FF14 from the CH14 experiment. In the future period the winter's dust optical depth and burden is again less in comparison to summer. Fine dust particle concentration during summer and winter is slightly increased (+4% to +8%) in comparison to the historical period. Consequently, the shortwave direct effect is enhanced in the future. Cloud fraction over the Sahel and Sahara increases by up to 0.05 during summer which

enhances the semi-direct effect in the LW spectrum. The daily maximum temperature over the Sahel decreases due to the extinction of fine particles and clouds by 0.9°C. Most of the positive or negative temperature differences over the desert are statistically significant with 90% according to the 2-tailed paired t.test. Over Europe the temperature differences are small and rarely statistically significant.

The difference between the FF14-FH14 as well as the CF14-CH14 simulations represents the climate change caused by the continuous emittance of the greenhouse gases concentration based on the RCP4.5 scenario for the 21st century. In the first case the dust radiative feedback on climate is taking into account (FF14-FH14), while in the second it does not (CF14-CH14). By subtracting the spatial field of CF14-CH14 and FF14-FH14 we come up with the impact of the direct and semi-direct dust radiative effect on future climate projection. According to CF14-CH14 results the average temperature over continental Europe, Sahara and Mediterranean (land+ocean grid points) in both winter and summer rises up to 2°C, 2.5°C and 1.5°C respectively. The highest summer daily maximum temperature increase in the future is observed over the Sahel (~2.8°C). When including the dust feedback on climate (FF14-FH14 - CF14-CH14), the robust summer daily maximum temperature increase due to climate change over the Sahel is reduced by 0.3°C and further increases by about 0.2°C over eastern Sahara. Although the dust radiative effect on future climate projection changes are small, they are important if we consider how delicate and sensitive Earth's climate. Minor variation may lead up to a positive/negative climate feedback effect which are not considered here (e.g. landuse changes).

6. Conclusions and Key Remarks

The present PhD dissertation investigates various dust-climate intertwined processes with the use of a regional climate model (RegCM4) that includes a detailed online dust production-transport-deposition scheme. The manuscript consists of three distinct result Chapters (3, 4 and 5), where the output of the model is analyzed in order to examine the role of dust on climate and its importance on terrestrial and marine ecosystems as well as dust horizontal and vertical distribution, dust transport path, dust seasonal characteristics and dust future projection. All the above mentioned dust related aspects include only mineral dust that is produced through physical processes (emitted above arid and semi-arid environments through wind friction), which means that the anthropogenic produced dust is not considered in the simulations. The evaluation of the model is conducted using numerous ground-based gridded observational, satellite-derived and re-analysis datasets such as LIVAS, CRU, ERA-interim, CERES, TRMM and CMSAF. Overall the spatial focus of this work is related to dust produced in the Sahara desert, its episodic transport northward over the Mediterranean and Europe and its long-range intercontinental transport westward towards the Atlantic ocean and the American continent. The temporal range of the simulations refers mainly in the period December 2006 to November 2014 due to the availability of satellite derived dust extinction measurements of LIVAS, while the historical/future climate projection analysis focuses on the first (2000-2009) and the last (2090-2099) decade of the 21st century. A detailed summary presents the results of this work below, followed by the concluding remarks in a point by point concise form.

6.1 Conclusions

6.1.1 Dust size discretization

The optical depth, total column burden and radiative effect of dust above Sahara, Sahel, Mediterranean and Europe was investigated for the period December 2006 to November 2014 using the regional climate model RegCM4. In order to understand the potential model biases and link them with the size-dependent emission and atmospheric processes, dust optical depth and dust extinction of the model were evaluated using the LIVAS dust product. Generally, RegCM4 overestimates dust optical depth over the eastern and western Sahara by 0.083 (Pbias:63.1%) and 0.043 (PBias:26.2%) respectively and in Mediterranean by 0.027 (PBias:54.7%).

The dust optical depth annual cycle of LIVAS correlates with RegCM4 adequately in most regions. In

the western Mediterranean, the model shows an annual cycle with a summer maximum similarly to LIVAS. In eastern Mediterranean it captures the spring maximum observed in LIVAS but additionally it illustrates a secondary maximum in summer. In the western Sahara, the RegCM DOD annual cycle correlates with LIVAS, although there is a constant overestimation during summer and autumn while in the eastern Sahara RegCM shows a broad spring-summer maximum while the observations show a clear spring maximum. In the Sahel, the model captures the observed DOD summer maximum.

According to the annual cycle of the meridional wind component in ERA-interim, the model underestimates the southward wind in eastern Sahara and probably decreases the outflow of dust in the area. Furthermore, the 0.9 percentile value of the averaged wind over the desert is 4.93m·s-1 and 5.92m·s-1 for RegCM and ERA-interim respectively, which indicates that the model potentially overestimates dust emission flux. At the Sahel during April, May and June the total precipitation is overestimated by the model in comparison with the CRU database. Thus, wet deposition is enhanced and emission flux is decreased since the ground has higher moisture. Overall, this process-level analysis suggests that meteorological drivers such as wind and precipitation may explain some model biases with observations.

RegCM overestimates DEX in all subregions in the middle and upper troposphere. That can be either attributed to an overestimation of dust convective transport or to an underestimation of some other deposition process (e.g. sedimentation). In the Western Sahara and Sahel, DEX is underestimated by RegCM below 5km, suggesting that the emissions and deposition processes are not well-balanced in the model. Our one year sensitivity study showed that the PBL mixing scheme can potentially improve the dust vertical distribution in the boundary layer by reducing overactive mixing.

The effect of the two different approaches on the number and the partitioning method of dust size bins was investigated in the model with two experiments: a 4 size bin simulation based on the isolog approach (DUST4) and a 12 size bin simulation based on the isogradient approach (DUST12). The DUST12 experiment increases the deposition lifetime by 3.5 hours and 2 minutes for fine and coarse particles respectively in comparison to DUST4. Consequently, the dust column burden increases by 4% (fine) and 3% (coarse) that boosts DOD by approximately 10% over the desert and the Mediterranean.

The negative surface radiative effect of DUST12 experiment in the shortwave spectrum is regionally enhanced by -0.5W·m-2 while the top of the atmosphere radiative effect is intensified by almost

-1W·m-2 (10%). The negative changes in the surface radiative effect are concentrated in the western part of Africa and extend over the Eastern Atlantic, where the near-constant annual dust plume is located. On the longwave spectrum DUST12 experiment enhances the positive RE at the surface and TOA by 0.1W·m-2 (3% and 7% respectively) in a large portion of the Sahara desert, the northern part of the Arabian Peninsula and the middle east. Although the radiation transfer scheme RRTM, known for its detailed integration on the longwave spectrum, revealed that these longwave RE changes can be also locally negative and therefore smaller when spatially averaged over the Sahara desert.

The DOD, dust column burden and radiative effect differences between the two dust size bin treatments (DUST4 and DUST12) are relatively small. The 12-bin isogradient method represents more realistically the physical processes such as deposition and optical properties of dust, nevertheless the 4-bin isolog method is numerically efficient and can be useful for long term regional climate simulations. We have to note that other typical size distribution could be much more sensitive to the binning partitioning method and number which will generate bigger changes in dust column burden DOD and RE.

6.1.2 Dust Trans-Atlantic transport

Various simulations under different convective schemes were conducted with the regional climate model RegCM4 for an extended domain that includes large parts of Africa, the Atlantic as well as Central and South America. The temporal range of the experiments spans between December 2006 and November 2014. The goal was to simulate the Trans-Atlantic transport of Saharan dust, validate its seasonal characteristics, evaluate the output of the model with satellite-derived measurements and quantify dust deposition flux in the North Atlantic and the phosphorus-limited ecosystem of the tropical Amazon forest.

In comparison to LIVAS climatology, the model overestimates DOD by 23% and displays a moderate overestimation in Eastern Sahara (<0.1), a weak underestimation in western Sahara and Sahel (<0.05), and a slight overestimation along the South Atlantic. The model captures the summer DOD June-July peak in North Atlantic and Caribbean but it underestimates it by ~0.1 and ~0.05 respectively. The South Atlantic winter maximum is not captured and the annual cycle in the same region is flat, almost constant throughout the year. In the Amazon DOD is slightly overestimated in all months. Generally the mean annual cycle of the model exhibit lower standard deviation in comparison to LIVAS dataset over all regions, except Amazon. The dust vertical distribution in the warm (May-September) and the

cold (December-April) period showed that the model tends to perform better at the northern part of the ocean rather than the southern part. The model underestimates dust extinction in the first 5km and overestimates between 5-10km. The processes that are responsible for these biases (cumulus convective transport, sedimentation, horizontal and vertical advection) have been discussed in Chapter 3.

In terms of precipitation the model displays a limited range of FGE (68%-75%) under four combinations of land-ocean convective scheme. The best convective scheme combination in term of the MNMB is Emmanuel over sea and Grell over land (TRANS-EG). There is an underestimation of total cloud fraction over the ocean by 20% when Emanuel scheme is used over sea (TRANS-EG and TRANS-E) and about 10% with Tiedtke scheme over sea (TRANS-T and TRANS-TG). All the experiments show that the dust total column burden over the coast of South America is about 40 mg and FWET almost one over the Atlantic ITCZ path, which indicates the dominating role of wet deposition due to heavy precipitation over that area.

The size discretization experiments (TRANS4 and TRANS12) depicted the averaged DOD over all subregions depicted in Figure 3.1, is higher in the TRANS12 experiment by 0.03 (32%), which is similar to the 0.05 (10%) increase presented in Tsikerdekis et al. (2017) for a smaller domain. The actual differences averaged for each subregion range between 0.01 and 0.05. Subregions close to dust sources display moderate percentage increase 18-19% while as dust moves westward over the Atlantic the percentage increase of TRANS12 experiment accumulates. The averaged, over all regions, TOA and surface RE enhances by $0.7 W \cdot m^{-2}$ (59%) and $-1.3 W \cdot m^{-2}$ (25%) respectively. The weaker longwave RE enhances by $0.1 W \cdot m^{-2}$ in TOA and surface (33% and 29%).

A dust global climate multi-model inter-comparison and the TRANS4 experiment were used to investigate the generic diversities and similarities of dust processes over the North Atlantic. The total and over land DOD of TRANS4 simulation (0.13, 0.20) lies between the range of the 5 global simulations, with the lower being HadGEM2 (0.04, 0.06) and the higher being GOCART (0.17, 0.33). Over the Atlantic all the models display FWET that ranges from 0.4 to 0.8, with RegCM4 value (0.54) laying well between these bounds.

The total, dry and wet dust as well as the analogous phosphorus deposition were calculated using the 8-year TRANS4 simulation and the spatial delimitation of the Amazon, Caribbean and Amazon. According to TRANS4 simulation $4.3 \pm 0.4\ Tg \cdot yr^{-1}$ of dust are deposited in and close to the Amazon

basin which is lower than what was reported in previous researches. This can be can partially explained by the lack of wet deposition due to the underestimation of convective precipitation over the Amazon basin, when Grell scheme is active. Gravitational settling due to the weight of dust particles (dry column), is the major mechanism that deposits dust over the Amazon (2.9 Tg·yr-1, 67.4%) and the Atlantic (137.3 Tg·yr-1, 88.9%), contrary to the Caribbean where rain washout dominates (8.8 Tg·yr-1, 85.4%). Over the Amazon the fine (0.09-2.5μm) and coarse (2.5-63μm) particle contribute the same amount of total dust deposition (2.1 $Tg \cdot yr^{-1}$), while over the Atlantic and the Caribbean coarse particles are the major contributor of dust deposition (132.2 $Tg \cdot yr^{-1}$ and 8.3 $Tg \cdot yr^{-1}$ respectively). Dust deposition can diverse by more than 20% in the Amazon basin and the Caribbean depending on the cumulus convective scheme in use.

6.1.3 Dust-Climate radiative effect

The direct and semi-direct effect of dust on the historical (1999-2009) and future (2089-2099) climate is explored using the regional climate model RegCM4. The future simulations account for the climate change following the Representative Concentration Pathways 4.5 (RCP4.5). The climate change forcing affects only the state of the troposphere and it is not coupled with the land surface model.

Prior to the decadal historical and future simulations, 3-yearly (2007 to 2009) experiments were conducted to calibrate the model's DOD in respect to LIVAS dust product. CH14 experiment displayed the most promising results, in which the soil erodibility factor was raised to 1.4 and the default simplistic dust vertical convective transport was deactivated. The simulation still contained a slight underestimation over the Sahel (Bias:-0.03, MNMB=-14%, FGE=28%) and a minor overestimation over the Sahara (Bias=0.02, MNMB=13%, FGE=28%) and the Mediterranean (Bias=0.01, MNMB=22%, FGE=36%). The experimental set up of this experiment was used to create the decadal Control and Feedback simulations for the historical and future period.

The decade ControlHistorical14 (CH14) simulation was evaluated in terms of the mean daily near surface temperature over land as well as for its total-cloud, high-cloud, middle-cloud and low-cloud fraction using the gridded ground-based CRU and the satellite-derived CMSAF observational dataset respectively. Near surface daily temperature is underestimated in both winter and summer over Sahel and Sahara (1.6 to 2.8°C) and slightly overestimated during summer in Mediterranean by about 1°C. Overall a distinct underestimation of all cloud fraction is observed in Mediterranean and generally over the Atlantic ocean. The averaged absolute differences of the three subregion between CMSAF and

CH14 simulation is lower that 25% in all cases (total, low, middle, hight clouds).

The subtraction of FeedbackHistorical14 (FH14) from the CH14 shows the dust direct and semi-direct effect on climate during the historical period and the changes on total cloud fraction as well as mean, maximum and minimum near surface daily temperature. The winter's dust optical depth, fine and coarse column burden is lower in all examined subregions in comparison to summer. Thus, the shortwave and longwave direct effect is more prominent in summer. The combined effect of the direct and semi-direct effect decreases the net downward shortwave radiation on the surface by about 6% to 10% over the Sahara and Sahel and by 2% over the Mediterranean. The LW semi-direct effect is quite important in summer where it contributes about 7% and 12% to the surface downward LW radiation. During the same season there is noteworthy statistical significant increase of clouds that reaches up to 0.03 and stretches across the eastern and western Sahara desert. Also, the near surface mean daily temperature drops by about 0.4°C in Sahel, which is partially due to the increase of total cloud fraction. In contrast, the local decline of temperature in winter is lower and scattered across all the Sahara and Sahel (0.2°C). In summer the combined LW direct and semi-direct RE increases the downward LW radiation by $8 W \cdot m^{-2}$ which increases locally the near surface minimum air temperature by more that 0.5°C over the desert.

The dust direct and semi-direct outcome for the future period can be quantified by differentiating the FeedbackFuture14 (FF14) from the ControlFuture14 (CF14) experiment. At the end of the 21st century the winter's dust optical depth and burden is again less in comparison to summer. Fine dust particle concentration during summer and winter is slightly increased (+4% to +8%) in comparison to the historical period. Consequently, the shortwave direct effect is enhanced in the future. Cloud fraction over the Sahel and Sahara increases by up to 0.05 during summer which enhances the semi-direct effect in the LW spectrum. The daily maximum temperature over the Sahel decreases due to the extinction of fine particles and clouds by 0.9°C. Most of the positive or negative temperature differences over the desert are statistically significant with 90% according to the 2-tailed paired t.test. Over Europe the temperature differences are small and rarely statistically significant.

The difference between the FF14-FH14 as well as the CF14-CH14 simulations represents the climate change caused by the continuous emittance of the greenhouse gases concentration based on the RCP4.5 scenario for the 21st century. In the first case the dust radiative feedback on climate is taking into account (FF14-FH14), while in the second it does not (CF14-CH14). By subtracting the spatial field of

CF14-CH14 and FF14-FH14 we come up with the impact of the direct and semi-direct dust radiative effect on future climate projection. According to CF14-CH14 results the average temperature over continental Europe, Sahara and Mediterranean (land+ocean grid points) in both winter and summer rises up to 2°C, 2.5°C and 1.5°C respectively. The highest summer daily maximum temperature increase in the future is observed over the Sahel (~2.8°C). When including the dust feedback on climate (FF14-FH14 - CF14-CH14), the summer daily maximum temperature increase due to climate change over the Sahel is reduced by 0.3°C and further increased by about 0.2°C over eastern Sahara. Although the dust radiative effect on future climate projection changes are small, they are important if we consider how delicate and sensitive Earth's climate is. Minor variation may lead up to a positive/negative climate feedback effect which are not considered here (e.g. landuse changes).

6.2 Key Remarks

- The evaluation of RegCM4 with the newly developed satellite dust product LIVAS shows that the model simulates adequately the spatial distribution and seasonal characteristics of dust over the Sahara, the Sahel and the Mediterranean.
- Dust optical depth is overestimated over eastern Sahara and underestimated over the Sahel and close to the gulf of Guinea by the model. Both of these biases can be partially explained due to model discrepancies in the low Troposphere wind velocity and precipitation.
- The model captures the constant reduction of dust extinction with height. But it overestimates dust extinction above 5km due to the excess vertical transport of dust within convective clouds.
- The newly developed 12bin-isogradient method (DUST12) increases the deposition lifetime of fine and coarse particles by 3.5 hours and 2 minutes respectively in comparison to the default 4bin-isolog method (DUST4). Consequently, fine (+3%) and coarse (+4%) dust column burden as well as dust optical depth (+10%), shortwave (10%) and longwave (+7%) radiative effect at the top of the atmosphere increase.
- The intercontinental Trans-Atlantic transport and the estimation of dust deposition rates was simulated for the first time using a regional climate model (RegCM4). Previous estimates of deposition rates used global climate models or satellite approximations.
- The model slightly underestimates and overestimates dust optical depth along the North and

South Atlantic ocean (as defined on this study) respectively.

- The Grell convective scheme is quite dry over the Amazon tropical forest. Tiedtke is drier in comparison to Emanuel over south Atlantic. The best combination in terms of the MNMB is Emanuel over sea and Grell over land (1%). Although Emanuel over sea and land shows the lowest FGE (68%).

- According to the model 4.3±0.4 $Tg \cdot yr^{-1}$ of dust are deposited in and close to the Amazon basin, 154.5±10.7 $Tg \cdot yr^{-1}$ over the Atlantic and 10.3±0.6 $Tg \cdot yr^{-1}$ to the Caribbean. Dry deposition is the major mechanism that deposits dust over the Amazon (2.9 Tg·yr-1, 67.4%) and the Atlantic (137.3 Tg·yr-1, 88.9%), contrary to the Caribbean where rain washout dominates (8.8 Tg·yr-1, 85.4%). Dust deposition can diverse by more than 20% in the Amazon basin and the Caribbean depending on the cumulus convective scheme in use.

- The direct and semi-direct effect of dust was estimated using the coupled chemistry-climate regional model RegCM4 for the first (historical) and the last (future) decade of the 21st century. Dust radiative effect decreases the net downward shortwave radiation on the surface by 6% to 10% over the Sahara and Sahel and by 2% over the Mediterranean. The LW semi-direct effect on the other hand contributes about 7% and 12% to the surface downward LW radiation in summer. During the same season the radiative presence of dust creates (semi-directly) a noteworthy statistical significant increase of clouds that reaches up to 0.03 and stretches across the eastern and western Sahara desert, which drops the near surface mean daily temperature by about 0.4°C.

- The future climate change increases dust particle concentration during summer and winter (+4% to +8%) over the desert which consequently enhances the radiative effect of dust on clouds (+2%) and near surface temperature (±0.2°C).

- Climate change (driven by the RCP4.5 scenario) shows that the average temperature over continental Europe, Sahara and Mediterranean (land+ocean grid points) in both winter and summer rises up to 2°C, 2.5°C and 1.5°C respectively. The highest summer daily maximum temperature increase in the future is observed over the Sahel (~2.8°C).

- Dust feedback effect on future climate projection is limited during summer and over the desert.

For example it can restrain the increase of near surface maximum daily temperature due to climate change over the Sahel by -0.3°C or enhance it over the Eastern Sahara by +0.2°C. Nevertheless, it can probably become important considering other climate change feedback mechanisms (e.g. landuse changes).

Abstract

The present PhD dissertation investigates various dust-climate intertwined processes with the use of a regional climate model (RegCM4) that includes a detailed online dust production-transport-deposition scheme. The evaluation of the model is conducted using numerous ground-based gridded observational, satellite-derived and re-analysis datasets such as LIVAS, CRU, ERA-interim, CERES, TRMM and CMSAF. In the first one an encyclopedic description of dust related processes (emission, transport, deposition) is given followed by an analytical description of the online dust scheme of RegCM4. The second chapter describes the observational and modeling datasets used. In the third chapter the sensitivity of dust bin size discretization in the regional climate model RegCM4 for the period 2007-2014 over the Sahara and the Mediterranean is investigated. Two discretization methods of the dust size distribution are applied, keeping the total mass constant: 1) the default RegCM4 4-bin approach, where the size range of each bin is calculated using an equal, logarithmic separation of the total size range of dust, using the diameter of dust particles and 2) a newly implemented 12-bin approach with each bin defined according to an isogradient method where the size ranges are dependent on the dry deposition velocity of dust particles. The new dust binning approach increases the dust column burden by 4% and 3% for fine and coarse particles respectively, which increases DOD by 10% over the desert and the Mediterranean. In the fourth chapter the westward Trans-Atlantic transport of dust from the Sahara towards the South and Central America is simulated using the regional climate model RegCM4 for the period December 2006 to November 2014. According to RegCM4 the total dust deposition for the examined 8 year period is 4.3±0.4 $Tg \cdot yr^{-1}$, 154.5±10.7 $Tg \cdot yr^{-1}$ and 10.3±0.6 $Tg \cdot yr^{-1}$ for the Amazon basin, the Atlantic ocean and the Caribbean respectively. Dry deposition is the dominant deposition process in the Atlantic accounting for 88.9% of the total deposition in contrast to Caribbean where wet deposition accounts for 85.4%. In the Amazon basin dry deposition takes up to 67.4% of total deposition. In the fifth chapter the radiative direct and semi-direct effect of dust is explored using the regional climate model RegCM4 over the Mediterranean, Sahara and Sahel. The simulations cover a historical decade which spans from 1999-01-01 to 2009-11-30 and a future decade that ranges from 2089-01-01 to 2099-11-30. The future atmospheric climate changes are driven by the Representative Concentration Pathway 4.5 (RCP4.5). The results for the historical period show that the direct RE of dust dominates in comparison to the semi-direct RE in both winter and summer, although during summer the semi-direct effect in the longwave spectrum accounts for almost 50% of total radiative

effect over some parts of the desert. In the future period the dust concentration are spatially similar to the historical period but enhanced over the desert (+8%). When dust is radiatively active in a future climate simulation it can decrease the summer daily maximum temperature by 0.3°C over Sahel and increase it locally in eastern Sahara and western Sahel up to 0.2°C.

Περίληψη

Στην παρούσα διδακτορική διατριβή χρησιμοποιήθηκε το κλιματικό μοντέλο περιοχής RegCM4, για τη μελέτη των διάφορων διεργασιών που αφορούν την ατμοσφαιρική σκόνη και το κλίμα. Το RegCM4 περιλαμβάνει ένα λεπτομερές σχήμα εκπομπής, μεταφοράς και εναπόθεσης της σκόνης. Η αξιολόγηση του μοντέλου πραγματοποιείται με τη χρήση διάφορων δεδομένων παρατήρησης από επίγειους σταθμούς, δορυφορικές μετρήσεις και δεδομένα μοντέλων επ-ανάλυσης (LIVAS, CRU, ERA-interim, CERES, TRMM και CMSAF). Στο πρώτο κεφάλαιο αναλύονται περιγραφικά οι διεργασίες σκόνης που λαμβάνουν μέρος στην ατμόσφαιρα και μια αναλυτική περιγραφή του σχήματος σκόνης που χρησιμοποιεί το RegCM4. Στο δεύτερο κεφάλαιο γίνεται παρουσίαση του μοντέλου RegCM4 και δεδομένων παρατηρήσεων και δορυφορικών μετρήσεων. Το τρίτο κεφάλαιο εξετάζει την ευαισθησία του μοντέλου στον αριθμό των ομάδων μεγέθους σκόνης (bin) που χρησιμοποιεί. Η περίοδος αναφοράς είναι μεταξύ 2007 και 2014 και το χωρικό πεδίο ορισμού περιλαμβάνει την Σαχάρα την Μεσόγειο και ένα τμήμα της Ευρώπης. Δύο μέθοδοι διαχωρισμού των ομάδων μεγέθους σκόνης. Η πρώτη προκαθορισμένη μέθοδος του μοντέλου δημιουργεί 4 ομάδες μεγέθους σκόνης, όπου η έκταση κάθε ομάδες ορίζεται ισο-λογαριθμικά χρησιμοποιώντας την διάμετρο των σωματιδίων σκόνης (4bin-isolog). Στην δεύτερη περίπτωση οι ομάδες σκόνης είναι 12 και η έκταση κάθε ομάδας ορίζεται σύμφωνα με την ταχύτητα ξηρής εναπόθεσης των σωματιδίων σκόνης (12bin-isogradient). Η καινούργια μέθοδος διαχωρισμού των ομάδων σκόνης αυξάνει τις συγκεντρώσεις των μεγάλων και μικρών σωματιδίων σκόνης κατά 4% και 3% αντίστοιχα. Επίσης, αυξάνει το οπτικό βάθος της σκόνης κατά 10% πάνω από την Μεσόγειο και την Σαχάρα. Το τέταρτο κεφάλαιο μελετά την μεταφορά σκόνης από την Σαχάρα προς τον Ατλαντικό και την ήπειρο της Αμερικής χρησιμοποιώντας το κλιματικό μοντέλο περιοχής RegCM4 για την περίοδο Δεκέμβριος 2006 με Νοέμβριο 2014. Το μέσο οπτικό βάθος του μοντέλου προσομοιώνεται ικανοποιητικά, με μια μικρή (0.05) υποεκτίμηση/υπερεκτίμηση για το Νότιο και Βόρειο τμήμα του Ατλαντικού ωκεανού αντίστοιχα. Σύμφωνα με το RegCM4 η συνολική εναπόθεση σκόνης για την 8ετή περίοδο εξέτασης είναι 4.3±0.4 $Tg \cdot yr^{-1}$, 154.5±10.7 $Tg \cdot yr^{-1}$ και 10.3±0.6 $Tg \cdot yr^{-1}$ για την λεκάνη του Αμαζονίου, τον Ατλαντικό ωκεανό και την Καραϊβική αντίστοιχα. Η ξηρή εναπόθεση παίζει πρωταγωνιστικό ρόλο στον Ατλαντικό (88.9%) και την Καραϊβική (85.4%), ενώ η υγρή εναπόθεση είναι αρκετά σημαντική στην λεκάνη του Αμαζονίου (67.4%). Η τρίτη ενότητα αποτελεσμάτων εξετάζει την άμεση και ήμι-άμεση επιρροή της σκόνης στην ακτινοβολία πάνω από την Μεσόγειο, την Σαχάρα και την Σαχέλ για την πρώτη (1999-01-01 εώς 2009-

11-30) και την τελευταία (2089-01-01 το 2099-11-30) δεκαετία του 21ου αιώνα. Η μελλοντική κλιματική αλλαγή προσομοιώνεται σύμφωνα με το σενάριο εκπομπών θερμοκηπικών αερίων RCP 4.5. Η άμεση επίδραση της σκόνης στην ακτινοβολία είναι ισχυρότερη από την ήμι-άμεση την ψυχρή και την θερμή περίοδο του έτους, αν και κατά την διάρκεια του καλοκαιριού η ήμι-άμεση επιρροή της σκόνης στην μεγάλου μήκους ακτινοβολίας φτάνει το 50% πάνω ορισμένες περιοχές της ερήμου. Στην μελλοντική δεκαετία οι συγκεντρώσεις της σκόνης και η επίδραση της στην ακτινοβολία, την θερμοκρασία και τα νέφη ενισχύεται. Επίσης, η επίδραση της σκόνης στις μελλοντικές προβολές μειώνει την άνοδο της θερμοκρασία λόγω κλιματικής αλλαγής κατά 0.3°C πάνω από την Σαχέλ και την ενισχύει κατά 0.2°C πάνω από την ευρύτερη περιοχή της Σαχάρας.

Acknowledgments

Results presented in this PhD dissertation have been produced using the AUTH Scientific Computing Centre Infrastructure and technical support. This work was also supported by computational time granted from the Greek Research & Technology Network (GRNET) in the National High Performance Computing facility ARIS under the projects “Direct Climate Feedback of Dust (DCFD)” and “Dataset for dUst effect on Climate, Health, Economy and Society Studies (DUCHESS)”. Also, the support from the high-performance computing cluster Flux in the University of Michigan was important since some simulations of this work were conducted there. I would like to acknowledge the use of data from the LIVAS (http://lidar.space.noa.gr:8080/livas), CM SAF (http://www.cmsaf.eu), CERES (https://ceres.larc.nasa.gov) TRMM (https://pmm.nasa.gov/data-access/downloads/trmm), CRU (https://crudata.uea.ac.uk/cru/data/hrg) and ERA-interim (http://apps.ecmwf.int/datasets) databases. I want to thank the support for international research staff exchange through the REQUA (Regional climate-air quality 787 interactions) project (FP7-PEOPLE-2013-IRSES – Marie Curie Action, PIRSES-GA-2013-612671) and ACTRIS-2 project (grant agreement no. 654109, funded through the European Union’s Horizon 2020 programme).

References

Ackerman a. S (2000) Reduction of Tropical Cloudiness by Soot. Science (80-) 288:1042–1047. doi: 10.1126/science.288.5468.1042

Albrecht BA (1989) Aerosols, Cloud Microphysics, and Fractional Cloudiness. Science (80-) 245:1227–1230. doi: 10.1126/science.245.4923.1227

Alexandri G, Georgoulias a. K, Zanis P, et al. (2015) On the ability of RegCM4 regional climate model to simulate surface solar radiation patterns over Europe: an assessment using satellite-based observations. Atmos Chem Phys 15:13195–13216. doi: 10.5194/acp-15-13195-2015

Alexandri G, Georgoulias AK, Meleti C, et al. (2017) A high resolution satellite view of surface solar radiation over the climatically sensitive region of Eastern Mediterranean. Atmos Res 188:107–121. doi: 10.1016/j.atmosres.2016.12.015

Alfaro SC, Gaudichet A, Gomes L, Maillé M (1998) Mineral aerosol production by wind erosion: Aerosol particle sizes and binding energies. Geophys Res Lett 25:991–994. doi: 10.1029/98GL00502

Alfaro SC, Gaudichet A, Gomes L, Maillé M (1997) Modeling the size distribution of a soil aerosol produced by sandblasting. J Geophys Res 102:11239. doi: 10.1029/97JD00403

Alfaro SC, Gomes L (2001) Modeling mineral aerosol production by wind erosion: Emission intensities and aerosol size distributions in source areas. J Geophys Res 106:18075. doi: 10.1029/2000JD900339

Ali A, Lebel T (2009) The Sahelian standardized rainfall index revisited. Int J Climatol 29:1705–1714. doi: 10.1002/joc.1832

Alpert P, Kishcha P, Shtivelman a, et al. (2004a) Vertical distribution of Saharan dust based on 2.5-year model predictions. Atmos Res 70:109–130. doi: 10.1016/j.atmosres.2003.11.001

Alpert P, Osetinsky I, Ziv B, Shafir H (2004b) Semi-objective classification for daily synoptic systems: application to the eastern Mediterranean climate change. Int J Climatol 24:1001–1011. doi: 10.1002/joc.1036

Amiridis V, Marinou E, Tsekeri a., et al. (2015) LIVAS: a 3-D multi-wavelength aerosol/cloud database based on CALIPSO and EARLINET. Atmos Chem Phys 15:7127–7153. doi: 10.5194/acp-15-7127-2015

Amiridis V, Wandinger U, Marinou E, et al. (2013) Optimizing CALIPSO Saharan dust retrievals. Atmos Chem Phys 13:12089–12106. doi: 10.5194/acp-13-12089-2013

Anderson RS, Haff PK (1991) Aeolian Grain Transport 1. doi: 10.1007/978-3-7091-6706-9

Anderson RS, Haff PK (1988) Simulation of eolian saltation. Science (80-) 241:820–823.

Aoki T, Tanaka TY, Uchiyama A, et al. (2005) Sensitivity Experiments of Direct Radiative Forcing Caused by Mineral Dust Simulated with a Chemical Transport Model. J Meteorol Soc Japan 83A:315–331.

Baars H, Kanitz T, Engelmann R, et al. (2016) An overview of the first decade of PollyNET: an emerging network of automated Raman-polarization lidars for continuous aerosol profiling. Atmos Chem Phys 16:5111–5137. doi: 10.5194/acp-16-5111-2016

Bagnold RA (1941) The Physics of Blown Sand and Desert Dunes. Methuen, New York

Baker AR, French M, Linge KL (2006) Trends in aerosol nutrient solubility along a west-east transect of the Saharan dust plume. Geophys Res Lett 33:10–13. doi: 10.1029/2005GL024764

Baker AR, Jickells TD (2006) Mineral particle size as a control on aerosol iron solubility. Geophys Res Lett 33:1–4. doi: 10.1029/2006GL026557

Bangert M, Nenes a., Vogel B, et al. (2012) Saharan dust event impacts on cloud formation and radiation over Western Europe. Atmos Chem Phys 12:4045–4063. doi: 10.5194/acp-12-4045-2012

Basart S, Pérez C, Nickovic S, et al. (2012) Development and evaluation of the BSC-DREAM8b dust regional model over Northern Africa, the Mediterranean and the Middle East. Tellus B Chem Phys Meteorol 64:18539. doi: 10.3402/tellusb.v64i0.18539

Benas N, Finkensieper S, Stengel M, et al. (2017) The MSG-SEVIRI-based cloud property data record CLAAS-2. Earth Syst Sci Data 9:415–434. doi: 10.5194/essd-9-415-2017

Bohren CF, Huffman DR (1998) Absorption and Scattering of Light by Small Particles. doi: 10.1002/9783527618156

Boucher O, Randall D, Artaxo P, et al. (2013) The Physical Science Basis. Contribution of Working Group I to the Fifth Assessment Report of the Intergovernmental Panel on Climate Change [Stocker, T.F., D. Qin, G.-K. Plattner, M. Tignor, S.K. Allen, J. Boschung, A. Nauels, Y. Xia, V. Bex and P.M. Midg.

Bretherton CS, McCaa JR, Grenier H (2004) A New Parameterization for Shallow Cumulus Convection and Its Application to Marine Subtropical Cloud-Topped Boundary Layers. Part I: Description and 1D Results. Mon Weather Rev 132:864–882. doi: 10.1175/1520-0493(2004)132<0864:ANPFSC>2.0.CO;2

Brioude J, Cooper OR, Feingold G, et al. (2009) Effect of biomass burning on marine stratocumulus clouds off the California coast. Atmos Chem Phys Discuss 9:14529–14570. doi: 10.5194/acpd-9-14529-2009

Bristow CS, Hudson-Edwards K a., Chappell A (2010) Fertilizing the Amazon and equatorial Atlantic with West African dust. Geophys Res Lett 37:L14807. doi: 10.1029/2010GL043486

Cakmur R V., Miller RL, Perlwitz J, et al. (2006) Constraining the magnitude of the global dust cycle by minimizing the difference between a model and observations. J Geophys Res 111:D06207. doi: 10.1029/2005JD005791

Carlson TN, Prospero JM (1972) The Large-Scale Movement of Saharan Air Outbreaks over the Northern Equatorial Atlantic. J Appl Meteorol 11:283–297. doi: 10.1175/1520-0450(1972)011<0283:TLSMOS>2.0.CO;2

Chadwick OA, Derry LA, Vitousek PM, et al. (1999) Changing sources of nutrients during four million years of ecosystem development. Nature 397:491–497. doi: 10.1038/17276

Cheng Y-S, Yeh H-C, Allen MD (1988) Dynamic Shape Factor of a Plate-Like Particle. Aerosol Sci Technol 8:109–123. doi: 10.1080/02786828808959176

Chin M, Diehl T, Tan Q, et al. (2014) Multi-decadal aerosol variations from 1980 to 2009: a perspective from observations and a global model. Atmos Chem Phys 14:3657–3690. doi: 10.5194/acp-14-3657-2014

Chomette O, Legrand M, Marticorena B (1999) Determination of the wind speed threshold for the emission of desert dust using satellite remote sensing in the thermal infrared. J Geophys Res Atmos 104:31207–31215. doi: 10.1029/1999JD900756

Choobari OA, Zawar-Reza P, Sturman A (2014) The global distribution of mineral dust and its impacts on the climate system: A review. Atmos Res 138:152–165. doi: 10.1016/j.atmosres.2013.11.007

Claquin T, Schulz M, Balkanski YJ (1999) Modeling the mineralogy of atmospheric dust sources. J Geophys Res Atmos 104:22243–22256. doi: 10.1029/1999JD900416

Cziczo DJ, Froyd KD, Hoose C, et al. (2013) Clarifying the Dominant Sources and Mechanisms of Cirrus Cloud Formation. Science (80-) 340:1320–1324. doi: 10.1126/science.1234145

d'Almeida GA, Schütz L (1983) Number, Mass and Volume Distributions of Mineral Aerosol and Soils of the Sahara. J Clim Appl Meteorol 22:233–243. doi: 10.1175/1520-0450(1983)022<0233:NMAVDO>2.0.CO;2

de Wrachien D, Ragab R, Giordano A (2006) CLIMATE CHANGE, LAND DEGRADATION, AND DESERTIFICATION IN THE MEDITERRANEAN ENVIRONMENT. Desertif. Mediterr. Reg. A Secur. Issue. Kluwer Academic Publishers, Dordrecht, pp 353–371

Dee DP, Uppala SM, Simmons AJ, et al. (2011) The ERA-Interim reanalysis: configuration and performance of the data assimilation system. Q J R Meteorol Soc 137:553–597. doi: 10.1002/qj.828

Dickinson RE, Henderson-Sellers A, Kennedy PJ (1993) Biosphere-Atmosphere Transfer Scheme (BATS) Version 1e as Coupled to the NCAR Community Climate Codel. NCAR/TN-387+STR. Boulder, Colorado

Dubovik O, Holben B, Eck TF, et al. (2002) Variability of Absorption and Optical Properties of Key Aerosol Types Observed in Worldwide Locations. J Atmos Sci 59:590–608. doi: 10.1175/1520-0469(2002)059<0590:VOAAOP>2.0.CO;2

Emanuel KA (1991) A Scheme for Representing Cumulus Convection in Large-Scale Models. J Atmos Sci 48:2313–2329. doi: 10.1175/1520-0469(1991)048<2313:ASFRCC>2.0.CO;2

Engelstaedter S, Tegen I, Washington R (2006) North African dust emissions and transport. Earth-Science Rev 79:73–100. doi: 10.1016/j.earscirev.2006.06.004

Engelstaedter S, Washington R (2007) Atmospheric controls on the annual cycle of North African dust. J Geophys Res 112:D03103. doi: 10.1029/2006JD007195

Fan S-M, Horowitz LW, Levy H, Moxim WJ (2004) Impact of air pollution on wet deposition of mineral dust aerosols. Geophys Res Lett 31:2–5. doi: 10.1029/2003GL018501

Fasham MJR (2003) Ocean Biogeochemistry. doi: 10.1007/978-3-642-55844-3

Fécan F, Marticorena B, Bergametti G (1999) Parametrization of the increase of the aeolian erosion threshold wind friction velocity due to soil moisture for arid and semi-arid areas. Ann Geophys 17:149–157. doi: 10.1007/s00585-999-0149-7

Fletcher B (1976a) The erosion of dust by an airflow. J. Phys. D. Appl. Phys. 9:

Fletcher B (1976b) The incipient motion of granular materials. J. Phys. D. Appl. Phys. 9:

Foret G, Bergametti G, Dulac F, Menut L (2006) An optimized particle size bin scheme for modeling mineral dust aerosol. J Geophys Res 111:D17310. doi: 10.1029/2005JD006797

Formenti P, Schütz L, Balkanski Y, et al. (2011) Recent progress in understanding physical and chemical properties of African and Asian mineral dust. Atmos Chem Phys 11:8231–8256. doi: 10.5194/acp-11-8231-2011

Forster P, Ramaswamy V, Artaxo P, et al. (2007) Changes in Atmospheric Constituents and in Radiative Forcing. In: Climate Change 2007: The Physical Science Basis. Contribution of Working Group I to the Fourth Assessment Report of the Intergovernmental Panel on Climate Change [Solomon, S., D. Qin, M. Ma. Cambridge United Kingdom and New York, NY, USA.

Ganor E, Osetinsky I, Stupp A, Alpert P (2010) Increasing trend of African dust, over 49 years, in the eastern Mediterranean. J Geophys Res 115:D07201. doi: 10.1029/2009JD012500

Gao Y, Fan S-M, Sarmiento JL (2003) Aeolian iron input to the ocean through precipitation scavenging: A modeling perspective and its implication for natural iron fertilization in the ocean. J Geophys Res 108:4221. doi: 10.1029/2002JD002420

Georgoulias AK, Alexandri G, Kourtidis KA, et al. (2016a) Spatiotemporal variability and contribution of different aerosol types to the aerosol optical depth over the Eastern Mediterranean. Atmos Chem Phys 16:13853–13884. doi: 10.5194/acp-16-13853-2016

Georgoulias AK, Alexandri G, Kourtidis K a., et al. (2016b) Differences between the MODIS Collection 6 and 5.1 aerosol datasets over the greater Mediterranean region. Atmos Environ 147:310–319. doi: 10.1016/j.atmosenv.2016.10.014

Gibson ER, Hudson PK, Grassian VH (2006) Aerosol chemistry and climate: Laboratory studies of the carbonate component of mineral dust and its reaction products. Geophys Res Lett 33:L13811. doi: 10.1029/2006GL026386

Gillette DA, Marticorena B, Bergametti G (1998) Change in the aerodynamic roughness height by saltating grains: Experimental assessment, test of theory, and operational parameterization. J Geophys Res Atmos 103:6203–6209. doi: 10.1029/98JD00207

Giorgi F (1988) Dry deposition velocities of atmospheric aerosols as inferred by applying a particle dry deposition parameterization to a general circulation model. Tellus B 40B:23–41. doi: 10.1111/j.1600-0889.1988.tb00210.x

Giorgi F (1989) Two-dimensional simulations of possible mesoscale effects of nuclear war fires: 1. Model description. J Geophys Res 94:1127. doi: 10.1029/JD094iD01p01127

Giorgi F, Anyah R (2012) INTRODUCTION The road towards RegCM4 F. Giorgi1,*, R. O. Anyah2. Clim Res 52:3–6. doi: 10.3354/cr01089

Giorgi F, Chameides WL (1986) Rainout lifetimes of highly soluble aerosols and gases as inferred from simulations with a general circulation model. J Geophys Res 91:14367. doi: 10.1029/JD091iD13p14367

Giorgi F, Coppola E, Solmon F, et al. (2012) RegCM4: model description and preliminary tests over multiple CORDEX domains. Clim Res 52:7–29. doi: 10.3354/cr01018

Gkikas a., Hatzianastassiou N, Mihalopoulos N, et al. (2013) The regime of intense desert dust episodes in the Mediterranean based on contemporary satellite observations and ground measurements. Atmos Chem Phys 13:12135–12154. doi: 10.5194/acp-13-12135-2013

Goldstein H, Reynolds R, Reheis M, et al. (2005) Particle Size, CaCO3, Chemical, Magnetic, and Age Data from Surficial Deposits in and around Canyonlands National Park, Utah. Canyonlands Research Bibliography. Paper 1.

Gong SL (2003a) Characterization of soil dust aerosol in China and its transport and distribution during 2001 ACE-Asia: 2. Model simulation and validation. J Geophys Res 108:4262. doi: 10.1029/2002JD002633

Gong SL (2003b) Canadian Aerosol Module: A size-segregated simulation of atmospheric aerosol processes for climate and air quality models 1. Module development. J Geophys Res 108:4007. doi: 10.1029/2001JD002002

Goudie a. S, Middleton NJ (2001) Saharan dust storms: nature and consequences. Earth-Science Rev 56:179–204. doi: 10.1016/S0012-8252(01)00067-8

Greeley R, Iversen JD (1985) Wind as a Geological Process on Earth, Mars, Venus and Titan. Geol Mag 122:578. doi: 10.1017/S0016756800035640

Grell GA (1993) Prognostic Evaluation of Assumptions Used by Cumulus Parameterizations. Mon Weather Rev 121:764–787. doi: 10.1175/1520-0493(1993)121<0764:PEOAUB>2.0.CO;2

Grell GA, Dudhia J, Stauffer DR (1994) A Description of the Fifth-Generation Penn State / NCAR Mesoscale Model (MM5). National Center for Atmospheric Research, Boulder, Colorado

Hänel A, Baars H, Althausen D, et al. (2012) One-year aerosol profiling with EUCAARI Raman lidar at Shangdianzi GAW station: Beijing plume and seasonal variations. J Geophys Res Atmos 117:D13201. doi: 10.1029/2012JD017577

Hansell R a., Tsay SC, Ji Q, et al. (2010) An Assessment of the Surface Longwave Direct Radiative Effect of Airborne Saharan Dust during the NAMMA Field Campaign. J Atmos Sci 67:1048–1065. doi: 10.1175/2009JAS3257.1

Hansen J (2005) Efficacy of climate forcings. J Geophys Res 110:D18104. doi: 10.1029/2005JD005776

Hansen J, Sato M, Lacis A, Ruedy R (1997) The missing climate forcing. Philos Trans R Soc B Biol Sci 352:231–240. doi: 10.1098/rstb.1997.0018

Harris I, Jones PD, Osborn TJ, Lister DH (2014) Updated high-resolution grids of monthly climatic observations - the CRU TS3.10 Dataset. Int J Climatol 34:623–642. doi: 10.1002/joc.3711

Helmert J, Heinold B, Tegen I, et al. (2007) On the direct and semidirect effects of Saharan dust over Europe: A modeling study. J Geophys Res Atmos 112:n/a-n/a. doi: 10.1029/2006JD007444

Hill AA, Dobbie S (2008) The impact of aerosols on non-precipitating marine stratocumulus. II: The semi-direct effect. Q J R Meteorol Soc 134:1155–1165. doi: 10.1002/qj.277

Hillel D (1982) Introduction to Soil Physics.

Holtslag AAM, De Bruijn EIF, Pan H-L (1990) A High Resolution Air Mass Transformation Model for Short-Range Weather Forecasting. Mon Weather Rev 118:1561–1575. doi: 10.1175/1520-0493(1990)118<1561:AHRAMT>2.0.CO;2

Hsu NC, Tsay S-C, King MD, Herman JR (2006) Deep Blue Retrievals of Asian Aerosol Properties During ACE-Asia. IEEE Trans Geosci Remote Sens 44:3180–3195. doi: 10.1109/TGRS.2006.879540

Huang N, Zhang Y, D'Adamo R (2007) A model of the trajectories and midair collision probabilities of sand particles in a steady state saltation cloud. J Geophys Res 112:D08206. doi: 10.1029/2006JD007480

Hudson-Edwards K a., Bristow CS, Cibin G, et al. (2014) Solid-phase phosphorus speciation in Saharan Bodélé Depression dusts and source sediments. Chem Geol 384:16–26. doi: 10.1016/j.chemgeo.2014.06.014

Huneeus N, Schulz M, Balkanski Y, et al. (2011) Global dust model intercomparison in AeroCom phase I. Atmos Chem Phys 11:7781–7816. doi: 10.5194/acp-11-7781-2011

Iacono MJ, Mlawer EJ, Clough SA, Morcrette J-J (2000) Impact of an improved longwave radiation model, RRTM, on the energy budget and thermodynamic properties of the NCAR community climate model, CCM3. J Geophys Res 105:14873. doi: 10.1029/2000JD900091

Intergovernmental Panel on Climate Change (2014) Climate Change 2013 - The Physical Science Basis. doi: 10.1017/CBO9781107415324

Israelevich P, Ganor E, Alpert P, et al. (2012) Predominant transport paths of Saharan dust over the Mediterranean Sea to Europe. J Geophys Res 117:D02205. doi: 10.1029/2011JD016482

Israelevich PL (2002) Desert aerosol transport in the Mediterranean region as inferred from the TOMS aerosol index. J Geophys Res 107:4572. doi: 10.1029/2001JD002011

Israelevich PL (2003) Annual variations of physical properties of desert dust over Israel. J Geophys Res 108:4381. doi:

10.1029/2002JD003163

Iversen JD, White BR (1982) Saltation threshold on Earth, Mars and Venus. Sedimentology 29:111–119. doi: 10.1111/j.1365-3091.1982.tb01713.x

Jickells TD (2005) Global Iron Connections Between Desert Dust, Ocean Biogeochemistry, and Climate. Science (80-) 308:67–71. doi: 10.1126/science.1105959

Johnson BT, Shine KP, Forster PM (2004) The semi-direct aerosol effect: Impact of absorbing aerosols on marine stratocumulus. Q J R Meteorol Soc 130:1407–1422. doi: 10.1256/qj.03.61

Journet E, Desboeufs K V., Caquineau S, Colin J-L (2008) Mineralogy as a critical factor of dust iron solubility. Geophys Res Lett 35:n/a-n/a. doi: 10.1029/2007GL031589

Kahn RA, Gaitley BJ, Garay MJ, et al. (2010) Multiangle Imaging SpectroRadiometer global aerosol product assessment by comparison with the Aerosol Robotic Network. J Geophys Res 115:D23209. doi: 10.1029/2010JD014601

Kain JS (2004) The Kain–Fritsch Convective Parameterization: An Update. J Appl Meteorol 43:170–181. doi: 10.1175/1520-0450(2004)043<0170:TKCPAU>2.0.CO;2

Kain JS, Fritsch JM (1990) A One-Dimensional Entraining/Detraining Plume Model and Its Application in Convective Parameterization. J Atmos Sci 47:2784–2802. doi: 10.1175/1520-0469(1990)047<2784:AODEPM>2.0.CO;2

Kallos G, Papadopoulos A, Katsafados P, Nickovic S (2006) Transatlantic Saharan dust transport: Model simulation and results. J Geophys Res 111:D09204. doi: 10.1029/2005JD006207

Kang J-Y, Yoon S-C, Shao Y, Kim S-W (2011) Comparison of vertical dust flux by implementing three dust emission schemes in WRF/Chem. J Geophys Res 116:D09202. doi: 10.1029/2010JD014649

Karyampudi VM, Carlson TN (1988) Analysis and Numerical Simulations of the Saharan Air Layer and Its Effect on Easterly Wave Disturbances. J Atmos Sci 45:3102–3136. doi: 10.1175/1520-0469(1988)045<3102:AANSOT>2.0.CO;2

Karydis V a., Kumar P, Barahona D, et al. (2011) On the effect of dust particles on global cloud condensation nuclei and cloud droplet number. J Geophys Res Atmos 116:D23204. doi: 10.1029/2011JD016283

Kasibhatla P, Chameides WL, John JS (1997) A three-dimensional global model investigation of seasonal variations in the atmospheric burden of anthropogenic sulfate aerosols. J Geophys Res Atmos 102:3737–3759. doi: 10.1029/96JD03084

Katragkou E, García-Díez M, Vautard R, et al. (2015) Regional climate hindcast simulations within EURO-CORDEX: evaluation of a WRF multi-physics ensemble. Geosci Model Dev 8:603–618. doi: 10.5194/gmd-8-603-2015

Kaufman YJ, Koren I, Remer LA, et al. (2005) Dust transport and deposition observed from the Terra-Moderate Resolution Imaging Spectroradiometer (MODIS) spacecraft over the Atlantic Ocean. J Geophys Res 110:D10S12. doi: 10.1029/2003JD004436

Kiehl JT, Hack JJ, Bonan GB, et al. (1996) Description of the NCAR Community Climate Model (CCM3). National Center for Atmospheric Research, Boulder, Colorado

Kim D, Chin M, Yu H, et al. (2014) Sources, sinks, and transatlantic transport of North African dust aerosol: A multimodel analysis and comparison with remote sensing data. J Geophys Res Atmos 119:6259–6277. doi: 10.1002/2013JD021099

Kinne S (2003) Monthly averages of aerosol properties: A global comparison among models, satellite data, and AERONET ground data. J Geophys Res 108:4634. doi: 10.1029/2001JD001253

Kinne S, Schulz M, Textor C, et al. (2006) An AeroCom initial assessment – optical properties in aerosol component modules of global models. Atmos Chem Phys 6:1815–1834. doi: 10.5194/acp-6-1815-2006

Klose M, Shao Y, Karremann MK, Fink AH (2010) Sahel dust zone and synoptic background. Geophys Res Lett 37:n/a-n/a. doi: 10.1029/2010GL042816

Knippertz P (2014) Mineral Dust. doi: 10.1007/978-94-017-8978-3

Koch D, Del Genio AD (2010) Black carbon semi-direct effects on cloud cover: review and synthesis. Atmos Chem Phys 10:7685–7696. doi: 10.5194/acp-10-7685-2010

Koffi B, Schulz M, Bréon F-M, et al. (2012) Application of the CALIOP layer product to evaluate the vertical distribution of aerosols estimated by global models: AeroCom phase I results. J Geophys Res 117:D10201. doi: 10.1029/2011JD016858

Kok JF (2011a) Does the size distribution of mineral dust aerosols depend on the wind speed at emission? Atmos Chem Phys 11:10149–10156. doi: 10.5194/acp-11-10149-2011

Kok JF (2011b) A scaling theory for the size distribution of emitted dust aerosols suggests climate models underestimate the size of the global dust cycle. Proc Natl Acad Sci U S A 108:1016–21. doi: 10.1073/pnas.1014798108

Kok JF, Parteli EJR, Michaels TI, Karam DB (2012) The physics of wind-blown sand and dust. Rep Prog Phys 75:106901. doi: 10.1088/0034-4885/75/10/106901

Kok JF, Renno NO (2009) A comprehensive numerical model of steady state saltation (COMSALT). J Geophys Res 114:D17204. doi: 10.1029/2009JD011702

Koren I, Kaufman YJ, Washington R, et al. (2006) The Bodélé depression: a single spot in the Sahara that provides most of the mineral dust to the Amazon forest. Environ Res Lett 1:14005. doi: 10.1088/1748-9326/1/1/014005

Kosmas CS, Danalatos NG (1994) Climate Change, Desertification and the Mediterranean Region. Soil Responses to Clim. Chang. Springer Berlin Heidelberg, Berlin, Heidelberg, pp 25–38

Lau K-M, Kim K-M (2006) Observational relationships between aerosol and Asian monsoon rainfall, and circulation. Geophys Res Lett 33:L21810. doi: 10.1029/2006GL027546

Laurent B, Marticorena B, Bergametti G, et al. (2008) Modeling mineral dust emissions from the Sahara desert using new surface properties and soil database. J Geophys Res 113:D14218. doi: 10.1029/2007JD009484

Levy RC, Remer LA, Kleidman RG, et al. (2010) Global evaluation of the Collection 5 MODIS dark-target aerosol products over land. Atmos Chem Phys 10:10399–10420. doi: 10.5194/acp-10-10399-2010

Li W-Q, Zhou Y-H (2007) Statistical behaviors of different-sized grains lifting off in stochastic collisions between mixed sand grains and the bed in aeolian saltation. J Geophys Res 112:D22106. doi: 10.1029/2006JD007888

Liao H, Seinfeld JH (1998) Radiative forcing by mineral dust aerosols: Sensitivity to key variables. J Geophys Res Atmos 103:31637–31645. doi: 10.1029/1998JD200036

Liu Z, Vaughan M, Winker D, et al. (2009) The CALIPSO Lidar Cloud and Aerosol Discrimination: Version 2 Algorithm and Initial Assessment of Performance. J Atmos Ocean Technol 26:1198–1213. doi: 10.1175/2009JTECHA1229.1

Loeb NG, Wielicki BA, Doelling DR, et al. (2009) Toward Optimal Closure of the Earth's Top-of-Atmosphere Radiation

Budget. J Clim 22:748–766. doi: 10.1175/2008JCLI2637.1

Lohmann U, Feichter J (2004) Global indirect aerosol effects: a review. Atmos Chem Phys Discuss 4:7561–7614. doi: 10.5194/acpd-4-7561-2004

Lohmann U, Feichter J (2001) Can the direct and semi-direct aerosol effect compete with the indirect effect on a global scale? Geophys Res Lett 28:159–161. doi: 10.1029/2000GL012051

Loosmore G a, Hunt JR (2000) Dust resuspension without saltation. J Geophys Res 105:20663–20672. doi: 10.1029/2000JD900271

Mahowald N, Albani S, Kok JF, et al. (2014) The size distribution of desert dust aerosols and its impact on the Earth system. Aeolian Res 15:53–71. doi: 10.1016/j.aeolia.2013.09.002

Mahowald NM, Artaxo P, Baker AR, et al. (2005a) Impacts of biomass burning emissions and land use change on Amazonian atmospheric phosphorus cycling and deposition. Global Biogeochem Cycles 19:n/a-n/a. doi: 10.1029/2005GB002541

Mahowald NM, Baker AR, Bergametti G, et al. (2005b) Atmospheric global dust cycle and iron inputs to the ocean. Global Biogeochem Cycles 19:n/a-n/a. doi: 10.1029/2004GB002402

Mahowald NM, Luo C (2003) A less dusty future? Geophys Res Lett 30:n/a-n/a. doi: 10.1029/2003GL017880

Mahowald NM, Muhs DR, Levis S, et al. (2006) Change in atmospheric mineral aerosols in response to climate: Last glacial period, preindustrial, modern, and doubled carbon dioxide climates. J Geophys Res Atmos 111:n/a-n/a. doi: 10.1029/2005JD006653

Marticorena B, Bergametti G (1995) Modeling the atmospheric dust cycle: 1. Design of a soil-derived dust emission scheme. J Geophys Res 100:16415. doi: 10.1029/95JD00690

Marticorena B, Bergametti G (1996) Two-year simulations of seasonal and interannual changes of the Saharan dust emissions. Geophys Res Lett 23:1921–1924. doi: 10.1029/96GL01432

Martin JH, Fitzwater SE (1988) Iron deficiency limits phytoplankton growth in the north-east Pacific subarctic. Nature 331:341–343. doi: 10.1038/331341a0

Martínez-Garcia A, Rosell-Melé A, Geibert W, et al. (2009) Links between iron supply, marine productivity, sea surface temperature, and CO2 over the last 1.1 Ma. Paleoceanography 24:1–14. doi: 10.1029/2008PA001657

Mbourou GN, Bertrand JJ, Nicholson SE (1997) The Diurnal and Seasonal Cycles of Wind-Borne Dust over Africa North of the Equator. J Appl Meteorol 36:868–882. doi: 10.1175/1520-0450(1997)036<0868:TDASCO>2.0.CO;2

Menut L, Forêt G, Bergametti G (2007) Sensitivity of mineral dust concentrations to the model size distribution accuracy. J Geophys Res 112:D10210. doi: 10.1029/2006JD007766

Menut L, Pérez C, Haustein K, et al. (2013) Impact of surface roughness and soil texture on mineral dust emission fluxes modeling. J Geophys Res Atmos 118:6505–6520. doi: 10.1002/jgrd.50313

Meskhidze N, Chameides WL, Nenes A, Chen G (2003) Iron mobilization in mineral dust: Can anthropogenic SO 2 emissions affect ocean productivity? Geophys Res Lett 30:10.1029/2003GL018035. doi: 10.1029/2003GL018035

Miller RL, Cakmur R V., Perlwitz J, et al. (2006) Mineral dust aerosols in the NASA Goddard Institute for Space Sciences ModelE atmospheric general circulation model. J Geophys Res 111:D06208. doi: 10.1029/2005JD005796

Mlawer EJ, Clough SA (1997) On the Extension of Rapid Radiative Transfer Model to the Shortwave Region Longwave

Method and. U.S. Department of Energy, CONF-9603149

Mlawer EJ, Taubman SJ, Brown PD, et al. (1997) Radiative transfer for inhomogeneous atmospheres: RRTM, a validated correlated-k model for the longwave. J Geophys Res 102:16663. doi: 10.1029/97JD00237

Moulin C, Lambert CE, Dayan U, et al. (1998) Satellite climatology of African dust transport in the Mediterranean atmosphere. J Geophys Res 103:13137. doi: 10.1029/98JD00171

Myhre G, Shindell D, Bréon F-M, et al. (2013) Anthropogenic and Natural Radiative Forcing. In: Intergovernmental Panel on Climate Change (ed) Clim. Chang. 2013 - Phys. Sci. Basis. Cambridge University Press, Cambridge, pp 659–740

Nabat P, Solmon F, Mallet M, et al. (2012) Dust emission size distribution impact on aerosol budget and radiative forcing over the Mediterranean region: a regional climate model approach. Atmos Chem Phys 12:10545–10567. doi: 10.5194/acp-12-10545-2012

Nabat P, Somot S, Mallet M, et al. (2014) Direct and semi-direct aerosol radiative effect on the Mediterranean climate variability using a coupled regional climate system model. Clim Dyn 44:1127–1155. doi: 10.1007/s00382-014-2205-6

Nicholson SE (2013) The West African Sahel: A Review of Recent Studies on the Rainfall Regime and Its Interannual Variability. ISRN Meteorol 2013:1–32. doi: 10.1155/2013/453521

Okin GS, Bullard JE, Reynolds RL, et al. (2011) Dust: Small-scale processes with global consequences. Eos (Washington DC) 92:241–242. doi: 10.1029/2011EO290001

Okin GS, Mahowald N, Chadwick OA, Artaxo P (2004) Impact of desert dust on the biogeochemistry of phosphorus in terrestrial ecosystems. Global Biogeochem Cycles. doi: 10.1029/2003GB002145

Oleson KW, Lawrence DM, Bonan GB, et al. (2013) Technical Description of version 4.5 of the Community Land Model (CLM) Coordinating. NCAR/TN-503+STR NCAR. Boulder, Colorado

Omar AH, Winker DM, Vaughan M a., et al. (2009) The CALIPSO Automated Aerosol Classification and Lidar Ratio Selection Algorithm. J Atmos Ocean Technol 26:1994–2014. doi: 10.1175/2009JTECHA1231.1

Owen PR (1964) Saltation of uniform grains in air. J Fluid Mech 20:225–242. doi: 10.1017/S0022112064001173

Pal JS, Small EE, Eltahir E a. B (2000) Simulation of regional-scale water and energy budgets: Representation of subgrid cloud and precipitation processes within RegCM. J Geophys Res Atmos 105:29579–29594. doi: 10.1029/2000JD900415

Pincus R (2003) A fast, flexible, approximate technique for computing radiative transfer in inhomogeneous cloud fields. J Geophys Res 108:4376. doi: 10.1029/2002JD003322

Prenni AJ, Petters MD, Kreidenweis SM, et al. (2009) Relative roles of biogenic emissions and Saharan dust as ice nuclei in the Amazon basin. Nat Geosci 2:402–405. doi: 10.1038/ngeo517

Priestley CHB (1959) Estimation of surface stress and heat flux from profile data. Q J R Meteorol Soc 85:415–418. doi: 10.1002/qj.49708536611

Prospero JM, Collard F-X, Molinié J, Jeannot A (2014) Characterizing the annual cycle of African dust transport to the Caribbean Basin and South America and its impact on the environment and air quality. Global Biogeochem Cycles 28:757–773. doi: 10.1002/2013GB004802

Prospero JM, Ginoux P, Torres O, et al. (2002) Environmental characterization of global sources of atmospheric soil dust identified with the NIMBUS 7 Total Ozone Mapping Spectrometer (TOMS) absorbing aerosol product. Rev Geophys

40:1002. doi: 10.1029/2000RG000095

Prospero JM, Glaccum RA, Nees RT (1981) Atmospheric transport of soil dust from Africa to South America. Nature 289:570–572. doi: 10.1038/289570a0

Qian Y, Giorgi F, Huang Y, et al. (2001) Regional simulation of anthropogenic sulfur over East Asia and its sensitivity to model parameters. Tellus B 53:171–191. doi: 10.1034/j.1600-0889.2001.d01-14.x

Ramanathan V, Crutzen PJ, Kiehl JT, Rosenfeld D (2001) Aerosols, climate, and the hydrological cycle. Science 294:2119–24. doi: 10.1126/science.1064034

Rice MA, Willetts BB, McEwan IK (1995) An experimental study of multiple grain-size ejecta produced by collisions of saltating grains with a flat bed. Sedimentology 42:695–706. doi: 10.1111/j.1365-3091.1995.tb00401.x

Ridley D a., Heald CL, Ford B (2012) North African dust export and deposition: A satellite and model perspective. J Geophys Res 117:D02202. doi: 10.1029/2011JD016794

Rodríguez S, Cuevas E, Prospero JM, et al. (2015) Modulation of Saharan dust export by the North African dipole. Atmos Chem Phys 15:7471–7486. doi: 10.5194/acp-15-7471-2015

Ryder CL, Highwood EJ, Rosenberg PD, et al. (2013) Optical properties of Saharan dust aerosol and contribution from the coarse mode as measured during the Fennec 2011 aircraft campaign. Atmos Chem Phys 13:303–325. doi: 10.5194/acp-13-303-2013

Sayer AM, Hsu NC, Bettenhausen C, et al. (2015) Effect of MODIS Terra radiometric calibration improvements on Collection 6 Deep Blue aerosol products: Validation and Terra/Aqua consistency. J Geophys Res Atmos 120:12,157-12,174. doi: 10.1002/2015JD023878

Sayer AM, Munchak LA, Hsu NC, et al. (2014) MODIS Collection 6 aerosol products: Comparison between Aqua's e-Deep Blue, Dark Target, and "merged" data sets, and usage recommendations. J Geophys Res Atmos 119:13,965-13,989. doi: 10.1002/2014JD022453

Schuster GL, Vaughan M, MacDonnell D, et al. (2012) Comparison of CALIPSO aerosol optical depth retrievals to AERONET measurements, and a climatology for the lidar ratio of dust. Atmos Chem Phys 12:7431–7452. doi: 10.5194/acp-12-7431-2012

Seinfeld JH, Pandis SN (1998) Atmospheric Chemistry and Physics: From Air Pollution to Climate Change.

Shalaby a., Zakey a. S, Tawfik a. B, et al. (2012) Implementation and evaluation of online gas-phase chemistry within a regional climate model (RegCM-CHEM4). Geosci Model Dev 5:741–760. doi: 10.5194/gmd-5-741-2012

Shao Y (2009) Physics and Modelling of Wind Erosion. doi: 10.1007/978-1-4020-8895-7

Shao Y, Ishizuka M, Mikami M, Leys JF (2011a) Parameterization of size-resolved dust emission and validation with measurements. J Geophys Res 116:D08203. doi: 10.1029/2010JD014527

Shao Y, Lu H (2000) A simple expression for wind erosion threshold friction velocity. J Geophys Res 105:437–443.

Shao Y, Raupach MR, Findlater PA (1993) Effect of saltation bombardment on the entrainment of dust by wind. J Geophys Res 98:12719. doi: 10.1029/93JD00396

Shao Y, Wyrwoll K-H, Chappell A, et al. (2011b) Dust cycle: An emerging core theme in Earth system science. Aeolian Res 2:181–204. doi: 10.1016/j.aeolia.2011.02.001

Skibba R (2016) Climate-change study raises spectre of advancing Mediterranean desert. Nature. doi:

10.1038/nature.2016.20894

Slinn SA, Slinn WGN (1980) Predictions for particle deposition on natural waters. Atmos Environ 14:1013–1016. doi: 10.1016/0004-6981(80)90032-3

Slinn WG. (1982) Predictions for particle deposition to vegetative canopies. Atmos Environ 16:1785–1794. doi: 10.1016/0004-6981(82)90271-2

Sokolik IN, Toon OB (1999) Incorporation of mineralogical composition into models of the radiative properties of mineral aerosol from UV to IR wavelengths. J Geophys Res Atmos 104:9423–9444. doi: 10.1029/1998JD200048

Sokolik IN, Winker DM, Bergametti G, et al. (2001) Introduction to special section: Outstanding problems in quantifying the radiative impacts of mineral dust. J Geophys Res Atmos 106:18015–18027. doi: 10.1029/2000JD900498

Solmon F, Elguindi N, Mallet M (2012) Radiative and climatic effects of dust over West Africa, as simulated by a regional climate model. Clim Res 52:97–113. doi: 10.3354/cr01039

Solmon F, Giorgi F, Liousse C (2006) Aerosol modelling for regional climate studies: application to anthropogenic particles and evaluation over a European/African domain. Tellus B 58:51–72. doi: 10.1111/j.1600-0889.2005.00155.x

Solmon F, Mallet M, Elguindi N, et al. (2008) Dust aerosol impact on regional precipitation over western Africa, mechanisms and sensitivity to absorption properties. Geophys Res Lett 35:L24705. doi: 10.1029/2008GL035900

Spyrou C, Kallos G, Mitsakou C, et al. (2013) Modeling the radiative effects of desert dust on weather and regional climate. Atmos Chem Phys 13:5489–5504. doi: 10.5194/acp-13-5489-2013

Steiner A, Tawfik A, Shalaby A, et al. (2014) Climatological simulations of ozone and atmospheric aerosols in the Greater Cairo region. Clim Res 59:207–228. doi: 10.3354/cr01211

Stengel MS, Kniffka AK, Meirink JFM, et al. (2014) CLAAS: The CM SAF cloud property data set using SEVIRI. Atmos Chem Phys 14:4297–4311. doi: 10.5194/acp-14-4297-2014

Stephens GL, Wood NB, Pakula LA (2004) On the radiative effects of dust on tropical convection. Geophys Res Lett 31:1–4. doi: 10.1029/2004GL021342

Sullivan RC, Moore MJK, Petters MD, et al. (2009) Effect of chemical mixing state on the hygroscopicity and cloud nucleation properties of calcium mineral dust particles. Atmos Chem Phys Discuss 9:2609–2644. doi: 10.5194/acpd-9-2609-2009

Swap R, Garstang M, Greco S, et al. (1992) Saharan dust in the Amazon Basin. Tellus B 44:133–149. doi: 10.1034/j.1600-0889.1992.t01-1-00005.x

Tegen I (2003) Modeling the mineral dust aerosol cycle in the climate system. Quat Sci Rev 22:1821–1834. doi: 10.1016/S0277-3791(03)00163-X

Tegen I, Koch D, Lacis AA, Sato M (2000) Trends in tropospheric aerosol loads and corresponding impact on direct radiative forcing between 1950 and 1990: A model study. J Geophys Res 105:26971. doi: 10.1029/2000JD900280

Tegen I, Schepanski K, Heinold B (2013) Comparing two years of Saharan dust source activation obtained by regional modelling and satellite observations. Atmos Chem Phys 13:2381–2390. doi: 10.5194/acp-13-2381-2013

Tegen I, Werner M, Harrison SP, Kohfeld KE (2004) Relative importance of climate and land use in determining present and future global soil dust emission. Geophys Res Lett 31:n/a-n/a. doi: 10.1029/2003GL019216

Tesche M, Wandinger U, Ansmann a., et al. (2013) Ground-based validation of CALIPSO observations of dust and smoke

in the Cape Verde region. J Geophys Res Atmos 118:2889–2902. doi: 10.1002/jgrd.50248

Textor C, Schulz M, Guibert S, et al. (2006) Analysis and quantification of the diversities of aerosol life cycles within AeroCom. Atmos Chem Phys 6:1777–1813. doi: 10.5194/acpd-5-8331-2005

Thomson AM, Calvin K V., Smith SJ, et al. (2011) RCP4.5: A pathway for stabilization of radiative forcing by 2100. Clim Change 109:77–94. doi: 10.1007/s10584-011-0151-4

Tiedtke M (1989) A Comprehensive Mass Flux Scheme for Cumulus Parameterization in Large-Scale Models. Mon Weather Rev 117:1779–1800. doi: 10.1175/1520-0493(1989)117<1779:ACMFSF>2.0.CO;2

Tiedtke M (1993) Representation of Clouds in Large-Scale Models. Mon Weather Rev 121:3040–3061. doi: 10.1175/1520-0493(1993)121<3040:ROCILS>2.0.CO;2

Tsikerdekis A, Zanis P, Steiner A, et al. (2015) Dust size parameterization in RegCM4: Impact on aerosol burden and radiative forcing. AGU 2015 Fall Meet. San Francisco, p A33L–0357

Tsikerdekis A, Zanis P, Steiner AL, et al. (2017a) Simulated Dust Over the Sahara and Mediterranean with a Regional Climate Model (RegCM4). pp 615–620. COMECAP 2016.

Tsikerdekis A, Zanis P, Steiner AL, et al. (2017b) Impact of dust size parameterizations on aerosol burden and radiative forcing in RegCM4. Atmos Chem Phys 17:769–791. doi: 10.5194/acp-17-769-2017

Tsikerdekis A, Zanis P, Steiner AL, et al. (2016a) Dust over the Mediterranean using an online climate-chemistry regional climate model (REGCM4). Mediterr. Clim. Var. 2016 Conf.

Tsikerdekis A, Zanis P, Steiner LA, et al. (2016b) Modeling the Trans-Atlantic transportation of Saharan dust. Proceeding 14th Int. Congr. Geol. Soc. Greece

Twomey S (1977) The Influence of Pollution on the Shortwave Albedo of Clouds. J Atmos Sci 34:1149–1152. doi: 10.1175/1520-0469(1977)034<1149:TIOPOT>2.0.CO;2

Van Der Does M, Korte LF, Munday CI, et al. (2016) Particle size traces modern Saharan dust transport and deposition across the equatorial North Atlantic. Atmos Chem Phys 16:13697–13710. doi: 10.5194/acp-16-13697-2016

Vaughan M a., Powell K a., Winker DM, et al. (2009) Fully Automated Detection of Cloud and Aerosol Layers in the CALIPSO Lidar Measurements. J Atmos Ocean Technol 26:2034–2050. doi: 10.1175/2009JTECHA1228.1

Wandinger U, Tesche M, Seifert P, et al. (2010) Size matters: Influence of multiple scattering on CALIPSO light-extinction profiling in desert dust. Geophys Res Lett 37:L10801. doi: 10.1029/2010GL042815

Washington R, Bouet C, Cautenet G, et al. (2009) Dust as a tipping element: the Bodele Depression, Chad. Proc Natl Acad Sci U S A 106:20564–71. doi: 10.1073/pnas.0711850106

Washington R, Todd M, Middleton NJ, Goudie AS (2003) Dust-Storm Source Areas Determined by the Total Ozone Monitoring Spectrometer and Surface Observations. Ann Assoc Am Geogr 93:297–313. doi: 10.1111/1467-8306.9302003

Williams ER (2008) Comment on “Atmospheric controls on the annual cycle of North African dust” by S. Engelstaedter and R. Washington. J Geophys Res 113:D23109. doi: 10.1029/2008JD009930

Winker DM, Vaughan M a., Omar A, et al. (2009) Overview of the CALIPSO Mission and CALIOP Data Processing Algorithms. J Atmos Ocean Technol 26:2310–2323. doi: 10.1175/2009JTECHA1281.1

Woodage MJ, Slingo A, Woodward S, Comer RE (2010) U.K. HiGEM: Simulations of Desert Dust and Biomass Burning

Aerosols with a High-Resolution Atmospheric GCM. J Clim 23:1636–1659. doi: 10.1175/2009JCLI2994.1

Woodward S, Roberts DL, Betts R a. (2005) A simulation of the effect of climate change-induced desertification on mineral dust aerosol. Geophys Res Lett 32:n/a-n/a. doi: 10.1029/2005GL023482

Yamashita K, Murakami M, Hashimoto A, Tajiri T (2011) CCN Ability of Asian Mineral Dust Particles and Their Effects on Cloud Droplet Formation. J Meteorol Soc Japan 89:581–587. doi: 10.2151/jmsj.2011-512

Young S a., Vaughan M a. (2009) The Retrieval of Profiles of Particulate Extinction from Cloud-Aerosol Lidar Infrared Pathfinder Satellite Observations (CALIPSO) Data: Algorithm Description. J Atmos Ocean Technol 26:1105–1119. doi: 10.1175/2008JTECHA1221.1

Yu H, Chin M, Bian H, et al. (2015) Quantification of trans-Atlantic dust transport from seven-year (2007–2013) record of CALIPSO lidar measurements. Remote Sens Environ 159:232–249. doi: 10.1016/j.rse.2014.12.010

Zakey a. S, Solmon F, Giorgi F (2006) Implementation and testing of a desert dust module in a regional climate model. Atmos Chem Phys 6:4687–4704. doi: 10.5194/acp-6-4687-2006

Zakey AS, Giorgi F, Bi X (2008) Modeling of sea salt in a regional climate model: Fluxes and radiative forcing. J Geophys Res 113:D14221. doi: 10.1029/2007JD009209

Zanis P, Katragkou E, Tegoulias I, et al. (2012a) Regional Air Quality Simulations Over Europe in Present and Future Climate: Evaluation and Climate Change Impacts on Near Surface Ozone. COMECAP, Athens, pp 1–6

Zanis P, Ntogras C, Zakey a, et al. (2012b) Regional climate feedback of anthropogenic aerosols over Europe using RegCM3. Clim Res 52:267–278. doi: 10.3354/cr01070

Zender CS, Bian H, Newman D (2003) Mineral Dust Entrainment and Deposition (DEAD) model: Description and 1990s dust climatology. J Geophys Res 108:4416. doi: 10.1029/2002JD002775

Zhang L (2001) A size-segregated particle dry deposition scheme for an atmospheric aerosol module. Atmos Environ 35:549–560. doi: 10.1016/S1352-2310(00)00326-5

Zimmermann F, Weinbruch S, Schütz L, et al. (2008) Ice nucleation properties of the most abundant mineral dust phases. J Geophys Res 113:D23204. doi: 10.1029/2008JD010655

Zipser EJ, Twohy CH, Tsay S-C, et al. (2009) The Saharan Air Layer and the Fate of African Easterly Waves—NASA's AMMA Field Study of Tropical Cyclogenesis. Bull Am Meteorol Soc 90:1137–1156. doi: 10.1175/2009BAMS2728.1

Appendix

Statistical Formulas

Modified Normalized Mean Bias (MNMB): $MNMB = \frac{2}{N}\sum_i \frac{\mathrm{sim}_i - obs_i}{\mathrm{sim}_i + obs_i}$

Fractional Gross Error (FGE): $FGE = \frac{2}{N}\sum_i \left|\frac{\mathrm{sim}_i - obs_i}{\mathrm{sim}_i + obs_i}\right|$

Lower Confidence Interval 95% (LCI): $LCI = MEAN - \frac{1.96 * SD}{\sqrt{N}}$

Upper Confidence Interval 95% (UCI): $UCI = MEAN + \frac{1.96 * SD}{\sqrt{N}}$

Percent Bias (P.Bias): $P.Bias = \frac{100 \cdot [\sum(\mathrm{sim} - obs)]}{\sum(obs)}$

where obs and sim is the observed and model quantities, respectively. N is the population. SD is the standard deviation of the population. MEAN is the average value of the population.

Dust Related Formulas

Fraction of wet deposition to total deposition (FWET): $FWET(Unitless) = \frac{Wet\ Deposition}{Total\ Deposition}$

Deposition Lifetimes (DL): $DL(day) = \frac{Dust\ Column\ Burden}{Total\ Deposition}$

Loss Frequency (LF): $LF(day^{-1}) = \frac{Total\ Deposition}{Dust\ Column\ Burden}$

Mass Extinction Efficiency (MEE): $MME(m^2 \cdot mg^{-1}) = \frac{Dust\ Optical\ Depth}{Dust\ Column\ Burden}$

Dust optical properties in RegCM4

Table 1. 4-Bin specific dust extinction coefficient used in RegCM4 for the CCM3 radiative scheme. The first column depicts CCM3 radiation bands range (nm).

EXT	1	2	3	4
200-245	5.083	0.901	0.373	0.178
245-265	4.736	0.900	0.375	0.179
265-275	4.560	0.905	0.376	0.179
275-285	4.445	0.913	0.377	0.179
285-295	4.332	0.923	0.379	0.180
295-305	4.222	0.935	0.379	0.180
305-350	3.941	0.962	0.380	0.181
350-640	2.723	0.948	0.391	0.184
640-700	1.779	1.083	0.390	0.186
700-5000	0.263	0.609	0.501	0.239
701-5000	0.262	0.609	0.502	0.239
701-5000	0.262	0.609	0.502	0.239
701-5000	0.262	0.609	0.502	0.239
701-5000	0.262	0.609	0.502	0.239
702-5000	0.262	0.609	0.502	0.240
702-5000	0.262	0.609	0.502	0.240
2630-2860	0.040	0.483	0.668	0.193
4160-4550	0.008	0.134	0.444	0.310

Table 2. 4-Bin asymmetry parameter used in RegCM4 for the CCM3 radiative scheme. The first column depicts CCM3 radiation bands range (nm).

ASY	1	2	3	4
200-245	0.737	0.920	0.945	0.948
245-265	0.703	0.905	0.943	0.948
265-275	0.688	0.898	0.942	0.948
275-285	0.679	0.893	0.940	0.948
285-295	0.670	0.889	0.939	0.947
295-305	0.660	0.885	0.937	0.947
305-350	0.633	0.868	0.928	0.946
350-640	0.539	0.708	0.836	0.890
640-700	0.461	0.623	0.761	0.821
700-5000	0.121	0.483	0.676	0.687
701-5000	0.120	0.483	0.676	0.687
701-5000	0.120	0.483	0.676	0.687
701-5000	0.120	0.483	0.676	0.687
701-5000	0.120	0.483	0.676	0.687
702-5000	0.120	0.483	0.676	0.687
702-5000	0.120	0.483	0.676	0.687
2630-2860	0.059	0.528	0.714	0.593
4160-4550	0.023	0.276	0.667	0.667

Table 3. 4-Bin single scattering albedo used in RegCM4 for the CCM3 radiative scheme. The first column depicts CCM3

radiation bands range (nm).

SSA	1	2	3	4
200-245	0.734	0.549	0.536	0.543
245-265	0.766	0.563	0.536	0.541
265-275	0.780	0.574	0.537	0.541
275-285	0.788	0.583	0.539	0.541
285-295	0.796	0.593	0.541	0.540
295-305	0.803	0.604	0.544	0.540
305-350	0.828	0.642	0.557	0.542
350-640	0.922	0.832	0.749	0.670
640-700	0.960	0.951	0.903	0.838
700-5000	0.663	0.977	0.971	0.942
701-5000	0.663	0.977	0.971	0.942
701-5000	0.663	0.977	0.971	0.942
701-5000	0.663	0.977	0.971	0.942
701-5000	0.663	0.977	0.971	0.942
702-5000	0.663	0.977	0.971	0.942
702-5000	0.663	0.977	0.971	0.942
2630-2860	0.649	0.984	0.986	0.950
4160-4550	0.484	0.973	0.990	0.980

Table 4. 12-Bin specific dust extinction coefficient used in RegCM4 for the CCM3 radiative scheme. The first column depicts CCM3 radiation bands range (nm).

EXT	1	2	3	4	5	6	7	8	9	10	11	12
200-245	7.167	5.722	1.553	0.663	0.412	0.291	0.233	0.185	0.129	0.073	0.043	0.028
245-265	5.464	5.762	1.527	0.666	0.414	0.292	0.235	0.186	0.129	0.074	0.043	0.028
265-275	4.815	5.710	1.505	0.667	0.416	0.293	0.235	0.186	0.129	0.074	0.043	0.028
275-285	4.382	5.673	1.499	0.669	0.417	0.294	0.235	0.186	0.130	0.074	0.043	0.028
285-295	3.967	5.631	1.498	0.674	0.419	0.294	0.236	0.187	0.130	0.074	0.043	0.028
295-305	3.584	5.586	1.492	0.680	0.419	0.295	0.236	0.187	0.130	0.074	0.043	0.028
305-350	2.754	5.382	1.522	0.690	0.420	0.296	0.237	0.187	0.130	0.074	0.043	0.028
350-640	0.893	3.484	2.008	0.724	0.433	0.303	0.242	0.191	0.132	0.075	0.044	0.028
640-700	0.212	1.849	2.328	0.709	0.431	0.300	0.248	0.197	0.134	0.075	0.044	0.028
700-5000	0.024	0.224	0.577	0.611	0.537	0.431	0.343	0.250	0.148	0.084	0.047	0.029
701-5000	0.024	0.223	0.576	0.610	0.537	0.431	0.343	0.250	0.148	0.084	0.047	0.029
701-5000	0.024	0.223	0.576	0.610	0.537	0.431	0.343	0.250	0.148	0.084	0.047	0.029
701-5000	0.024	0.223	0.576	0.610	0.537	0.431	0.343	0.250	0.148	0.084	0.047	0.029
701-5000	0.024	0.223	0.576	0.610	0.537	0.431	0.343	0.250	0.148	0.084	0.047	0.029
702-5000	0.024	0.223	0.576	0.610	0.537	0.431	0.343	0.250	0.148	0.084	0.047	0.029
702-5000	0.024	0.223	0.576	0.610	0.537	0.431	0.343	0.250	0.148	0.084	0.047	0.029
2630-2860	0.004	0.019	0.206	0.678	0.747	0.517	0.290	0.173	0.162	0.083	0.046	0.030
4160-4550	0.002	0.004	0.043	0.211	0.422	0.494	0.462	0.342	0.148	0.093	0.044	0.030

Table 5. 12-Bin asymmetry parameter used in RegCM4 for the CCM3 radiative scheme. The first column depicts CCM3 radiation bands range (nm).

ASY	1	2	3	4	5	6	7	8	9	10	11	12
200-245	0.605	0.731	0.881	0.935	0.945	0.947	0.948	0.948	0.948	0.949	0.949	0.949
245-265	0.522	0.725	0.841	0.926	0.942	0.946	0.947	0.948	0.948	0.949	0.949	0.949
265-275	0.495	0.724	0.818	0.920	0.940	0.945	0.947	0.948	0.948	0.949	0.949	0.949
275-285	0.479	0.722	0.805	0.915	0.938	0.945	0.947	0.948	0.948	0.949	0.949	0.949
285-295	0.462	0.721	0.789	0.911	0.936	0.944	0.946	0.947	0.948	0.949	0.949	0.949
295-305	0.443	0.721	0.775	0.907	0.934	0.943	0.946	0.947	0.948	0.949	0.949	0.949
305-350	0.383	0.715	0.742	0.890	0.923	0.938	0.943	0.946	0.948	0.949	0.949	0.949
350-640	0.175	0.617	0.667	0.787	0.826	0.857	0.872	0.887	0.906	0.928	0.940	0.946
640-700	0.082	0.487	0.674	0.666	0.754	0.772	0.803	0.819	0.843	0.879	0.910	0.931
700-5000	0.014	0.097	0.324	0.577	0.669	0.692	0.689	0.682	0.690	0.787	0.817	0.842
701-5000	0.014	0.097	0.324	0.577	0.669	0.692	0.689	0.682	0.690	0.787	0.817	0.842
701-5000	0.014	0.097	0.324	0.577	0.669	0.692	0.689	0.682	0.690	0.787	0.817	0.842
701-5000	0.014	0.097	0.324	0.577	0.669	0.692	0.689	0.682	0.690	0.787	0.817	0.842
701-5000	0.014	0.097	0.324	0.577	0.669	0.692	0.689	0.682	0.690	0.787	0.817	0.842
702-5000	0.014	0.097	0.324	0.577	0.669	0.692	0.689	0.682	0.690	0.787	0.817	0.842
702-5000	0.014	0.097	0.324	0.577	0.669	0.692	0.689	0.682	0.690	0.787	0.817	0.842
2630-2860	0.005	0.036	0.270	0.649	0.729	0.695	0.570	0.510	0.741	0.768	0.804	0.841
4160-4550	0.002	0.015	0.101	0.432	0.642	0.723	0.738	0.699	0.557	0.761	0.745	0.801

Table 6. 12-Bin asymmetry parameter used in RegCM4 for the CCM3 radiative scheme. The first column depicts CCM3 radiation bands range (nm).

SSA	1	2	3	4	5	6	7	8	9	10	11	12
200-245	0.8309	0.7538	0.5861	0.5368	0.5344	0.5377	0.5401	0.5423	0.5449	0.5474	0.5487	0.5491
245-265	0.8301	0.8040	0.6073	0.5456	0.5354	0.5366	0.5387	0.5410	0.5440	0.5469	0.5484	0.5490
265-275	0.8273	0.8258	0.6182	0.5515	0.5373	0.5366	0.5382	0.5404	0.5436	0.5467	0.5483	0.5489
275-285	0.8251	0.8382	0.6273	0.5575	0.5401	0.5366	0.5380	0.5401	0.5433	0.5465	0.5482	0.5489
285-295	0.8232	0.8505	0.6358	0.5654	0.5432	0.5373	0.5381	0.5399	0.5430	0.5464	0.5481	0.5488
295-305	0.8217	0.8609	0.6461	0.5749	0.5462	0.5388	0.5382	0.5397	0.5427	0.5462	0.5480	0.5488
305-350	0.8259	0.8865	0.6879	0.6088	0.5623	0.5465	0.5420	0.5408	0.5424	0.5458	0.5478	0.5487
350-640	0.8628	0.9524	0.8835	0.8093	0.7615	0.7244	0.7004	0.6761	0.6405	0.5962	0.5683	0.5554
640-700	0.8818	0.9781	0.9757	0.9364	0.9097	0.8866	0.8704	0.8498	0.8039	0.7269	0.6486	0.5947
700-5000	0.2747	0.6896	0.9532	0.9798	0.9740	0.9654	0.9571	0.9466	0.9256	0.8913	0.8461	0.7959
701-5000	0.2746	0.6895	0.9532	0.9799	0.9740	0.9655	0.9571	0.9466	0.9256	0.8914	0.8462	0.7960
701-5000	0.2746	0.6895	0.9532	0.9799	0.9740	0.9655	0.9571	0.9466	0.9256	0.8914	0.8462	0.7960
701-5000	0.2746	0.6895	0.9532	0.9799	0.9740	0.9655	0.9571	0.9466	0.9256	0.8914	0.8462	0.7960
701-5000	0.2746	0.6895	0.9532	0.9799	0.9740	0.9655	0.9571	0.9466	0.9256	0.8914	0.8462	0.7960
702-5000	0.2745	0.6895	0.9532	0.9799	0.9740	0.9656	0.9571	0.9467	0.9257	0.8915	0.8462	0.7960
702-5000	0.2745	0.6895	0.9532	0.9799	0.9740	0.9656	0.9571	0.9467	0.9257	0.8915	0.8462	0.7960
2630-2860	0.1624	0.6990	0.9660	0.9882	0.9884	0.9822	0.9672	0.9464	0.9431	0.9129	0.8666	0.8222
4160-4550	0.0568	0.4688	0.9185	0.9840	0.9901	0.9909	0.9899	0.9855	0.9643	0.9478	0.9145	0.8887